

DOCTORAL DISSERTATION

Computer Simulation of FIB Sputtering

Completed as part of the degree program: Doctorate in (Technical) Engineering Sciences

By:

Sloan Jobe Lindsey, BS, MSc

Matriculation Number: 1028783

Rudolf-Nurejew-Promenade 9/20/13

1220 Wien

At the Vienna University of Technology

School of Electrical Engineering and Information Technology

Institute for Solid State Electronics

Under the Advisement of:

Ao. Univ.-Prof. Dipl.-Ing. Dr. Techn. Gerhard Hobler

Wien, February 2015

Eidesstattliche Erklärung

Ich erkläre hiermit an Eides Statt, dass ich die vorliegende Arbeit selbständig und ohne Benutzung anderer als der angegebenen Hilfsmittel angefertigt habe.

Die aus fremden Quellen direkt oder indirekt übernommenen Gedanken sind als solche kenntlich gemacht.

Die Arbeit wurde bisher in gleicher oder ähnlicher Form keiner anderen Prüfungsbehörde vorgelegt und auch noch nicht veröffentlicht.

Wien, am 30.01.2015

Unterschrift

(Sloan Jobe Lindsey)

Abstract

Tool-making is one of the defining traits of human civilization. This process involves transforming raw materials into new objects through the physical modification of the shape and properties of the underlying material. Human arts, through the industrial revolution, have been quite adept at physical modification of materials at all manner of dimensional scales. The micro-scale (further difficult the nanoscale) has been, and continues to be a challenging arena since the beginning of the 20th century. The computer revolution has been driven by the ability and the desire to make use of micro- and smaller devices to enable previously impossible frontiers of human endeavor. Of the known methods of physical modification at the micro-scale, most —such a photolithography— are quite restrictive in the manner in which they may be used; however, some methods such as milling by Focused Ion Beams (FIB) offer degrees of expressional freedom similar to those seen at the macro-scale. FIB milling by sputtering is a technique that allows for the direct modification of topography on a near nanoscale through the targeted removal of material via energy imparted by a finely focused beam of energetic ionized atoms. In order to better understand and exercise control over the FIB milling process, simulation is used to convert physical theories into testable outcomes.

In this dissertation a computationally efficient method for the simulation of the phenomena involved in FIB milling by sputtering, including sputtering by the beam, redeposition of sputtered particles, sputtering by backscattered beam ions, and redeposition of atoms sputtered by backscattered beam ions is presented making use of a continuum model employing statistical sputtering properties gleaned from Monte-Carlo simulation. An inverse modeling algorithm utilizing a unique cage-function restriction on dose profiles to improve efficiency is also demonstrated; where the inverse modeler employs the demonstrated sputtering model in order to generate a dose profile that will result in a user-defined final topography.

Special care is also taken to optimize the statistical parameters used as input for the model. This optimization occurs through the comparison of parameters obtained by Monte-Carlo atomistic simulation of ion impacts (making use of the binary collisions approximation) to experimental data. This optimization indicated that surface roughness is essential for the precise reproduction of the exper-

imental data. Numerous models for simulating surface roughness were considered and a novel 1D model of surface roughness was implemented using a gradient in the density between the simulated target and the vacuum over the length of a small surface layer. It was determined that a surface layer 8.27 Å thick is needed to replicate the experimental data; however, an alternative 2D model of surface roughness predicts a smaller thickness indicating that these roughness models, while useful in the presented modeling context, may not serve to extract the true roughness values.

The effects of the energy spectrum of sputtered particles were studied in a second continuum model. This energy-resolved model indicates that for higher aspect ratio features ($> 3 : 1$) sputtering due to energetically sputtered atoms re-impinging the target (reflexive sputtering), may result in a 28% increase in the final simulated milling depth—in the studied system of 30 keV gallium impinging on silicon. These results advance the state of the art with respect to simulation of FIB milling and offer the opportunity for further improvements in mankind's ability to control the shape of materials on the micro- and nanoscale.

Kurzfassung

Die Herstellung von Werkzeugen ist eines der wichtigsten Merkmale der menschlichen Zivilisation. Dabei handelt es sich um einen Prozess, bei dem Werkstoffe durch physikalische Veränderungen ihrer Form und der Eigenschaften ihres Materials in neue Objekte umgewandelt werden. Mit der industriellen Revolution entwickelte sich eine große Kunstfertigkeit und Erfahrung im Bereich der physikalischen Modifizierung von Werkstoffen in sämtlichen Dimensionen. Der Mikrobereich (und noch schwieriger, der Nanobereich) bietet seit dem Beginn des 20. Jahrhunderts eine besondere Herausforderung. Die Nutzung von Mikro- und noch kleineren Geräten stellte eine der treibenden Kräfte der Computerrevolution dar und ermöglichte das Überschreiten völlig neuer Grenzen menschlichen Strebens. Die meisten bekannten Methoden für physikalische Modifizierung im Mikrobereich, wie beispielsweise die Fotolithographie, sind in ihren Anwendungsmöglichkeiten relativ eingeschränkt; einige Methoden jedoch, wie die Oberflächenmodifizierung mit Hilfe von fokussierten Ionenstrahlen (Focused Ion Beams FIB), bieten ein Maß an Gestaltungsfreiheit wie bislang meist nur aus dem Makrobereich bekannt. Beim Sputtern mit fokussierten Ionenstrahlen handelt es sich um eine Technik, welche eine direkte topographische Modifizierung annähernd im Nanobereich ermöglicht, indem gezielt Material durch einen energetischen feinfokussierten Strahl ionisierter Atome abgetragen wird. Zum besseren Verständnis sowie zur systematischeren Kontrolle dieses „Ätzprozesses“ durch FIB kommt die Simulation, bei der physikalische Theorien in überprüfbare Resultate umgewandelt werden können, zum Einsatz.

In der vorliegenden Dissertation wird eine rechnerisch effiziente Methode zur Simulation jener Phänomene präsentiert, welche mit dem Sputtern mit fokussierten Ionenstrahlen in Zusammenhang stehen - darunter Materialabtragung durch den Strahl, Redeposition von gesputterten Teilchen, Sputtern durch rückgestreute Ionen, sowie Redeposition von Atomen, welche von diesen rückgestreuten Ionen gesputtert werden. Hierfür kommt ein Kontinuumsmodell zum Einsatz, das statistische Daten über das Sputter-Verhalten nutzt, die durch Monte-Carlo-Simulation gesammelt wurden. Ebenso wird ein Algorithmus zur inversen Modellierung präsentiert, welcher eine speziell entwickelte Käfigfunktion und ihre Beschränkung auf Dosisprofile zur Verbesserung der Effizienz nutzt; für eine

inverse Modellierung kann das gezeigte Sputter-Modell angewendet werden, um ein Dosisprofil zu erzeugen, das zu einer durch den Benutzer kontrollierten, endgültigen Topographie führt.

Ein besonderer Fokus dieser Arbeit liegt außerdem auf der Optimierung der statistischen Parameter, welche als Input für das Modell verwendet wurden. Diese Optimierung erfolgt durch den Vergleich der Resultate atomistischer Monte-Carlo-Simulationen des Ionenbeschusses mit experimentellen Daten (hierfür kommt die Binary Collision Approximation BCA zur Anwendung). Durch diese Optimierung zeigte sich, dass Oberflächenrauigkeit für die präzise Reproduktion der experimentellen Daten unerlässlich ist. Mit dem Hinzuziehen zahlreicher Modelle für die Simulation von Oberflächenrauigkeit konnte ein neues 1D-Modell mit einem Dichtegradienten vom Vakuum in Richtung Target entwickelt und angewendet werden. Es konnte gezeigt werden, dass eine Oberflächenschicht von 8,27 Å für die Replikation der experimentellen Daten erforderlich ist. Ein alternatives 2D-Modell für Oberflächenrauigkeit berechnet jedoch eine geringere Dicke, was darauf hinweist, dass mit Rauigkeitsmodellen, so nützlich sie im vorliegenden Modellierungskontext auch sein mögen, keine tatsächlichen Rauigkeitswerte gewonnen werden können.

Die Auswirkungen des Energiespektrums der gesputterten Teilchen wurde anschließend anhand eines zweiten Kontinuummodells untersucht. Dieses nach konkreten Energiewerten aufgeschlüsselte Modell zeigt, dass Sputtern bei höheren Aspektverhältnissen ($> 3 : 1$) aufgrund der energiereicheren gesputterten Atome, welche wieder auf das Target auftreffen (reflexives Sputtern), zu einer 28% höheren simulierten Abtragungstiefe führen könnte —was bei dem untersuchten System der Fall ist, bei welchem 30 keV Gallium auf Silizium auftreffen. Diese Untersuchungsergebnisse erweitern den Stand der Technik im Bereich der Simulation der Oberflächenmodifikation mit fokussierten Ionenstrahlen. Sie bieten die Möglichkeit, die menschlichen Fähigkeiten bei der Strukturierung von Werkstoffen im Mikro- und Nanobereich weiter auszubauen.

For my Mother.

Contents

Abstract	i
Kurzfassung	iii
1 Introduction	1
1.1 Introduction to FIB	1
1.1.1 Properties of modern FIB apparatuses	2
1.1.1.1 Gallium Ion Sources for FIB	2
1.1.1.2 Gas Field Ionization Sources	3
1.1.1.3 Optics System for FIB	4
1.1.1.4 Specimen Stage for FIB	5
1.1.1.5 Vacuum System for FIB	5
1.1.1.6 Detectors for FIB	5
1.1.1.7 Optional Features: Electron Gun	6
1.1.1.8 Optional Features: Gas Injection System	6
1.1.2 FIB Applications	6
1.1.2.1 FIB Microanalysis	7
1.1.2.2 TEM Sample Preparation	8
1.1.2.3 VLSI Circuit Analysis and Editing	9
1.1.2.4 Lithography Mask Editing and Correction	11
1.1.2.5 Micro and Nano-patterning	12
1.1.2.6 Precision Implantation for Prototyping and Exotic Devices	14
1.2 Simulation	15
1.2.1 What is Sputtering?	15
1.2.2 Why Do We Simulate?	16
1.2.3 Why Simulate Sputtering?	17
1.2.4 Methods Used to Simulate Sputtering	17
1.2.4.1 Molecular Dynamics	18

1.2.4.2	Binary Collisions	19
1.2.4.3	Continuum models	21
1.2.5	What is this Work?	23
1.2.5.1	The Hybrid Approach	23
1.2.5.2	Inverse Modeling	24
2	Forward Modeling	25
2.1	Equations of Motion	27
2.1.1	Beam Sputtering Flux	28
2.1.2	Redeposition Flux	29
2.1.3	Sputtering by Backscattered Ion Flux	30
2.1.4	Redeposition of Atoms Sputtered by Backscattered Ions	31
2.1.5	Fluxes to Motion	32
2.2	Gridding	33
2.2.1	Definition of the Surface Normal at the Node	33
2.2.2	Length-Segment Calculations	34
2.2.3	Loop Avoidance	34
2.2.4	Adaptive Gridding	35
2.2.4.1	3D Gridding	36
2.2.5	Materials Properties	37
2.2.6	Visibility and Shadowing	38
2.3	Typical Physical Inputs	38
2.3.1	1D Spline Fits	38
2.3.1.1	Sputtering Yield vs Incidence Angle	39
2.3.1.2	Backscattered Ion Yield vs Incident Angle	39
2.3.2	2D Spline Fits	40
2.3.2.1	Probability of a Sputtered Atom Emerging with an Exit Angle Due to Excitation by an Ion with an Incidence Angle.	42
2.3.2.2	Backscatter angular distribution	44
2.4	Typical Simulation Results	44
2.5	Scaling Results	47
3	Inverse Modeling	51
3.1	Motivation	51
3.2	State of the Art	52

3.3	Presented Algorithm	54
3.3.1	Mappings to Dose Profiles and Optimization of Parameters	55
3.3.1.1	Direct Pixel Dwell Times	55
3.3.1.2	Cage Function to Define Pixel Dwell Times	58
3.3.2	Performance	60
3.3.2.1	Refinement of Simulation Parameters	61
3.3.2.2	Parallelization of Jacobian Estimation	64
3.3.2.3	Comparison of Scaling Between Pixel Dwell Time Mappings	64
3.4	Comparison of Quasi-stationary and Stationary Solutions	66
3.5	Experimental Verification	67
3.6	Experimental Anomaly	69
4	Physical Sputtering Properties	71
4.1	Motivation for Experimental Confirmation	72
4.2	Experimental Results for 30 keV Ga on Si at Glancing Angles	73
4.3	Effects of BCA Model Parameters	74
4.3.1	Influence of Ga Implantation	74
4.3.2	Influence of Electronic Stopping	76
4.3.3	Influence of Surface Binding Energy	77
4.4	Influence of Surface Roughness on Sputter Yield	80
4.4.1	Geometric Approximation of Surface Roughness	81
4.4.1.1	Sinusoidal Model	83
4.4.1.2	Fitting to Experimental Data	83
4.4.1.3	Limitations of Strictly Periodic Structures	84
4.4.1.4	Pink Noise Model	85
4.4.2	Density Approximation of Surface Roughness	87
4.4.2.1	Fitting to Experimental Data	89
4.4.2.2	Comparison of Density Profiles Between Linear and Sinusoidal Models	89
4.4.2.3	<i>Bridging the Gap Between Surface Roughness Models</i>	90
4.5	Influence of Surface Roughness on Angular Distribution	94
4.6	Interpolability of Surface Roughness	97
5	Simulation Including Sputtering by Sputtered Target Atoms	103
5.1	Motivation for Investigating a Reflexive Sputtering Model	104
5.2	Old Equations of Motion in New Nomenclature	107

5.2.1	Sputtering Model Presented in the New Nomenclature	108
5.3	Reflexive Sputtering Equations of Motion	115
5.3.1	Assumptions Employed by the Energy-Resolved Sputtering Model	116
5.3.2	Equations of Motion: Energy-Resolved Sputtering	119
5.3.2.1	General i^{th} Order Form	119
5.3.2.2	Zeroth, First, and Second-Order Equations of Motion	121
5.3.3	2D Simulation of the Energy-Resolved Model	126
5.4	Physical Inputs and their Parameterizations	127
5.4.1	Energy Resolved Angular Distributions	127
5.4.2	Energy-Resolved Backscatter Distributions	128
5.4.3	Sputtering Rates as a Function of Species and Energy	130
5.4.4	Energy Distribution of Sputtered and Backscattered Atoms	135
5.5	Comparison of Simulation Results to the Simple Model	136
5.6	Comparison to Simpler Approximations of Reflexive Sputtering	140
5.6.1	Simulations Neglecting Energy-Resolved Angular Distributions	141
5.6.2	Simulations Compressing Similar Energy-Resolved Angular Distributions	143
5.7	Comparison to Experimental Deep Trench	144
6	Conclusion and Outlook	147
6.1	Discoveries	147
6.2	Viability of Hybrid Simulation Approach	149
6.3	Complexity “Is This Method Optimal?”	150
6.4	Utility	151
6.5	Outlook and Future Works	152
6.5.1	Further Study on Surface Roughness	153
6.5.1.1	Simulation of the Evolution of Surface Roughness	153
6.5.1.2	Measurement of Surface Roughness	154
6.5.1.3	Glancing Angle Yield Studies at Different Energies	155
6.5.2	Possible Inverse Modeling Improvements	155
6.5.3	Consideration of Implanted Species	156
6.5.4	Full 3D Simulations	156
6.5.5	GPU and/or Massively Parallel Implementation	157
6.5.6	Experimental Confirmation of Reflexive Sputtering	158
6.6	Closing Words	158

A	3D Effects with Reflexive Sputtering Model	159
A.1	Validity of 3D Simulations	159
B	Shadowing Effects	169
B.1	Limited Effects of Shadowing On Deep Trenches	169
C	2nd Order Redeposition from Reflexive Sputtering	173
C.1	A Supposedly Minor Approximation	173
C.2	Backscatter Angular Distribution Visualization	175
C.3	Importance of the Effect	177
D	Calculation of Equivalent Yields	179
	Acknowledgements	183
	Bibliography	184
	Acronyms	209
	Index	214
	CV	217

List of Figures

2.0.1	Sputtering Model Sketch (String Approach)	26
2.1.1	Sputtering Model Sketch (Beam Sputtering)	28
2.1.2	Sputtering Model Sketch (Redeposition)	29
2.1.3	Sputtering Model Sketch (Redeposition and Backscattering)	30
2.1.4	Sputtering Model Sketch (Full Model)	32
2.2.1	Calculation of Surface Normals	34
2.2.2	Loop Avoidance	35
2.2.3	Adaptive Grid (Node Crowding)	36
2.2.4	Adaptive Grid in 3D	37
2.3.1	Sputter Yield 30 keV Ga on Si	40

2.3.2	Backscatter Yield 30 keV Ga on Si	41
2.3.3	Sputtering Angular Distributions at Selected Angles (Polar)	43
2.3.4	Interpolated Sputtering Angular Distribution	44
2.3.5	Backscatter Angular Distributions at Selected Angles (Polar)	45
2.3.6	Interpolated Backscatter Angular Distribution	45
2.4.1	Typical Trench Simulations	47
2.5.1	Geometric Scaling of Simulations	48
2.5.2	Characterization of Microtrench Formation	49
3.3.1	Algorithm: Pixel Dwell Times	56
3.3.2	Inverse Modeling Error Evaluation	57
3.3.3	Piecewise Linear Cage Function	59
3.3.4	Algorithm: Piecewise Linear Cage Function	61
3.3.5	Algorithm: Piecewise Linear Cage Function Refinement	62
3.3.6	Cage Function Refinement	63
3.3.7	Comparison of Pixel and Cage Function Optimization	65
3.4.1	Effect of Number of Passes on Inverse Modeling Solutions	67
3.5.1	Experimental Verification	68
3.6.1	Experimental Anomaly	70
4.2.1	30 keV Ga on Si Experimental and Simulated Sputter Yields	74
4.3.1	Influence of Implanted Gallium on Simulated Sputtering Yield	75
4.3.2	Influence of Electronic Stopping Model on Simulated Sputtering Yield	77
4.3.3	Schematic Diagram: Surface Binding Energy	78
4.3.4	Influence of Surface Binding Energy on Simulated Sputtering Yield	79
4.4.1	Geometric Surface Roughness Schematic	82
4.4.2	Sinusoidal Surface Roughness: Yield Variance with Respect to Wavelength and Amplitude	84
4.4.3	Sinusoidal Surface Roughness: Simulated Sputtering Yield Fitted to Experimental Data	85
4.4.4	Pink Noise Roughness: Visualization of Geometric Profiles	86
4.4.5	Pink Noise Roughness: Yield Variance with Respect to Cutoff Wavelength and RMS Height	88
4.4.6	Density Gradient Surface Roughness Schematic	89
4.4.7	Fitting of Density Gradient Roughness Yields to Experimental Data	90

4.4.8	Density Profiles Compared: Sinusoidal and Linear	91
4.4.9	Sensitivity of Density Gradient Model	92
4.4.10	Density Gradient Model Emulating a Sinusoidal Density Profile	93
4.4.11	2D Roughness Model Emulating the Gradient Density Model	94
4.5.1	Sputtering Angular Distribution Roughness Effects: Normal Incidence	96
4.5.2	Sputtering Angular Distribution Roughness Effects: Normal Incidence (Grazing Ejection Angles)	97
4.5.3	Sputtering Angular Distribution Roughness Effects: 80°	98
4.5.4	Sputtering Angular Distribution Roughness Effects (Linear plot): 80°	99
4.6.1	Best Fit Simulated Yield: 5 keV (Density Gradient Model)	100
4.6.2	Variance in Fit Quality versus Interface Layer Thickness for 30 keV and 5 keV Simulations	101
5.1.1	Energy Resolved Sputtering Angular Distribution $\theta = 80^\circ$	105
5.1.2	Energy Distribution of Ejected Target Atoms $\theta = 80^\circ$	107
5.2.1	Relative Coordinate System for New Nomenclature	111
5.4.1	Angular Distribution of Sputtered Target Atoms by Energy Band	129
5.4.2	Angular Distribution of Backscattered Ions by Energy Band	131
5.4.3	Polar Plot of Backscattered Ions By Energy Band: $\theta = 80^\circ$	132
5.4.4	Energy Resolved Sputtering Yields for Gallium Impinging on a Pure Silicon Target	133
5.4.5	Energy Resolved Sputtering Yields for Silicon Impinging on a Silicon Target	133
5.4.6	Energy Resolved BackScattering Yields for Silicon Impinging on a Silicon Target .	134
5.4.7	Silicon Ejection Energy Fractions as a Function of Incidence Angle	136
5.4.8	Gallium Ejection Energy Fractions as a Function of Incidence Angle	136
5.5.1	Energy Resolved Simulation Vs. Non Energy Resolved Simulation	137
5.5.2	Energy Resolved Simulation Vs. Non Energy Resolved Simulation Vs. Energy Resolved Simulation without Reflexive Sputtering	139
5.6.1	Reflexive Sputtering Neglecting Energy-Resolved Angular Distributions	142
5.6.2	Compressed Energy Intervals Vs Logarithmic Energy Intervals	145
5.7.1	Comparison of Reflexive Sputtering Model To Experiment	146
A.1.1	Coordinate System for 2D Histograms	160
A.1.2	Relative Coordinate System for New Nomenclature	161
A.1.3	Virtual Trench Wall Parallel	162
A.1.4	Virtual Trench Wall Anti-Parallel	162

A.1.5	Virtual Trench Wall Perpendicular	163
A.1.6	Beta Dependence $\theta = 80^\circ$ 1-2 keV Ejection Energy	164
A.1.7	Energy Resolved 3D Effects vs Ejection Angle α	165
A.1.8	3D Effects vs Ejection Angle α (non energy-resolved)	166
A.1.9	Comparison of 3D Effect Models as Applied to Topography Simulation	168
B.1.1	Effect of Shadowing on Topography Simulations	170
C.2.1	Silicon-Silicon Backscatter Angular Distributions	176
C.3.1	Comparison of Silicon Backscattering Approaches in Simulation	178
D.0.1	Sputtered Particle Energy Distribution as a Function of Incidence Angle	181

List of Tables

5.2.1	Assumptions Presumed in the Simple Sputtering Model	110
5.2.2	Equations of Motion: Simple Model	115
5.3.1	Assumptions Presumed in the Energy Resolved Sputtering Model	118
5.3.2	Equations of Motion: Energy Resolved	126

Chapter 1

Introduction

1.1 Introduction to FIB

Focused Ion Beam (FIB) technologies are a fantastically flexible technique for materials modification on the micro- and nanoscale. FIB presents the rather unique ability to be used for precision doping as well as for topographical modification, both as a subtractive as well as an additive process. Furthermore, FIB can generally be used across a wide variety of materials, including heterogeneous materials, and it is this flexibility that has made FIB a standard processing technique in the field of transmission electron microscopy (TEM) sample preparation.

Focused Ion Beams are, as the name suggests, charged matter beams that are focused through vacuum to a target substrate by means of electrostatic lenses. The engineering problem of designing a FIB is largely unimportant in this work, but there have been commercial FIB systems for nearly thirty years [1]. What differentiates FIB techniques is the wide variety of possible applications and methods in which they can be used to modify materials.

There are four widely acknowledged methods of direct materials modification possible using a FIB: precision doping, sputtering, gas assisted deposition, and gas assisted etching. In the case of doping, small doses of impurities are implanted into the target under the surfaces exposed to focused irradiation. Sputtering refers to the process by which target atoms or molecules receive sufficient energy from the matter beam that they are ejected from the target substrate. Sputtering is the primary focus of the research presented in this dissertation. The other two methods are both gas assisted methods by which a semi-stable chemical precursor gas is activated by the matter beam leading to either deposition of a payload atom (W, Si, Al) or the localized activation of an etchant. The exact mechanism for this activation is still under debate and seems to vary with the choice of precursor. The notable factor of all four of these methods is the strong locality enabled by the

focused and steered matter beam. This locality and relative material insensitivity is what makes FIB an interesting technique; there are other methods for topographical modification, but they either lack strong locality (as in the case of microtome and dimpling), or they are more difficult to apply to heterogeneous materials (as is the case with electron beam assisted etching), or they require extensive post processing (as in the case of traditional photo-lithography).

1.1.1 Properties of modern FIB apparatuses

A Focused Ion Beam system consists of an ion source, objective lenses, and a sample holder system all located within a supporting vacuum system. Since the introduction of high brightness liquid metal sources in the late 1970s [2] FIBs employing gallium ions have emerged as the predominant choice for analytical and micro-machining purposes. Gallium possesses certain features that make it attractive as an ion source including ease of manufacturing for the physical source, longevity of the source, high attainable beam currents, high brightness, and sufficient mass to be useful for micro-milling through sputtering [3].

1.1.1.1 Gallium Ion Sources for FIB

Gallium ion sources of the liquid metal ion source (LMIS) type are used most in FIBs where a special ion species is not required. LMIS have the advantage over gas plasma sources in that they are simple to manufacture and maintain [3], though recent work on gas field ionization sources (GFIS) promises a higher resolving future alternative for imaging applications [4]. However, this dissertation focuses on gallium as the ion species as it is the current state of the art and will continue to be a useful tool for micro/nano-milling.

LMIS are characterized by having a fine needle that is whetted by a liquid metal or alloy held at a high voltage, with respect to an extraction electrode [5], leading to field evaporation (FEV) at the end of the needle. The FEV is driven by the high electric fields present at the needle apex. These electric fields are generally in the range of 10V/nm and act to electrostatically pull the liquid metal to an even finer tip where thermodynamically excited ionization occurs [3]. These factors lead to a point-like ion emission site with an apparent optical size of about 50nm, though the liquid metal tip size is on the order of 5nm. LMIS therefore act as near optimal sources around which to build an instrument.

A reservoir of the liquid metal is used to continuously feed metal to the emitter tip. In the historical development of the LMIS, capillary tubes were used, but a whetted needle has replaced this method in current sources. The liquid metal is transferred across the surface of the needle from the reservoir to the emitter tip by capillary forces along the surface of the needle. Modern needles are optimized

with grooves to reduce the drag and optimize flow in the operating beam current range. The metal is brought to its melting point through resistive heating using either the reservoir itself or an external heater coil [3].

Gallium specifically has a number of features which make it particularly attractive for use in a LMIS. The low melting temperature of approximately 30°C simplifies the heating requirements needed in order to force gallium into a liquid state. Furthermore, the low vapor pressure of gallium simplifies the requirement that a FIB and its source operate under high vacuum conditions. Gallium also does not strongly react with tungsten which is the material of choice for needle manufacture [5]. Gallium also has the strong advantage of being predominately singly ionized to Ga⁺ [3], further simplifying instrument design by removing the requirement of an ion filter. The other commonly used LMIS is an alloy containing Au-Si-Be [6] which allows for the selection of multiple ion species through the use of an ion filter. Though these sources exist and present unique opportunities for localized doping and ion mixing [7], they do not currently compete with gallium sources outside of highly specialized applications.

1.1.1.2 Gas Field Ionization Sources

A fairly recent advancement in the focused ion beam field has been the development of GFIS. Gas field ionization sources are a spiritual development of the field ion microscope (FIM) which was first mentioned in publications in 1951 [8] and provided atomic resolution by 1956 [9]. In a FIM a large electric field is generated between a sharpened metal tip (usually tungsten) acting as an emitter and a collector under ultra high vacuum conditions while small quantities of noble gas (usually helium) are added. At the sharpened tip a small number of atoms each act as individual ion emitters taking neutral noble gas atoms and ionizing them, whereafter the ionized atoms are accelerated by the electric field along narrowly defined paths. These ions can be later detected using a phosphorescent plate and due to the extremely point-like emission characteristics that occur at surface atom locations, atomic resolution can be achieved. Practical GFIS make use of this point-like emission; however, they seek to use the ions escaping from a single atomic location, usually through the construction of a atomic trimer [4] (a point formed by three atoms) coupled with an aperture used to select a single atom from the trimer as the active emitter. There has also been recent success in creating single atom terminated (SAT) tungsten tips using (111) oriented tungsten and field etching. These tips have been demonstrated to be reproducible and robust allowing for multiple reshaping [10]; additionally, SAT appear to be more tolerant to the use of neon as the ionized gas [11]. However, as of the time of writing there remains only a single commercial producer of helium ion microscopy (HIM) systems, and indications are that a trimer tip geometry is used in these systems, even when neon experiments

are done.

The choice of ion species used with GFIS is limited to gases with ionization energies higher than that of the typical UHV gas contaminants, the highest of which is N_2 with an ionization energy of 15.6 eV [11, 12]. This limitation is due to the fragile atomic geometry required at the tip, where a single foreign adatom would disrupt the precarious surface geometry destroying the single or triple emission condition. Practically, this limitation means that helium and neon are the only viable noble gases with argon sitting on the edge of viability at 15.8 eV. Helium and neon have different ion-surface interactions due to both differences in size and differences in mass. As compared to gallium, both noble gases present the advantage of being chemically inert once implanted. However, neon in particular has been linked to bubble formation in certain substrates [12] such as silicon, but neon has a much more useful sputter rate when compared to helium. In both gases, the interaction volume is significantly larger than the focused spot size, as indicated by larger features than those irradiated by the beam [12, 13] implying that application of the extremely high resolution available from GFIS to substrate modification will not be as easy as the resolution suggests.

1.1.1.3 Optics System for FIB

Directly following the ion source in a FIB column, one finds the FIB optics which work to direct the accelerated ions to the specimen. The lenses in a FIB column are all electrostatic lenses as the small charge/mass ratio of ions would necessitate prohibitively large electromagnetic lenses [5]. The simplest arrangement of FIB optics is a single lens system with an aperture, a beam blanker and Faraday cup, and an octapole for beam deflection and beam scanning. However, two and three lens systems are also widely available with the extra lenses used for aberration correction. Due to space charge effects, whereby ions repel each other in flight as a result of coulomb repulsion, crossover points are generally minimized in FIB optical design [3].

There are three major sources of resolution limiting aberrations in a FIB; spherical aberrations, chromatic aberrations, and beam spread due to space charge crowding. The standard spherical aberrations and chromatic aberrations lead to the center of a beam having a Gaussian distribution with a well defined full width at half maximum (FWHM) near the center of the beam. However, due to space charge effects, there is additional broadening of the beam that follows a Holtsmark distribution leading to extremely broad beam tails that increase with increasing current density [14–16]. Practical FIB apparatuses are therefore always constrained by trade-offs between the different aberrations and must operate in intermediate current and acceleration zones where performance is acceptable.

1.1.1.4 Specimen Stage for FIB

FIB systems generally have a 5-axis-stage; x,y,z plus rotation and tilt around an eucentric point [5]. The eucentric point allows the stage to be tilted with the specimen in place, without changing the focal distance or displacing the field of view from the area of interest. In FIB systems equipped with an electron gun (so called twin-beam systems) the eucentric point is located where the two beams cross in space; in systems with only an ion beam the eucentric point is located along the optical axis at the optimal working distance. The stage also provides grounding for the sample to minimize charging and also to facilitate specimen current measurement in FIB imaging.

Another notable feature of most commercial FIB systems is that the specimen sample holder accepts large samples, normally with volumes of many cubic centimeters. For example, the Phillips device quotes a maximum sample size of 4cm x 4cm x 2cm [17] allowing a large fraction of macroscopic specimens to be used without any special preparation to identify and extract an area of interest before experiments can be conducted [18]. Sample size flexibility compared to even optical microscopy acts as a major strength of the FIB technique for destructive analysis; it must be mentioned, however, that scanning electron microscopes (SEM) have similarly relaxed specimen size restrictions.

1.1.1.5 Vacuum System for FIB

The entire system requires at least high vacuum; this is because the mean free path of the ions is proportional to the inverse cube of the pressure inside the instrument. While low vacuum imaging is available with SEM in order to image insulating specimens, FIB requires high vacuum [19], with high vacuum in the case referring to pressures $<1\text{E-}3$ Torr [20]. Furthermore, residual gas can lead to unintended gas deposition on the specimen [21]. The vacuum system is therefore essential to the proper operation of a FIB apparatus.

1.1.1.6 Detectors for FIB

A major strength of FIB apparatuses is the ability to visualize, analyze, and modify a specimen using the same system. FIB systems can therefore be equipped with a number of detectors to aid in the analysis of specimens. The simplest detector is the sample stage, which is equipped to measure the specimen current as a function of time. The specimen current reflects the current needed to equalize the charge of the specimen in response to the process of charge equalization due to implanted positive ions, ejected secondary specimen ions, and ejected secondary electrons.

The ejected species may also be analyzed individually through the use of secondary ion or secondary electron detectors. When the mass of the secondary ions is determined, the process is known

as secondary ion mass spectroscopy (SIMS) and elemental composition can be studied with high lateral and extremely high depth resolution [22]. Collecting the secondary electrons at the surface with a secondary electron detector allows for greater lateral resolution as the signal is limited to electrons released from a smaller interaction volume [23].

Additionally photo-emissions in the visible to X-ray regime can be collected and analyzed with dedicated detectors. An advantage of Energy-Dispersive X-ray Spectroscopy (EDX) is that it can be excited with an electron beam and thus allows for composition analysis to be made from a FIB-milled surface in a non-destructive manner. Other such detectors such as electron backscatter diffraction spectrometry (EBSD) allow for phase and compositional analysis to be made non-destructively [24]. In general most SEM detectors can be used for analysis with FIB apparatuses.

1.1.1.7 Optional Features: Electron Gun

A drawback to FIB imaging is that by imaging the specimen, one is also removing material from the specimen and changing what is being imaged due to sputtering and redeposition. Therefore many modern FIBs also have an electron gun that is focused to the same spot as the ion beam, thus allowing for less destructive imaging before the ion beam is used. Furthermore, as the electron beam has the opposite charge of the ion beam, it can be used for charge neutralization [25]. There also exist FIB systems with a charge-compensating flood electron gun used for the sole purpose of charge neutralization with specimens that are insulators [3].

1.1.1.8 Optional Features: Gas Injection System

For gas assisted etching and gas assisted deposition it is necessary to introduce gases into the vacuum chamber where they can be adsorbed onto the surface of the specimen. Gases are introduced into the system through capillary needles that are mechanically placed very near to the sample [26]. For reasons of practicality the gas injection system is usually attached to the column near the end of the ion gun, thus avoiding plumbing complications with the movable specimen stage. A control system is usually in place to allow for the preheating of vapors and the selection of multiple gases [27].

1.1.2 FIB Applications

Focused Ion Beam systems have many practical applications used in research and industry. This section will provide a brief overview of a few of the FIB applications found in literature. These FIB applications include scanning ion microscopy (SIM) and SIMS for specimen analysis, TEM sample preparation, VLSI circuit analysis and debugging, lithography mask editing, micro and nano-

patterning for use as novel manufacturing methods and in the production of microelectromechanical systems (MEMS), and as a method to perform precision implantation.

1.1.2.1 FIB Microanalysis

The use of FIB for micro analysis is one of the most mature fields of FIB application. There are two major techniques in which FIBs are used strictly as analysis tools: SIM and SIMS. These two techniques make use of different ion-beam induced effects to perform analysis that is difficult or impossible to reproduce with other techniques.

The scanning ion microscopy technique is used to directly image specimens. Specimens can be prepared ahead of time by mechanical preparation techniques, by FIB milling or by a combination of both. The area of interest is rasterized by the scanning ion beam and the electron response is correlated to this scanning allowing for the production of an image. As was mentioned in section 1.1.1.6 on page 5, there are a variety of ways of detecting an electron response. In general a number of secondary electron detectors will be used to track the emergence of secondary electrons from the specimen. These secondary electrons are excited by a number of nuclear and electronic scattering mechanisms, but the ones that escape into vacuum and reach the detectors come mostly from a region near the specimen surface [3]. In general the secondary electron yield is dependent upon a number of factors including beam incidence angle, electron collection angle, chemical composition, crystal orientation, and local electric fields due to charging or other phenomena [28, 29].

In crystalline materials ion channeling can occur; during ion channeling, ions can travel down low density paths in the crystal lattice. When an ion encounters a channel it can travel much deeper into the crystal without being scattered. As previously mentioned, the excitation of secondary electrons is driven by scattering and the detection is dependent upon these secondary electrons reaching vacuum; therefore, the secondary electron yield can be strongly correlated to the amount of ion channeling, which in turn is strongly correlated to crystal orientation. SIM imaging therefore has a strong channeling contrast mechanism which is commonly used when analyzing polycrystalline materials to image individual grains [30]. Channeling contrast is highly material dependent and requires that the specimen have a higher amorphization threshold than the ion dose required to produce an image. Once the specimen becomes amorphous the channels are destroyed and the contrast mechanism is attenuated. Many metallic samples have a sufficiently high amorphization threshold to make this technique highly useful as an analytic tool in the field of materials science [31, 32].

SIMS is another mature technique for specimen analysis using both focused and unfocused ion beams. In SIMS the secondary ions emerging from the specimen due to sputtering are collected and detected according to the mass of the ejected ion. This mass specificity is a powerful prop-

erty because it not only allows for the identification of individual chemical species of ejected ions, but additionally for the detection of individual isotopes. Experiments may be conducted with *non-interacting* tracer isotopes of the same species of the host matrix, thereby greatly simplifying certain experiments [33–35].

The other notable advantage of SIMS is its high depth selectivity with a depth resolution in the nanometer range. Additionally, as the secondary ions are produced through sputtering, it is possible to resolve depth profiles using SIMS. As each surface volume is sputtered away and the constituent chemical species are analyzed according to mass, a new surface volume is presented for analysis [36]. This depth selectivity allows for the analysis of things such as doping profiles over large depth ranges from tens of nanometers [37] to microns [38]. SIMS is thus heavily used in the microelectronics industry as it affords the possibility to investigate the doping profiles on manufactured devices.

1.1.2.2 TEM Sample Preparation

FIB milling used in the preparation of TEM samples has become a mature application of FIB technology. The technique is well suited to the goal of producing high quality TEM samples as the FIB allows for both location of an area of interest and preparation of the lamella in the same instrument. TEMs operate in the transmission mode, measuring the deflection or attenuation of high energy electrons after they pass through a specimen. It is therefore necessary that specimens used for TEM analysis be sufficiently thin as to become at least partially transparent to the probing electron beam; generally the required thickness for analysis is <100 nm [18]. There exist mechanical methods for thinning and production of a TEM lamella such as microtome [39] and mechanical polishing and grinding followed by broad beam ion milling [40, 41]; however, these mechanical techniques generally have low site specificity.

The lift-out technique has become a mainstay among users of FIB techniques for the production of TEM samples. There are variations of the lift-out technique for both cross-section and plan-view [42] sample preparation; however, only the cross-section technique will be described here [18]. In the lift-out technique the area of interest is first protected and mechanically stiffened through the application of a protective metal film, usually applied through gas assisted deposition, two V-shaped trenches are then milled on either side of the area of interest, leaving a thin lamella. This lamella will usually undergo additional ion milling-polishing from the FIB at decreasing beam energy in order to remove the FIB induced damage zone [43]. The sample is then removed from the substrate by cutting away the edges of the lamella, in the *in-situ* [44] lift-out technique the prepared lamella is welded to a needle manipulator also through gas deposition. In the *ex-situ* technique the lamella is fished

out of the trench after the sample has been removed from the FIB through the use of a charged fine glass rod. The prepared lamella may then be attached to a TEM grid and analyzed. Use of the FIB for TEM sample preparation has a high yield and great flexibility, especially for use in the microelectronics industry where the described cross-sectional lift-out technique is a good match for the thin, flat structures produced by photo-lithography.

1.1.2.3 VLSI Circuit Analysis and Editing

Very large scale integration (VLSI) refers to integrated circuitry containing greater than 10,000 gates (as compared to LSI, MSI, and SSI for large[$\leq 10,000$], medium[$\leq 1,000$], and small[≤ 10] scale integration) [45] and as a result of the computer revolution, has become a very lucrative business with global semiconductor industry revenues reaching \$260B in 2008 [46]. The feature density of these devices has increased with time in the pursuit of performance and profit, with modern SRAM bit-cells occupying between 0.10 to 0.15 μm^2 [47], it becomes easy to understand the difficulty presented in applying failure analysis to such devices. The microelectronics industry has therefore welcomed and actively developed the unique capabilities of FIB technology in order to suit their needs. In this section a number of FIB applications used in the microelectronics industry on these VLSI devices will be highlighted.

There are primarily three ways that FIB is used in the microelectronics industry with regards to completed devices: as an analytical tool in its own right, as a modification tool that enables further electrical analysis and testing, and finally as a tool capable of performing direct modifications that change the performance of a manufactured VLSI device.

One of the earliest FIB applications described in VLSI literature was the use of a FIB to modify existing structures in order to electrically debug the integrated circuit [48]. Electrically conducting contacts, usually of FIB deposited tungsten, are used to manufacture precision wires and contact points that can be probed externally, using a traditional needle probe. This procedure for producing *post-hoc* debug structures is especially well suited to FIB capabilities, as it requires the milling away of passivation, and the subsequent deposition of the metal contacts; both of which can easily be done with the FIB. However, it was not long until the feature density became high enough that locating the area of interest presented its own challenge. The microelectronics industry therefore developed computer aided design (CAD) systems that would couple the stage and beam locations with the design schematics for the device in question [49, 50], thus limiting unnecessary FIB exposure to the sample. As the number of metalization layers increased with increased transistor density, reaching test sites became difficult with simple ion milling, due to the limited hole aspect ratio available using FIB sputtering, gas assisted etching was therefore adopted to enable deeper holes. Gas assisted etching allows

for steep sidewalls ($\sim 84^\circ$) with window openings as small as $1\mu\text{m}^2$ [51] and aspect ratios $>100\times$ in some materials [52]. Furthermore, in VLSI devices which are layered structures, gas assisted etching provides materials specificity [53]. This materials specificity and the increased precision offered by FIB assisted gas etching makes the technique preferable in many applications to other material removal techniques such as laser ablation, even though laser ablation has a faster removal rate [54]. Preparation of these external contacts retains its value as device geometries continue to shrink and external probing continues to lend insight into the failure modes of devices even when high resolution SEM and TEM are unable to detect the cause of failure. Electrical characterization of individual transistors as afforded by FIB processing is an integral step to diagnosing and correcting even *invisible* circuit defects [55].

FIB technology, as demonstrated above, allows for both the removal and addition of conducting and insulating material on completed VLSI devices, which naturally can be used to correct defects in manufactured devices. Using both frontside [55] or backside [56] techniques it is possible to correct defective metalization either through the removal of conductors or the rewiring of conductors. Furthermore, if care is taken to minimize FIB-induced damage, gross defects such as the unintended integration of foreign debris [57] can be removed from manufactured devices, thereby restoring them to the functional specification. Providing functional edits is difficult and requires excellent knowledge of the underlying circuitry as well as the ability to precisely control the depth of the etched access windows. The process of controlling the etching depth is known as endpointing and it utilizes the effect of sputter redeposition to detect when a metal line has been milled into, even for very high aspect ratio holes [58]. FIB modification of an existing component is expensive compared to the incremental production cost; however, compared to the cost of new masks (2009 costs in the low millions of dollars per complete mask set [59]) the cost of repairing a VLSI device by FIB makes sense in the development phase and for certain low volume custom applications. Recent advances even allow for the FIB deposition of conductors with variable resistance [60], thus enabling a greater range of repairs to be made.

On the analytical side, FIB is used for the same analytical techniques mentioned in 1.1.2.1 on page 7 and 1.1.2.2 on page 8, where the imaging and milling properties are used for analytical imaging and preparation for imaging by other techniques such as SEM or TEM. As the metalization lines used in VLSI techniques are predominantly polycrystalline and grain structure has a strong influence on the susceptibility of these lines to electro-migration [61], the channeling contrast afforded by SIM has high utility when inspecting VLSI structures [62]. In addition to the standard FIB analytical techniques, FIB (and SEM) presents another avenue for failure analysis along the metalization of VLSI devices, as short circuits and open metal lines can be identified due to charging contrast, making cer-

tain manufacturing defects extremely visible under FIB/SEM analysis [55]. Due to the dependence upon precision doping in VLSI devices the SIMS method (as enabled by FIB) is invaluable for its ability to probe dopant concentrations in manufactured devices [49, 62, 63]. The final application for FIB analysis in VLSI technique is FIB tomography; in this process a dual beam (FIB and SEM) apparatus is used to remove slices and image a specimen after each slice, allowing for subsequent reconstruction of the topography of the materials domains [64]. FIB tomography has strong applications when there is uncertainty as to what structures are being produced, as might be found in the development of a new manufacturing node.

1.1.2.4 Lithography Mask Editing and Correction

Historically, another major use of FIB technology in the VLSI industry came in its use as a tool for lithographic mask repair. As was mentioned earlier, the cost of mask sets has always been high and has continued to increase as feature sizes decrease [59]. This economic pressure provided the impetus for the development of FIB as a device repair technology for completed devices; once these devices are debugged it is sometimes possible to use the FIB to repair the masks and thus avoid having to produce a complete mask set from scratch. Mask repair is enabled by multiple factors including imaging and the ability to both remove and deposit material. Numerous defects can be repaired in lithographic masks and it is even possible to deposit SiO_2 using the FIB [65].

Mask repair is challenging even with the use of FIB, as the Ga^+ beams often used will implant gallium into the SiO_2 mask substrate. This implanted gallium leads to a reduction in transparency known as staining. There are numerous post-processing steps that can be taken to reduce this subsequent mask staining [66], additionally sub-resolution biasing can be used to compensate for the staining effect [67]. However, as mask feature sizes have continued to decrease and the industry has been forced to adopt an ever increasing array of resolution increasing tricks (optical proximity correction, and phase shifting), the resolution of the LMIS FIB has struggled to keep up and was further hindered by the unwanted byproduct of gallium staining, leading to the development of electron beam techniques for lithographic mask repair [68] for use on bleeding edge technology nodes. These current limitations of FIB mask repair are highly implementation specific, and future FIB technologies using a different ion species may once again find a way back into favor in this specific application space.

1.1.2.5 Micro and Nano-patterning

The previous sections addressed the highly mature and standardized applications of FIB technology. In this section and the following section, newer FIB applications will be discussed —applications that are in many cases an exploration of the possible uses of FIB technology. Micro and nano patterning using FIBs is a simple enough concept, and actually the enabling feature for many of the mature applications mentioned in the earlier sections. This section will focus on the use of FIB as a patterning technique for novel applications where the desired patterning is more complex than the fixing of a metal line or the removal of a thin layer of material for imaging. The following paragraphs address topographical patterning implemented by three processes; direct topographical modification (by means of sputtering, deposition, or etching), physical templating, and chemical or developed patterning.

Direct topographical modification refers to the use of a focused ion beam to either remove or deposit material in a site specific manner. In addition to the milling involved with TEM sample preparation, the milling and deposition used in circuit edits, and the milling and deposition done in mask repair, there are other smaller applications for the FIB's unique abilities. Some applications include the modification of MEMs based micro-grippers, where FIB milling is used to produce sharpened SiO₂ grip extensions that are fine enough to pick and place 100nm spheres [69], and the milling of apertures in AFM tips to enable the creation of new tools for either nanodispensers [70], or to possibly enable quantum computing through precise single ion doping [71]. Another use is the direct fabrication of nanowires through gas assisted deposition; these deposited tungsten and platinum wires can either facilitate other research, such as the use of platinum wires to conduct electrical measurements of other nanostructures [72], or be interesting research on their own, as in the case of the superconducting transition measured in FIB deposited tungsten nanowires [73]. Gas assisted deposition is not strictly limited to FIB applications and can also be incited by an electron beam [74–76]; although, when an electron beam is used resolution is lost due to the great degree of scattering experienced by the relatively light electron in the target. Electron beams are still quite desirable due to their lack of target doping, with the recent development of stable GFIS, however, it is now possible to bridge the gap between electron incited and ion incited gas assisted deposition through the use of light noble gases such as Helium and Neon [13, 77, 78], now an active field of research in contemporary times. As stated before, FIB milling is relatively materials insensitive which allows it to be used as a prototyping tool for layered devices to develop thermally activated bimorph microactuators [79] and even spintronic devices [80]. FIB need not even be the primary method of fabricating structures, as exemplified by research demonstrating large structures formed by photo-lithography but completed by FIB

milling, structures such as accelerometers [81] and miniaturized nanoSQUIDS [82, 83]. Flexibility for prototyping makes FIB a valuable tool for research that requires fine 3D manipulation; especially in areas where there is question as to whether devices can even be built.

A major drawback to the *direct modification of topography* approach is that FIB modification is in general a serial process and is quite slow compared to un-scanned processes. Therefore there exists another interesting application whereby FIB is used to do difficult work once, in order to produce a template that can be reused at a production scale. An example application where templates are required is in the research area of nanoimprint lithography (NIL). NIL is a high fidelity lithographic technique that works by physically embossing a polymer resist to produce a 3D structure with nanoscale or larger features. NIL can use a variety of methods to pattern the resist to the template, from simple pressure leading to plastic deformation, to hot embossing using heat, to UV curing resists that harden when light is projected through a transparent template, to cast-in-place resists that are transferred from the template to the substrate [84]. While these methods offer huge amounts of flexibility and relatively low infrastructure costs, NIL is still plagued by the limitation that in order to create a duplicate of a template one must first have a template; FIB is one possible solution to this template problem. The typical research systems used for FIB generated templates with NIL have been templates for optical microlenses. Subtractive [85] and additive [86] methods have both been used to produce demonstration negative templates for polymer microlenses. Microlenses are a nice model system because they require truly three dimensional features, a requirement not easily met by traditional micro/nanofabrication techniques like photo-lithography. The difficulty, however, is that instead of the relatively simple task of generating a line or a cut, arbitrary 3D structures must be produced; this requires either modeling or tedious amounts of trial and error. Production of nanoimprint templates using FIB therefore continues to be an active field of research.

A third class of patterning technique, those techniques which make use of latent FIB effects to form topography, as opposed to direct deposition or milling, can be referred to as developed patterning. In the simple case, a resist such as Poly(Methyl MethAcrylate) (PMMA) or a Spin On Glass (SOG) developed for electron beam lithography can be exposed by FIB, yielding a pattern after resist development. A drawback to direct resist exposure is that the low projected range of the ions in amorphous polymers limits the maximum exposure depth to approximately 30nm [87]. As an upside, FIB sources are normally significantly brighter than electron beam sources, making for a pronounced increase in efficiency; ions also present the opportunity for higher edge acuity as lateral straggling is reduced with ions, particularly in comparison to electrons. Certain resists transform into a hard mask under large Ga⁺ doses, which leads to complementary techniques, where even the shallow interaction volume is useful when combined with highly anisotropic etching [88]. In silicon, Ga⁺ acts

as an etch stop with a reported etch selectivity of $\geq 1000:1$ between doped and undoped substrate. This etch stop behavior, when coupled with anisotropic etching such as Deep Reactive Ion Etching (DRIE) [89], or tetramethylammonium hydroxide (TMAH) wet etching [90], opens possibilities for interesting hybrid techniques. Specifically interesting is that Ga^+ appears to reduce the reactivity of silicon and appears to be rather ambivalent to the etchant used, as exemplified by its effectiveness with even a strictly chemical wet etchant such as TMAH. A limitation of this etch stop effect in silicon is a lack of linearity which limits applications to pseudo 2D structures; however, these limitations might be addressed by future modeling and simulations. It is also possible to do chemistry using the implanted ion species as demonstrated by experiments forming nanowires through implantation, solid-state crystallization, and subsequent revelation through etching [91]. A final development technique is to use deposited material such as platinum as a selectively positioned catalyst for chemical vapor deposition (CVD) nanowire growth. This catalytic nanowire growth technique can also be performed with Ga^+ in silicon if the implanted gallium is first driven to the surface through an annealing step [92]. Targeted growth of nanowires continues to be a stumbling block in the functionalization of nanowires for electronic devices. These targeted catalyst approaches offer the promise of harnessing nanowires in the future through nano-patterning.

1.1.2.6 Precision Implantation for Prototyping and Exotic Devices

When an ion hits a target a number of phenomena happen; the ion is deflected into the target and rearranges atoms creating damage in the form of vacancies and interstitials, rearranged atoms with sufficient energy and optimal position may leave the target in sputtering, the target is locally ionized as target atom bonds are broken and reformed, leading to the release of secondary electrons, and finally the energetic ion might come to rest in the target and act as a local impurity. The final application of focused ion beam technology is precision doping, whereby these impurities are purposely implanted.

In the simplest application a mass filtered LMIS is used to FIB implant typical silicon dopants of arsenic and boron for the production of prototype transistor structures. These implantation FIBs are different from standard analytical FIBs in that they are optimized to enable a wide variability to the beam energies, thus allowing for the tuning of the implantation depth. Furthermore, these doping techniques can be combined with gas assisted deposition to enable exotic transistor geometries, as nearly the complete fabrication can be done on a single tool [93].

Another field where FIB is finding use is when combined with Molecular Beam Epitaxy (MBE) to produce 2D electron (or hole) gas devices. MBE gives the high precision control of the deposition in the depth axis, while FIB acts as a complementary tool for lateral doping. In some cases the two techniques are even combined into the same vacuum chamber [94], though in most cases the

FIB doping takes place after construction of the superlattice [95, 96]. Still other 2DEG studies eschew MBE and use scanning tunneling microscopy (STM) techniques to move donors around using standard gallium ion FIB to define the acceptor wires. Once again the advantage here, with FIB, is the direct controllable implantation of species with high lateral resolution and without the need for lithographic masks.

1.2 Simulation

The topic of this dissertation is topography simulation of FIB milling through the process of sputtering. As was mentioned in the applications section, there are many commercial and research applications that make use of simple LMIS ion beam sputtering. The related processes of deposition and gas assisted etching are not directly addressed in this work, though there have been related discourses published on these gas assisted techniques. In the following sections arguments will be made justifying simulation as a practice, followed by a focused justification of the study of sputtering simulation; finally an overview will be presented of the applicable techniques for sputtering simulations.

1.2.1 What is Sputtering?

Sputtering refers to the ejection of matter from a substrate due to the impact of an energetic particle. Specifically in this work, the energetic particle is an ion of a certain species that has been emitted with a known energy E_0 from the ion source (in this work it is assumed that the ion is Ga⁺ emerging from a LMIS) and interacting with a target material. In this work the target material is taken to be amorphous silicon, though other solids and even liquids have also been studied. When the ion intersects with the target, energy from the ion is transferred to the constituent atoms of the target leading to some fraction of the target atoms to take on sufficient energy to leave the target. The transferal of energy to target atoms alone is not sufficient to lead to sputtering, as the direction of the movement of these excited particles must also be such that they can leave the target. The process leading up to successful ejections from the target is known as sputtering, and those atoms (or molecules in certain cases) that are successfully ejected from the target are said to have been sputtered.

The topic of the theory of sputtering is well covered in the literature [97, 98]; however, it is useful to present a broad framework herein of the theoretical concepts that govern sputtering. Sputtering theory had converged as early as the late 1960s [97] to the point where sputtering was taken as distinct from evaporation and chiefly driven by the transfer of kinetic energy through nuclear collisions. It was accepted that the mechanism of energy transfer took place through a collision cascade, whereby the

energetic ion would scatter off a target atom* and transfer some energy in the process; this scattered target atom would scatter more target atoms while the ion would also continue to scatter and continue to transfer kinetic energy. Through this collision cascade the point-like energy of the ion would be spread over an interaction volume[†], and additionally the multiple collisions would allow for a possible reversal of velocity vector, thus enabling backwards sputtering. Only the energetic collisions that reach the surface with a direction pointing away from the surface and sufficient energy to overcome the binding energy of the surface will result in sputtering.

1.2.2 Why Do We Simulate?

Simulation serves two purposes; the first purpose is to drastically reduce the cost of conducting science by reducing the number of physical world experiments that need to be completed; the other purpose is to better understand the limitations of theories and models for the refinement of scientific understanding. These two processes naturally feed into each other. Knowledge of the limitations feeds the design of experiments and the optimization of experimental conditions can lead to insight into the shortcoming of models. Efficiency is always a major concern with simulations, having a super precise model that is impossible to evaluate leads to no reduction in the number of experiments required. Thus as a general rule, simplicity is king.

It can scarcely be denied that the supreme goal of all theory is to make the irreducible basic elements as simple and as few as possible without having to surrender the adequate representation of a single datum of experience.

ALBERT EINSTEIN, Herbert Spencer lecture delivered at Oxford, Jun. 10, 1933

The manner by which one evaluates a given theory is through experimentation and simulation. The goal of experimental design is to choose parameters for the experiment that allow a single element of the theory to be tested; however, in many cases the uncertainties of the experiment make it difficult to decouple a single element of the theory to be tested. In these cases, modeling and simulation can be used to create a predictive model from theory, the predictive results can then be compared to experimental situations, which mirror the simulation. Simulation thus acts to simplify the testing of complex or subtle theories in addition to replacing and simplifying certain classes of repetitive experiments.

*These scattering events are characterized by the scattering cross-section of an atom at rest for an (energetic) other atom at a given energy, which is zeroth-order dependent upon the masses of the atomic pair and the velocity of the energetic particle.

[†]The interaction volume is governed by the distance that projectiles may travel before losing all their energy through either electronic stopping or nuclear stopping, where nuclear stopping is strongly influenced by the target density at moderate energies.

1.2.3 Why Simulate Sputtering?

In the previous section on applications the primary capabilities of FIB were presented; these capabilities were imaging, implanting, gas assisted deposition and etching, and milling by sputtering. When only the capabilities unique to FIB are considered, one is left with just implanting and sputtering, though as was discussed in the application section, implantation represents only a small portion of active FIB research and application, leaving sputtering as the most valuable unique FIB topic.

From the application side, FIB-induced sputtering is quite a valuable phenomenon, it is the enabling phenomenon for SIMS and for the highly lucrative application of TEM sample preparation. FIB-induced sputtering inherently possesses greater flexibility for arbitrary milling due to the possibility to mill almost any solid material; gas assisted etching, while faster and geometrically more flexible, requires that the etchant match the target material. Sputtering rates do vary from material to material posing an interesting problem to be solved by simulation; yes, nearly any material can be sputtered, but can the milling rate be understood and controlled? Furthermore, the sputtering rate for a given ion-target pairing is highly incidence-angle dependent [99], meaning that the response of topography to FIB irradiation is not intuitively obvious, coupled with effects such as redeposition and reflection; simulation quickly appears to be the only method available to study the complex interplay presented as an irradiated surface evolves away from a conceptually simple flat surface.

Through the simulation of sputtering it is possible to refine the understanding of the subtle symphony of momentum and mass transfer present during ion milling. This understanding would allow for the optimization of milling strategies and even the prediction of milling rates in both FIB processing and SIMS. Additionally, it provides opportunity for the constant refinement, through simulation, analysis, and comparison to experiment, of the theories and models that apply to radiation-induced mass transfer.

1.2.4 Methods Used to Simulate Sputtering

Sputtering can be modeled in two ways: either as a continuum with analytical properties of sputtering, or as a discrete model based on atomic collisions. The atomic collisions model is more physical and less dependent upon the results of experimental data. As an ion enters a target, it transfers energy in a path-dependent manner in two forms: as electronic and as nuclear scattering. Though it is possible to directly study the electronic stopping [100], it is entirely impractical to simulate sputtering through *ab-initio* techniques; as a result the electronic and nuclear scattering are separated in practice. Furthermore it has been shown that sputtering is dominated by nuclear interactions [97]. The electronic scattering is considered only as a path dependent energy loss term approximated through the use

of any number of dielectric approximations. Nuclear scattering is handled separately through either molecular dynamics (MD) or the use of the binary collisions approximation (BCA). MD can be much more precise and offers a greater degree of sophistication, while BCA is fast enough to be practical for the extraction of statistical properties. The following sections will describe and briefly highlight the capabilities and drawbacks of these three approaches to the simulation of sputtering as well as notable occurrences in the literature.

1.2.4.1 Molecular Dynamics

Molecular dynamics tracks the evolution of the configuration and the potential and kinetic energy of a system with respect to time through the evaluation of atomic motion in response to inter-atomic potentials. As such, in pure MD the only changeable parameters for the simulation are the inter-atomic potentials [101]. The other major factors that affect the accuracy of MD simulations are system size, boundary conditions, initial conditions, time-step, and any range truncation used in the force evaluations. System size is important, as MD is used to evaluate many-body problems, and the movements of atoms in a nanoparticle are often different than in a bulk material; it is therefore important that enough atoms be considered to be meaningful. Optimally the simulation system should completely contain the linear recoil cascade, particularly when dealing with sputtering. This places limitations on the energies that can be simulated as increasing energy can increase the volume of the resultant cascade.

Numerous studies have been completed that use MD to explore the phenomenon of sputtering, and increasing computational power keeps pushing the boundaries for precision and number of atoms used in simulations ever higher [102], however BCA will continue to be the simpler and faster solution where many-bodied effects are not of great concern. Inter-atomic potentials continue to be a potential stumbling block where the choices between semi-empiric and ab-initio derived potentials have measurable effects on the simulated sputtering yields, even for such well studied systems as silicon [103]. On the other hand, MD seems to offer the only method for simulating thermal spike situations where localized electronic heating occurs such as in water ices or polymers [104]. In these simulations a parameterized spatial distribution of the electronic energy is converted to heat by random kicks in proportion to that spatial distribution [105, 106]. Thermal spikes need not be caused strictly through electronic heating and thermal spikes due to nuclear stopping occur in various materials, which can lead to localized melting and viscous flow [107, 108] or even localized evaporation [109], thereby requiring the use of MD or intermediate models. These thermal spike models are of interest to SIMS applications and as basic science.

Another application of MD to simulate sputtering is in the simulation of cluster bombardment for

SIMS. At times in SIMS a cluster of numerous atoms forming super molecules such as C_{60} are used instead of single ions in order to increase sputter yield and decrease substrate damage [110]. These many-bodied clusters represent a clear field for MD with a good industrial applications background. Furthermore, when sputtering polymer targets, it is possible that the ejecta are not simply the constituent atoms but actually organic molecules [111] whose complex structure requires careful many-body simulation due to the wide variety of excitation modes present in large organic molecules.

Finally the strength and weakness of MD is that it has explicit atomic positions and thus an explicit set of initial conditions which may or may not be physical. A physical ensemble of the initial positions can be produced through the use of simulated annealing, whereby a physically reasonable amount of entropy is added to the system through thermal vibrations. In recent times it has been possible to simulate the evolution of the free sputtered surface, whereby surface topography can be realistically created from a virgin surface due to simulated ion bombardment [112]. This simulated surface topography is of course computationally expensive and care must be taken to determine how sensitive a given simulated property is to the simulation initial conditions.

1.2.4.2 Binary Collisions

There are a number of BCA software packages that are available and used in the community. The most well known are MARLOWE [113] and TRIM.SP [114], though this work uses the less well known but mature package of IMSIL [115]. All of these packages function as Monte Carlo (MC) simulators whereby a large number of deterministic calculations with one or more random components are performed in order to study the statistical behavior of systems. In these simulations a simulated ion trajectory meets the simulated surface which can be crystalline or amorphous; in the simplest case of a monocrystalline target at zero temperature the simulation can be deterministic after the first random selection of the impact parameter; however, finite temperatures and amorphous targets act to decrease the determinism. The collision cascade is simulated in a sequential binary manner, whereby only a single collision between a single pair of atoms is simulated at any given time. Subsequent collisions are simulated in an arbitrary sequential order as defined by the simulation package, e.g. MARLOWE always evaluates the highest energy projectiles first.

Contrary to the case of MD, BCA simulations are inherently time-independent. Collisions are assumed to occur in zero time and no effort is made to track the dynamics of the projectiles between collisions. Each collision results in a new direction and energy for the two collision partners. This information and the position is the only information needed to continue generating collisions in a crystalline or amorphous material. As the projectiles are assumed to travel on their asymptotic trajectories, the simulated paths of the atoms involved in a collision cascade (between intermediate

collisions) are straight lines. This asymptotic approximation is known to be less accurate at lower energies (single eV) due to both computational precision and an increased effect of multi-body effects at lower energies [98, 116]. Surprisingly however, BCA simulations still show very good agreement to experiment with better statistics than MD can usually provide due to being 4-5 orders of magnitude faster.

Historically, most of these simulation packages were developed in order to simulate the range of ions in matter as applied to damage* and doping. In order to use the BCA to simulate sputtering, one must carefully track the energy and direction of projectiles as they near the surface. The detection of a sputtering event is usually used with a planar surface binding energy potential, whereby a projectile is sputtered if its perpendicular energy component exceeds a predefined or calculated surface binding energy. Work has been done showing the limitations of the planar surface potential in certain systems [117]; however, as mentioned, BCA has been shown to be reliable as compared to experiment, even in the case of sputtering.

A recent development in the class of BCA simulations are simulations attempting to couple secondary electron emission with traditional BCA simulation, which determines the distribution of ion energy into the target. These simulations considering secondary electrons, of which a notable example of the type is the code IONISE [118], are valuable because they approximate the emission of secondary electrons, which enables in-depth analysis of SIM effects and additional simulations of the mechanisms governing gas assisted deposition where secondary electrons are known to play a role in precursor decomposition[†]. IONISE makes use of a pseudo-empirical law to relate the statistics of secondary electron emission with energy deposited in the target by the ion, both due to nuclear and electronic stopping [118]. These simulations are especially useful for simulating gas assisted deposition by light noble atoms such as helium [119] and neon [120], which represent a recently developed technique enabled by the development of bright and stable GFIS.

A final interesting class of BCA simulation are those so-called dynamic simulations, an egregious misnomer because of the assumed time independence of the BCA; in these simulations the simulated material is allowed to generate a history and change between impacts. There are dynamic simulation packages based on all of the aforementioned BCA codes (including MARLOWE [121] and IMSIL [122, 123]) though Tridyn [124] based on TRIM seems to be the best known. These dynamic simulation codes can allow the direct simulation of the surface evolution as well as effects of radiation-induced

*Damage here is referring to the disruption of the crystalline lattice through the introduction of sufficiently many defects (in the form of vacancies or interstitials or clusters thereof) so as to permanently change the lattice and thereby the physical or electrical properties of the crystal.

[†]The importance of secondary electrons for gas assisted deposition very much depends on the exciting particle; for instance electrons and light ions, due to their greater degree of surface interaction, produce many energetic secondary ions that can lead to precursor decomposition. With heavier ions it is possible that secondary electrons are produced deeper in the target and may not reach the surface whereby the location of the ion impact should dominate the growth rate.

mixing. The dynamic simulations function by subdividing the simulation volume into regions (cells) and tracking the concentration and species of implanted or displaced atoms and vacancies. After a predetermined number of simulated ions these cells undergo a relaxation step to allow for volume changes. Physical properties of any intermixed cells, e.g. the surface binding energy of a silicon cell with a high gallium concentration, are handled through interpolation. A drawback of the cellular Monte Carlo method is that sufficient particles must be modeled for each affected cell, thereby leading to a trade-off between computational speed and simulation noise or resolution. Furthermore, the only mechanism of atomic displacement is the collision cascade leading to the loss of bulk properties such as relaxation due to stress or strain; although recent work has been done to couple bulk properties to dynamic BCA simulations in the simulator IMSIL [125].

1.2.4.3 Continuum models

Sigmund's work made use of transport theory to derive a set of analytical equations that describe sputtering in a continuous amorphous or polycrystalline medium which show good agreement with experimental data in the medium energy range ~ 1 keV to 1MeV [97]. Later work was done to develop a semi-empirical model to predict the sputtering yield with respect to the ion energy [126–128], experimental data in this work was supplemented with BCA simulations. Additionally these semi-empirical models address the failure of the Sigmund model to correctly address the decline in sputtering yield at glancing incidence angles; without the changes introduced the calculated sputter yield does not return to zero for extreme glancing angles [129]. These semi-empirical models were later extended and revised to better handle low energy angular distributions of sputtered ions [130]. These analytical and semi-empirical models offer the advantage of being directly calculable, which makes them enticing as an input for topographical simulations, however even in the mature models shown in the later works [130] there still exist deviations from the experimental and simulated data.

While surface topography can be simulated atomistically, as in the case of the large scale MD simulations [112], the memory requirements of keeping track of individual atoms quickly becomes a limiting factor; therefore, it is necessary to use continuum approximations when large topographies are to be simulated. There exist a number of approaches that have been used to map the evolution of topographies to a continuous medium, however all of them make use of spatial discretation. There are three commonly used methods for tracking the evolution of the target topography in these spatial discretations, namely three-dimensional cells, level-set, and strings.

A cell-based approach is often used in dynamic-BCA simulations as it enables the tracking of materials changes inside of the target; additionally, BCA simulations explicitly consider the bulk nature of the target. In this method a grid of rectangular or rectangularly prismatic cells is used to represent the

simulation volume [123,131]. As the simulation progresses, atoms and ions are sputtered, implanted, and redistributed among the cells. A relaxation step is taken at intervals to adjust the volume of each cell to match the mass of atoms attached to the cell, in this method empty cells can be reduced to zero volume thereby creating topography. A drawback to this method comes from the prismatic cells which introduce corners and therefore noise at the interface; however, if the grid is chosen to be small enough the discretation errors can be safely ignored. As with the case of the atomistic MD simulations, the memory requirements for a large grid are non-negligible, though this method, when coupled with BCA simulations, implicitly handles higher order effects such as redeposition and reflection of ions.

The level set approach represents an alternative method to string methods (see the following paragraph) for tracking the evolving topography in continuum simulations. The level set method implicitly handles difficulties such as cusps and merging topographies and has been demonstrated for focused ion beam simulation [132]. The technique is highly used in the field of semiconductor process modeling and offers many opportunities to simplify the simulation of 3D topographies. Specifically, level set methods enable the direct simulation of intersecting cuts in a self consistent manner, without resorting to the use of heuristics to determine the correct reconstruction method for overlapping string domains. The simulation of cuts is expected to be useful in simulating FIB processes such as lift-out TEM sample preparation (section 1.1.2.2) and cutting post processing as associated with MEMS construction (section 1.1.2.5).

String methods represent the other extreme of simple methods used for tracking the evolution of FIB surfaces; these methods explicitly track the interface between the substrate and the vacuum as represented by a set of nodes connected by line segments of some dimensionality. In many cases the nodes are connected by linear line segments; however, there are also examples with higher order approximations [133]. This method is extensible to both 2D and 3D simulations, though the 3D examples require careful handling of the triangularization [134] in order to stay memory efficient. The alternative to triangularization is to do a naive implementation using a grid of 2D strings which scales as the product of the number of horizontal and lateral nodes composing a string. As described in section 2.2.4 it is generally desirable to maintain a fixed surface spacing between grid points, which with a naive 3D implementation leads to the addition of M nodes for every additional node added to a string of N nodes on a $N \times M$ surface grid. In string methods the surface is advanced either by moving the nodes [115,129,135,136], usually along an angle bisector, or by moving the segments [135]. The velocity of the nodes or segments is calculated over a discrete time step by associating a volume with each node and adjusting that volume by the mass transfer due to sputtering or redeposition. The string approach is compatible with shadowing and higher order effects such as redeposition,

and reflection [137] though they must each be explicitly handled in the mass transfer equations. The string approach is used in the majority of FIB simulations that do not explicitly conduct BCA simulations between time steps and even in certain cases where BCA simulations are conducted between time steps [134].

1.2.5 What is this Work?

The work presented herein describes a continuum topography simulator (referred to in this text as TopSim) whereby a string method is used to track surface advancement in two dimensions; the model presented takes into account sputtering due to primary FIB ions, redeposition of target atoms along the trench, secondary sputtering due to both reflected ions and energetically sputtered target atoms, and redeposition due to both sputtered atoms and reflected ions. Sputtering yields are pre-calculated from statistical significant simulations conducted with the BCA simulator IMSIL [115] and special care is taken to ensure that the simulated ion behavior is physically relevant at normal and glancing angles. This relevancy is obtained through careful comparison with experimental sputtering yield data. Additionally, a method of inverse modeling to determine ion beam dose profiles required to produce user defined topographies is presented.

There exists previous work in the field of FIB topography simulation, notably the work presented in the references of the previous section with respect to continuum models. This work is an example of a subclass of hybrid simulations where physical sputtering properties are derived from BCA simulation instead of analytical, empirical, or semi-empirical inputs. The hybrid approach offers the significant advantage of being tunable to different ions, targets, and energies, simply by changing the parameters of the BCA simulation; additionally BCA simulations provide significantly more data with respect to the population distributions of sputtered and backscattered species than can practically be obtained with experimental techniques. Of this class of hybrid FIB topographical simulation there exist further examples of 2D and 3D simulators with both offline [132, 138–143] and online [134, 144] BCA simulation, with the distinction arising from whether sputtering properties are pre-simulated for a representative target element or whether BCA simulations are conducted for sub-domains intermediately inside of the topography simulation. This presented work is a 2D offline simulation, though a subset of features are also available for use in 3D topography simulations.

1.2.5.1 The Hybrid Approach

Details of the hybrid simulation model will be communicated in the following chapters, with chapter 2 beginning with a description of the general process for modeling the mass transfer and topography

simulation using a simplified model that does not attempt to resolve the effect of sputtering due to sputtered particles. This simple model is presented first, as it lays much of the groundwork for the self-sputtering model and presents interesting physical effects, while having the advantage to be clearly and concisely described. The physical inputs for the model will be discussed in passing in this chapter but will be examined in greater detail in a later chapter (chapter 4).

In the last presentational chapter, chapter 5, the extension to the model required to simulate the sputtering due to sputtered atoms will be explained. The addition of a second sputtering species and the consideration of the angular energy distributions of sputtered atoms and backscattered ions necessitate several additional levels of complexity as compared to the simpler model presented in chapter 2. The nomenclature of the mass transfer equations is therefore changed between chapter 2 and chapter 5, where, in addition to the formulation of the model, simulations based on this enhanced model will be demonstrated. It will be shown in chapter 5 that there exists evidence suggesting that self-sputtering does occur in certain geometries, namely that the commonly accepted high order sputtering terms of redeposition and sputtering by backscattered ions are insufficient to explain the types of micro-trenching seen in certain experiments.

1.2.5.2 Inverse Modeling

An inverse modeling technique making use of the topography simulator is demonstrated in chapter 3 by means of which dose profiles may be optimized for user-defined geometries. This example provides a valuable tool that could have the future power to enable the direct engineering of structures formed by FIB. In this research it is also important because it highlights a shortcoming of the simpler model that neglects self sputtering. Through the use of the inverse modeler it is possible to derive dose profiles that result in the milling of shapes with very straight and well-defined sidewalls while directly compensating for the earlier, well characterized effects of redeposition and sputtering by backscattered ions. Existence of the inverse modeler provided the catalyst that lead to the collection of experimental evidence indicating that additional unaccounted for sputtering might be occurring. These experiments, which did not exhibit the modeled response, prompted the development of the self sputtering model presented in chapter 5.

Chapter 2

Forward Modeling

This chapter presents the general model used for topography simulation of focused ion beams in 2D. Specifically, a monoenergetic model is presented here that does not discriminate over the energy of either backscattered ions or sputtered atoms; this model is sufficient for most topography simulations. An energy-resolved model is presented in chapter 5 wherein special attention is paid to the energy of sputtered and backscattered particles, thus enabling the simulation of sputter events caused by sputtered target atoms. This energy-resolved model is the logical extension of the monoenergetic model and the comparative simplicity of the monoenergetic model is superior for the purpose of explaining the underlying concepts of the simulation; additionally, most of the work presented in this dissertation was completed using a variant of the monoenergetic model.

The models presented in this work are part of the software package TopSim, which is implemented as computer code in the interpreted language Python [145] (version 2.7). TopSim refers to a software package comprised of both the forward modeler (presented in this chapter) and the inverse modeler (presented in chapter 3). Python is chosen as the language for implementation as Python represents a nice balance between readability, maintainability, clarity, and numeric performance [146]. Python allows for high-level abstraction of concepts and data-structures while also providing the capability for performance optimized numerical routines through packages such as NumPy [147] and SciPy [148]. As this work is performed in an educational setting at a university, the clarity and extensibility of the underlying language is particularly valuable, as multiple generations of students could conceivably contribute to a single code-base. Python in particular is strong for readability as it enforces strict rules for white-space, which guarantee a level (albeit sometimes low) of code formatting and unified style. This project is the extension of a pre-existing Python reimplementations of the IonShaper [115] code, which contained a functional model for beam-sputtering with simple cosine redeposition which has since been extended as described in this chapter, coupled with inverse modeling (chapter 3), and

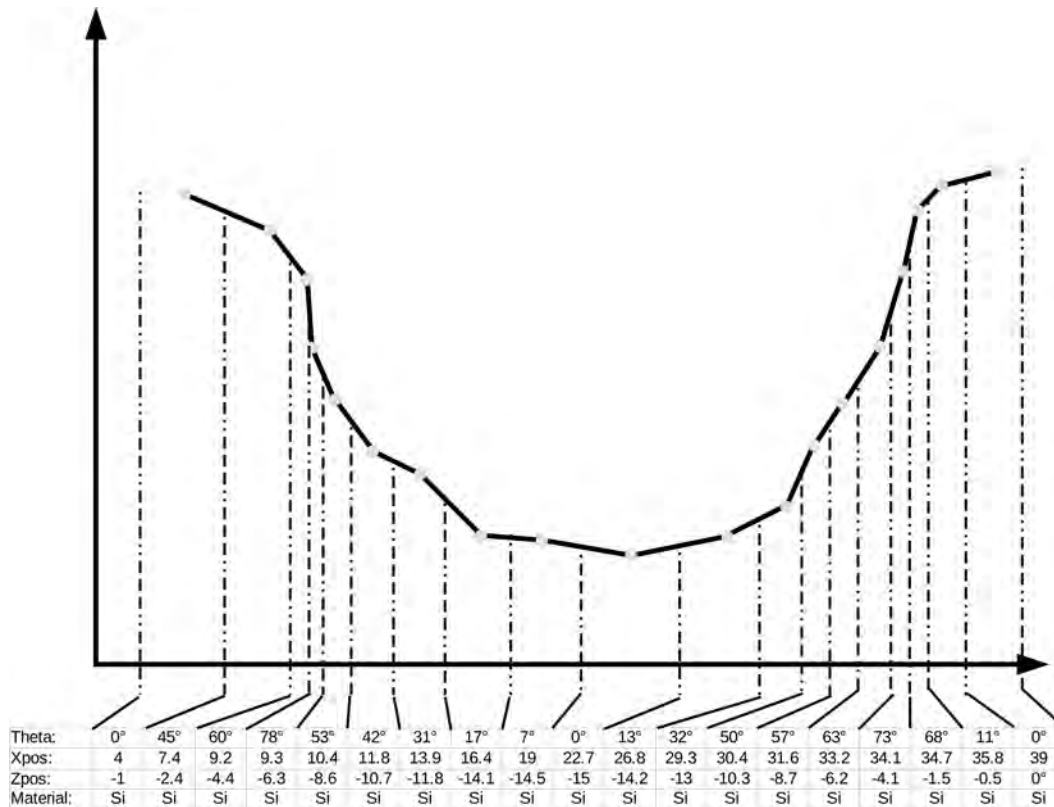


Figure 2.0.1 – A schematic sketch of the 2D string model used to simulate topographies in TopSim. The string is made of up nodes (light blue circles) which contain geometric and materials information used along with the equations of motion to calculate the displacement of nodes during a given time-step.

further extended to model energy-resolved reflexive-sputtering (chapter 5).

Topographical simulations in this work were carried out using a string model made up of attribute containing nodes connected by simple line segment representing the time advancing surface (see: figure 2.0.1). A discrete ion dose is applied to these nodes by mapping a hypothetical spacial dose distribution simulated by a number of Gaussian beams representing pixels specified to a FIB. The spacial dose distribution may be time-dependent but is often assumed to be time-invariant in order to use the approximation of an overlapped beam profile which is valid for fast FIB scan rates. Use of the overlapped beam profile allows for the decoupling of the beam advancement from the simulation of the surface advancement which enables the use of more aggressive time-steps in the simulation of the topography evolution. The model is therefore a doubly discrete simulation in time and space; in each time-step a spacial dose is applied proportional to the product of the simulated beam current and the time-step, this dose results in mass redistribution (governed by the equations of motion: section §2.1) and loss by sputtering which is spatially sampled at each node, resulting in velocity driven by the change in volume at the node. Nodes move a distance along their normals determined by the velocity and the time-step. In this manner the evolution of the topography is simulated over time.

The chapter is presented in five parts. Initially the equations of motion are given and described highlighting the phenomena of direct sputtering, sputtering by backscattered ions, and the redeposition of target atoms sputtered by both phenomena. The second part focuses on the properties of the spatial discretization or gridding, the third section presents representative examples of the statistical functions used in the equations of motion for the system of 30 keV gallium ions impinging on a silicon target. In the fourth section representative simulation results will be shown. Finally the strict angular dependence of the model will be used to show that a scaling relation exists for results, allowing simulation results to be scaled across time and space.

2.1 Equations of Motion

The topographical simulation of focused ion beams makes use of physical equations of motion that track the transference of matter from one sampling point to another sampling point across the simulated topography. Of note is the fact that no attempt is made to spread received or emitted flux across multiple nodes; each node in this simulation is a point-like sink or source, making this specific form of simulation strictly *local*. A non-local simulation [115] would account for the lateral displacement of ejection sites resulting from the finite volume of the recoil cascade.* However, as the projected range of gallium in silicon is $\approx 30\text{nm}$, there remain a number of applications where non-local effects can be neglected. One notable exception is the simulation of gas-assisted deposition or etching, where it has been shown that the non-local effects can be significant. For systems with features larger than tens of nanometers the local model is sufficient.

*The volumetric energy distribution, as defined by the recoil cascade for a specific energy-species pairing, has a characteristic shape and if that volume were to be truncated due to surface curvature (or conversely if the path length to the surface were to increase), the BCA derived sputtering yield would no longer be precise. Coarse and large scale simulations, as presented herein, should be unaffected; however, the Ebm paper [115] was concerned with the simulation of gas assisted processes where a strictly *local* model is not appropriate.

2.1.1 Beam Sputtering Flux

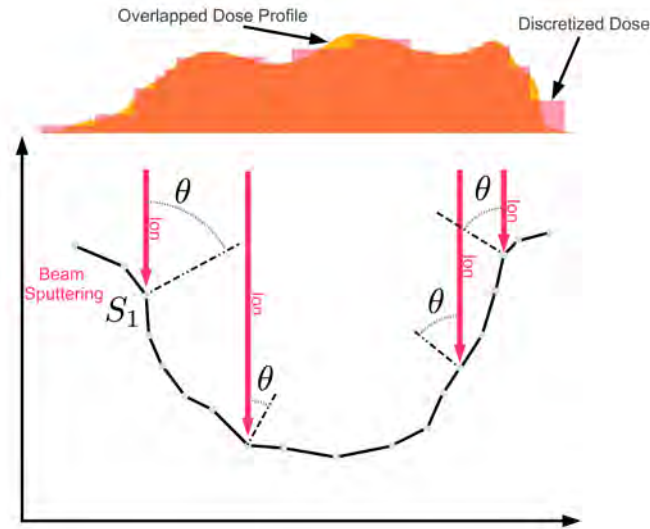


Figure 2.1.1 – A sketch showing the procedure for calculating the sputtering due to beam ions. The overlapped dose profile for the timestep is discretized over the nodes of the string providing a dose per node. The incidence angle θ is used with equation (2.1.1) to calculate the number of target atoms sputtered at a given simulation node.

The flux of sputtered atoms due strictly to direct sputtering by the ion beam in the simulation is governed by equation (2.1.1) which describes the flux of sputtered atoms F_{sput} produced by the beam flux F_{ion} impinging a surface element of the target with an incidence angle of θ (figure 2.1.1) [where the incidence angle θ is defined as the deviance from perpendicular, wherein an ion beam impinging the target perpendicularly would have an incidence angle of 0°]. Beam sputtering is dependent on the geometric projection of the beam exposure area on the surface as indicated by the cosine term.

$$F_{sput_1}(S_1) = F_{ion} \cdot Y_{sput}(\theta) \cdot \cos(\theta) \quad (2.1.1)$$

Beam sputtering, also referred to as first-order sputtering by ions (first-order sputtering), is modeled as depending solely on the topography, the dose profile, and the sputtering yield $Y_{sput}(\theta)$. The sputtering yield is unique for a given ion-target pairing and is derived from BCA simulations using IM-SIL, though the sputtering yield can also be measured experimentally with high precision. Example sputtering yield data will be shown in section 2.3.1.1 on page 39.

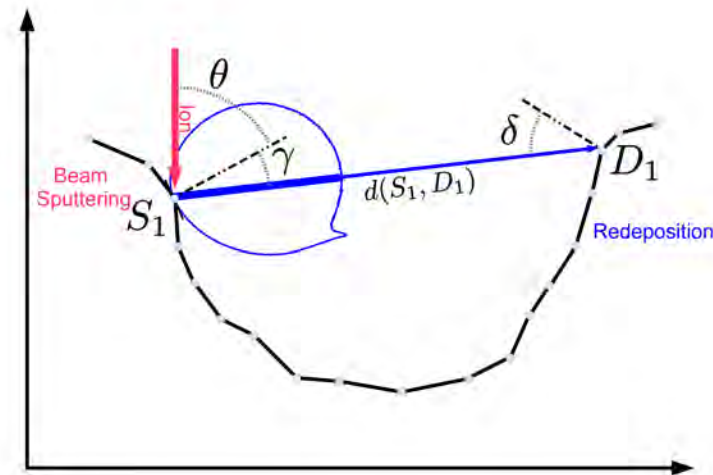


Figure 2.1.2 – A sketch showing the procedure for calculating the portion of redeposition flux arriving at the destination node D_1 due to sputtering that occurs at the source node S_1 . Note that the total redeposition flux arriving at D_1 is the summation over all source nodes. The angular distribution for the redeposition flux is indicated as a blue polar plot at S_1 , note that for this incidence angle there exists a degree of asymmetry and additionally a visible peak near the expected angle of a specular reflection. This peak is caused by target atoms sputtered due to early collisions with the ion. These so called first-knock-on occurrences have a distinct energy signature and will be further discussed in a later chapter (appendix A).

2.1.2 Redeposition Flux

As atoms are sputtered from the target, they escape to vacuum with a given angular distribution $f_{sput}(\gamma, \theta)$; if these atoms encounter no other surfaces (as in the case of initial sputtering from a virgin surface) then all of the matter comprising the beam sputtering flux F_{sput} is removed; however, if there exist surfaces in these paths, these surfaces will receive matter in the form of atoms sticking to the visible surfaces. The redeposition flux F_{reddep} (shown in blue in figure 2.1.2) is therefore strongly dependent on the simulated topography. A commonly used function for approximating the sputtering angular distribution $f_{sput}(\gamma, \theta)$ assumes a cosine relationship of the form $c_1 \cdot \cos^n(\gamma)$ which presents the advantage of being independent of the incidence angle θ ; however, it will be shown in 2.3.2.1 on page 42 that this approximation is only remotely valid near normal incidence and preserving the θ dependence is valuable when feasible. The redeposition flux is characterized by equation (2.1.2). Where $l(S_1)$ represents the length (area in 2D) of the node S_1 and $d(S_1, D_1)$ represents the distance between nodes S_1 and D_1 .

$$F_{reddep_1}(D_1) = \sum_{\text{visible } S_1} F_{sput_1}(S_1) \cdot f_{sput_1}(\gamma, \theta) \cdot \frac{\cos \delta \cdot l(S_1)}{d(S_1, D_1)} \quad (2.1.2)$$

It should be noted that the sputtered atoms comprising the sputtering angular distribution $f_{sput}(\gamma, \theta)$

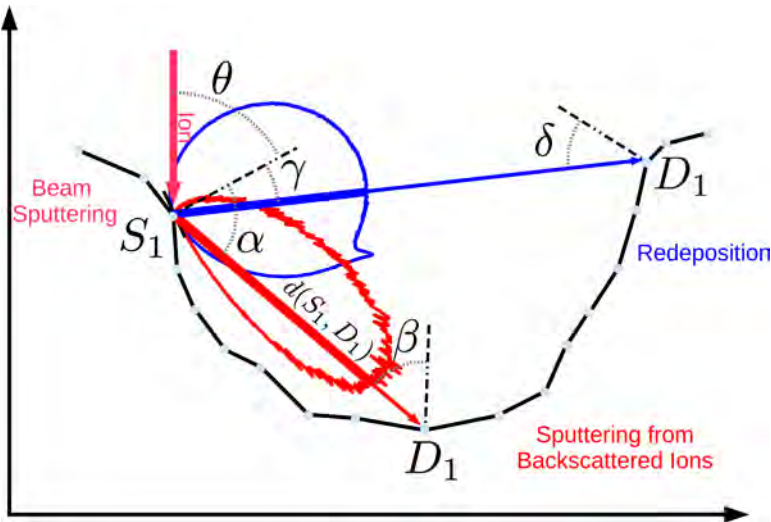


Figure 2.1.3 – This sketch shows the calculation for sputtering by backscattered or reflected ions (flux indicated by a *red* arrow) at a destination point D_1 , as in the case of the redeposition flux; the total sputtering at the node D_1 is the sum across all source nodes. Note that the backscatter angular distribution (*red* polar plot) is significantly less symmetrical as compared to the sputter angular distribution (*blue* polar plot); it should also be noted that both distributions are normalized and the absolute magnitudes are incomparable.

are not mono-energetic as was the case with the ions that make up the primary beam sputtering flux. These sputtered atoms not only vary in the direction with which they leave the target, but also in the energy that they carry in the form of velocity as they are ejected into vacuum. The implicit assumption used in this formulation of the redeposition flux is that all ejecta leave with low energy and upon any further interactions with the target topography result only in redeposition, sticking to the target producing a positive matter gain at the node. For many cases this assumption is reasonable as more than half of the sputtered atoms retain energies of less than 20 eV (figure 5.1.2), however as will be shown in chapter 5, there are situations when this assumption breaks down.

2.1.3 Sputtering by Backscattered Ion Flux

Incident ions are not implanted with one hundred percent efficiency; especially at the low energies simulated in this work, a certain fraction of ions will experience collisions that lead to a reversal of their initial velocity vector and through subsequent collisions reach the surface with sufficient energy to escape the surface binding energy. These so-called backscattered ions, because they are scattered back into the direction from which they came, often (quantified in chapter 5) have sufficient energy to stimulate further sputtering. In the monoenergetic model presented in this chapter it is assumed that ions lose negligible energy when they are backscattered, though an energy-dependent model is presented in chapter 5; the flux of target atoms removed by these backscattered ions is modeled with equation (2.1.3) and equation (2.1.4). Where the flux of backscattered ions (equa-

tion (2.1.3)) is calculated analogously to the flux of atoms sputtered by the beam (equation (2.1.1)) with the substitution of the ion backscatter yield $Y_{back}(\theta)$ for the sputter yield $Y_{sput}(\theta)$. The sputtering caused by these backscattered ions is calculated by equation (2.1.4), which is itself analogous to the redeposition flux (equation (2.1.2)) with the notable substitution of the backscatter angular distribution $f_{back}(\alpha, \theta)$ for the sputter angular distribution and the addition of a sputtering yield at the destination $Y_{sput}(\beta)$, which is necessary as the backscattered ions are not simply redeposited but also cause additional sputtering at the destination (figure 2.1.3).

$$F_{back}(S_1) = F_{ion} \cdot Y_{back}(\theta) \cdot \cos(\theta) \quad (2.1.3)$$

$$F_{sput_2}(D_1) = \sum_{\text{visible } S_1} F_{back}(S_1) \cdot f_{back}(\alpha, \theta) \cdot \frac{\cos \beta \cdot l(S_1)}{d(S_1, D_1)} \cdot Y_{sput}(\beta) \quad (2.1.4)$$

Both the backscatter yield $Y_{back}(\theta)$ and the backscatter angular distribution $f_{back}(\alpha, \theta)$ have characteristic shapes that are different from those of their sputtering counterparts, and the features of these functions will be discussed in greater detail in 2.3.1.2 on page 39 and 2.3.2.2 on page 44 respectively.

2.1.4 Redeposition of Atoms Sputtered by Backscattered Ions

As the backscatter sputter flux causes an additional mechanism for the removal of mass, there must also be opportunity for these atoms to be redeposited in order to maintain the conservation of mass in the simulation. This final redeposition step uses the cosine approximation for the angular distribution of sputtered ions as the full calculation of the redistribution flux is computationally expensive and this is taken as a valid approximation in the final low magnitude term of the model (see the cyan angular distribution shown in figure 2.1.4). The equation (2.1.5) shows the formula for the flux of redeposited atoms sputtered by backscattered ions F_{reddep_2} , which is directly analogous to equation (2.1.2), with the sole differences being the coordinates and angles and the substitution of $c_1 \cdot \cos^n(\varepsilon)$ (where n is the power of the cosine used and c_1 is a scaling prefactor, which for 2D simulations is $n = 1$, $c_1 = \frac{1}{2}$) for the sputtering angular distribution $f_{sput}(\gamma, \theta)$.

$$F_{reddep_2}(D_2) = \sum_{\text{visible } S_2} F_{sput_2}(S_2) \cdot c_1 \cdot \cos^n(\varepsilon) \cdot \frac{\cos \varphi \cdot l(S_2)}{d(S_2, D_2)} \quad (2.1.5)$$

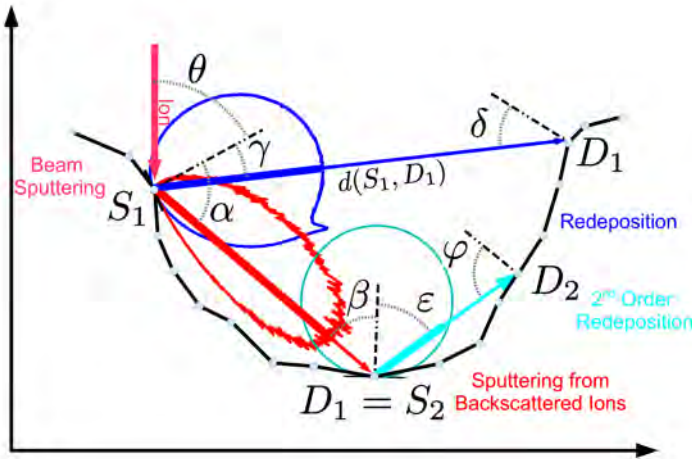


Figure 2.1.4 – A sketch showing the geometric arrangement and angular distributions used with the equations of motion presented in this chapter. Note the addition of the term for redeposition due to sputtering by backscattered ions; also note the three angular distributions shown: sputter *blue*, backscatter *red*, and the cosine *cyan* approximation.

2.1.5 Fluxes to Motion

In the preceding paragraphs a system of matter fluxes was presented that can be used to model the manner in which matter is instantaneously displaced across a given topography; however, the evolution of the topography has not yet been thoroughly described. The fluxes hitherto described (the primary beam sputtering flux: $F_{sput_1}(S_i)$, the first order redeposition flux: $F_{redep_1}(D_i)$, the second order sputtering flux by backscattered ions $F_{sput_2}(D_i)$, and the second order redeposition flux due to sputtering by backscattered ions $F_{redep_2}(D_i)$) possess the units of number of target atoms per square nanometer per second ($\frac{N}{nm^2 \cdot s}$). After the fluxes have been calculated across all nodes for a given spatial configuration of nodes it becomes possible to convert this collection of fluxes into a node velocity as shown in equation (2.1.6)* by making use of the inverse of the atomic density of the target v_{target} as defined in cubic nanometers per atom ($\frac{nm^3}{N}$), thereby yielding a velocity with units $\frac{nm}{s}$. This velocity can then be multiplied times the current time-step to yield the distance a node moved along its surface normal (see section 2.2.1) over a given time-step.

$$V(S_i) = v_{target} \cdot [-F_{sput_1}(S_i) + F_{redep_1}(S_i) - F_{sput_2}(S_i) + F_{redep_2}(S_i)] \quad (2.1.6)$$

As a convention, sputtering fluxes are taken to produce a negative velocity (corresponding to material loss at the node). However, due to the choice of coordinate systems used within TopSim, it

*The nomenclature changed in this equation and no differentiation is made between source nodes and destination nodes. This is due to the fact that every node has the opportunity, except when constrained by visibility, to be both a source and a destination.

is necessary to negate the displacement internally in order to produce the expected behavior whereby trenches trend toward greater negatives heights as their maximum depth is approached.

2.2 Gridding

Once the beam effects have been considered it is necessary to have a well-behaved scheme for tracking the topography evolution of the simulated surface. The grid which defines the simulated surface exists as its own conceptual and computational object. This grid must serve two purposes; it must enable the simulation of the physics described in the preceding section, and it must evolve through time in a numerically stable manner. Gridding refers to the conceptual and algorithmic process of defining and evolving the collection of interconnected nodes through the course of a simulation. The gridding strategy used here is a string based model with linear line segments connecting points. As the geometry only changes after the successful completion of a time-step, node properties derived from the geometric state are stored for each node on the string. This decoupled calculation of the grid properties is computationally more efficient due to the avoidance or recalculation of static parameters and performance increases due to the use of vectorizable[†] forms.

2.2.1 Definition of the Surface Normal at the Node

It is advantageous to pre-calculate the surface normal at each node as this vector is used both for the advancement of the surface (which moves along the surface normal in proportion to the volume gain or loss) and in calculating the incidence angle between the beam components (see figure 2.1.4) and the surface. The strictest geometrical definition of an equivalent normal vector at the node would be the angle bisector. Note that mathematically the first derivative is discontinuous at the nodes of a piecewise linear function like the one used in this string model. There has been work done to develop a surface model that does not exhibit these discontinuities [133]; however, this higher order surface model is not yet available in TopSim. In this work the angle bisector is further approximated through the use of a normalized 90° rotation of the vector connecting a node's left and right nearest neighbors. This approximation approach, demonstrated in figure 2.2.1, is both computationally more efficient and numerically stable as it avoids an additional vector normalization step. As compared to the angle bisector approach, which was also implemented for testing, there is no apparent functional difference between the two calculation methods under normal simulation circumstances. This rotated-vector

[†]Vector here refers to the computational concept whereby a single operation is carried out in parallel across multiple data entries using a single instruction as a SIMD instruction.

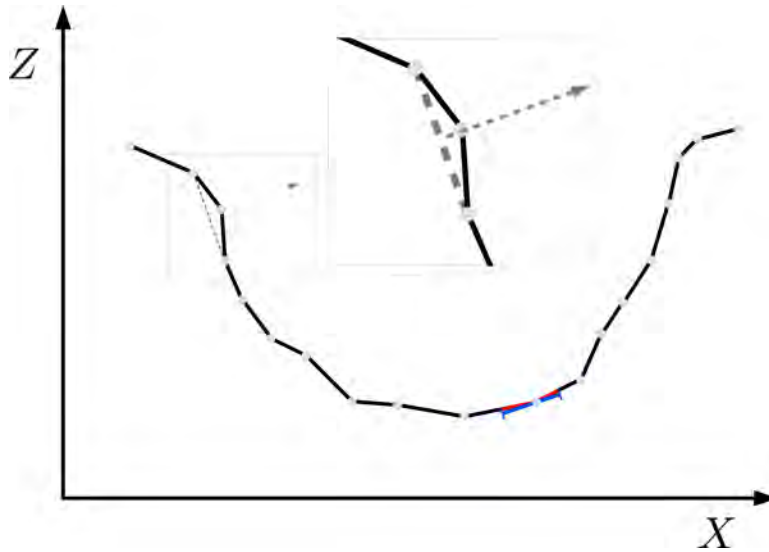


Figure 2.2.1 – A sketch showing how the surface normals are calculated at the node (in gray). Note that this is not a strict angle bisector calculation. Also shown (in blue) is the calculation for the associated length for a node.

approach is robustly defined for every node point except the end-points of a given string. Edge cases presented by the two endpoints are handled by mirroring the existing neighboring segment.

2.2.2 Length-Segment Calculations

As this text focuses on the 2D model, each node contains an effective length for the segment, as was shown in equation (2.1.2), equation (2.1.4), and equation (2.1.5), this is a length in the 2D simulation because a virtual depth into the simulation plane is used. In 3D this length-segment quantity would be contained in the equations as an actual area. The length associated with each node is defined as the arithmetic mean between the length of the segment to the left and the segment to the right of the node in 2D (shown schematically in figure 2.2.1). Practically, scan profiles used in 2D simulations to be compared to experiment often assume a large number of pixels projecting into the simulated plane as simulated structures are usually trenches or troughs. In 3D there exist length segments in both directions, the resulting area of the quadrilateral defined by these two orthogonal length segments is trivial to compute.

2.2.3 Loop Avoidance

A drawback of string methods is their susceptibility to loops (see figure 2.2.2); loops are avoided in this simulation by ensuring that the X-axis coordinates remain sorted and interpolating the location on

the Z-axis* of nodes back to a predefined grid on the X-axis. If a cross-over is detected, the time-step is halved and restarted from a point before the crossing occurred. A drawback to this requirement of non-overlapping X coordinates is that it excludes the possibility of simulating overhanging structures. However, for typical simulation structures of trenches, this limitation is acceptable. Due to the modular nature of the simulation code, it would be possible to implement a different form of loop detection and allow the existence of overhanging structures.

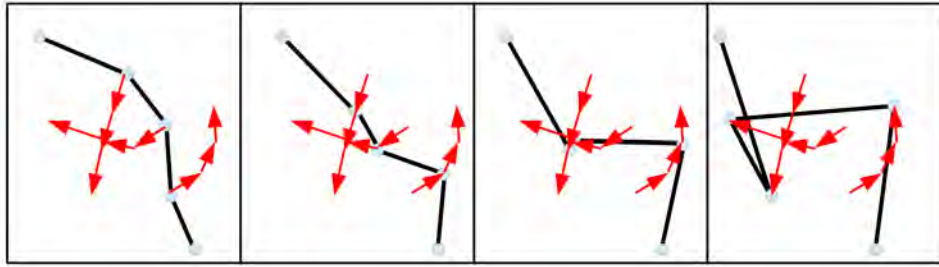


Figure 2.2.2 – An idealized sketch showing the evolution of a surface loop over a small number of time-steps (indicated with red arrows). Loops are avoided in TopSim through the requirement that the horizontal components of the surface nodes must always be increasing. If this condition is not met, the time-step is reduced and the calculation repeated for the offending time segment.

2.2.4 Adaptive Gridding

Node density presents an outstanding problem for string models and most other finite sampling approaches. As the simulation of higher order effects such as redeposition and milling due to backscattered ions requires the calculation of sum of the fluxes emerging from each node, additional nodes represent a clear cost in computational efficiency. However, sufficient nodes must be used to adequately represent the features of scientific interest; quite often the features of a simulated trench wall are of scientific importance. In the simplest approach to grid specification, nodes are defined upon initialization with a fixed linear spacing in the horizontal axis. This presents problems at trench sidewalls as the euclidean distance between grid points increases with increasing depth for a fixed grid. Node-crowding, defined as the uneven or suboptimal distribution of nodes along the bottom of a simulated trench with respect to the density along the sidewalls (shown in figure 2.2.3) results in a conflict between resolution and computational efficiency. To address this problem, an adaptive grid is defined along domains that attempts to maintain a fixed two-space (three-space in 3D simulations) distance between nodes as defined by the segment length. This distance is maintained through the addition and deletion of intermediate nodes. Furthermore, adaptive grid regions can be spec-

*This is the first place that named coordinates are used (see 2.2.1), the assumed axis used for these simulations is a rightward positive X axis and a virtual Y axis going into the simulation plane, the Z axis follows the right-hand rule, and 2D simulations are carried out on the X-Z plane.

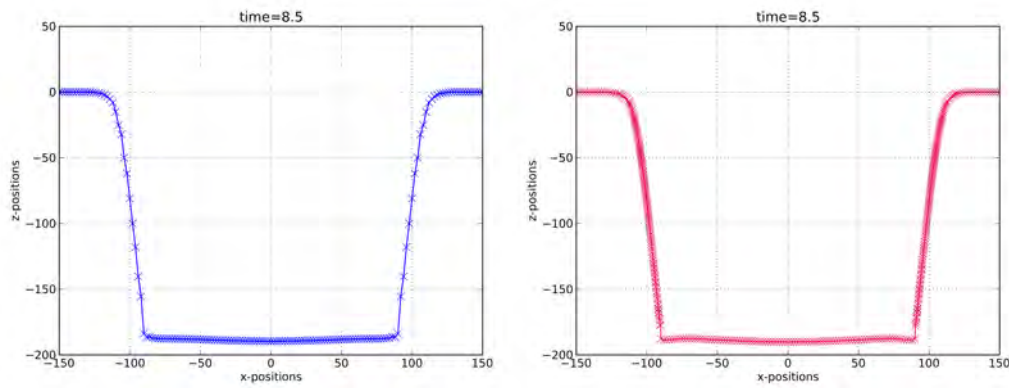


Figure 2.2.3 – Simulation results from two nearly identical TopSim simulations: The left *blue* curve is conducted with a fine fixed grid (lateral spacing: 2 nm), the right *red* curve is conducted with an adaptive grid (target distance between nodes: 2 nm). Note that the nodes shown as crosses are equally distributed along the sidewall in the adaptive simulation. The fixed grid simulation shows strong node-crowding.

ified piecemeal across the simulated dimensions with different target densities in different regions. Through use of the adaptive grid, sufficient node density can be guaranteed in the area of interest without needlessly inflating the total number of simulated nodes.

2.2.4.1 3D Gridding

The adaptive gridding algorithm presented also functions in 3D, but with greatly reduced efficiency due to the fact that each additional horizontal or lateral node generates a complete string of nodes that often extend out of the spacial volume needing refinement.

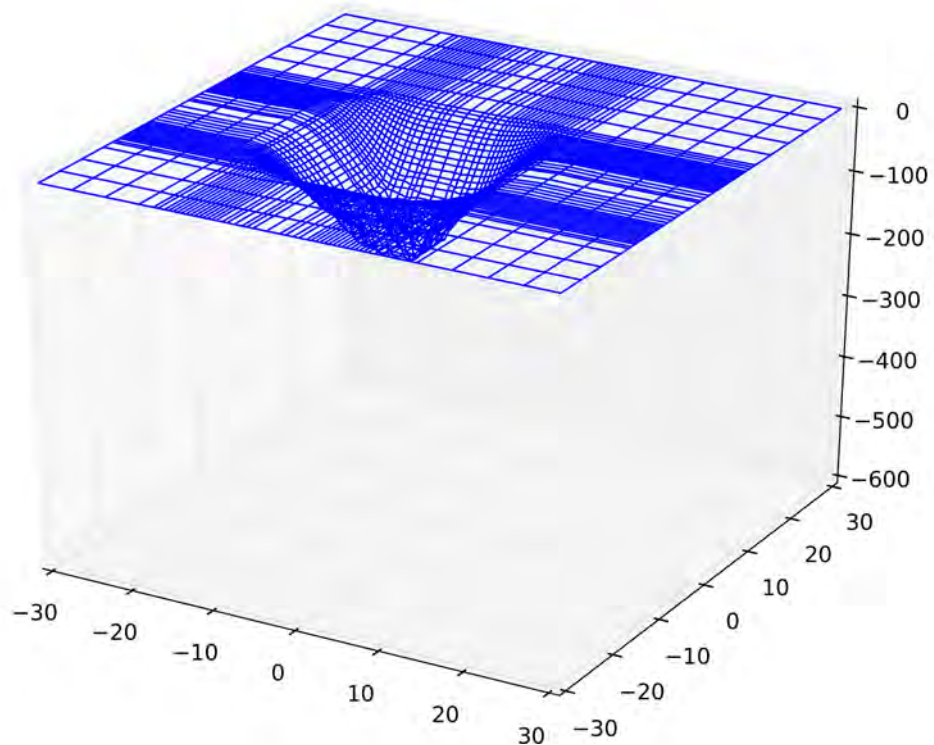


Figure 2.2.4 – A 3D simulation including simple cosine redeposition and an adaptive grid run to saturation. A 5nm beam is simulated scanning a 12x12 pixel region with a 1.25x1.25nm pixel spacing a target maximum segment length of 5nm is specified for the adaptive grid. Note how the adaptive grid is denser along the corners of the box-mill; these additional grid lines are required to provide additional resolution along the long sidewalls of the milled hole.

This limitation of the simple 3D-adaptive grid is demonstrated in figure 2.2.4. When this simple adaptive grid is used in 3D, additional lines of nodes must be inserted at the edge of deep features. A Quadtree [149] or triangulation approach, as used in other sputter simulators [134], would greatly increase the efficiency of the 3D simulations conducted in TopSim. Due to the modular nature of TopSim it is conceivable that an extension utilizing one of these methods could be implemented; however, the emphasis of this work is on 2D simulations. In simple 2D simulations the 2D adaptive grid is sufficiently efficient.

2.2.5 Materials Properties

When simulating heterogeneous targets, the materials properties of sub-volumes are described using spatially pre-defined materials volumes that have different properties. The materials properties of a node; the density and physical sputtering properties including the sputtering yield, change as the node moves through each material volume. Functionally, this is accomplished by updating the material properties of each node after each completed time-step. Sub-volumes are described in a

configuration file by defining rounded rectangular prisms that can be combined through binary arithmetic. This approach works for the simulation of non-interacting inclusions; however, it neglects any effects of ion-induced mixing, viscous flow, or ion-induced porosity and densification.

2.2.6 Visibility and Shadowing

All of the higher order fluxes (redeposition, backscattering, and redeposition from backscattering) contain a term summing over the visible source nodes. Visibility is handled in two ways in the simulation; one way is referred to as simple visibility, and the other uses rigorous shadowing. The shadowing algorithm and the visibility algorithm are both described in appendix B, where the effects of each upon simulated features are described. For symmetrical structures such as the trenches commonly used as test cases in this work the error from using simple visibility over shadowing is minor. Furthermore, the simple linear string algorithm used to track the surface evolution is known to occasionally be unstable when the shadowing algorithm is used; especially in cases where an overlapped beam is used. Therefore, in this work simple visibility is used for all presented simulations unless otherwise noted; this choice has little effect on the simulation results as is shown in appendix B.

2.3 Typical Physical Inputs

The equations of motion make use of the sputtering yield $Y_{sput}(\theta)$, the ion backscattering yield $Y_{back}(\theta)$, and the angular distributions of both sputtered ions $f_{sput}(\gamma, \theta)$ and backscattered ions $f_{back}(\alpha, \theta)$. These are implemented as spline fits in 1D or 2D of histograms obtained from the BCA simulator IMSIL. The IMSIL data shown in this chapter represents a best current practices simulation utilizing optimized simulation parameters including the simulation of surface roughness effects simulated through the use of a density gradient model for surface roughness with a low density interface layer that is 8.27 Å thick (section 4.4.2.1).

2.3.1 1D Spline Fits

The sputtering yield and backscatter yield can be adequately fit with a single spline apiece. A smoothing criterion is chosen based on the statistical uncertainty of each simulated yield as a function of incidence angle. Specifically the *SciPy* library function *splrep* [150], which itself is an implementation of smooth spline fitting routines for experimental data devised by Dierckx [151–154], is used to generate a noise tolerant smooth spline fit of the BCA sputtering data taken from IMSIL. The fitting algorithm makes use of a weighting variable uniquely describing each observation (here each sim-

ulated sputtering yield for a given incidence angle) which in this case is taken to be the reciprocal of the standard deviation of the simulated sputtering yield. This weighting function determines how precisely the spline interpolation will seek to match a given point in the dataset. The advantage of the resulting smoothing is that the primary drawback to spline interpolations, namely oscillations between observations, is avoided. A secondary visual check of the results of the spline interpolation is also performed, which can indicate that a greater degree of sampling with respect to incidence angle is required. A secondary advantage to using a smoothed spline representation is that the total number of spline nodes needed to represent a given quantity is minimized, thereby reducing the computational overhead of the interpolation function.

2.3.1.1 Sputtering Yield vs Incidence Angle

The sputtering yield curve as a function of incidence angle $Y_{sput}(\theta)$ is shown in figure 2.3.1. Raw data as well as the error bars for a typical simulation and additionally the fitted spline are plotted in figure 2.3.1. Error bars are exaggerated in figure 2.3.1 to be 100 times greater than the calculated uncertainty in order to be visible. The error bars scale roughly with the sputter yield as these simulations were optimized to produce a constant number of sputter events thus unifying later data analysis of trajectory files. The vertical axis indicates the number of sputtered target atoms per ion arriving at the proscribed incidence angle for the simulated target (silicon under 30 keV gallium bombardment shown here).

In silicon under 30 keV gallium bombardment, the sputtering yield curve is characterized by a slow increase in sputtering as the incidence angle increases away from perpendicular bombardment. As the beam angle becomes more glancing, the interaction volume of the recoil cascade penetrates less deeply into the target leading to a greater proportion of energy deposition near the surface, which in turn leads to increased sputtering. The sputtering yield reaches a maximum as the fraction of backscattered ions increases and energetic beam ions leave the target before exciting target atoms over the sputtering threshold. As the incidence angle increases approaching parallel, the sputtering yield trends towards zero as the incident ions are reflected from the target. As will be shown in chapter 4, this simulated yield curve (shown for simulations utilizing a density gradient model of surface roughness) compares favorably to experimental data.

2.3.1.2 Backscattered Ion Yield vs Incident Angle

The backscattering yield curve $Y_{back}(\theta)$ shown in figure 2.3.2 indicates the fraction of ions that leave the target after hitting the target. These simulations neglect the yield of previously implanted ions

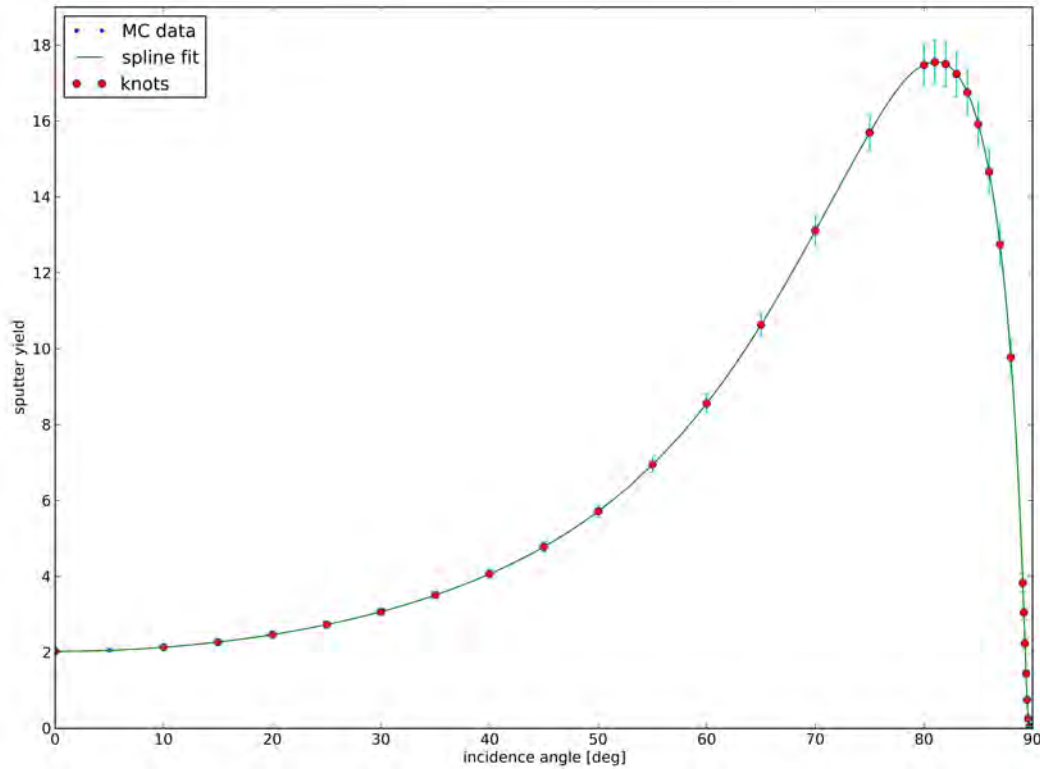


Figure 2.3.1 – A typical sputtering yield curve for 30 keV Ga on a Si target as generated by the BC Monte Carlo simulator IMSIL. Surface roughness is simulated with a linearly decreasing atomic density over a region 8.275\AA thick. Error bars are shown magnified 100x.

and it will be demonstrated in chapter 4 that it is reasonable to neglect the intermixed ions.

The backscatter yield of 30 keV gallium on silicon is characterized by an initially small or zero yield that increases with increasing incidence angle. The small or nearly zero backscattering yield at perpendicular incidence angle is due to the high implantation fraction, which is in turn dictated by the target-to-ion-mass-ratio and the bombardment energy. As the incidence angle increases and becomes more glancing, more ions have the opportunity to leave the target as backscatter events. The backscatter yield approaches unity as the incidence angle approaches 90° , the simulated surface roughness used in this dataset retards the total reflection state indicated by a backscatter yield of unity. In chapter 4 it will be demonstrated that a degree of simulated surface roughness is helpful in reproducing experimental yields at extreme glancing angles.

2.3.2 2D Spline Fits

The angular distributions are normalized so that for a given incidence angle, the total probability for sputtering across all exit angles is unity. This normalization agrees with equation (2.1.2) as the sputter yield $Y_{sput}(\theta)$ shown in equation (2.1.1) is explicitly decoupled from the sputtering angular distribution $f_{sput}(\gamma, \theta)$, or analogously the backscattering yield $Y_{back}(\theta)$ and the backscatter angular

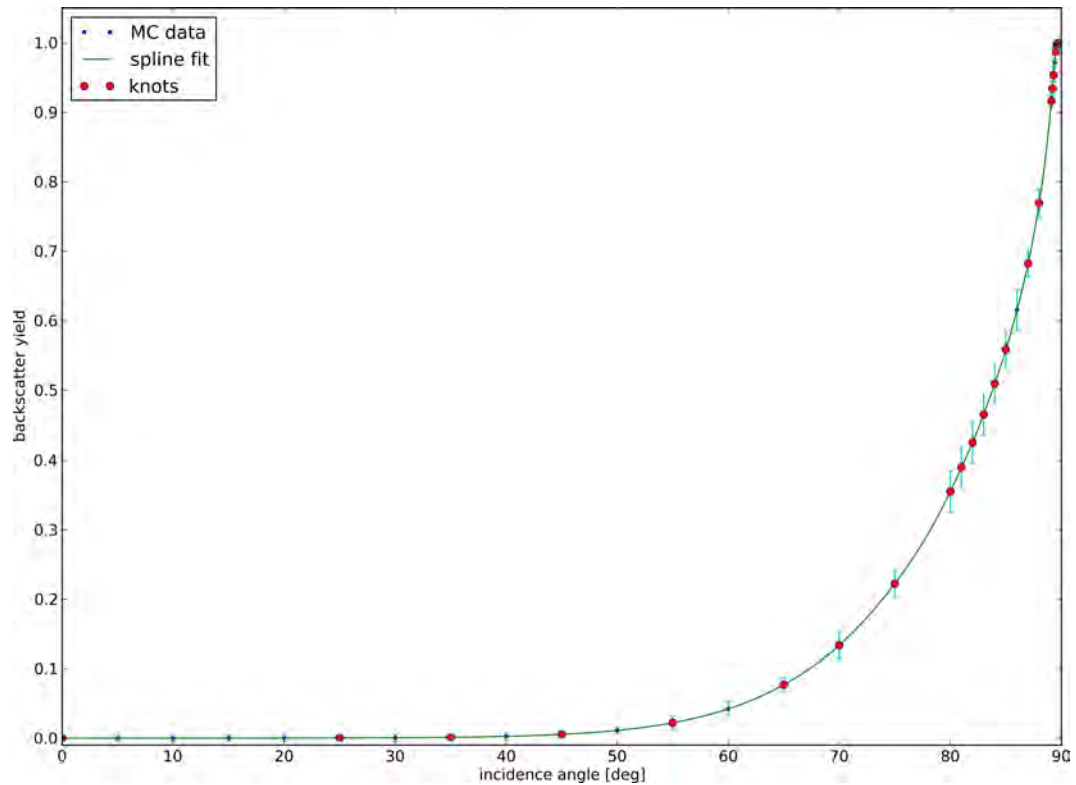


Figure 2.3.2 – A typical backscattering yield curve for 30 keV Ga on a Si target as generated by the BC Monte Carlo simulator IMSIL. Surface roughness is simulated with a linearly decreasing atomic density over a region 8.275Å thick. Error bars are shown magnified 100x.

distribution $f_{back}(\alpha, \theta)$. These 2D functions are dependent both on the incidence angle θ and the exit angle α and therefore require interpolability on both variables necessitating the use of a 2D function. 2D splines or slightly modified splines are used in this work to meet these requirements; however, full 3D simulations might require a more nuanced method.

As the characteristic shapes between the two demonstrated types of 2D distributions are very different, a different fitting procedure is used for each distribution type with one procedure being used for the angular distribution of sputtered target atoms and a slightly different procedure being employed for the angular distribution of the backscattered ions. Furthermore, the precise standard deviations for the bins of the simulated angular distributions for both sputtered and backscattered atoms are not automatically obtained by the BCA simulator IMSIL; therefore, the weighting factor for the smooth splines used in the fits must be estimated.

Efficient fitting of the angular distribution of the sputtered target atoms presents a challenge due to the characteristic shape of the angular distribution. The first knock on peak (described in the next section) presents itself as a sharp ridge along a smoothly curved hull that generally resembles a cosine distribution. However, this ridge itself is extremely linear with respect to the incidence angle, therefore allowing the approach used to fit the data, which is to extract the linear portion through

detection of the peak, followed by fitting the peak and ridge separately and recombining them upon evaluation. The remaining smoothly curved portion is fitted using the 2D version of *splrep* known as *SmoothBivariateSpline* [155], both functions are part of the numerical python package *SciPy*. As with the 1D spline fit described in section 2.3.1, smoothing is used to improve noise resistance with sample weighting being determined using an estimate of the standard deviation*. However, as there are a greater number of partitions per simulated ion (as compared with the 1D case), the results are often still noisy; therefore an enhancement factor† is often used in addition to the estimated standard deviation where fit quality is confirmed by visual inspection of the plotted data.

Angular distribution data of backscattered ions presents a slightly different fitting challenge because of both the high dynamic range of the angular distributions on the α (ejection angle) axis as well as noise due to the relatively low yield when compared to the angular distribution of sputter atoms. The high dynamic range is addressed by fitting the natural log of the normalized distributions, thereby smoothing the distribution to be fit. Upon evaluation, the interpolated values are re-exponentiated in order to obtain unscaled results. Noise issues are dealt with through the use of a decreased weighting factor (which leads to smoother fits) arising from an alternate estimate of the standard deviation for the data‡ coupled with semi-automatic grid refinement. The increased smoothing factor leads to a looser spline fit which is then procedurally refined through that addition of spline knots in the regions of greatest error until the fit is judged to be sufficient by the operator performing the fit. This semi-automatic fit is sub-optimal as it relies on operator judgment; however, when good statistics are obtained through the simulation of millions of impacts, the initial fits can be used without additional refinement. In order to enable the low level refinement of the 2D spline nodes, the low level *SciPy* command *bisplrep* [156] is used instead of *SmoothBivariateSpline* when fitting the backscatter angular distribution. Functionally, the algorithms employed in both library functions are the same, *SmoothBivariateSpline* is simply a convenience wrapper for *bisplrep*.

2.3.2.1 Probability of a Sputtered Atom Emerging with an Exit Angle Due to Excitation by an Ion with an Incidence Angle.

The normalized exit angle probability distributions $f_{sput}(\gamma, \theta)$ are shown for a small number of incidence angles as a polar plot in figure 2.3.3. A strict cosine distribution is plotted for comparison;

*The standard deviation for the angular distribution of sputtered atoms is estimated to be $\frac{\sqrt{k}}{n_{ions} \cdot bin_{width}}$ where $k = n_{ions} \cdot bin_{width} \cdot bin_{height}$, where each set of simulated ions and bins is defined per simulated incidence angle.

†The enhancement factor is used as a multiplier to the standard deviation, by increasing the apparent standard deviations of the bins a greater smoothing factor is applied, thereby resulting in less apparent noise in the 2D spline fit.

‡The standard deviation used to fit backscatter angular distributions is approximated by $\frac{1}{\sqrt{k}}$, where $k = n_{ions} \cdot bin_{width} \cdot bin_{height}$.

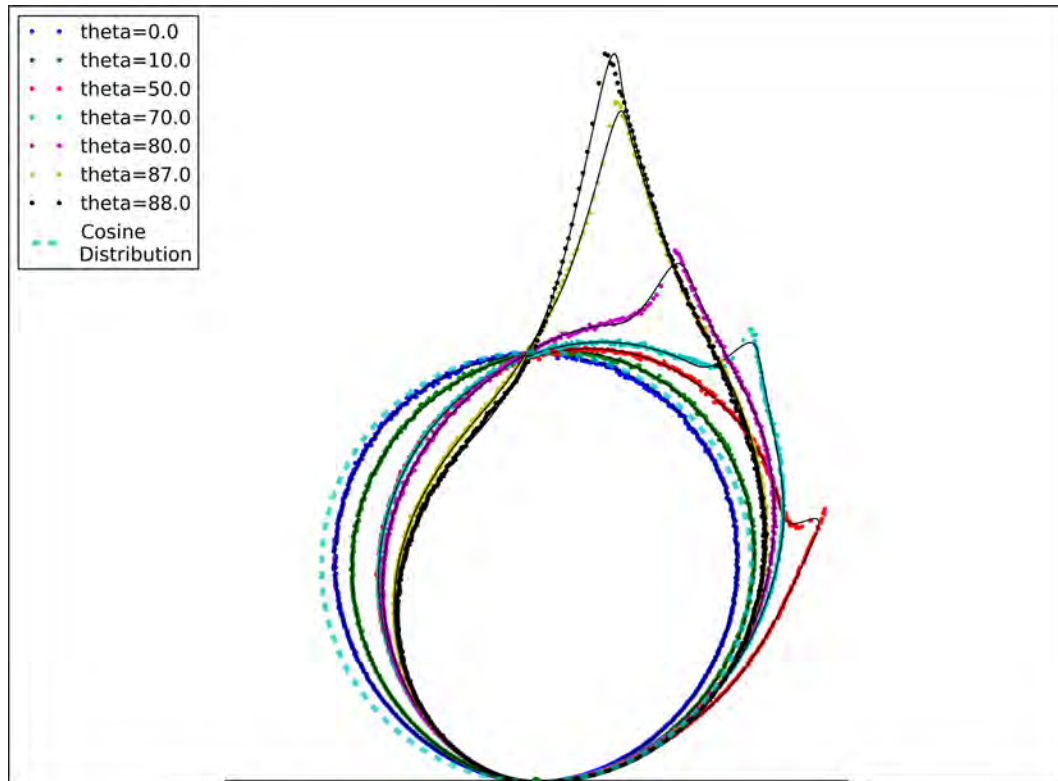


Figure 2.3.3 – Normalized angular sputter distributions both as the fitted spline (solid lines) and raw data in a polar plot. A cosine distribution is shown with a dashed line as comparison to the simulated sputtering angular distributions, even perpendicular bombardment does not result in a perfect cosine distribution. It is assumed that the beam enters the target from the left to the point located at the bottom center of the figure. The ridge visible in many of the distributions (attributed to low order knock-on sputter events) necessitates use of a modified spline.

notably the cosine distribution is an imperfect fit, even for theta equal to 0° with the cosine distribution overestimating the angular distribution at glancing or near glancing exit angles. Also notable is the systematic rightward shift as the incidence angle increases (corresponding to a counter clockwise rotation to the left from perpendicular), this shift is due to the increased lateral energy transference as the beam leaves perpendicular. At higher incidence angles ($>50^\circ$ in figure 2.3.3) an additional peak is apparent in the angular distribution. This peak is widely attributed [157] to low order knock-on events and the work presented in chapter 5 supports this hypothesis. This peak occurs around the region perpendicular to the incident beam direction and increases in relative magnitude as the incidence angle increases, continuing to increase even after the sputter yield peak. A special linear region is added to the 2D spline used to fit this data to better represent this peak.

The entire interpolated sputtering angular distribution is shown in figure 2.3.4 where both the shift to higher positive ejection angles with increasing incidence angle and the low order knock-on ridge are plainly visible.

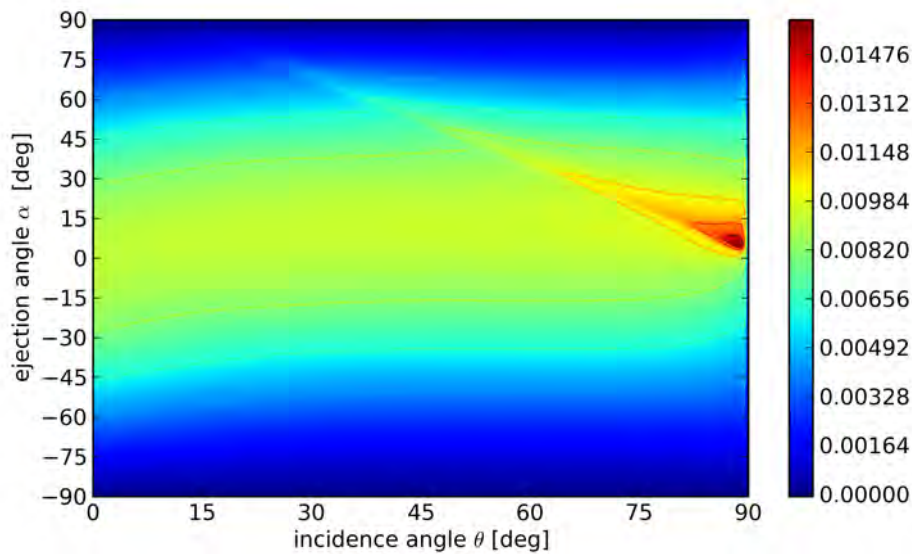


Figure 2.3.4 – A contour plot of the modified 2D spline interpolation of the sputtering angular distribution for 30 keV gallium on silicon is shown.

2.3.2.2 Backscatter angular distribution

This distribution is pointier and less diffused; there are very few counts for near normal incidence angles due to the extremely small backscatter sputter yield at low incidence angles. It is therefore necessary to fit a spline to the $\log(f_{back}(\theta, \alpha))$; some noise in the fit still remains at low incidence angles; however, the probability distribution is later multiplied by the backscattering yield $Y_{back}(\theta)$ which is zero for these low values.

A polar plot of the exit angular distribution for a number of exit angles is shown in figure 2.3.5. Notice that significant noise still exists in the lower incidence angles of 30° and 40° . This noise is due to the high statistical unlikelihood of backscattering a 30 keV gallium ion from a silicon target at that angle, the accompanying backscatter yield (figure 2.3.2) is still nearly zero for these angles. The extremely sharp and pronounced rightward shift in the angular distribution indicates that events where the ion is reflected along its incoming path are extremely rare even at less extreme incidence angles. The entire interpolated backscatter angular distribution is shown in figure 2.3.6; note that the sharply peaked distribution necessitates the use of a logarithmic color scale in the contour plot. This sharp peak corresponds to the region of the backscatter yield at or near unity.

2.4 Typical Simulation Results

Simulations showing a reference trench with and without backscattering/second-order redeposition and redeposition models are shown in figure 2.4.1. The results shown in figure 2.4.1 demonstrate

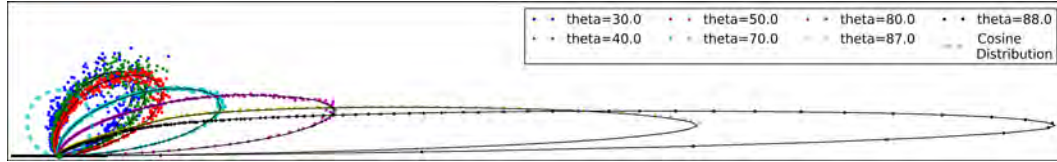


Figure 2.3.5 – A polar plot of backscattered angular distributions for a number of incidence angles. The cosine distribution is shown as a blue dashed line, the raw data is shown as points and the spline fit is shown as solid black lines. Note how the rightward shift is highly pronounced in the backscatter angular distribution.

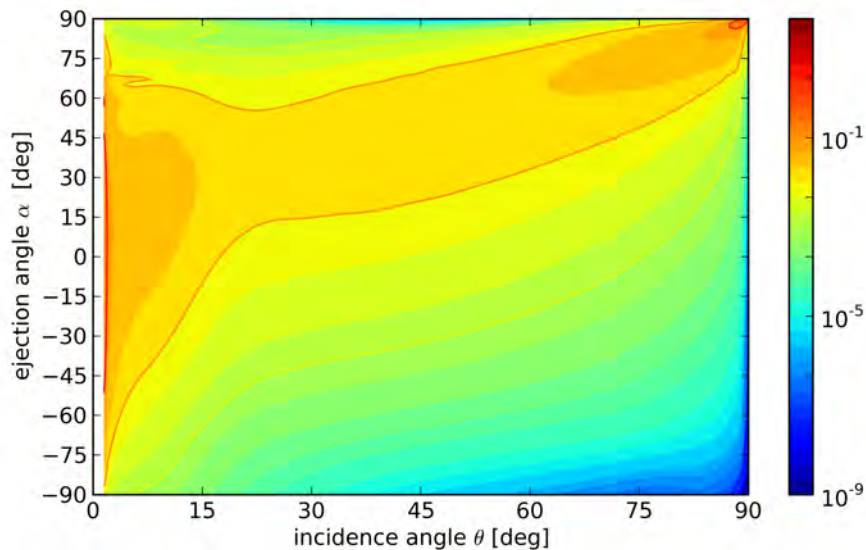


Figure 2.3.6 – A contour plot of the 2D spline interpolation of the backscatter angular distribution for 30 keV gallium on silicon is shown; note the color scale is logarithmic. The distribution comes to a sharp peak near an incidence angle and ejection angle of 90° as expected in the case of reflection or near reflection.

the time evolution of a simulated trench milled with a current density of $5 \text{ mA} \cdot \text{cm}^{-2}$ across a scan area of $2\mu\text{m}$ with a 15nm beam. For simulation efficiency the beam profile is simulated using an error function beam that emulates the scanning of a 15nm beam across the $2\mu\text{m}$ scan area if the scan were to be completed in an infinite number of passes. This approximation is known as an overlapped beam where it is assumed that the spatial dose profile is independent of time and remains constant. Further discussion of the validity of this approximation is discussed in section §3.4, on page 66.

The left side of figure 2.4.1 shows the evolution of the trench under continued exposure, the effect of redeposition can be seen in the tapering of the trench that occurs with increasing dose. Target atoms are redistributed according to their sputtering angular distributions (section 2.3.2.1) and those that encounter trench sidewalls stick counteracting the milling from the beam. As the aspect ratio of the trench increases the fraction of sputtered atoms that fail to escape into vacuum and thus are redeposited increases; eventually the aspect ratio becomes significantly high that the fraction of un-redeposited atoms becomes negligible and the trench ceases to increase in depth. This condition, where milling ceases to continue, is known as saturation. The saturation point is not shown for these simulations, although the continued narrowing of the trench walls in the later time slices previews the arrival of saturation. However, as these simulations neglect the volume of implanted ions, it is thereby impossible to simulate the steady-state condition where no further sputtering occurs in these simulations; although, a similar reduction in milling efficiency occurs even in these presented simulations. The second notable feature on the left side of figure 2.4.1 is the visible microtrenches exemplified by the 12 second time slice; these microtrenches are caused by sputtering from backscattered primary ions. Due to the highly directed shape of the backscatter angular distributions (section 2.3.2.2) the additional sputtering caused by these backscattered ions is mostly focused on the trench corners. Broad angle backscatter emission is found at less glancing incidence angles; however, this effect is countered by the accompaniment decrease in the backscatter yield found near normal incidence (figure 2.3.2). Therefore, the notable effect of including sputtering due to backscattered ions is the formation of microtrenches caused by the pseudo reflection of primary ions off the sidewalls exhibiting a glancing incidence-angle with respect to the ion beam.

The right side of figure 2.4.1 demonstrates the full sputtering model as compared to simplified models considering only primary sputtering (dash-dotted lines) and only primary sputtering combined with redeposition of sputtered atoms (dashed lines). When completely neglecting higher order effects and considering only primary sputtering, an increase in relative sputtering efficiency is observed, this increased efficiency continues to grow with increasing aspect ratio as redeposition plays an increasing role when the aspect ratio increases. The relative milling efficiency between the model including backscattering/second-order redeposition effects (solid line) and a model considering only

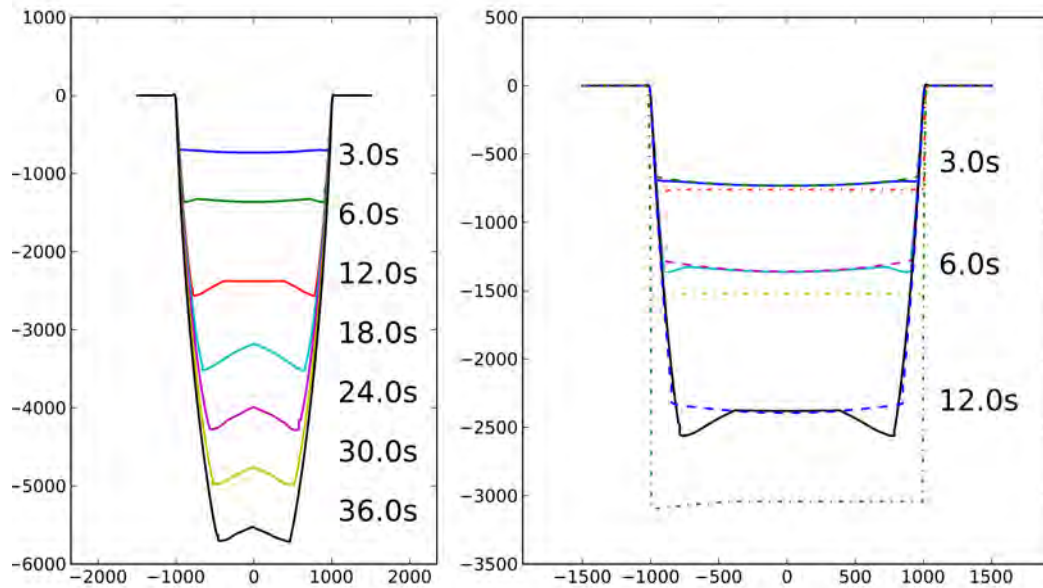


Figure 2.4.1 – Typical results for a simulated 2 μm wide trench milled by a 15 nm beam with a current density of $5 \text{ mA} \cdot \text{cm}^{-2}$ using gallium ions on a silicon substrate. The left figure shows an abbreviated time evolution of a simulation model including primary sputtering, redeposition, backscattering, and second-order redeposition. Notice that in the complete model microtrenches form, but as milling continues the trench trends towards saturation. The right figure shows the differences between different model sophistications, the complete model is shown as solid lines, a model considering only redeposition is shown with a dashed line, and a simulation modeling only primary sputtering is shown as a dot-dashed line. These simulation models are shown across three time intervals. Length and height scales are expressed in nanometers.

redeposition is demonstrably small neglecting the microtrenches discussed previously. However, the addition of second-order redeposition (redeposition resulting from sputtering incited by backscattered ions) leads to a visible narrowing of the trench width near the bottom of the simulated structure, as is visible in the 12 second time slice. All of the fluxes considered in the model presented in this chapter therefore show the expected effects with regards to topography simulation. However, as more complex structures are simulated, the effects of the various model components become more difficult to explain and predict, thus demonstrating the value of a functional simulation model.

2.5 Scaling Results

All four flux equations (equation (2.1.1), equation (2.1.2), equation (2.1.4), equation (2.1.5)) are independent with respect to length scaling, the fraction $\frac{l(S_1)}{d(S_1, D_1)}$ (as seen in the projection term of all the higher order fluxes) pertains only to the discretization of the grid; in fact the only places where lengths enter the simulation are in the beam diameter ($FWHM$) and the scan length (in 2D) ΔW [§]. It is therefore possible to characterize simulation results for a simple trench by expressing them in terms

[§]These simulations maintain a constant beam fluence; therefore, the current is scaled with ΔW .

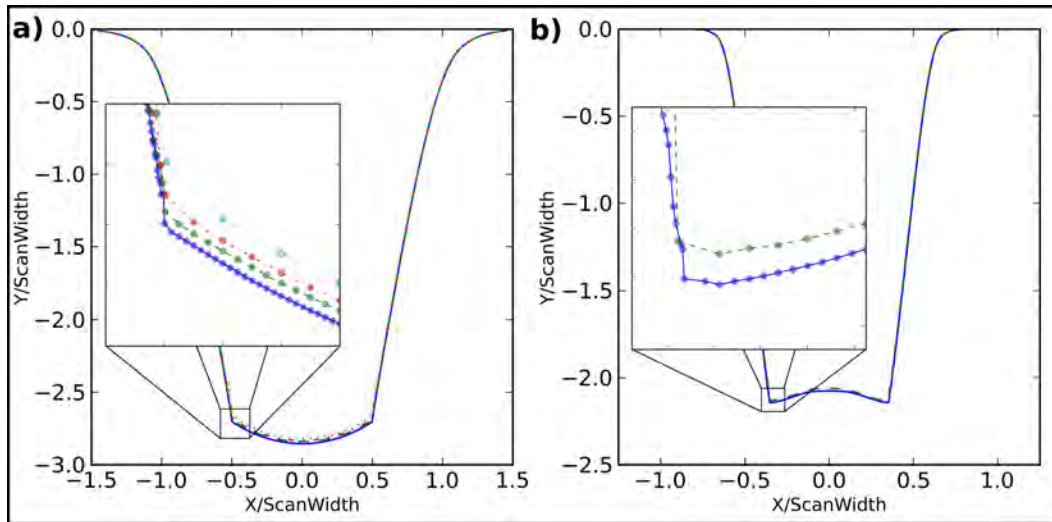


Figure 2.5.1 – A demonstration of the geometric scalability of trench simulations using this local model. The left side shows four simulations with a scan width to FWHM ratio ($\Delta W/FWHM$) of 0.8 ($\Delta W = 25, 50, 100, \text{ and } 200 \text{ nm}$; $FWHM = 20, 40, 80, 160 \text{ nm}$), while the right side shows simulations with a scan width to FWHM ratio of 0.2 ($\Delta W = 100 \text{ and } 200 \text{ nm}$; $FWHM = 20 \text{ and } 40 \text{ nm}$). All simulations are carried out on a fixed grid spacing and deviations are the result of discretization errors.

of $\Delta W/FWHM$ when that trench is assumed to be in the overlapped beam regime. This implies that the movement of the beam is not so slow as to exhibit the snow-plow effect[¶], and specifically that it approaches the limit of removing infinitesimal portions of the target with each pass. This scaling property of simulation results is demonstrated in figure 2.5.1, where good agreement is shown between simulations. The deviations between simulation results are caused by discretization errors that result from the use of a fixed grid in all six of the presented simulations. These discretization errors arise from the segment length that is used in the flux equations; however, the good agreement over four orders of magnitude indicates that the grid is sufficiently fine.

This scalability of the model allowed for the study and characterization of the conditions required to form microtrenches as shown in figure 2.5.2, where it is demonstrated that for certain scan beam ratios and scaled total doses, microtrenches can be formed [136]. The formed microtrenches continue to grow with increasing dose until the two wave-fronts meet and the microtrenches are saturated; further dose reduces the height of the microtrenches until finally the typical V-shape of a saturated trench emerges. This kind of analysis can be performed due to the geometric and strictly local nature of the presented model; furthermore, for beam $FWHM$ s greatly in excess to the ion range in the target, this model should hold up experimentally as well.

[¶]When a slow moving beam is scanned across a target, the trench wall nearest to the direction of travel can develop a sharp edge while the surrounding target material is softened by the effects of redeposition. This resembles the effect of pushing a plow through snow where the snow directly in front of the plow is tightly controlled but excess snow is spread around, behind, and to the sides of the plow. In FIB milling this effect leads to pattern asymmetry at lower scan speeds, even if the spatial dose is kept constant.

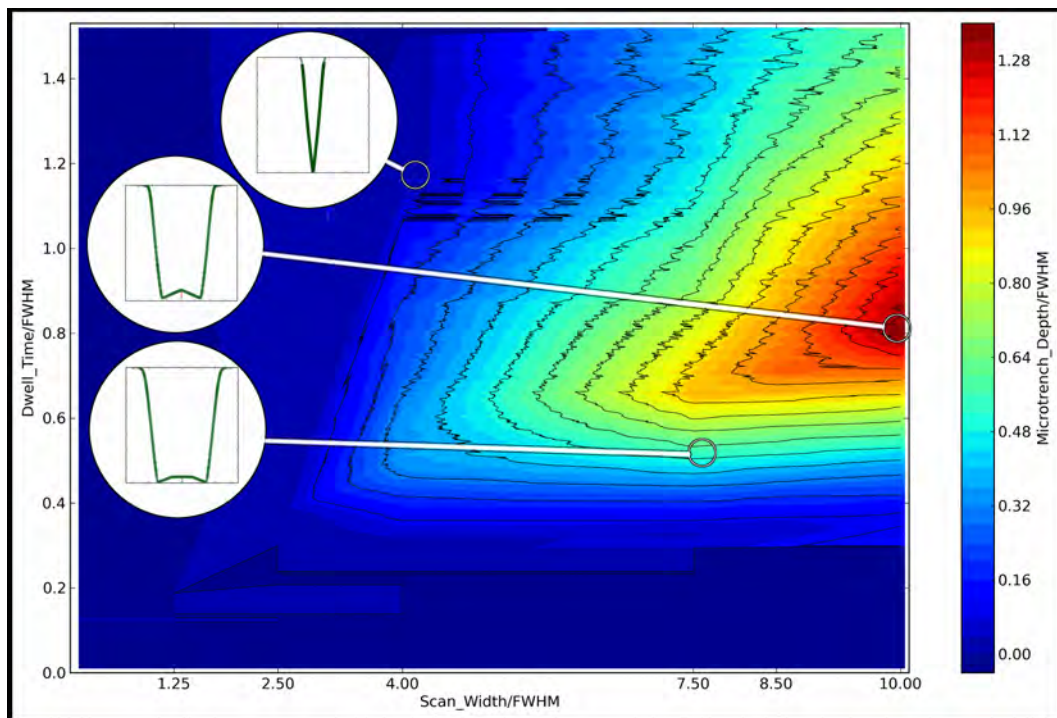


Figure 2.5.2 – A map of the scan width ΔW and beam width ($FWHM$) ratios as compared to scaled doses that lead to the formation of microtrenches. Three specific microtrench formations are expressed; simple microtrenches, saturated microtrenches, and saturated trenches where microtrenches no longer exist.

Chapter 3

Inverse Modeling

Inverse modeling refers to the practice of finding a set of input parameters that yields a desired solution in a complex system. In the case of FIB inverse modeling the input parameters are a set of beam positions and dwell times that can be used to produce an arbitrary user-defined topography. In this chapter an inverse modeling method utilizing the forward simulator TopSim will be described and compared to experimental work showing the effectiveness of the method [158]. The chapter will end with an experimental result that does not match the expected simulation; this anomalous experimental result provides an impetus for the extended model presented in chapter 5. Inverse modeling is therefore not only useful as a practical tool for developing arbitrary topographies in an applications standpoint, but also as a mechanism to test the veracity of the forward simulation model itself outside the bounds of simple test geometries.

3.1 Motivation

As was conveyed in chapter 1, FIB technology is interesting for a variety of reasons not the least of which being its usefulness as a means to directly modify surface topographies through sputtering or gas assisted techniques. However, this usefulness is limited by the fact that a large subset of desirable topographies for applications are non-trivial to produce with a FIB due to complications presented by a number of inseparable factors associated with FIB milling or deposition. As this text focuses on sputtering, gas assisted techniques will be neglected; however, the factors that influence and complicate sputtering include beam shape, dependence of sputtering yield on incidence angle, effects from redeposition, and sputtering by reflected ions*.

*As will be shown in section §3.6, even higher order fluxes than those presented in chapter 2 may play a role in a certain subclass of target topographies; chapter 5 is a preliminary exploration of a possible shortcoming of the model presented in chapter 2.

Specifically the beam shape, due to its non-uniform spatial distribution, acts to prevent perfectly sharp interfaces between milled and un-milled areas. In the simplest approximation the beam shape necessitates the modification of the spatial dose at the edges of milled areas. This modification is usually accomplished through a scaling of the pixel dwell time. As the topography evolves from an assumed flat 2D surface (though modification of nonplanar initial topographies is also possible) a second complication of incidence-angle dependent sputter yield arises. In chapter 2, figure 2.3.1, it was demonstrated that for 30 keV gallium on silicon the sputtering yield increases by nearly a factor of 8x between normal incidence bombardment and the sputter yield maximum at an incidence angle of approximately 80°; the spatial dose must therefore also compensate for the local incidence angle as milling occurs. Finally, when fine beams are used with large scanning areas and high aspect ratios (shown in figure 2.5.2), micro-trenching occurs, presenting a further complication that must also be compensated for in the inverse modeling solution.

The factors make it clear that an effective inverse modeling approach depends on the sophistication and precision of the forward modeling simulation. The method by which inverse modeling is accomplished depends strongly on the solutions required and the desired application space. Various inverse modelers for FIB milling have been demonstrated with varied dose generation strategies and various degrees of sophistication in the forward modeling portions. Good results in restricted solution spaces have been demonstrated even with rather primitive models; however, increased sophistication on the part of the forward modeler should lead to an evermore general and universal inverse modeling approach.

3.2 State of the Art

There have been numerous presented solutions to the inverse modeling problem for FIB milling [159–163] and gas assisted etching [164], though the approaches can be clearly divided into quasi-stationary and non-stationary approaches. As mentioned in 3.1, pixel dose is normally modified by means of changing the pixel dwell time as modifying the beam current without readjusting the beam column is impractical; therefore, all dose profiles have an implicit time dependence. The distinction between quasi-stationary and non-stationary approaches arises in the manner in which they deal with multiple passes, with quasi-stationary approaches being characterized by the explicit reapplication of a singular spatial dose profile (normally defined as a set of pixels defining spatial positions with unique dwell times) across multiple passes; an approach that changes the spatial dose profile over subsequent passes is non-stationary. In the trivial case of milling completed in a single pass, the solution is explicitly time-dependent and thus an example of a non-stationary approach.

Single pass solutions are not usually preferred due to the snow-plow effect, whereby a moving beam removing a large volume of target will redeposit the target atoms along the previously milled path. Most inverse modeling approaches therefore attempt to limit the amount of material removed per pass as the snow-plow effect severely limits the solution space of available topographies. In multi-pass non-stationary inverse modelers, the basic approach is to create 3D topographies by dividing the target erosion volume into a number of discrete stacked sub-volumes which are milled away sequentially. The simplest non-stationary FIB inverse modelers simply defined a target layer thickness to remove, and sequentially milled the target while neglecting the effects of beam spread and the angular dependence of the sputtering yield [159,160]. Later inverse modelers incorporated beam spread and simplified models for the angular dependency of the sputtering yield [161,162,164]. More recently, even redeposition has been incorporated into a non-stationary inverse modeler described by Kim [163], this advanced non-stationary inverse modeler targets intermediate dose profiles. A functional forward modeler implementing redeposition is used to optimize intermediate solutions in order to increase the stability and decrease the complexity of the inverse modeling procedure. Despite the relative unsophistication of the forward modelers employed in these inverse modelers, the inverse modeling solutions have been experimentally demonstrated to be effective in their distinct application spaces. Non-stationary models seemingly do not require extremely complex simulations of the topography evolution because they employ scanning strategies that keep the eroded sub-volumes in or near the linear regime.

The other approach is a quasi-stationary approach which maintains a constant dose profile during feature milling. This class of inverse modeler requires that the evolution of the surface be carefully tracked in the non-linear regime, begging the question as to why a non-stationary solution is not simply used. The non-stationary approach breaks down, or at minimum requires more stringent forward modeling, when the aspect ratio of the feature becomes large enough that redeposition begins to play a significant role. A quasi-stationary approach has been demonstrated with the goal of producing solutions that can be used to manufacture imprint molds for microlenses [164]. The work presented herein also takes the quasi-stationary approach to find static dose profiles that can be used to produce user-defined topographies making use of the forward simulator TopSim. Contrary to the quasi-stationary approach demonstrated in the literature [164], the present inverse modeler is not limited to simple first-order sputtering but also includes the effects of redeposition, second-order sputtering due to backscattered ions, and the second-order redeposition of those sputtered ions using the forward model presented in chapter 2.

3.3 Presented Algorithm

The basic approach to inverse modeling taken in this work is to generate a candidate dose profile by some means and use this dose profile (described by pixel centers and dwell times) as an input for a forward simulation. The result of the simulation is next evaluated with respect to the user defined topography (a 2D depth profile), the deviation from the target profile is then used as an optimization parameter which results in a perturbation of the candidate dose profile leading to another forward simulation and error evaluation. This optimization loop is repeated until either a minimum error criteria is reached or the perturbation algorithm detects a state of maximum convergence. Finally, simulation parameters such as the grid spacing and thereby resolution can optionally automatically be refined by starting another optimization loop after the convergence state.

In this work the convergence portion is handled by the *Scipy* [165] function “*leastsq*” (which is itself a wrapper for the MINPACK [166, 167] Fortran function “*lmdif*”) which implements a modified Levenberg-Marquardt [168] algorithm to minimize the error between the simulated surface derived from the forward modeling of the candidate dose profile and the target surface specified by the user. The “*leastsq*” function optimizes an N dimensional input vector[†] with a corresponding function that produces an M dimensional error vector where $M \geq N$. In the case of the inverse modeler; the corresponding function is a combination of a mapping function that maps the input vector to a dose profile (two mapping functions are described in this text; however, the inverse modeling optimizer does not discriminate between the two), a TopSim forward simulation using the derived dose profile, and an error evaluation function comparing the simulated surface and the target surface.

Two mapping functions are presented in this work; the first directly maps each element of the input vector to the dwell times of fixed pixels known as the direct pixel dwell time method, the other mapping abstracts the dwell times by defining the input vector as the spatial vertices of a polygon envelope for the dose profile; this second mapping has been named the cage function method. While the direct pixel method is significantly more intuitive, it presents a serious disadvantage when a non-trivial number of pixels are used to create the dose profile as the “*lmdif*” function must estimate the Jacobian between convergence steps. This estimation of the Jacobian is accomplished through small perturbations of the input vector, at minimum one perturbation per free parameter. Furthermore, the Jacobian estimation occurs frequently because in practice it can take tens to hundreds of convergence steps for the algorithm to completely converge. A performance comparison will be made in section 3.3.2.3, demonstrating the advantage of the cage function approach.

[†] Vector here refers to the computational construct, whereby a vector describes an ordered set of computational objects.

3.3.1 Mappings to Dose Profiles and Optimization of Parameters

In the following sections the details of the two methods by which input vectors are mapped to spatial dose profiles will be explained in further detail. As the error evaluation portion of the algorithm is the same for both methods, it will be explained for the direct pixel dwell time method, and referenced in the later description of the piece-wise linear polynomial cage function method. Dose profiles are defined as the 2D spatially resolved dose for a fixed current assuming Gaussian beam profiles with a predetermined *FWHM* and pixel spacing. As the shape and the current of the pixels are not optimized (which corresponds to real world milling practices) or varied over the course of a milling simulation, the dose profile for the simulation is strictly characterized by dwell time for each pixel.

3.3.1.1 Direct Pixel Dwell Times

In the case of the direct fitting of the pixel dwell times a simple optimization loop shown in figure 3.3.1 is used. The input parameters optimized by “*lmdif*” are described as the parameters p_j and the function is optimized by minimizing the square of the sum of the errors e_i (of length M) defined as $\sum_{i=1}^M e_i(p_1, p_2, \dots, p_N)^2$ where $N \leq M$ must be fulfilled. The free parameters to be optimized p_j are taken in the case of the direct pixel dwell time method to be the dwell times of a set of pixels with a set spacing in simulation space. Therefore, the first step shown in figure 3.3.1 “*Adjust Pixel Dwell Times*” refers to the generation of a pixel input file where each of the j pixels in the input file takes on the p_j th value from the input parameters that are optimized by “*lmdif*”. The user must of course specify a reasonable starting guess for the input parameters p_j ; however, it is usually sufficient to supply a constant dwell time that will produce a trench with the approximate target depth. A TopSim simulation is then completed using the generated pixel input file which results in a simulated surface (in the 2D case a contour) that can then be evaluated in the evaluation of errors step shown as the third step in figure 3.3.1 “*Evaluate Errors*”.

The user-defined target contour is sampled at n points with a fixed spacing in the X axis along the entire defined range of the target contour. The target contour is sampled even if the target can be sufficiently described by a lesser number of points, as the piecewise linear target contour often can, the sampling acts to guarantee the restriction of “*lmdif*” that the number of evaluation point N must always equal or exceed the number of free variables n . The error itself is calculated as the minimum Euclidean distance between the sample point on the target contour and the simulated contour. As the simulation contours are themselves piecewise linear, this Euclidean distance is practically defined as the minimum perpendicular distance from a line segment of the simulated profile to the sample point or the distance to one of the endpoints of the line segment if the point-to-point distance is smaller.

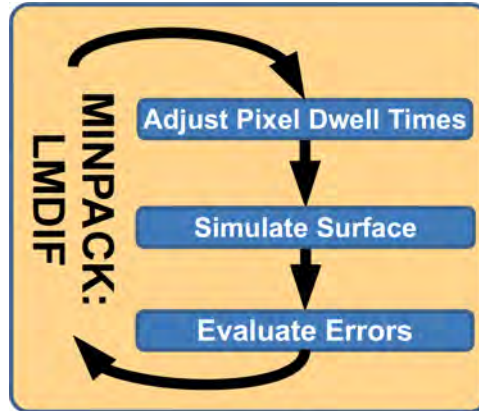


Figure 3.3.1 – A flow chart showing the inverse modeling algorithm as applied when pixel dwell times are directly optimized.

An example of the evaluated error for a simulated surface is shown in figure 3.3.2. Note how the error lines are perpendicular to the surface except at the kinks; this behavior at kinks is due to the secondary choice (minimum endpoint distance) for finding the nearest point.

Along the left side of the flowchart (figure 3.3.1) is the “*lmdif*” step where the evaluated error is utilized and a new set of input parameters (which are directly mapped to dwell times in the “*Adjust Pixel Dwell Times*”^{*} step) are generated. As previously mentioned, the “*lmdif*” function seeks to minimize the square of the calculated Euclidean error through the optimization of the input parameters. This minimum is by no means guaranteed to be a global minimum and is dependent both upon the static simulation parameters (unoptimized parameters such as grid spacing, time step, model complexity, and quality of the initial guess for the optimization parameters), as well as convergence parameters specified for the “*lmdif*” function. The primary tuning knob for “*lmdif*” is the step size for the finite estimation of the Jacobian. As the simulation itself cannot be trivially expressed in a manner that presents to Jacobian analytically, it is necessary to use an optimizer such as “*lmdif*” which can derive its own finite estimate of the Jacobian in the search for minima.

“*lmdif*” allows the user to specify a step-size for the forward difference approximation of the Jacobian for the entire minimization process. This step-size is specified in the *SciPy* wrapper *leastsq* with the keyword *epsfcn* [169]. The selection of this step-size plays a major role in determining if the “*lmdif*” function will successfully converge and must be specified as a value between two undesirable endpoints. Choice of an insufficiently large step-size will result in a total failure to converge due to the step-size being less than the available precision of the simulation. In this pathological case the optimization function attempts to estimate the Jacobian and fails due to noise introduced by the

^{*} “*Adjust Pixel Dwell Times*” refers to the portion of the algorithm responsible for mapping the input vector p_j into a spatial dose profile. In the direct pixel dwell times method this mapping is simply specifying the dwell times at fixed pixel centers for Gaussian beams. In the cage function method an intermediate abstraction is used to define a target superposition of Gaussian beams and the dwell times are solved to achieve this target.

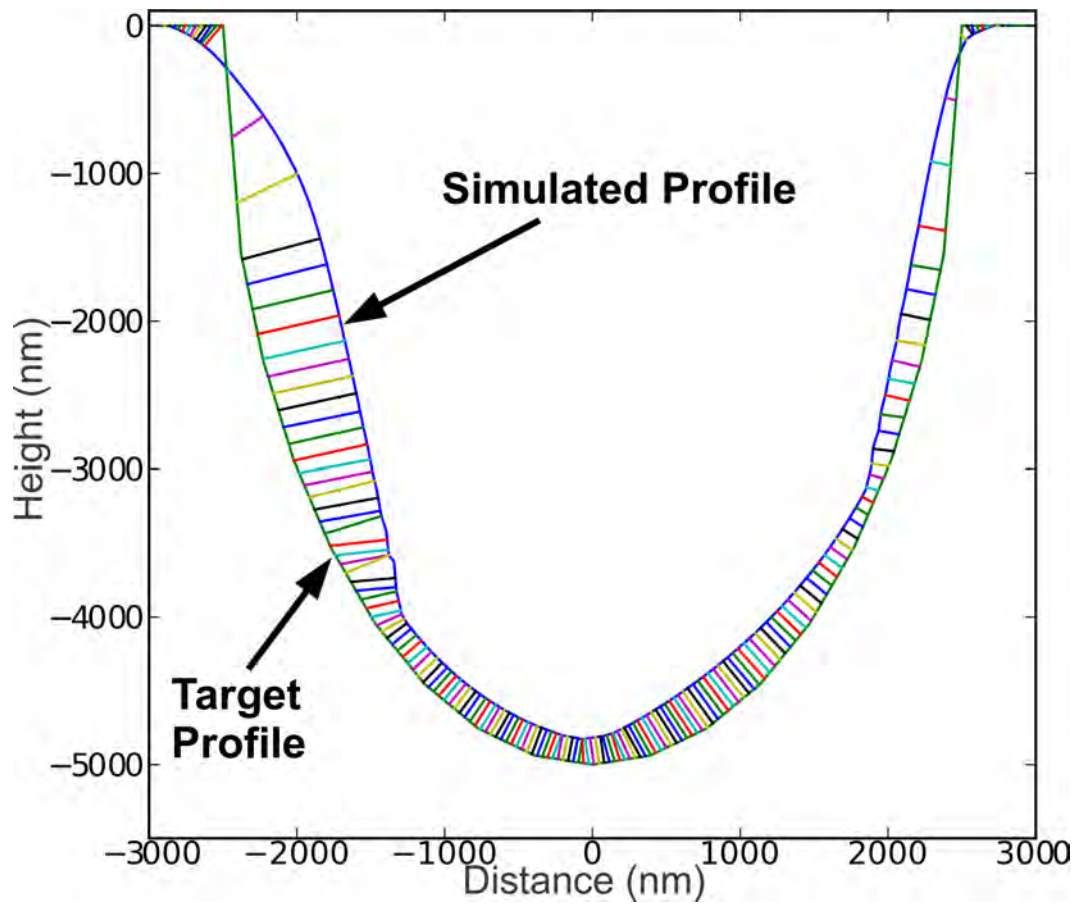


Figure 3.3.2 – An example of an error evaluation step is shown. The target contour is indicated with a long green line and the simulated contour is indicated with a long blue line. The short lines connecting the two lines are the sampled errors and show the distance between the simulated contour and sampling points on the target contour.

simulation. A second failure mode due to insufficient step-size results in the successful convergence of the minimization function, however with insufficient entropy to escape the numerous local minima in solution space. While the first underestimate failure is simple to detect (due to an error being thrown by the algorithm) the second can thus far only be detected through visual inspection of the simulation result by the user. Conversely too large a step length can generate sufficient entropy so as to prevent convergence, while the intermediate (and still nonoptimally large) value can result in successful convergences that approach useful minima while still lacking a small enough step-size to produce solutions with satisfactory precision. Though a fair amount of work has been done regarding self-tuning optimization algorithms [170, 171], these approaches are sufficiently challenging in their own right to be outside the scope of this initial implementation. The stock generic “*Imdif*” leads to satisfactory solutions if the step-size is properly defined; furthermore, the software implementation of the inverse modeler offers an additional outer loop which can be used to specify the refinement of the step-size (discussed in section 3.3.2.1) as well as the static simulation parameters. Optimization of this outer refinement loop does require user experience; however, as the best input parameters from previous optimization parameters are used as the initial guess, the later convergence requires fewer optimization steps to converge.

Estimation of the Jacobian is the most time-consuming portion of the inverse modeling process; and the estimation must be repeated between convergence steps; furthermore, the estimation step requires the completion of at least as many simulations as there are free input variables N . Luckily these simulations can be performed in parallel, as shown in section 3.3.2.2; however, this scaling represents a clear limitation to the direct pixel fitting method (demonstrated in section 3.3.2.3). Pixel dwell times as-fit normally only show strong variance at the edges when representative trench profiles are used as target contours. Though as the beam $FWHM$ compared to the scan area determines the available sharpness of the trench sidewalls (shown in figure 2.5.1), it is impractical to simply limit the number of pixels used in order to optimize a solution through inverse modeling. A method to decouple the number of pixels and therefore also the number of free input variables is presented in section 3.3.1.2 by means of an alternate mapping to pixel dwell times defined by a piecewise linear polynomial function acting to define the desired dose profile.

3.3.1.2 Cage Function to Define Pixel Dwell Times

There exist a large number of interesting target profiles that fit the restriction of being relatively simple (having a single global minimum) yet large with respect to the desired beam $FWHM$; such profiles include molds for optical micro-lenses and even simple shapes such as V-shaped trenches where sharp features preclude the use of a broad beam. Analysis of solutions obtained from inverse mod-

eling using a direct pixel fit demonstrate that there exist solutions for such simple yet large target profiles where the spacial derivative of the optimized pixel dose is smoothly and continuously defined outside of the inflection points represented by the center and edges of the pixel dose profile. This smoothness suggests that a linear approximation of the desired pixel dwell times can be used to significantly reduce the number of free variables n used to determine the inverse modeling solution. A cage function has been implemented in order to decouple the optimization of the input parameters from the pixel dwell times used as an input to the simulation.

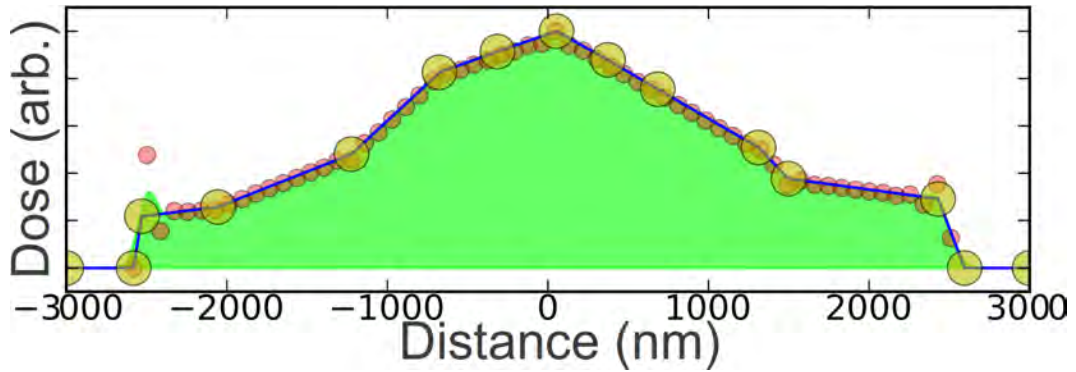


Figure 3.3.3 – An example of a piecewise linear cage function (defined by the yellow dots) showing the pixel dwell times (shown as red dots) and the resulting dose profile, modeled as a superposition of Gaussian beams (the green filled area), for a simulated $FWHM$ of 130nm.

The cage function mapping is defined as such that a piecewise linear cage function provides a mapping wherein the superposition of all the pixel doses (corresponding to the simulation dose profile) fits the value of the cage function at every pixel center $x_i, i = 1 \dots n^\dagger$. An example fitting is shown in figure 3.3.3 where the pixel dwell times (shown as red dots) are fitted such that the superposition of dose (shown as the filled green area) matches to the piecewise linear cage (shown as a solid line connecting yellow dots). The yellow dots shown at either end represent lateral limits chosen by the user, and all points except the inner points that demarc the green region are free variables in both the lateral (spatial) and vertical (dose) directions; the inner demarcation points are fixed vertically but are free laterally. The number of free parameters $N = 2k - 2$ where k is the number of free nodes, in figure 3.3.3 the number of free variables N is 24 while the number of pixel values is 60, representing in this case nearly a two-thirds reduction in the number of fitting parameters that must be optimized by “*lmdif*”.

Practically, the solution to the pixel values that correspond to a given set of input parameters defining the piecewise linear cage function are obtained through the solution of a system of linear equations as shown in equation (3.3.1) and equation (3.3.2).

[†]Little n is the number of pixels used in the simulation and is equal to or smaller than the length of the input vector with length N when using the cage function method. In the direct fit method $n = N$ as each entry in the input vector specifies a simulated Gaussian pixel.

$$\sum_{i=1}^n c(x_i, x_j) \cdot t_j = f(x_i), \quad i = 1 \dots n \quad (3.3.1)$$

where $f(x)$ denotes the cage function and

$$c(x_i, x_j) = \exp\left(\frac{-1}{2\sigma^2} \cdot (x_i - x_j)^2\right); \quad \sigma = \frac{FWHM}{\sqrt{8 \ln(2)}} \quad (3.3.2)$$

These equations describe the dose contribution of a given pixel with a beam center located at x_j to another pixel with a beam center located at x_i . The variable t_j refers to the dwell time (scaled by a simulated beam current) of the pixel at location x_j and in the case of sputtering the condition $t_j \geq 0$, as negative dwell times have no physical meaning. This nonnegative restriction on individual pixel dwell times t_j necessitates the use of a nonnegative solver (*scipy.optimize.nnls* [172, 173]) which, as the name suggests, uses a constrained least squares algorithm to solve the system of equations such that none of the t_j are negative. Solution of this system of linear equations takes trivial time as compared to the simulation of a single candidate profile.

The flowchart analogous to figure 3.3.1 for the algorithm used to conduct inverse modeling is shown in figure 3.3.4. Notably the only difference between the cage fit algorithm and the direct pixel dwell time algorithm is in the first step “*Adjust Cage Parameters*” where the perturbed input parameters coming from “*Imdif*” are mapped to pixel dwell times by means of equation (3.3.1). The pixel dwell times are then written to an input file and simulated with the error evaluation occurring in the same manner as that used in the direct pixel dwell time fitting algorithm. It should be noted, however, that in macro-structure[‡] cases the number of free variables N , and therefore the number of simulations required to estimate the Jacobian, is considerably reduced in the cage function algorithm.

3.3.2 Performance

Performance with respect to precision and execution time of the presented inverse modeling algorithms is strongly dependent upon the number of free variables and the requested simulation precision as specified by the grid spacing. Typical simulations run to a grid spacing of half the expected ex-

[‡]Macro-structure referring to an inverse modeling target requiring the use of multiple pixels to produce a structure such as a trench with given sidewall parameters and large features as compared to the beam *FWHM*. Certain pathological targets, such as a non-interacting array of holes, are not a good fit for the cage function algorithm.

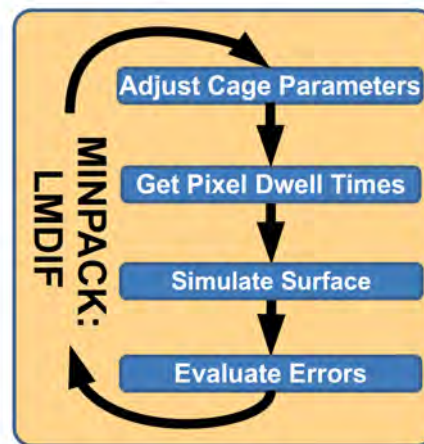


Figure 3.3.4 – A flow chart showing the inverse modeling algorithm as applied when pixel dwell times are optimized by means of a mapping to a piecewise linear cage function.

perimental *FWHM* can take from tens of hours to tens of days depending on the chosen algorithm, the user selected refinement strategy, the chosen simulation models, and whether parallelization of the Jacobian is used. In this section further details on the major performance considerations will be expanded upon.

3.3.2.1 Refinement of Simulation Parameters

As foreshadowed at the end of section 3.3.1.1, simulation parameters are often refined in an external loop to the optimization loops presented in figure 3.3.1 and figure 3.3.4. In the case of the direct dwell time fitting method, two major features are usually refined in an outer loop: the step-size for estimation of the Jacobian, and the grid spacing (which also usually necessitates a corresponding reduction in the simulation time-step). By coupling the refinement of both of these parameters two favorable outcomes are achieved, in the first case coarse simulations conducted on less fine grids are completed significantly faster (especially when considering redeposition and higher order effects which require a double loop over all simulation nodes leading to approximately quadratic scaling), which allows the user to determine if either the initial input parameters or the Jacobian step-size is poorly chosen. These coarse simulations can often be completed in a user-compatible amount of time, allowing for user interaction at an early stage. The second favorable outcome is that work completed from these coarse simulations acts to accelerate later simulations through the improvement of the initial input conditions which are recycled and refined through each refinement step. The choice of refinement steps is left to user judgment and no controlled studies have been made regarding refinement protocols; however, a 20% reduction in both grid size and Jacobian step-size across refinement steps has been shown as an effective, albeit conservative, protocol.

When working with the piecewise linear cage function method, a further outer refinement is available in the form of the number of free nodes defining the piecewise linear cage function. A flowchart showing the outer refinement loop including cage refinement is shown in figure 3.3.5. The primary optimization step described earlier (section 3.3.1.1 and section 3.3.1.2) is shown at the top of the flow chart; the optimized input parameters p_j emerge at the end of the inner optimization loop coupled with the evaluated error, this error is compared to the predefined stop conditions in the “Check Precision” step; if the error is sufficiently small and the target grid size has been obtained, the simulation will stop and the inverse modeling procedure is complete. If the stop conditions are not met, further refinement is required upon which condition the cage function polygon and/or the grid size and Jacobian step size are refined. The grid and Jacobian step-size are refined as per the user-defined refinement protocol while the cage function is refined through targeted subdivision.

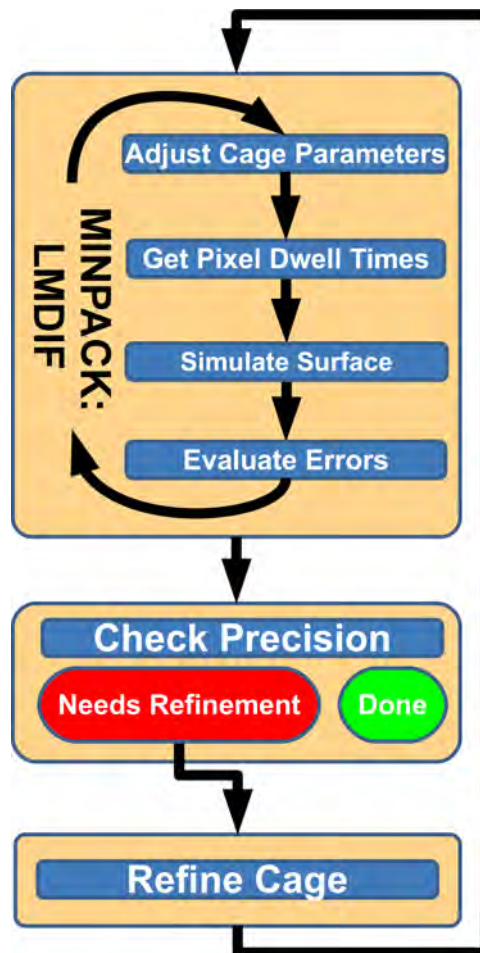


Figure 3.3.5 – A flow chart showing the inverse modeling algorithm as applied when pixel dwell times are optimized by means of a mapping to a piecewise linear cage function with the addition of an outer loop used to refine both the number of nodes in the cage function as well as normally the grid spacing and step-size used to estimate the Jacobian.

Cage refinement through targeted subdivision is demonstrated in figure 3.3.6, whereby it can be

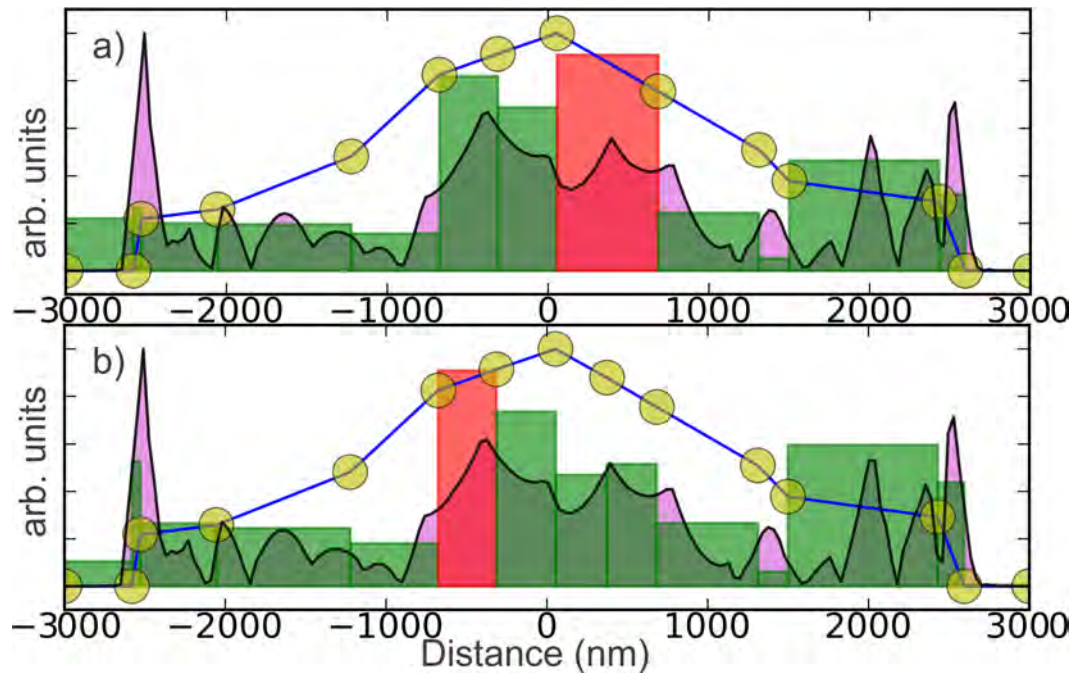


Figure 3.3.6 – A graphical demonstration of the cage refinement algorithm: top panel (a) shows a cage function before refinement, the bottom panel (b) shows the cage function after refinement through the addition of a single node at $\sim 300\text{nm}$. The magenta filled region in the background shows the spatial representation of the evaluated error, while the green and red bars show the total sum error between nodes of the cage function with the red bar drawing attention to the region of maximum error. Note that the green bars are normalized with respect to the red bar between figures.

seen that the algorithm targets edges of the polygon with maximum error and inserts an additional node at the midpoint of the line segment. The error criteria is defined as the sum of errors along a particular line segment, the obvious alternative approach of normalizing the error across the length of a segment is not used due to the peak artifacts visible in the spatial error plot (shown as a magenta filled region) near the endpoints of the polygon. This error plot corresponds well to the error evaluation shown in figure 3.3.2, whereby it can be shown that the target profile requests a sharper edge at the corner of the trench than can physically be produced by the simulated beam *FWHM*. This ill-specification of the target profile shows up in the spatial error evaluation shown in figure 3.3.6 as sharp peaks located at the endpoints. The normalized error over the length would prefer to subdivide in these regions and the “*lmdif*” algorithm would then be forced to move these points both laterally and vertically in order to utilize the additional degrees of freedom. Using the total unnormalized error avoids this problem and places new nodes in the regions with the largest error over the longest area. Note that regions of good convergence (such as the region shown between -2000 and -1200nm) are not subdivided even though they represent long regions in the error plot.

As with the grid and Jacobian step-size refinement, judgment as to the best level of refinement aggressiveness is left to the user. The cage refinement algorithm, while shown for a single node

refinement, may be repeated any number of times as long as the total number of free variables fits the criterion $N \leq M$ where N is the number of free variables to optimize and M is the number of sample points on which the error is evaluated. The refinement algorithm will continue to choose the longest regions with the greatest error, allowing for very aggressive refinement protocols; however, the strength of slow refinement is that the polygon is free to adapt to the requirements of the target contour with very little user involvement. Assuming that the user has foreknowledge of the number of required nodes in the cage polygon, as in the case of numerous optimizations over similarly shaped target profiles, the convergences can be made very quick by forgoing any form of cage function refinement.

3.3.2.2 Parallelization of Jacobian Estimation

The standard TopSim model presented in chapter 2 is a single threaded function as is the *SciPy* wrapper of *“Imdif”* implemented as *“leastsq”*; however, the majority of time spent in the inverse modeling procedure is used to approximate the Jacobian through a large number of distinct independent simulations. In order to increase the performance of the inverse modeling procedure and to make use of the current multi-core trend in desktop computing, mild parallelization is used to accelerate the estimation of the Jacobian. To accomplish this parallelization, dummy optimizations are conducted using a buffered output. In the dummy simulations garbage error values are returned to the *“leastsq”* function which proceeds to request the full set of input parameter perturbations necessary to complete the estimation of the Jacobian. After the Jacobian values have been requested, the *“leastsq”* function throws an error due to dummy data and a parallel process queue is started to process the requested input parameters needed to estimate the Jacobian. When the *“leastsq”* function is restarted, its Jacobian estimation requests are fulfilled from a pre-calculated cache on the disk. This approach leads to a 7-8x speed up when used on an 8 core desktop machine, indicating that the performance overhead due to the dummy requests and any CPU cache incoherency issues are relatively minor. Preliminary work was done on extending this parallelization to network processing, however a lack of infrastructure and suboptimal software architecture indicated that efforts to improve the refinement strategy and initial guess conditions were better short term optimization paths.

3.3.2.3 Comparison of Scaling Between Pixel Dwell Time Mappings

In order to demonstrate the efficiency and relative performance of the cage function method as compared to the direct pixel fitting method a direct computational comparison was conducted fitting various numbers of pixels to the same target profile, using both pixel dwell time mappings. Inverse mod-

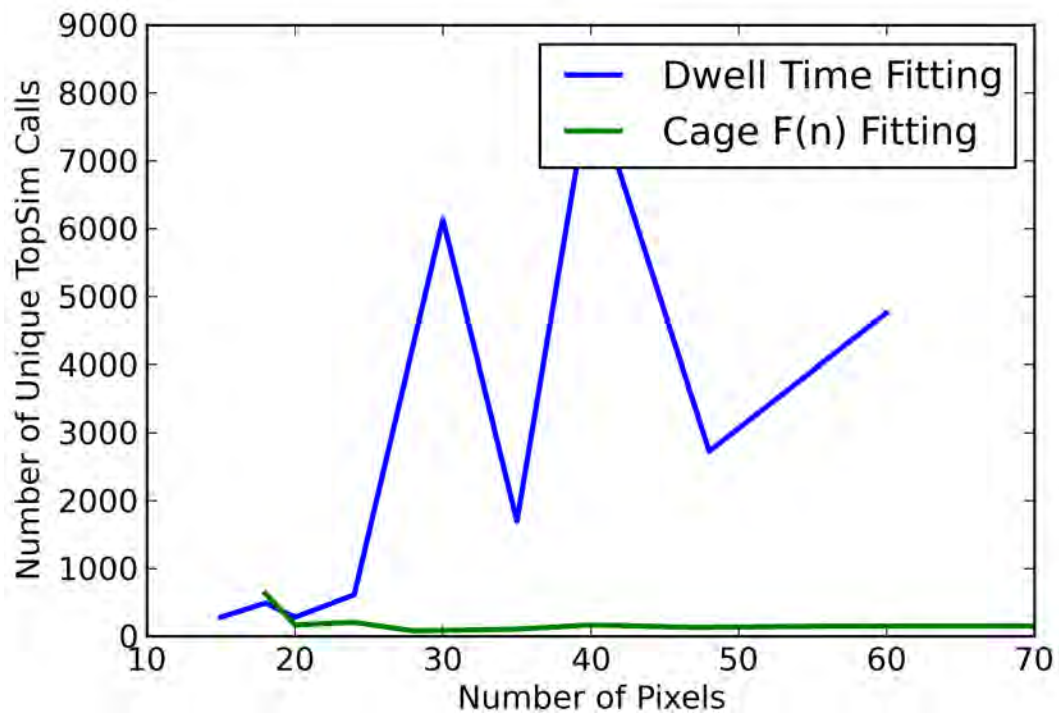


Figure 3.3.7 – A comparison of the relative performance of inverse modeling approaches. The cage function shown in green shows a nearly constant response while the direct dwell time approach shows a noisy linear response with an increasing number of simulated pixels.

eling solutions were obtained for the target profile shown in figure 3.3.2 for various beam *FWHM*s, the pixel spacing relative to the *FWHM* was kept constant for all of the executions of the inverse modeler. Variation of the pixel *FWHM* changes the number of pixels to be fitted by either mapping, thus enabling the comparison of the two mapping techniques. Both sets of simulations used a fixed grid spacing of 140nm and a fixed step size factor of 0.001 for the estimate of the Jacobian. An outer refinement loop was used for both sets of simulations with the best parameters being recycled if needed in the case of the direct pixel dwell time approach and an aggressive doubling (from 8 initially to 16) of simulation nodes and recycling of best parameters, also only if needed, being used in the cage function approach. The stop condition was set to be a mean error of 1% of the total target depth, which, in this case, translates to a mean error of 50nm. The initial starting parameters were set equally with a simple box mill that had a starting mean error of 600nm, and beam *FWHM*s of 140, 175, 210, 245, 280, 350, 420, 490, and 560nm were simulated.

As can be seen in section 3.3.2.3 the Cage fitting method is superior in all cases except where the number of free variables n is nearly equal (shown for 16 pixels and 14 degrees of freedom for the cage function). The scaling of the cage function is nearly constant with respect to the number of pixels in the simulation showing an effective decoupling of the inverse modeling solution and efficiency from the number of simulated pixels. Conversely the direct pixel dwell fitting method shows

a noisy linear increase in the number of simulation calls required to reach the desired precision. It must also be noted that figure 3.3.7 shows unique simulation calls and any backtracking done by the “*Imdif*” algorithm does not count against the total as far as this performance metric shows. The buffered execution used by the mild parallelization described in section 3.3.2.2 means that under operating cases the metric of unique calls is most applicable as there is negligible penalty to the minimization algorithm in the case of backtracking.

3.4 Comparison of Quasi-stationary and Stationary Solutions

The presented algorithm, regardless of the chosen mapping to pixel dwell times, is assumed to function in a quasi-stationary (first discussed in section §3.2) regime, where a spatially varying dose profile can be defined without an explicit time dependence. In simulation space it is trivial, and even convenient, to neglect the beam scanning time dependence and simulate using the spatial profile constructed of Gaussian beams with beam centers at pixel locations but exhibiting doses that are decoupled from the time required to actually move a beam. Furthermore, this construct assumes the simultaneous exposure of all pixel locations. This simulation construct is known internally within TopSim as an overlapped beam, and enables the use of more aggressive time-steps to simulate only gross transformation of the topography. An overlapped beam simulation represents a *fully stationary* solution; however, while a *fully stationary* solution can exist in simulation space, only varying degrees of *quasi-stationary* solutions can be physically implemented experimentally with a FIB. Simulation of the pixel scan without the use of an overlapped beam requires that the time step be sufficiently small to resolve each individual pixel dwell time. However, as previously mentioned in section §3.2, it is advantageous to mill features using a number of scans or passes in order to minimize the effects of redeposition as exemplified by the snow-plow effect. Pixel dwell times used for multiple scans can therefore be quite short and detrimental to the efficiency of the forward simulation, however at times it is necessary to account for these effects in the simulation in order to accurately match experimental conditions.

Scanning speed, which can be directly mapped to the number of passes required to deposit a dose profile, has been experimentally demonstrated to have a large effect on the measured effective sputtering yield [174]. The quasi-stationary solution, upon which the presented algorithm is based, maps to the use of an infinite number of infinitesimally short raster scans; however, this approach is infeasible to implement using an actual FIB apparatus as there are finite limits to the beam deflection speed. The number of experimentally achievable passes is further constrained by the real effects of sample and current drift. Experimental verification of the inverse modeling method therefore emu-

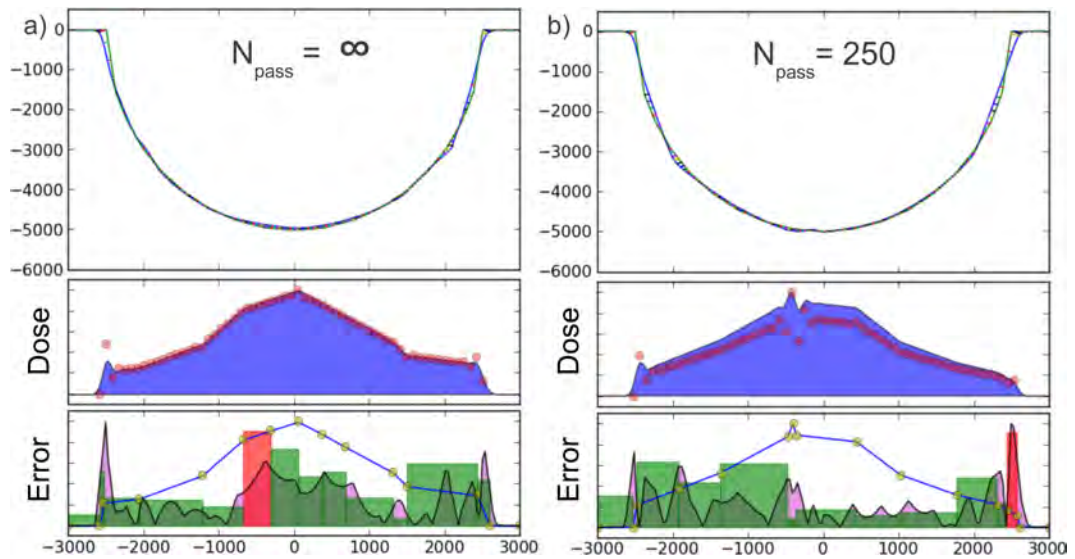


Figure 3.4.1 – Comparison of simulated dose profiles for an infinite number of passes (left: a) versus an experimentally useful number of passes (right:b).

lated the temporally decoupled spatial solution through the use of hundreds of passes which provide a rough approximation of the infinite number of passes upon which the algorithm was constructed.

The difference in simulated results between a stationary solution (“overlapped beam”) and a quasi-stationary solution (250 identical passes emulating a stationary solution) are shown in figure 3.4.1. Both simulations assumed the use of a 130nm gallium ion beam bombarding a silicon target with a beam current of 2.0nA. A cylindrical micro-lens with an elliptical cross section was chosen as the target profile with a width of $5\mu\text{m}$ and a maximum depth of $5\mu\text{m}$. An inverse modeling solution was solved using 60 pixels and the cage function mapping to pixel dwell times. Both the infinite pass and 250 pass solutions show good convergence to the target profile; however, the 250 pass solution exhibits a strong left right asymmetry. The asymmetry counteracts the preferential redeposition that occurs to the left of the beam as it scans from left to right. These results and the experimental verification shown in section §3.5 demonstrate that the presented inverse modeling algorithm, developed for temporally independent stationary solutions, is functional even in the quasi-stationary regime.

3.5 Experimental Verification

The experiments presented in the following sections were performed by Dr. Simon Waid as part of his dissertation work for the Vienna University of Technology. Dr. Waid acted as both a software tester and developer, refactoring the prototype inverse modeling code as well as providing feedback on usability, as well as doing the necessary FIB experimental work used to gain these results. This collaborative work was invaluable to the development of the presented inverse modeling software.

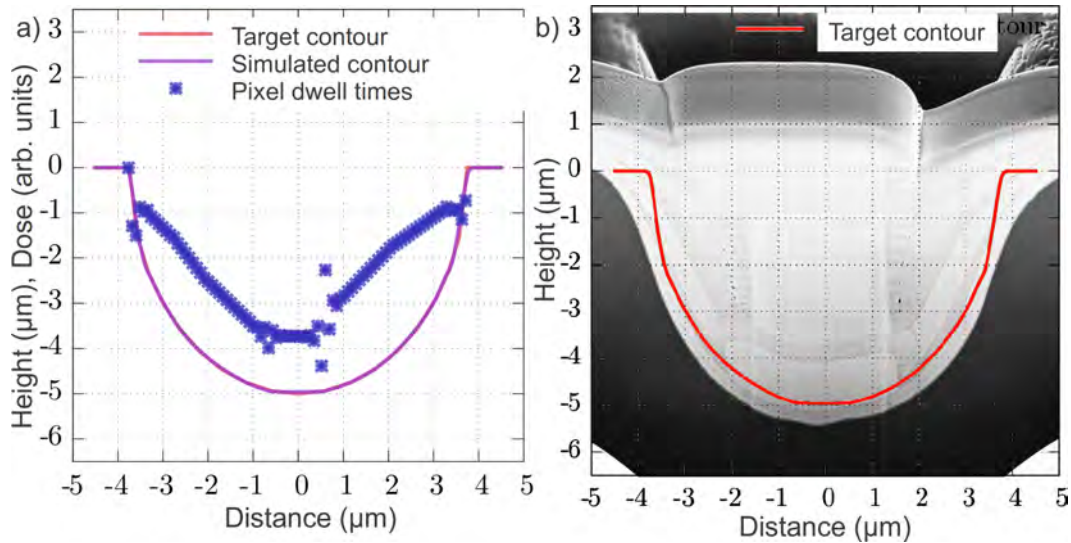


Figure 3.5.1 – A comparison of the target profile and simulated profile created by the pixel dwell times (blue Xs) (shown on the left) and the experimentally milled structure (right). The target contour is overlaid on the SEM micrograph.

The beam parameters and target geometry presented were chosen by Dr. Waid with knowledge of repeatably obtainable experimental conditions and judgments of useful target geometries.

The presented inverse modeling approach was experimentally verified [175] through the FIB milling of a hypothetical silicon imprint positive for a cylindrical micro-lens with an ellipsoidal cross-section defined by a $5\ \mu\text{m}$ width and a $5\ \mu\text{m}$ height. The experiment was conducted using an Orsay Physics Canion 31 ion gun with a measured beam current of 2.07nA at a beam energy of $30\ \text{keV}$ and a $FWHM$ of $130\text{nm} \pm 10\text{nm}$ using gallium ions on a silicon wafer target. Milling was completed in 250 passes implemented as line scans in the long direction (into the page in figure 3.5.1) with 90 specified pixel lines across the width of the trench; fast scanning was in the long axis.

The experimentally used input pixel dwell times are shown in the left of figure 3.5.1; note the asymmetry in the inverse modeling solution required to compensate for redeposition related to the scanning beam. An overlay of the target contour with respect to the milled surface (shown on the right of figure 3.5.1) demonstrates a good fit between the desired target profile and the milled profile. The error between simulation and experiment is $\sim 10\%$ at the maximum depth of the milled structure. The error in the maximum depth is attributed to uncertainty in the experimental beam current, while deviations from the simulated trench at the edges are conjectured to be due to non-Gaussian beam tails not accounted for by the simulation. Simulation of experimental beam tails would require careful experimental calibration and would be dependent upon a number of experimental factors including beam current, selected aperture, and beam alignment. Considering both the experimental and simulation uncertainties, these experimental results presented in figure 3.5.1 demonstrate the effec-

tiveness of the presented inverse modeling algorithm implementing a piecewise linear cage function to efficiently generate a quasi-stationary dose profile solution for the direct milling of user-specified contours.

3.6 Experimental Anomaly

The presented algorithm was shown to be effective for initial test structures (section §3.5) prompting further experiments making use of the completed inverse modeling approach. In order to study a scientifically relevant application of inverse modeling, it was proposed to create a set of silicon bio-scaffolds and study the effect of both preparation method and sidewall geometry on biological cells grown in the milled trenches with an additional goal of comparing the bio-compatibility of trenches produced via FIB and anisotropic methods such as Reactive Ion Etching (RIE) [176]. In the course of this experimental work, a limitation of the inverse modeling procedure was discovered: forward solutions derived via inverse modeling for target profiles with steep sidewalls and flat bottoms exhibited a characteristically different experimental profile from the simulated result. Notably, experimental trenches exhibited both extremely pronounced micro-trenching occurring in the corners of the milled trench and a notable left-right asymmetry in the size of the produced microtrenches. Considerable work was completed to ensure that these effects were not simply due to experimental errors or device uncertainties. Dr. Waid also followed up with an exhaustive perturbation analysis, using simulations of the converged solution to explore the effects of uncertainties in the *FWHM*, pixel dose, scan direction, grid size, choice of time-step, and even went so far as to artificially increase the simulated effects of redeposition (equation (2.1.2)) and second-order sputtering (equation (2.1.4)) [177]. The results of this perturbation analysis were inconclusive in all cases, the modified simulation contours failed to reproduce either the pronounced micro-trenching or the left-right asymmetry; furthermore, considerable divergences were exhibited in both sidewall angle and trench depth.

This experimental divergence from simulation is exhibited in figure 3.6.1 where it can be seen that the inverse modeling procedure functioned satisfactorily and produced a simulated contour that agrees with the target contour; however, it can also be seen that the experimental results do not agree with simulation. While experimental uncertainty remains, there appears to be a systematic divergence from simulation exhibited across a wide range of experiments over different geometries all of which share the feature of steep sidewalls. This systematic error implies a shortcoming on the part of the model used in the forward simulation. Furthermore, the systematic underestimation of the experimental milling depth for these structures implies the need for a model that will enhance the sputtering effect in the affected regions either through increased yield in gallium rich regions

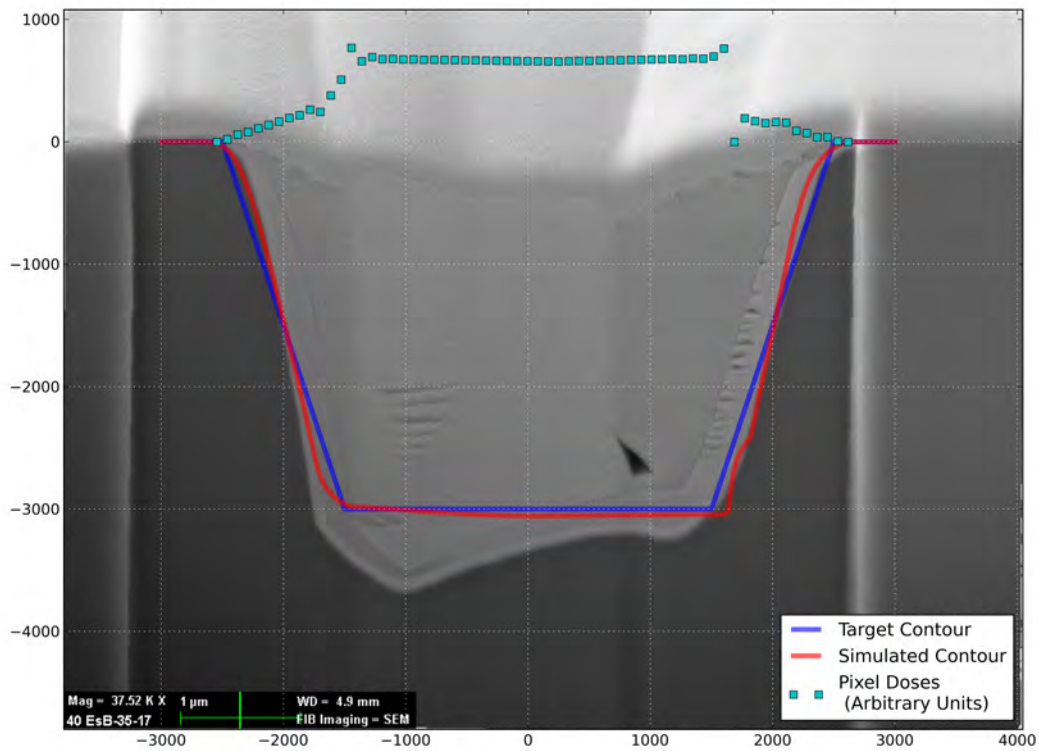


Figure 3.6.1 – An overlay showing the comparison of a representative experimental result for an inverse simulation involving steep sidewalls. The simulated contour (red) shows reasonable convergence with the target contour (blue) and the pixel doses (cyan) exhibit the ramped structure and asymmetry necessary to counteract redeposition and higher order effects producing sharp sidewalls when using a dose profile applied over 150 passes. A pixel *FWHM* of 140 nm was used for a beam current of 50 nA using a 30 keV gallium FIB on silicon. Note the pronounced asymmetrical microtrenches that develop in the experimental micrograph. These should not exist as the forward model should compensate for microtrenching. (linear dimensions in nm)

or through the addition of unconsidered fluxes to the model. In chapter 5 the effects of the previously unconsidered secondary sputtering by energetically sputtered atoms will be considered, and it will be shown that a forward simulation model including self-sputtering by target atoms leads to an improvement in the fit of simulation to experiment.

Chapter 4

Physical Sputtering Properties

Hitherto this chapter, it has been expressed that the string based model described in chapter 2 utilizes sputtering statistics derived from Monte Carlo simulations under the binary collisions approximation (BCA), obtained from the simulation package IMSIL [122]. However, no detail has been provided as to the specifics of these BCA simulations. In the course of this research a collaboration with FEI Company presented the rare opportunity to obtain high precision experimental sputtering yield data as a function of incidence angle; unique to this dataset was the focus on glancing incidence angles. High quality experimental sputtering data for glancing incidence angles has historically been rare. The gallium-silicon system especially, even though this pairing is commonly used in research and industry, lacks experimental data due to both the difficulties in performing glancing angle experiments coupled with the complexity of the system from a theoretical standpoint*, making it a poor choice for purely scientific sputtering studies. Basic sputtering research is usually performed on metallic or insulating targets, with preference for noble metals. A large number of the sputtering experiments performed on silicon involve the use of noble gas ions in order to eliminate chemical effects. Though *some* high quality experimental sputtering data is available for the gallium-silicon system (e.g. [179]), the available data focuses on the entire range of incidence angles and not glancing incidence angles. In the simulation of steep sidewalls, as occur in both deep trenches and in TEM sample preparation, intimate knowledge of the sputtering yield at glancing angle is invaluable.

In this chapter the experimental sputtering data for 30 keV (as well as 5 keV briefly[†]) gallium on silicon will be presented and compared to earlier published sputtering data as well as to Monte Carlo simulations. It will be shown that glancing-angle sputter yields require specific attention, and careful

*Silicon's semi-conducting nature, while not insurmountable, makes comparison of experimental data to basic theory more difficult. Silicon studies therefore have a more applications focus than noble metal experiments [178].

[†]The collaboration focused mainly on 30 keV yield measurements, though there was also high quality 5 keV data obtained by FEI that was not presented in earlier publications.

work must be done to reproduce the experimental trends with BCA simulation. The primary tuning parameters of the BCA model will be demonstrated with regards to their effect on the angular-dependent sputter yield, and it will be shown that BCA simulations require not only careful consideration of the initial conditions but also that surface roughness plays an important role in accurate simulation of the sputtering yield at glancing angles. A number of computational approximations for simulating surface roughness using the binary collisions approximation will be presented and discussed and finally a computationally elegant and efficient surrogate for surface roughness will be presented. The rest of the chapter will focus on higher order effects of surface roughness on statistical sputtering properties beyond the angularly dependent sputtering yield. The final section will present preliminary work looking at the application of the surface roughness model to experimental sputtering yields conducted at a different beam energy.

4.1 Motivation for Experimental Confirmation

As mentioned in section 1.2.4.2, modern binary collisions simulators make use of Monte Carlo methods to study the statistical properties of energy deposition and implantation in solids. In this case energy deposition is used to statistically simulate the sputtering properties of ion-target pairings for various energies of primary ion. While IMSIL [180] is capable of simulating crystalline structures, the normal formulation and the approach used in this work is to assume that the target is amorphous. In the amorphous formulation, once the energetic ion nears the target, simulation partners are chosen according to the statistical probability of randomly encountering a target atom based on the density, interaction volumes of each atom, and the potentials defined for the target. These collision partners undergo simulated collisions utilizing a mathematical model for the scattering cross section, and a portion of the ion's energy is transferred to the collision partner. Both particles adopt new trajectories based on the simulated collision. New collision partners are statistically chosen for each of the energetic particles and the process is repeated until the energies drop below a predetermined threshold. Energy loss due to transfer to the electronic structure of the target is also included in each simulated collision. Once trajectories reach the surface of the target, they must surmount the surface binding energy in order to be sputtered in the simulation; particles that fail to escape are deflected back into the target.

The beauty of this method is that it is computationally elegant as particles do not exist in the simulation unless they are energetic. BCA simulations are therefore quite memory-efficient and are significantly faster than MD simulations that attempt to simulate the entire target at once. However, both types of simulation are dependent upon the quality of their assumptions and input criteria as

well as the validity of any approximations made in the model in the parameter space of interest. Experimental verification is the only method[‡] by which one can check the assumptions made in the simulation, some explicit, some implicit; it must be borne in mind, however, that experiments themselves contain their own sets of uncertainties and assumptions. Great care must therefore be taken to conduct comparable simulations that carefully agree with experimental conditions. Often experiments leave much to be desired as far as precision and testability and it becomes necessary to compare a model or simulation to another model or simulation employing a different approach. In this chapter four assumptions of the IMSIL simulations used to simulate sputtering yield will be compared to experimental data. Three of these assumptions are explicit, namely the choice to neglect the effect of implanted gallium on the simulated sputtering yields, the choice of the electronic stopping model used, and finally the choice of the planar surface binding energy used in the simulation. A fourth implicit assumption, that an amorphously flat surface is sufficient to accurately simulate sputtering, is tested through the explicit specification of rough surface geometries.

Simulation of surface roughness through some means is essential to reproduce the angular dependence seen in the experimental data indicating that the implicit assumption of the viability of a flat surface is invalid at the experimentally tested incidence angles and energies. Experimental verification therefore acted to improve the quality of the sputtering yield simulations used as inputs to the string model demonstrated in chapter 2.

4.2 Experimental Results for 30 keV Ga on Si at Glancing Angles

Justification for experimental verification is clearly shown in figure 4.2.1, where four sets of angularly dependent sputtering data are shown for 30 keV gallium on silicon. The two experimental datasets, one from 2003 [179] by Frey et al. and the other from experiments done in 2012 by FEI Company [181], both show similar trends; however, the magnitudes of the error bars in the later experiments are significantly smaller. The simulation datasets, the default SRIM-2008 [182] simulation, and the best-practice IMSIL [180] simulation undertaken before the experimental verification, both show qualitative agreement with the experimental datasets; however, the SRIM simulations seem to strongly over-estimate the sputtering yield at glancing angles. It is suspected that ions in the SRIM-2008 simulations may have an insufficiently long free-flight-path before encountering the target, and therefore start unrealistically close, thus depositing more energy into the target than seen in the experimental data. While the IMSIL data shows good agreement with the newest experimental dataset,

[‡]MD represents an alternative method for validation of the BCA simulation but MD would also be susceptible to simulation size restrictions and would also require validation of the chosen inter-atomic potentials. Comparison to experiment represented the best available method of confirmation with the available experiential infrastructure.

there is a systematic divergence at highly glancing angles (see the right side of figure 4.2.1). In the following sections the various simulation model assumptions will be individually tested and it will be demonstrated in section §4.4 that this divergence is caused by insufficient surface roughness in the BCA simulation.

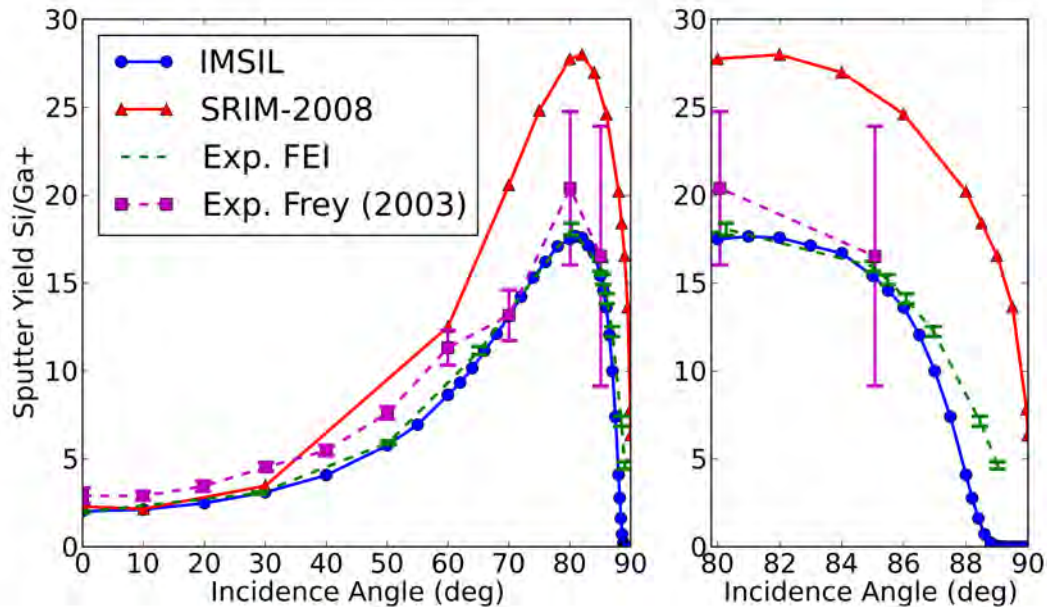


Figure 4.2.1 – Experimental and Simulated sputtering yields for 30 keV gallium bombarding a silicon target. Experimental data is shown with dotted lines while simulated data is shown with solid lines. Note that SRIM over-estimates the sputtering yield with increasing incidence angle, while the IMSIL simulation (shown for simulations not including surface roughness) under-estimates sputtering rates at extreme glancing angles.

4.3 Effects of Binary Collisions Model Parameters on Simulated Sputter Yields

In the following subsections the effects of the primary tuning parameters for IMSIL simulations upon sputtering yield are investigated. These parameters include the effect of implanted gallium in the target, choice of electronic stopping model used, and the effect of changes to the surface binding energy used in the simulation.

4.3.1 Influence of Ga Implantation

The 2003 Frey paper [179] demonstrated that the measured sputtering yield at normal incidence (an incidence angle of 0°) varies with increasing ion dose. This variance is attributed to the implantation of gallium in the target which in their experiments led first to swelling (negative apparent sputter

yield) and then to a steady state positive sputtering yield as the gallium concentration at the bottom of the milled region reached a steady state condition. As the forward topography simulation model presented in chapter 2 does not explicitly account for the accumulated ion dose, it was assumed that as long as doses were sufficiently high to be in the steady state regime, it was not necessary to use dynamic simulations to generate the steady state statistical data for normal incidence. It remained to be demonstrated though that the effect of gallium implantation was negligible at glancing incidence angles as such were the region of interest for the experimental confirmation. As can be seen in figure 4.3.1, implanted gallium plays a decreasing role in the simulated sputtering yield at increasingly glancing incidence angles. This reduction is due to the reduction in the concentration of gallium at the target surface for glancing angles, a reduction caused by the increase in the backscatter ion yield at glancing angles, as was shown in figure 2.3.2. Simply put: at glancing angle, fewer ions are implanted into the target, hence there is a reduced effect on the simulated sputtering yield. As there is relatively little change in the highly glancing-angle sputtering yield, gallium implantation cannot be used to explain the divergence between the experiment and simulation at angles greater than 85°. Furthermore, the limited effect of gallium implantation at less glancing angles supports the choice to forgo dynamic simulations when deriving the statistical inputs used in topography simulations.

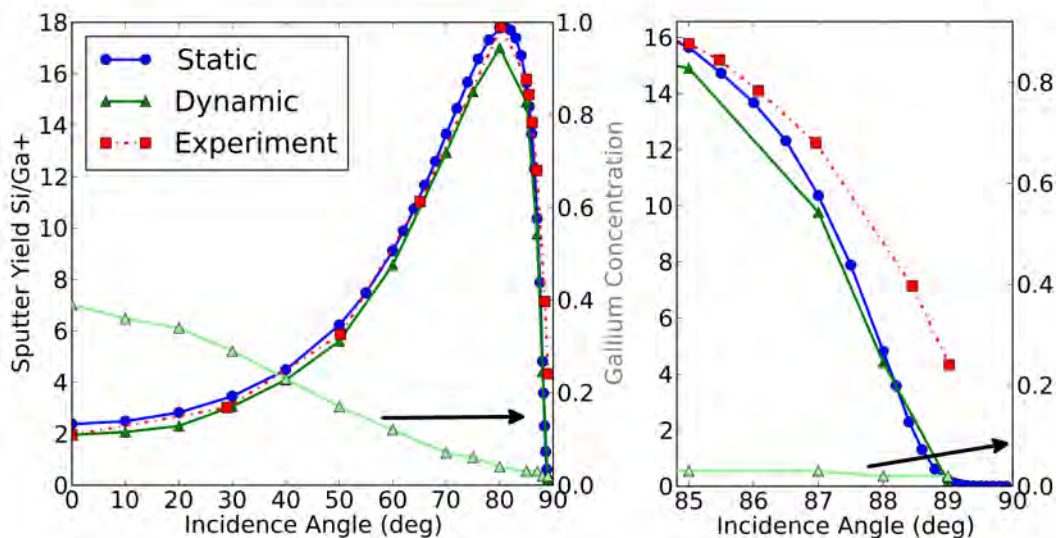


Figure 4.3.1 – A comparison of the simulated effect of gallium implantation upon sputtering yields. Light green data corresponds to the right axis indicating implanted gallium concentration at the simulated surface. Increased gallium concentration leads to a small but perceptible decrease in the sputtering yield for silicon target atoms. At more glancing angles the effect of implanted gallium is reduced as implanted gallium concentrations approach zero. All simulations were conducted for an atomically smooth amorphous surface.

4.3.2 Influence of Electronic Stopping

Electronic stopping is used to describe the phenomenon whereby an ion moving through a material loses energy to the material through inelastic collisions with bound or free electrons thus resulting in the retardation of the ion's velocity through the material. The total amount of energy lost by an atom by electronic stopping is therefore dependent upon the length of the path the ion takes through the material as well as the location of interacting fields in the simulation. Electronic stopping can play a significant role in the ion range of implanted ions and BCA simulators such as IMSIL, which were originally devised as dopant implantation simulators, have a wide variety of highly sophisticated models to simulate electronic stopping.

The *IMSIL-default* electronic stopping model used for normal or near normal incidence implantation and sputtering studies is a hybrid model that combines *non-local* electronic stopping using the Lindhard model [183] with a *local* Oen-Robinson [184] electronic stopping model. This default combined model functions well for perpendicular implantation; however, at glancing angles it becomes difficult to choose a physically robust interaction cutoff distance for the *non-local* model. The *sputtering-default* model used in these studies is therefore a *local* model with a 10 eV cutoff energy applied [185]; furthermore, special care is taken to calculate the midpoint energy loss before calculating the nuclear collision thus ensuring conservation of energy.

The effect of changing the utilized electronic stopping model is demonstrated in figure 4.3.2 where a number of electronic stopping modes are compared to the experimental data. Shown first is the dataset indicated by blue circles and the symbol *eminse*; this is the *sputtering-default* electronic stopping mode explained in the previous paragraph, namely a *local* model with a 10 eV cutoff. The next model *nose* indicated by green upward triangles is a simulation that completely neglects electronic stopping; as expected the absence of the retarding force leads to an increase in the simulated sputtering yield. In light blue squares labeled *loc_apsis* a formulation of the Oen-Robinson *local* model using the apsis of closest approach is used, which also yields an increased sputtering yield. A reduction in sputtering yield is shown when a purely *non-local* model is used as indicated by the yellow circles and the label *noinel_nl*. Finally the magenta and black models (*loc* and *noinel_loc*) indicate a purely local model with no cutoff energy and a purely local model without calculation of the midpoint energy prior to the nuclear collisions [186] respectively; the sputtering yield increases slightly as compared to the pure local model.

The notable effect of changing the electronic stopping model is to increase or decrease the sputtering yield for less glancing angles; however, the transition to reflection of the incident ions at more glancing angles is generally unaffected by these models. This transition to reflection is not seen in the

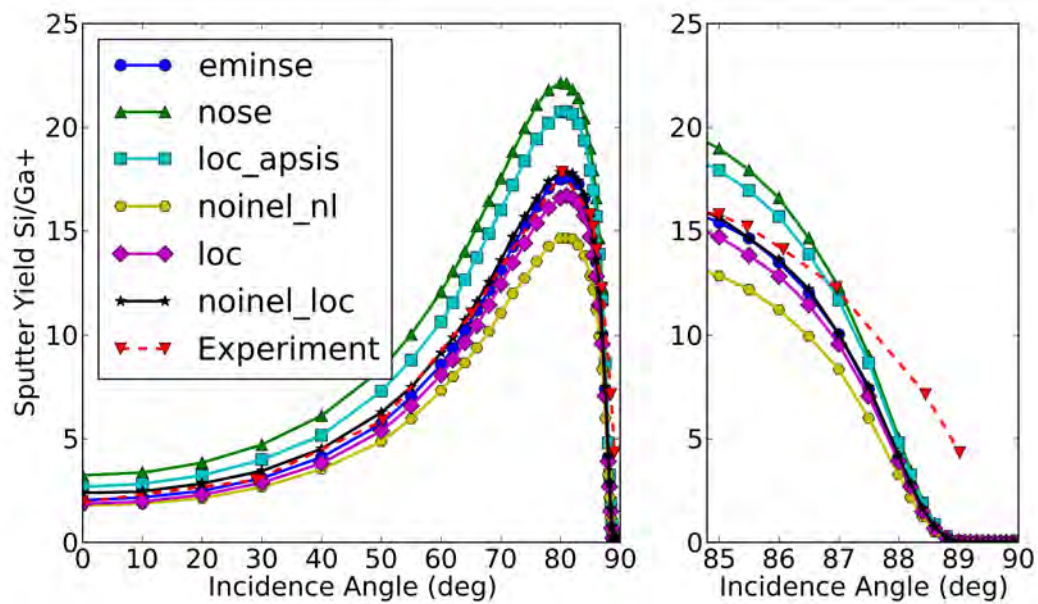


Figure 4.3.2 – A comparison of the influence of different available electronic stopping models (described in section 4.3.2) upon simulated sputtering yields. Note that the choice of the electronic stopping model has a minimal effect on the sputtering yield at extremely glancing angles.

sputtering yields presented earlier (figure 2.3.1), as later yield simulations incorporated an approximation to emulate surface roughness. While the choice of electronic stopping model can significantly affect the accuracy of the yield simulation at the sputtering yield maximum and even at normal incidence, the effect at extremely glancing angles is overshadowed by the non-consideration of surface roughness. The choice to use the model labeled *eminse* is therefore validated, because in addition to being conceptually the most physical model, the *eminse* model also fits the general trend of the experimental data.

4.3.3 Influence of Surface Binding Energy

Surface binding energy is described in BCA sputtering simulations using a planar potential to represent the attractive energy that holds solids in a solid state. Conceptually it is the energy required to remove a single atom from the surface of the target and it can be defined for both foreign atoms such as the bombarding ion or for target atoms of a single or varying species as in the case of non elemental targets. The concept of a binding energy defined for the surface that is largely independent of position is found even in the early analytical models of sputtering [97]. It is therefore no surprise that surface binding energy finds its way into BCA sputtering simulations. Surface binding energy is conceptually and geometrically well defined, as shown in figure 4.3.3, where it is used to determine both whether an energetic particle that has left the bulk of the target has sufficient energy to escape

into vacuum, and the deflection angle as the particle is refracted by the planar potential either into vacuum or back towards the target.

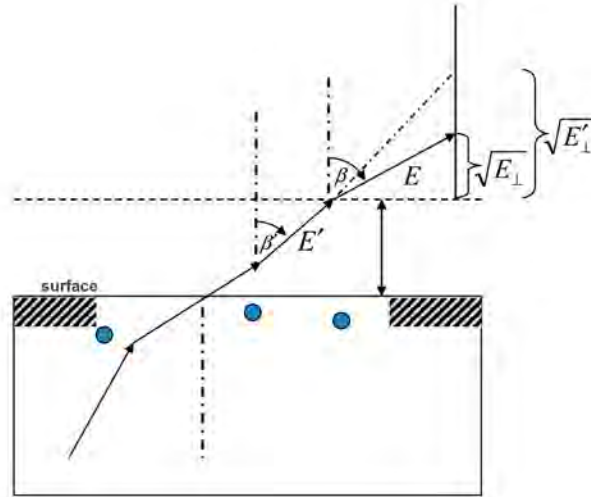


Figure 4.3.3 – A schematic diagram indicating the effect of the planar surface binding potential on a simulated particle as it leaves the surface resulting in the further deflection of particles as they cross the planar energy surface. Particles with insufficient energy to exceed the surface binding energy are deflected back into the target [186].

Real atoms, however, undergo bonding that is not isotropic, with characteristic bond angles that themselves define the crystal structures of solids. A given atom near the surface would therefore likely encounter a different attractive force depending on the spatial configuration of multitude of atoms located in the surface below it. Work has been done indicating the limitations of the planar surface binding energy concept with respect to low energy sputtering events as compared to MD [117]. However, the strength and weakness of BCA models is that they do not consider multi-body interactions —only two body interactions. Until a better alternative to the planar surface binding energy potential is found that can be applied to BCA sputtering simulations, it is likely that there will always remain an amount of uncertainty for low energy sputtering events with BCA. This is not to say that BCA is not extremely functional in the medium energy regime when using a planar surface binding potential, simply that this effectiveness could conceivably be extended with an alternative surface binding potential.

The heat of sublimation for a material is often taken as a nice estimate for the surface binding energy of a given target. As the heat of sublimation is defined as the statistical average energy required to drive an atom from the solid state to the gaseous state, the estimate has conceptual merit. In IMSIL simulations of silicon sputtering, a surface binding energy of 4.7 eV between silicon atoms and the silicon target is used, and this is also the heat of sublimation for silicon as described

in the literature. However, in these presented simulations, the surface binding energy between the gallium ion and the target is taken to be practically zero with a value of 0.001 eV. This surface binding energy is reasoned through studying the binary phase diagram for gallium and silicon [187] where a large miscibility gap is apparent, indicating little mixing and thereby negligible bonding between gallium and silicon. The miscibility gap argument suggests a lower, but not effectively zero surface binding energy for gallium with respect to silicon, the effectively zero number was chosen in response to detailed trajectory studies that indicated an extremely non-local artifact arising from the use of a planar surface binding potential in simulations without surface roughness and extreme glancing incidence angles ($> 89.9^\circ$). In these particular simulations the ions were noted to be trapped between the repulsive and attractive potentials oscillating above the surface for tens of microns, as a physical surface would likely have imperfections preventing this behavior and the use of a near zero gallium-silicon surface binding energy cured the artifact, the near zero energy was adopted. The proper response to this artifact is still an open question.

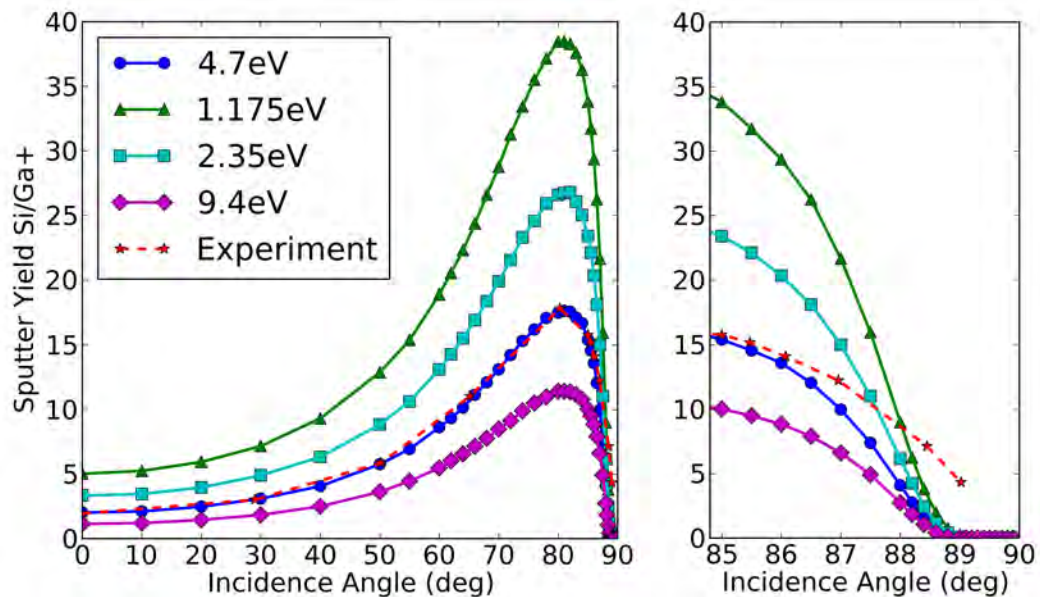


Figure 4.3.4 – A perturbation analysis of the effect of chosen surface binding energy on simulated sputtering yield. As expected, decreases in surface binding energy lead to increased sputtering due to the lower sputtering threshold, however extremely glancing-angle sputtering still converges to zero earlier than predicted by experimental data.

The effect of modifying the surface binding energy used in the simulation is demonstrated in figure 4.3.4, where, as expected, a reduction in the energy needed for particles to be considered sputtered leads to increased sputtering yields. An increase in the surface binding energy leads to a decrease in sputtering yield for all incidence angles under which sputtering occurs. Changing the simulated surface binding energy leads to a visibly nearly linear response as a function of surface

binding energy. Similarly to the results shown with the other modified model parameters, drastic changes in the simulated surface binding energy, while having a huge effect on less glancing angles, do not resolve the experimental discrepancy at glancing angles greater than 89° .

4.4 Influence of Surface Roughness as a Model Parameter on Simulated Sputter Yields

The final simulation parameter studied in the process of tuning the simulation parameters after experimental verification was surface roughness, surface roughness in this case describing the angstrom scale surface topography that may develop during the course of ion bombardment due to the localized emission of sputtered particles resulting from singular impacts. In a hypothetical case, with a bombardment target possessing infinite thermal conductivity and zero thermal energy, ion impacts would cause the permanent relocation of target atoms, some of which would be sputtered away leaving voids at the target-vacuum interface. If the sputtering yield were sufficiently high, craters analogous to those seen on the surface of the earth's moon might even develop leading to a clear small scale surface topography that develops under bombardment. In reality, the development of surface roughness during bombardment in real materials must also contend with effects such as target relaxation, and mass transfer due to surface diffusion, both of which trend towards the reduction of sharp surface topography at certain length scales. There is significant experimental work demonstrating that surface topographies develop under even broad beam ion bombardment [188–191], in fact an entire subfield is devoted to understanding this so-called spontaneous pattern, or ripple formation. The problem is difficult however, due to the multiple length scales involved in going from atomistic simulations to structures with nanometer scale spontaneously formed patterns, prompting the use of novel simulation tools to design a theory [192, 193] that is consistent with experiment across multiple target and ion species as well as bombardment energies and doses. There remains considerable contention as to the relevant mechanisms leading to what is characterized in this text as surface roughness. Without consistent models it is difficult to predict the character and scale of surface roughness that might have developed over the course of the experimental yield measurements, however this section will demonstrate that simulations including various plausible arbitrary representations of surface roughness lead to an improvement in the agreement between measured and simulated sputtering yield at glancing angles.

While it may be possible to use brute force techniques such as large scale MD to directly simulate the evolution of surface roughness, another approach is applied in this presented research:

simulation of plausible yet arbitrary representations of surface roughness. These simulated surface roughnesses are manifested by either simulating an actual 2D topographical profile with a geometric representation of the surface roughness or by exploiting a surface layer of decreasing density to randomly emulate surface roughness. Simulations utilizing these surface roughnesses are then compared to the experimental data leading to an improved simulation of the glancing-angle sputtering yield. The surface roughness parameters that best duplicate the experimental data are then used as simulation parameters for the forward simulation as described in chapter 2, including properties such as the sputtering angular probability distribution (section 2.3.2.1) which is a property that while experimentally measurable was not in the scope of the experimental work done by FEI. The effect of simulated surface roughness upon the angular probability distribution will be demonstrated in further detail in section §4.5.

This work is not the first work to study the effects of surface roughness on either yield [194] or sputtering angular distribution [195]. Yamamura et al. published two papers in 1987 exploring the effects of simulated surface roughness using the ACAT Monte Carlo code and simplified surface roughness models. In this earlier work it was shown that surface roughness has a large role near the sputter yield maximum; however, this work did not optimize roughness to fit experimental data, nor did it study the glancing incidence angles presented in this present research. The surface roughness models presented in this section are also more sophisticated than the earlier models from the Yamamura papers; furthermore, the energy and ion species presented in this chapter were not investigated in the earlier work.

4.4.1 Geometric Approximation of Surface Roughness

Two geometric models for surface roughness were investigated [185]; one emulating surface roughness as a 2D sinusoidal profile, and the other emulating surface roughness using a filtered random profile (pink noise). These models were chosen after study of spontaneous ripple formations which exhibit pseudo-periodicity and quantifiable amplitudes. It was therefore possible to study the effect of wavelength and amplitude on simulated sputtering yields. In the case of the pink noise function, wavelength was emulated by applying a low pass filter to a random height profile (generated by a uniform pseudo random number generator) with a defined cutoff frequency resulting in a profile with the suppression of wavelengths shorter than the inverse of the cutoff frequency. These filtered noise signals were then scaled such that the RMS (Root-Mean-Square) height of signal was equal to the investigated parameter, thus emulating the amplitude seen in the sinusoidal model.

Two-dimensional profiles were specified in IMSIL input files by means of a spatial coordinates

denoting a polygon that described a long slab of silicon target. The thickness of the simulated slab was set to 300 \AA with a length of $10,500 \text{ \AA}$, the long length was chosen through modeling of a flat surface and determining the maximum interaction length for a 99th percentile collision; ensuring that the simulated target was long enough to simulate 99% of all target-ion interactions. Due to internal performance optimizations in IMSIL, the simulation volume (area for 2D) is constrained by the desired spatial resolution of the sampled 2D profile, which was in these simulations 1 \AA in the lateral direction which necessitated the optimization of the simulated slab dimensions. IMSIL reports sputtering yields for transmission and backscattered sputter events separately, so even though 300 \AA is slightly less than the projected range for normal incidence 30 keV gallium ions ($\sim 330 \text{ \AA}$) simulated sputtering (and backscattering) yields are unaffected (other than by cascade truncation effects which were examined and found to be negligible) by the optimized slab thickness.

In order to avoid starting point biases, a line implantation was simulated for bombardment whereby simulated ions start their path with equal probability on a line that is located 2.567 \AA above the simulated surface. The height of the starting points, known as an implantation window, ensures that simulated particles are instantiated sufficiently far from the surface to be considered non-interacting and experiencing free-flight at the beginning of the trajectory simulation. The length of the line implantation was chosen to be one wavelength in the case of the sinusoidal model and a fixed length of 500 \AA in the case of the pink noise model. Line implants had a starting position that was 500 \AA from the left edge of the specified profile in order to ensure that ions that reversed their trajectory would not encounter a false cutoff in the leftward direction. A schematic sketch of the simulation layout for the geometric surface roughness simulations is shown in figure 4.4.1. All geometric simulations were simulated for at least 25,000 ions per investigated surface profile in order to obtain good statistical estimates of the sputtering yield.

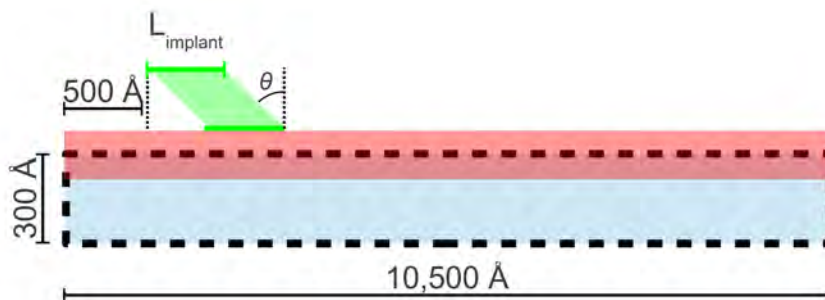


Figure 4.4.1 – A schematic representation of the simulation area used in geometric roughness simulations. The red region represents the sinusoidal or pink noise signal while the blue represents the long thin slab defining the boundary conditions. The length of the implant window L_{implant} is set to the wavelength of sinusoidal profiles and is fixed at 500 \AA for pink noise simulations. The height of the implantation window is carefully chosen to ensure a sufficiently long free flight path and to guarantee that ions have a chance to be deflected without sputtering if need be.

4.4.1.1 Sinusoidal Model

The sinusoidal profile was chosen due to its simplicity and obviousness as a starting point in an investigation of the effects of surface roughness upon sputtering yield. The experimental sputtering yield as shown in figure 4.2.1 at 88.5° demonstrates a nearly 650% higher yield than predicted by simulation for a flat surface and is therefore a good example data-point on which to demonstrate the effect of sinusoidal surface roughness on simulated sputtering yield. In order to explore the effect of both wavelength and amplitude on the simulated sputtering yield, a number of sputtering simulations were conducted at 88.5° for various sinusoidal roughness parameter pairs; the distillation of these simulations is plotted in figure 4.4.2. The color scale of the parameter plot expresses simulated sputtering yield with a white band indicating the region that agrees with the experimentally determined sputtering yield. As can be seen there is only a weak dependence on wavelength and a stronger amplitude dependence. Another feature shown in figure 4.4.2 is a white line demarking where the height to width of a single half-wavelength would be equal to one; it is presumed that sharp, tall profiles as would be located below the line are unlikely in real materials due to surface transport that would trend to minimize curvature. Also of note in the figure is the red circle which indicates the approximate position of the best fit solution to the entire experimental dataset (discussed in more detail in section 4.4.1.2).

Attempts were made to experimentally characterize the actual surface roughness* remaining after the experimental yield measurements with AFM [196, 197] (Atomic Force Microscopy); however, due to the rapidity with which silicon oxidizes satisfactory profiles were never obtained. The reported surface roughness has therefore not been experimentally confirmed and remains as a model fitting parameter necessary to replicate the experimentally determined sputtering yields.

4.4.1.2 Fitting to Experimental Data

As was mentioned at the beginning of section §4.4, the characterization of spontaneous surface roughness and its evolution is imperfectly understood; it would therefore not be unreasonable to assume that the surface roughness that develops might itself be dependent upon the incidence angle of ion bombardment. Attempts were made, however, to determine if a single equivalent surface roughness value could resolve the observed experimental discrepancy. Fits were performed by using a least-squares optimization algorithm to minimize the errors between simulation and experiment through the modification of the free parameters of roughness amplitude and wavelength. This fitting approach was extremely successful, as shown in figure 4.4.3, whereby a single roughness parameter

*AFM studies were conducted both by FEI and the University of Oregon on FEI's behalf.

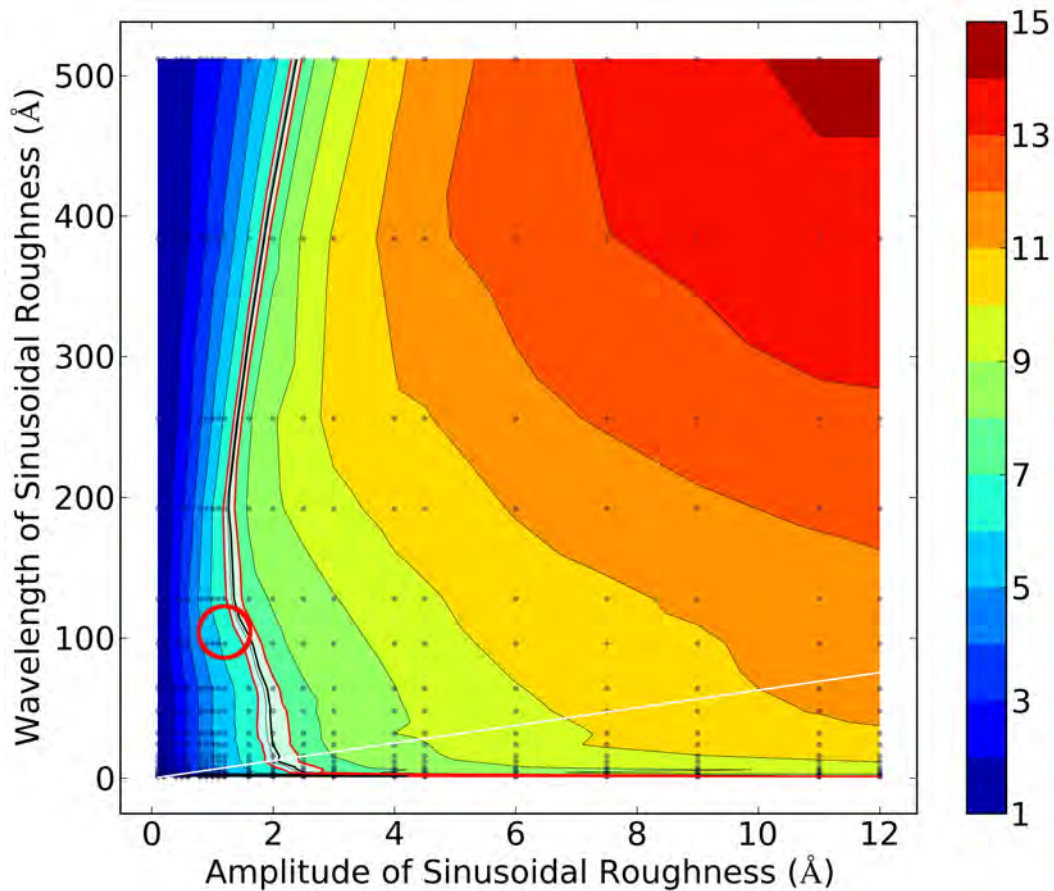


Figure 4.4.2 – Simulated sputter yield at an incidence angle of 88.5° shown as a function of the amplitude and wavelength of geometrically simulated sinusoidal surface roughness. Red circle indicates approximate region in which good fits were achieved to the complete set of experimental data. The white band indicates all parameters which fit the experimental data at 88.5° . Additionally a white line shows the demarcation of simulated surface structures with greater trough width than height.

with an amplitude of 1.05 \AA and a wavelength of 107.33 \AA is demonstrated as capable of fitting the experimental data with good agreement in the entire range of the experimental dataset. The sinusoidal model breaks down at more glancing angles, as will be discussed in section 4.4.1.3.

4.4.1.3 Limitations of Strictly Periodic Structures

The best fit sinusoidal model fits the experimental data extremely well in the range between 0° and 89.4° (figure 4.4.3); however, after 89.4 degrees an instability is exhibited. Analysis of the individual trajectories showed that for certain angles the simulated ion skipped from periodic peak to periodic peak and never entered the target, thus suppressing sputtering yields. This skipping is thought to be a direct effect of the periodic structure and indicates a limitation of the strictly periodic sinusoidal model for simulating surface roughness which prompted the construction of aperiodic alternatives as exemplified in section 4.4.1.4 and section 4.4.2.

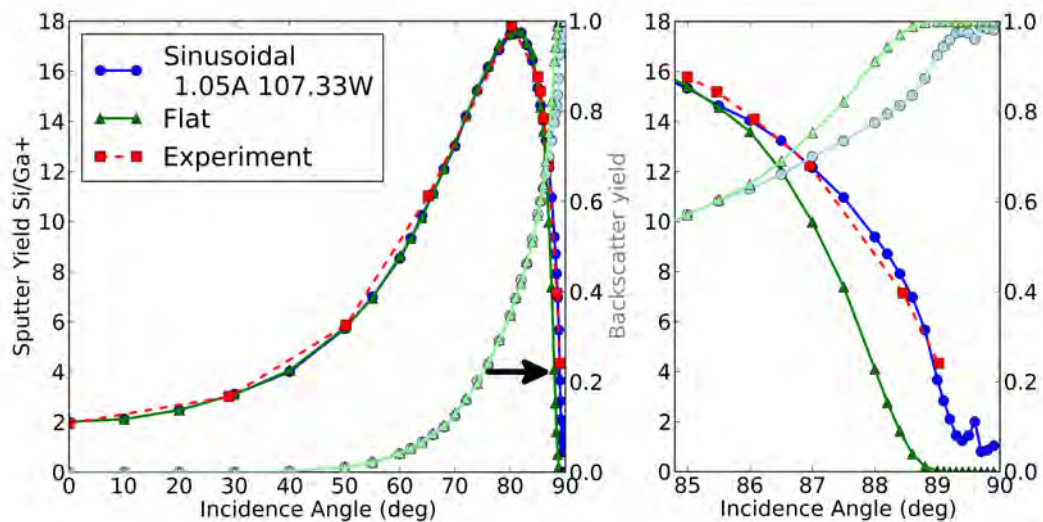


Figure 4.4.3 – Simulated sputtering and backscatter yields of best fit sinusoidal parameters (amplitude: 1.05\AA wavelength: 107.33\AA) shown in blue (lighter colors are backscatter) as compared to a simulation without roughness (green) and experimental data (red).

4.4.1.4 Pink Noise Model

To decouple the periodic effects and more accurately represent the more random nature of actual surface roughness an alternative geometric model was developed utilizing *pink noise*. Pink noise is used to describe white noise that has had high frequency bands removed, thereby, in an analogy to the visible electromagnetic spectrum, becoming more red. A graphical representation of the pink noise used to simulate surface roughness in simulations is shown in figure 4.4.4 where the effect of increasing cutoff wavelength is shown. The cutoff represents the minimum wavelength for a low pass filter and in the figure it can be seen that the high frequency signals are suppressed with increasing cutoff wavelength. Amplitude is emulated by scaling the calculated RMS height of the signal to obtain a goal RMS signal height.

The pink noise model solves the periodicity problems introduced by the sinusoidal model while still maintaining similar dimensionality. A new problem is created by the randomly chosen peak heights in that it is now possible to have a large spike acting as a wall into which all incident ions will collide over the course of a single simulation. While this possibility is also physically possible in real experiments, the simulation differs from the experiment in that the defined surface profile used in both geometric models for surface roughness is static and cannot be eroded away by sputtering. It was therefore necessary to sample a number of pink noise profiles with identical parameters but unique random seeds and thus unique structure. The resulting sputtering yields from these parametrically identical pink noise profiles were then averaged to calculate a representative sputtering yield; 20 samples were performed at each point in parameter space greatly increasing the computational workload of

the simulation.

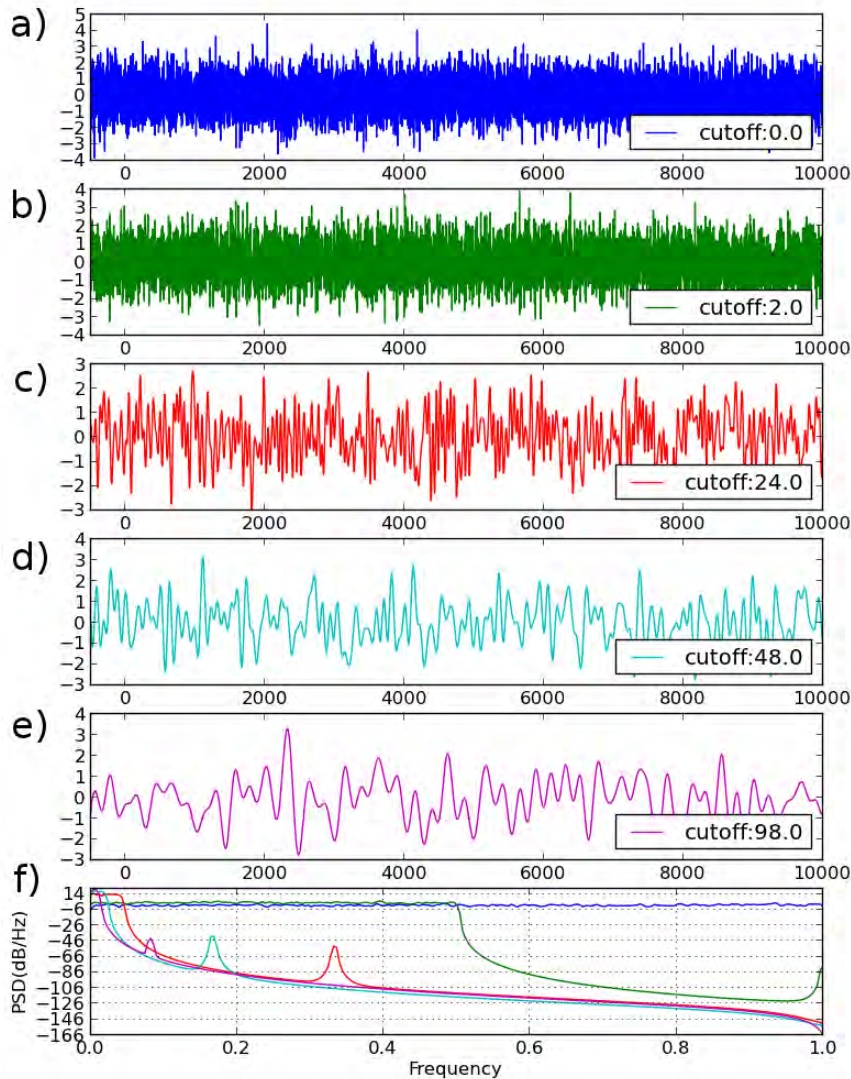


Figure 4.4.4 – Example profiles of the filtered random surface profiles (Pink Noise) showing no RMS height normalization. High frequency signals are lost with increasing minimum cutoff wavelength leading to smoother surface profiles. Note that large spikes remain even in filtered data. If these spikes occur in the simulated implant window, sputtering yield results will be skewed, therefore yield simulations were repeated across 20 unique random seeds and simulated yields averaged across all samples. The bottom-most plot shows the quality of the filtering method by means of a Power Spectral Density plot.

The parameter space plot analogous to the one shown for sinusoidal surface roughness is shown in figure 4.4.5 where the white band once again indicates the portion of parameter space that agrees with the experimental data. It is worth noting that the parameter plot for the pink noise model is not as smooth as the plot for the sinusoidal model; this is a direct consequence to the required sampling of each parameter point. Greater sampling at each point, in excess of the already used 20 samples, will lead to smoother transitions; however, the current data is sufficient to see the similar trends between the two data sets with a similarly predicted roughness amplitude of $\sim 2 \text{ \AA}$. This rough

agreement between models is taken as evidence that it is the existence of surface roughness and not the implementation that is mostly responsible for the change in simulated sputtering yield. This conclusion is important as it implies that surface roughness is a simulation parameter that should not be neglected when the correct response with respect to sputtering yield at glancing angles is required.

No attempt was made to produce a best parameter fit for the pink noise model; this is because the goal of these parameter fits was to obtain a suitable set of simulation input parameters that would produce the statistical sputtering properties used in the forward simulation of topography discussed in chapter 2. Though it is only mildly difficult to calculate the average sputtering yield across an ensemble of unique parametrically identical pink noise profiles, derivation of the sputtering and backscatter angular distributions would require the construction of a completely new tool chain in order to use the pink noise data in forward simulations. As will be shown in section 4.4.2, there exists a more elegant solution to simulating surface roughness that better fits the assumptions and constraints of the BCA model for sputtering simulation.

4.4.2 Density Approximation of Surface Roughness

The geometric representations of surface roughness as described in section 4.4.1 are the most intuitive approach to simulating surface roughness; however, they are not, as implemented, an optimal approach. Two problems are presented by geometrically simulating surface roughness, the first (described in section 4.4.1.3) relates to periodic artifacts resulting from the use of strictly periodic structures such as a sinus function to describe surface roughness; the second problem is the performance of BCA simulations utilizing a geometric approximation of surface roughness (as currently implemented in IMSIL). In order to track the particle as it leaves the geometrically defined rough surface it is necessary to both have a fine simulation grid (limiting simulation area) and to cycle through every line-segment defining the simulated surface. As long simulation regions are needed for glancing angle studies and the wavelengths of interest are small, geometric approximations require both a small grid to resolve the features and a high number of line-segments to define the polygon. This extra bookkeeping imposed by the geometrically defined rough surface severely impacts performance and makes obtaining a statistically significant sample difficult, especially when second-order statistics such as the sputtering angular probability distribution are desired. In order to address these shortcomings, a one-dimensional parametric alternative formulation for surface roughness was developed by approximating surface roughness through the use of a decaying density gradient located above the nominal surface.

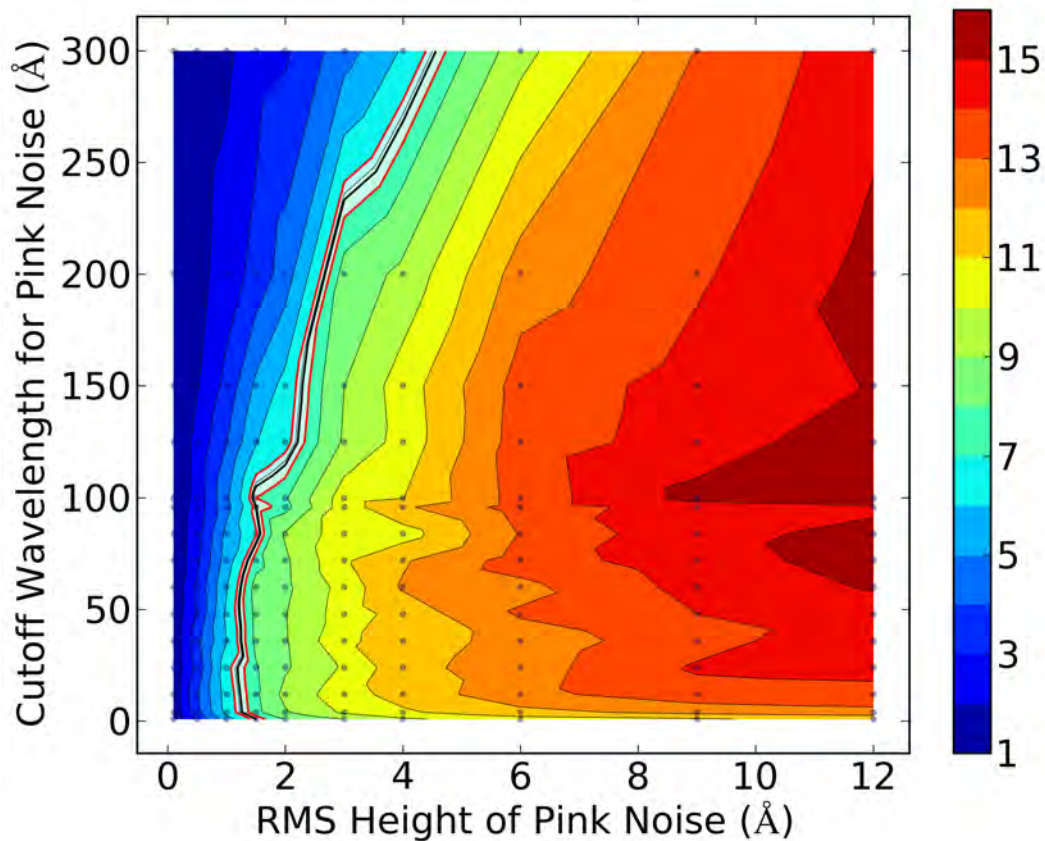


Figure 4.4.5 – Simulated sputter yield at an incidence angle of 88.5° shown as a function of the RMS height and cutoff wavelength of geometrically simulated filtered-random surface roughness. Due to the aperiodicity it was necessary to sample each parameter set 20 times to obtain smooth trends. Fits to the complete dataset were not attempted. The white band indicates all parameters which fit the experimental data at 88.5° .

This density approximation is graphically described in figure 4.4.6 whereby it can be seen that the bulk target density is maintained in the target. A low density region is simulated above the nominal surface that decays linearly to full vacuum over a user specified distance. The thickness of this density gradient region becomes a fitting parameter to adjust the glancing-angle sputter yield in order to better match the experimentally obtained data. The elimination of a lateral fitting parameter is justified by the weak wavelength response shown in the parameter plots for the sinusoidal (figure 4.4.2) and the pink noise (figure 4.4.5) models. The results of this fit are shown in section 4.4.2.1 where it is demonstrated that good agreement can be obtained between sputtering simulations utilizing the density gradient approximation of surface roughness and experimentally obtained sputtering yields. The density gradient approximation for surface roughness is complementary to the algorithms employed by BCA simulations because it makes use of the fact that collision partners are generated dynamically according to probability that an atom will be found over a certain distance which is itself dependent on the local target density. Furthermore, the probabilistically generated collision partners

do not exhibit any periodic structure, thus avoiding artifacts due to periodicity. Taken to unusual extremes, this lack of structure could become strongly a-physical as it is quite physically improbable for a cluster of target atoms to be found unconnected to the bulk, as is possible by strictly defining the probability of finding an atom away from the target surface. However practically, the fitted surface roughness thicknesses are in the sub 10\AA range, which translates into countably few mono-layers in silicon. Therefore, any probabilistically defined voids due to the density gradient model should be negligible.

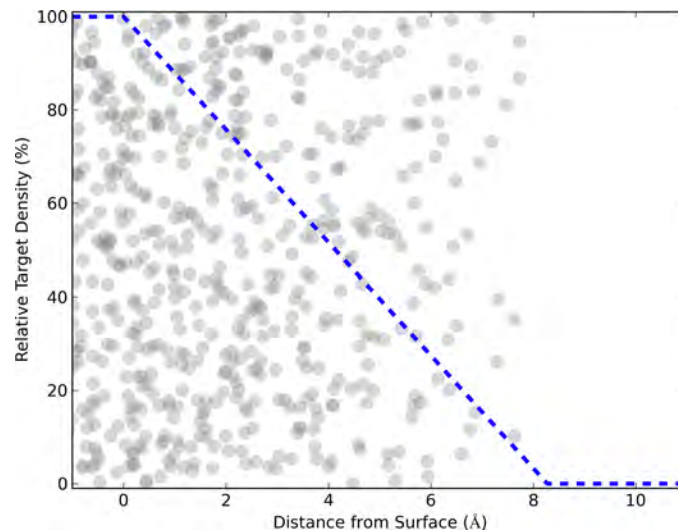


Figure 4.4.6 – A schematic diagram showing the reduction of relative target density (relative to the bulk density) as a function of distance from the nominal target surface. Density is shown with the blue dashed line and a visual representation of possible target atom positions is shown by the gray circles.

4.4.2.1 Fitting to Experimental Data

A similar optimization routine to that used in section 4.4.1.2 was used to fit the gradient density approximation of surface roughness to the experimental data. The result of this fit is shown in figure 4.4.7 where it is apparent that with respect to the sputtering yield, the gradient density approximation shows good agreement to the experimental data. Furthermore, at extremely glancing angles greater than 89.5° , the gradient density model does not exhibit periodic artifacts.

4.4.2.2 Comparison of Density Profiles Between Linear and Sinusoidal Models

The linear density gradient approach to surface roughness is not strictly comparable to the sinusoidal geometric roughness model, even though they both fit the experimental data similarly well. One-dimensional density profiles are shown in figure 4.4.8 for the best fits of both the linear density gradient approach and the sinusoidal model, where it is quite clear that a much thicker layer is re-

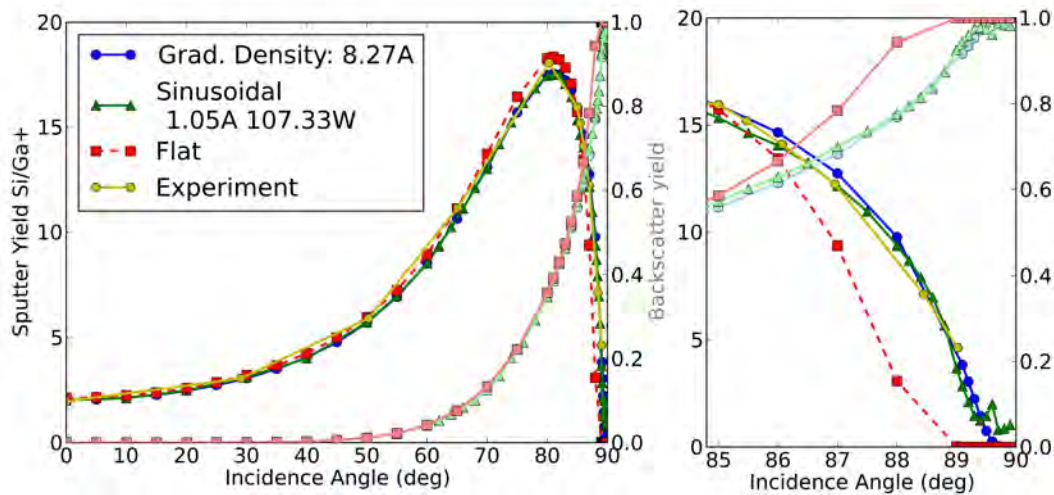


Figure 4.4.7 – Simulated sputtering and backscattering yields for different surface roughness approximations. The density gradient approximation (blue) uses a fitted surface roughness layer thickness of 8.27Å and agrees well with the experimental data (yellow) as well as the sinusoidal model (blue) without periodic artifacts at glancing angles. Both roughness models exhibit a better fit to the experimental data than the simulation neglecting surface roughness (red).

quired in the linear gradient model. Sputtering yield simulations forcing the layer thickness to match the sinusoidal thickness are shown in figure 4.4.9. Density gradient simulations conducted with a layer thickness corresponding to the sinusoidal best fit exhibit strong deviations at glancing angles as compared to the fitted simulations. This sensitivity to layer thickness indicates that the sputtering responses are critically different between the sinusoidal model and the density gradient model. More work should be done in the future to study the differences in sputtering resulting from these different surface roughness models; however, the experimental data presented is already difficult to obtain. One approach to validate these models as physically viable would be to perform MD simulation and actually generate surface roughness due to bombardment and then compare the resulting density profile to those used in BC simulations.

4.4.2.3 Bridging the Gap Between Surface Roughness Models

In order to understand the differences and sensitivity shown between the presented models for surface roughness, specialized simulations were carried out to determine the cause of the discrepancy between the density-gradient model and the sinusoidal roughness model. An initial approach of modifying the density distribution of the gradient density model to better coincide with the true density depth profile of the sinusoidal roughness profile is shown in figure 4.4.10 and discussed in the following paragraph. An alternative approach of emulating the density gradient model through the selection of an extremely short roughness wavelength and a roughness amplitude equal to the best fit for the density-gradient model was also studied and the simulation results are shown in figure 4.4.11.

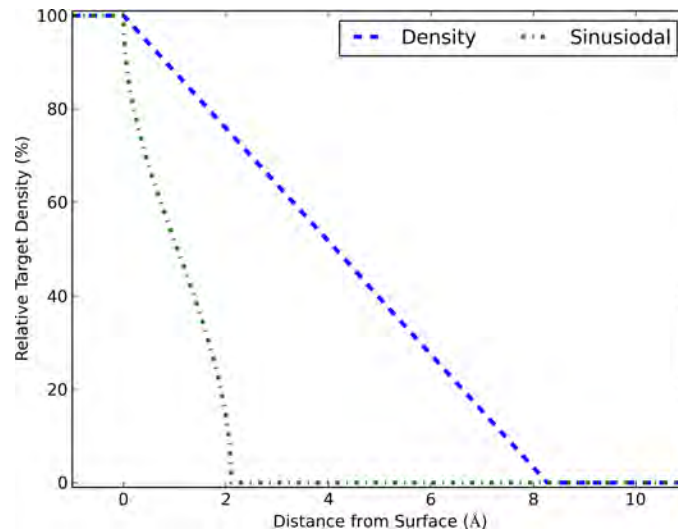


Figure 4.4.8 – A comparison of the density profiles between the sinusoidal model best fit and the linear density gradient approximation.

Both of the presented models for surface roughness function, with respect to the BCA simulation, in the same manner in that they act to smear out the interface between the bulk of the simulated target and the simulated vacuum. However, as was shown in figure 4.4.9, the best fit parameters that characterize this smeared interface show a significant mismatch between the two models. Namely, the linear gradient-density model shows a best fit to the experimental data with an interface thickness of approximately 8.27 Å, while the sinusoidal approximation shows a best fit to the experimental data when the interface thickness is approximately 2.11 Å thick (corresponding to a specified amplitude of 1.05 Å). In the previous topic of discussion (section 4.4.2.2) it was shown that this discrepancy is systematic—that it does not result simply from a wide variety of acceptable interface thicknesses in the linear density gradient model. Simply put, the best fits for each model are different. To address this discrepancy the differences between the models are closely investigated. As shown in figure 4.4.8 the density gradients that exist in the one-dimensional density profiles of each model are functionally quite different. The linear density gradient model exhibits, in accordance with its name, a linear density profile as a useful first approximation, while the sinusoidal model exhibits a higher order function for its one-dimensional density profile. Elementary calculus indicates that the density depth-profile for the sinusoidal model has the form of an arcsine function. This discrepancy in density profiles is a likely candidate as the source of the systematic differences between the fitted interface thickness between the models. A simulation implementing the correct arcsine model for the density gradient is shown in figure 4.4.10, with the new simulation being shown in red. The differences in the simulated yields between the improper linear-gradient (shown in green) and the arcsine gradient are imperceptible until glancing angles are considered. At glancing angles the density gradient model emulating

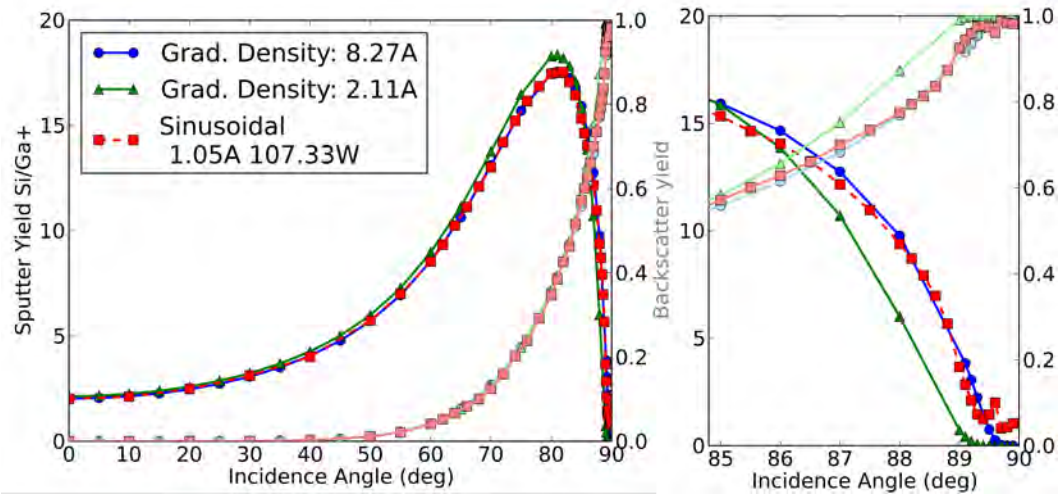


Figure 4.4.9 – A comparison of simulated sputtering and backscattering yields for different roughness models including a gradient density model with a thickness defined as the peak to trough height of the shown sinusoidal model (green). The decreased thickness of the density gradient layer as compared to the best fit layer (red) leads to an increased sputtering yield near the sputtering yield maximum and a reduction of sputtering yield at extremely glancing angles indicating that the density gradient model is sensitive to the chosen layer thickness.

the sinusoidal model shows slightly better agreement with the experimental best fits (shown in blue and yellow), in that there is a slight increase in the simulated glancing-angle sputtering yield. There remains, however, a large discrepancy in the simulated sputtering yield between even the emulated sinusoidal density model and the best fits to the experimental data. The resoluteness of the simulation discrepancy between the two models suggests that the assumption that the two-dimensional character of the sinusoidal model can be characterized with a one dimensional depth profile is invalid. However, the good experimental fits produced by the one-dimensional linear density-gradient model imply that a one-dimensional solution is sufficient to represent the available experimental data.

An alternative approach to emulating a two-dimensionally described roughness model with a one-dimensional model is the converse, namely emulating a one-dimensional solution using a two-dimensional model. There exist two practical limits of the two-dimensional sinusoidal surface model by which it can become strictly one-dimensional through manipulation of the wavelength. The first trivial solution is to increase the wavelength to infinity. This trivial mapping is uninteresting as it simplifies to an atomically flat surface with zero surface roughness. Therefore, the other solution is to reduce the wavelength to zero. Reduction of the wavelength to zero presents a number of practical limitations though, as the polygon defining the sinusoidal surface must be sampled at a finite number of points and the sampling frequency for the simulation grid (as mentioned in section 4.4.1) should be chosen to be higher than the surface sampling frequency. If the goal is simply to emulate the linear density-gradient depth profile, the sampling restrictions can be further simplified by specifying a sawtooth function instead of a sinusoidal function defining the surface polygon. The sawtooth function

naturally has a linear density gradient and can be sampled with a grid spacing that is only one quarter of the desired wavelength. A simulation at the practical sampling limit, using a wavelength of 1.0 \AA is shown in figure 4.4.11 as indicated by the yellow curve. At glancing angles there is a better agreement to the experimental fits for this sawtooth model exhibiting a linear density gradient that is 8.27 \AA thick; however, the fit is not perfect due to the finite sampling rate. Other simulations also conducted with larger wavelengths show the gradual movement towards higher yields at glancing incidence angles. These alternative simulations are not shown on the plot in order to enhance readability; however, they would appear between the green and yellow curves if shown.

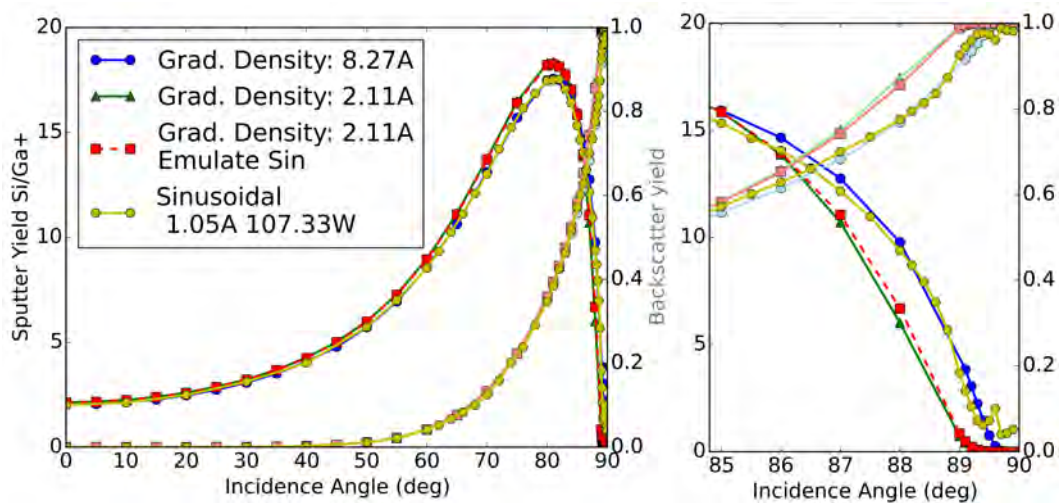


Figure 4.4.10 – The sensitivity of the density gradient model to the actual density distribution is shown by the red curve as compared to previously shown models for a linear density gradient and the sinusoidal surface best fit. The density profile of the red curve is not linear as with the blue and green data, it is instead simulated using an arcsine model which directly corresponds to the density distribution of the sinusoidal model. The thickness of the layer is chosen to correspond to the thickness of the sinusoidal rough layer shown in yellow.

Data shown in figure 4.4.10 and figure 4.4.11 imply that it would be possible to reduce the two-dimensional sinusoidal model to completely match the one-dimensional density-gradient model in the limit of infinitely small frequency. With respect to the relative validity of the two models and with respect to reality, the one-dimensional model appears to be the most plausible due to there being no requirement for spontaneously formed order. Furthermore, the best fit for the sinusoidal model has a wavelength that is a significant fraction of the projected range of gallium ions in silicon (107 \AA versus 300 \AA), and while it is a functional approximation that can be used to produce yield data fitting the experimental data it is a model fit to the data with two free parameters. As mentioned in section 4.4.2.2, the only real option to characterize the surface roughness and determine an accurate model is to perform MD simulations and grow rough surfaces that can be statistically analyzed. The existence of a mapping, however limited, between the sinusoidal model and the density-gradient

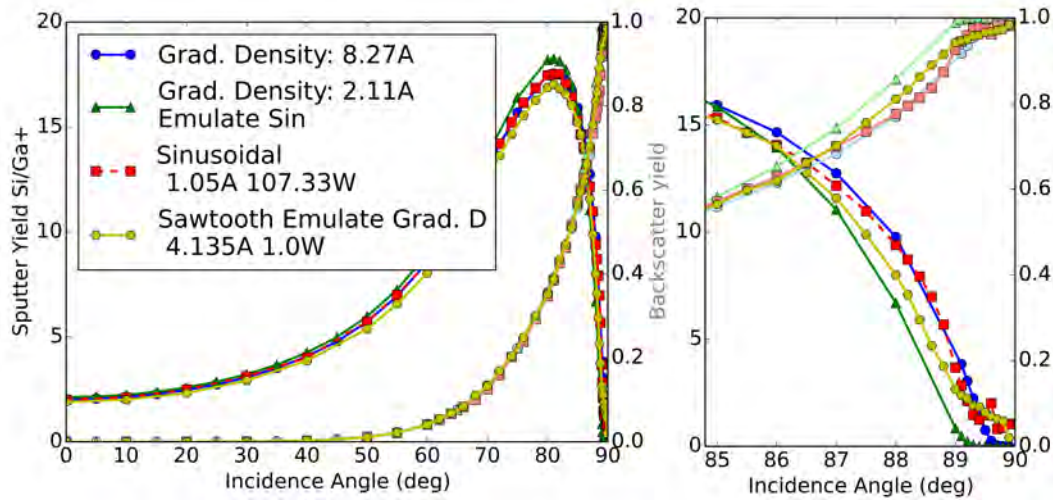


Figure 4.4.11 – The yellow curve shows simulated yields for a surface roughness simulation that attempts to emulate the gradient density model. This simulation is the practical limit of the 2D roughness model due to memory constraints and implements a sawtooth function with the minimum simulate-able wavelength of 1.0 Å necessitating an decrease in the lateral simulation grid to 0.25 Å. Lower sampling frequencies (not shown) lead to intermediate yield values between the green and yellow curves at glancing incidence angles.

model shows that the BCA simulations used in this work are self-consistent with respect to the effects of simulated roughness, thus supporting arguments for the inclusion of surface roughness through some means in sputtering simulations.

4.5 Influence of Surface Roughness on the Sputtering Angular Distribution

Surface roughness effects are not limited to the first-order statistical property of sputtering and backscattering yields, they also affect the angular distributions of the sputtered atoms. This is one area where further work to validate the choice of surface roughness model is direly needed, as the error-bars of experimentally determined sputtering angular distributions are quite sizable and dwarf the differences apparent between models. Experimentally, sputtering angular distributions are usually measured through the use of a hemispherical or half-cylindrical collection target into which an aperture has been cut [198]. The beam is fired through the aperture onto the target substrate for which angular distributions are to be collected and sputtered target atoms are embedded into the collection target with relative frequency determined by the sputtering angular distribution. The collection target is then analyzed by a spatial detection technique (often auger electron microprobe) which yields the amount of redeposition as a function of ejection angle [198]. This redeposition dose is integrated and normalized with the initial exciting ion dose. These experiments are difficult to perform

because the experimentalist must balance the detection thresholds of the technique with the depth detection limits, thereby optimizing the expected deposition thickness so as to avoid truncating the detection signal while still providing a sufficient number of the target species to be detectable. The experiment is further limited by the shadowing of glancing ejection angles as a crater is formed. For these reasons it is quite desirable to obtain the angular distributions used as simulation inputs from BCA simulations; however, at the same time, as shown in figure 4.5.1, figure 4.5.2, and figure 4.5.3, the choice of surface roughness model impacts simulated angular distributions.

At normal incidence angles, near perpendicular, the effects of surface roughness can already be seen, as shown in figure 4.5.1 for an incidence angle θ of 0° . Simulated angular distributions diverge from the cosine approximation and exhibit greater emission in all cases along less glancing ejection angles. The greatest amount of deviation is seen in the flat surface simulation neglecting surface roughness (shown in green), is believed that the greater relative probability of ejection at non-glancing angles is due to the atomically flat dense amorphous surface that acts to restrict possible ejection paths parallel to the simulated target surface. Conceptually this can be visualized by imagining a dense ordered crystal with an atomically flat surface; to eject a single atom from the crystal there must exist an exit path with respect to the neighboring atoms. In the limit of an infinitely dense hard sphere model where each atom is directly adjacent to its neighbors, one would expect that ejection paths near normal could exist. In the case of the simulated flat surface though, there are inter-atomic distances and a statistical function that describes the probability that a neighboring atom will be found within that atomic distance as the simulated flat surface is amorphous and not crystalline and at a finite temperature leading to variation in the atomic positions. As the rough surface models both work to reduce the simulated density over the target-vacuum interface, it is unsurprising that the best fit parameters for the density gradient and sinusoidal roughness models exhibit a lesser deviation from the cosine approximation, as the reduced density effectively opens ejection paths. The sinusoidal approximation for surface roughness acts as an intermediate between the flat surface and the gradient density model because any portion of the simulated surface described by the polygon is in fact a flat surface, the imparted geometry, however, provides opportunities for greater glancing-angle ejection (e.g. at the peak of a sign wave). The statistically defined density gradient exhibits a diffuse interface and provides a spatially independent opportunity for recoils to find a free path to glancing-angle ejection, counter to both the flat and sinusoidal simulations. The differences in near-glancing angle emission are shown with great clarity in figure 4.5.2, which shows only the glancing-angle portion of the polar plot of angular distributions shown in figure 4.5.1.

An additional effect of surface roughness on the angular distribution is seen for more glancing incidence angles as shown in figure 4.5.3 for an incidence angle θ of 80° , where the glancing ejection

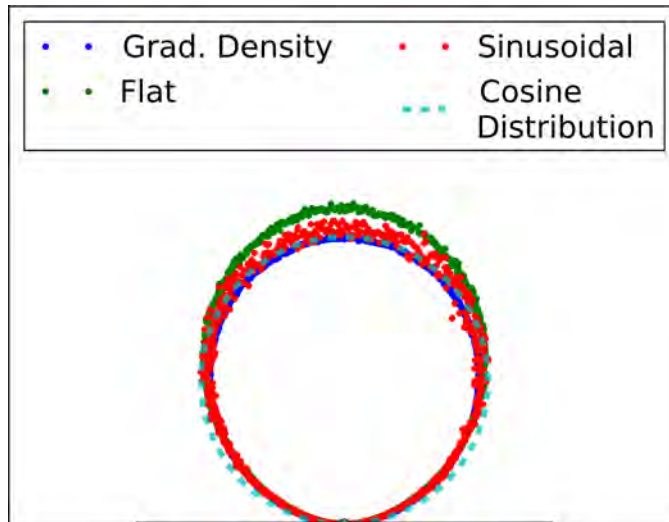


Figure 4.5.1 – A polar plot comparing the sputtering angular distributions at an incidence angle of 0° between different roughness models and a simulated surface not including surface roughness.

angles are not strongly affected; however, the behavior along the peak ejection probability changes between models. In figure 4.5.3 the first-knock-on peak is clearly visible in all three simulations; however, the intensity of this first-knock-on peak is most emphasized in the simulations including surface roughness. In fact the flat surface simulation has a higher probability of ejecting a particle for angles around the maximum of the first-knock-on peak, diffusing that emission over a greater range of polar angles. As the polar plot is not easily integrate-able by eye, the effect of the diffused emission is accentuated near normal ejection angles. The first-knock-on events usually occur near the target vacuum interface, as those are the target atoms that the ion encounters first. In the surface roughness models, the diffuse interface provides further opportunities for those atoms displaced by first-knock-on events (the term is used rather loosely here to describe early events in the collision cascade, not just those with order one) to result in sputtering. These early ejections emerge more along a vector rotated 90° from the ions trajectory. Due to the greater freedom with respect to the choice of valid ejection paths, the first-knock-on peak is highly accentuated when a diffuse interface (such as those caused by surface roughness) is used in the simulation. Particles involved in early collision events have greater opportunity to leave the target before interacting with other particles in the diffuse interface simulations due to the reduction in the density of interaction partners. Conversely, higher order collisions, which are more probable in the dense substrate lead to diffusion of the ejection vector as seen in the flat simulations. The low density region caused by the simulation of surface roughness affords an increased range of available exit angles. A linear plot of the normalized angular distribution for simulated flat and rough surfaces is shown in figure 4.5.4 where the area under the probability distribution curve shows the expected behavior, the data presented in figure 4.5.4 is the

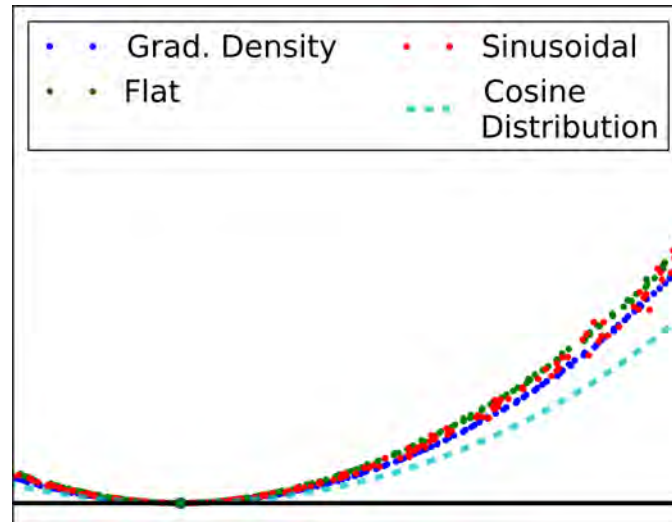


Figure 4.5.2 – A polar plot comparing the sputtering angular distributions at an incidence angle of 0° between different roughness models and a simulated surface not including surface roughness, shown magnified for ejection angles nearly parallel to the surface. Please note that the rough surface models better match the simple cosine behavior at grazing ejection angles.

same as in figure 4.5.3, only the plotting presentation has changed. In chapter 5 it will also be shown that there exist energetic differences among those atoms ejected along the path of the first-knock-on peak, as one would expect if atoms leave the target with a minimal number of interactions.

4.6 Interpolability of Surface Roughness 30keV Ga on Si vs 5keV Ga on Si Density model

Up until this point the main consideration has been the precise fitting of simulation models to 30 keV gallium beams impinging on amorphous silicon targets. This focus is well justified as this energy is commonly found on commercial FIB equipment and represents a starting place for high precision BCA simulations of sputtering statistical properties. In the preceding sections it was demonstrated that while there exist many factors for optimization among the BCA simulations in this work, the greatest source for error and the most important optimization parameter is ensuring that adequate surface roughness is included in any simulations that might include glancing angle effects. The notable successes, namely the ability to apply two different models for surface roughness and reproduce the experimental behavior at glancing angles of incidence, bring to mind questions as to the extensibility and plausibility of the surface roughness requirements when bombardment energies other than 30 keV are used.

There are therefore two questions to be answered with respect to FIB radiation at different energies, first, is it possible to fit simulations to experimental data conducted at other energies, and

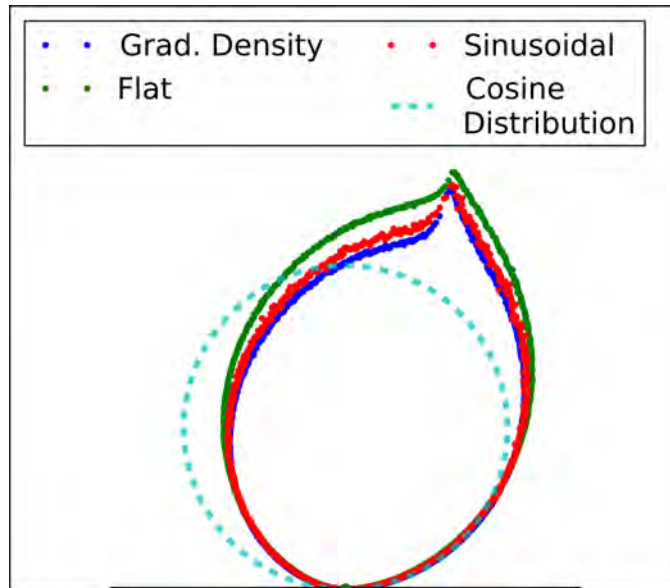


Figure 4.5.3 – A polar plot comparing the sputtering angular distributions between different roughness models and a simulated surface not including surface roughness at an incidence angle of 80° . Notice that the peak attributed to first knock-on interactions is more pronounced in the simulations including surface roughness.

secondly, does the available data and the results of the fits provide clues towards developing a simple model that can be used to predict the required rough interface for a given ion energy? To answer the first question, the reader is referred to figure 4.6.1, which shows a simulated yield curve as compared to experimental data [181] for 5 keV gallium on silicon. The simulation data shown uses a density gradient model with a layer thickness of 16.11 \AA , corresponding to a density gradient occurring over approximately 20 silicon mono-layers. This layer thickness was determined using the fitting procedure discussed in section 4.4.1.2, whereby an automated least-squares fitting procedure was conducted, comparing the simulated yield to the experimental yield at predetermined incidence angles with the optimization parameter specified as the thickness of the linear gradient-density layer. Though the fit is not perfect, it is a marked improvement over the simulation neglecting surface roughness and exhibits $>6x$ less variance as shown in figure 4.6.2.

The answer to the second question, as to whether these fits provide a hint as to a method by which to predict the required amount of surface roughness required in a simulation, is, with respect to the two experimental datasets, no. Conceptually it would be impossible to show with only two datasets that interpolation between the datasets is possible. If the thicknesses of the interface layers were similar, however, it would provide hope that the required interface layer thickness was not strongly dependent upon the energy of the impinging ion. The results shown, wherein the best fit for 5 keV is a 16.11 \AA thick layer and the best fit for 30 keV is a 8.27 \AA thick layer indicates that the thickness of the interface layer does change depending on the energy of the impinging ion. Furthermore,

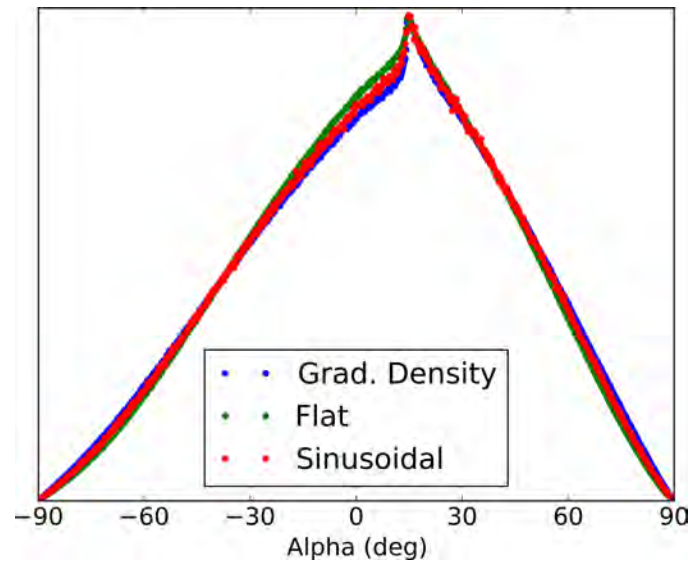


Figure 4.5.4 – A linear plot comparing the sputtering angular distributions between the different roughness models and a simulated surface not including surface roughness at an incidence angle of 80° . Notice that the apparent difference between the simulations is less pronounced in the linear plot than the polar plot shown in figure 4.5.3.

figure 4.6.2 shows the relative variances between the experimental data and various simulations including different layer thicknesses (where variance is defined in these plots as the sum of the squares of the errors at every simulated incidence angle between the experiment and simulation), which indicates that not only does the thickness of best fit change with bombardment energies, but the sensitivity of the fit also changes between bombardment energies. This extra degree of variability points to a non-linear dependence between the necessary thickness of the interface layer and the energy of the impinging ion.

This data must not be misconstrued; however, all that has been currently demonstrated is that the required layer thickness for a fit varies with energy (roughness is not constant), and that a linear approximation for that dependence does not pass through zero. Physically this is unsurprising, as clearly one would not reasonably expect zero roughness as bombardment energy approached zero. In this physical low energy regime, the effects of deposition itself would lead to roughness. In order to better understand the surface roughness dependence at different bombardment energies, two approaches exist. The straightforward approach would be to generate more experimental data for intermediate energies. This direct experimental approach would allow a semi-empirical rule to be derived that could be used to predict a required interface layer thickness. The alternative approach would be to use tools, such as MD, to actually simulate the roughening of the surface during bombardment. The advantage of this simulation approach is that the resulting simulation roughness could be better characterized; however, the question still remains of how to accurately compare simulated roughnesses with experimental roughnesses. Currently in this work it has been demonstrated that

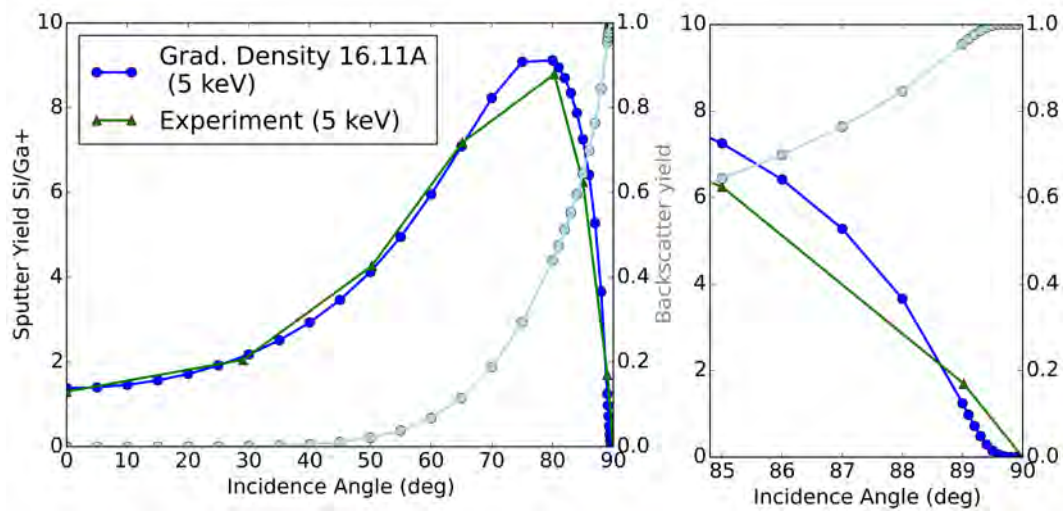


Figure 4.6.1 – Simulated yield for best fit parameters of a density-gradient model emulating surface roughness for 5 keV gallium impinging on silicon.

the procedure to fit interface layers using the density gradient model is still valid when applied other experimental datasets, though there remain numerous open questions as to predicting the amount of required surface roughness in lieu of actually performing additional experiments.

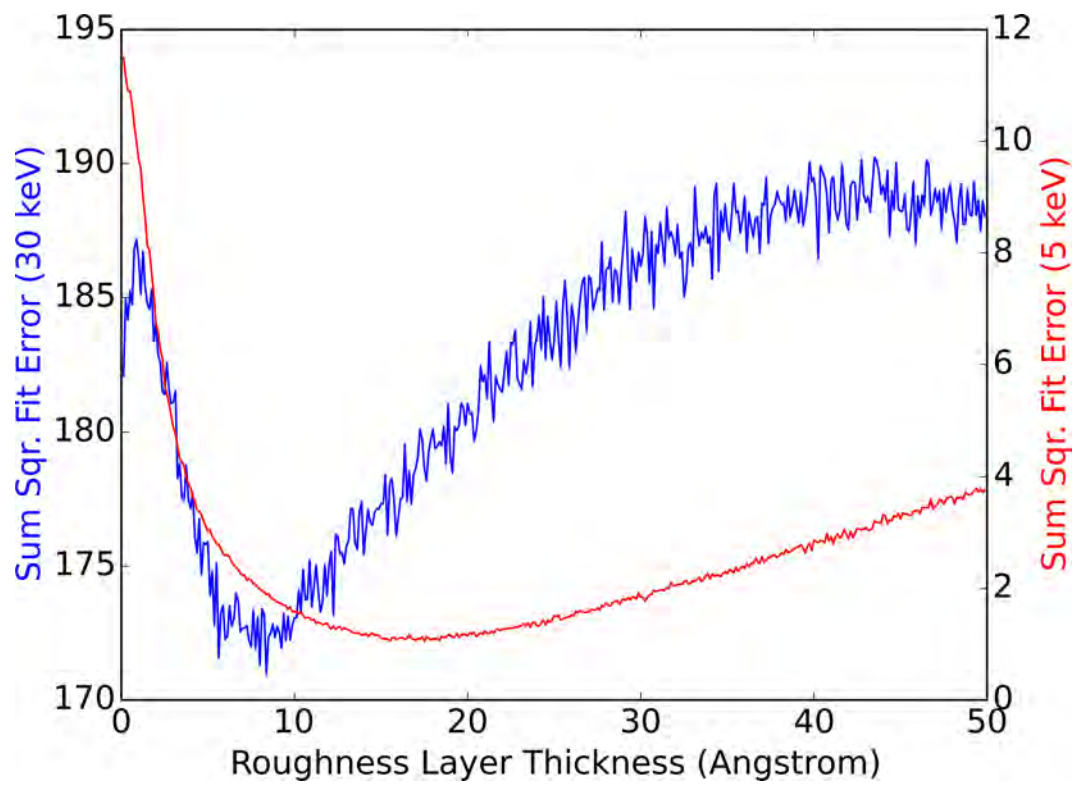


Figure 4.6.2 – The variance from the experimental data as a function of layer thickness. Variance here is defined as the sum of the square of the errors at the experimental data points. The 30 keV simulations are twitchier than the 5 keV simulations, in that the curvature of the minimum with respect to variance is high.

Chapter 5

Simulation Including Sputtering by Sputtered Target Atoms

In the two preceding chapters (chapter 3 and chapter 4) it was demonstrated that the presented model (chapter 2), which includes the effects of direct beam sputtering, redeposition of target atoms, additional sputtering due to backscattered ions, and redeposition resulting from backscatter-ion sputtering, is insufficient to describe the effects of milling with deep trenches even qualitatively (section §3.6); though good agreement was obtained for shallower structures (figure 3.5.1), it was also shown that the inclusion of a rough surface increases the relative magnitude of the first-knock-on peak in the sputtering angular distribution (section §4.5). The experimental evidence prompted the exploration of possible causes for the demonstrated increased sputtering occurring at the bottoms of trenches optimized to have steep and straight sidewalls. Two avenues of inquiry were investigated; the first being enhanced sputtering due to implanted gallium, the second being an additional source of sputtering due to secondary impacts by sputtered target atoms with high energy (referred to herein as reflexive sputtering). BCA dynamic simulations have indicated that there is indeed a preferential layer of gallium rich target material at the bottom of the trench [122] and implantation enhanced sputtering remains a promising research field. Initial estimates place the change in sputter depth due to implantation effects to be less than 10%. However, the enhanced first-knock-on peak shown for rough surfaces spurred further investigation into the angular distribution of sputtered ions as a function of ejection energy as obtained through BCA simulations using IMSIL. This investigation indicated a strong correlation between ejection angles near the first-knock-on peak and ejection energy. A non-trivial portion of these energetically sputtered target atoms possessed sufficient energy

to induce further sputtering (a sputtering yield greater than unity) with a direction vaguely* around the first-knock-on peak. This chapter describes the development and testing of an extended sputtering model that makes use of energy-resolved angular distributions for sputtering and backscattering of ions and target atoms in order to simulate the proposed phenomenon of reflexive sputtering occurring during FIB milling.

5.1 Motivation for Investigating a Reflexive Sputtering Model

The simple motivation for investigating reflexive sputtering is that the model presented in chapter 2 is insufficient to accurately model trenches with very steep sidewall angles. There exists, however, a plethora of alternative explanations for the experimental discrepancy seen in section §3.6 and some effort must be made to justify the overhead and the added complexity presented by using an energy-resolved reflexive sputtering model. In this section it will be demonstrated that the angular probability density of sputtered atoms is not uniform with respect to the ejection energy of said particles. Furthermore, it will be demonstrated that even though the total fraction of high energy sputtered particles is small, when combined with a sputtering yield greater than unity, these interactions should not be neglected. In section §5.3 a self-consistent model will be demonstrated, but this section will focus on back-of-the-envelope justifications for the developed model, including the effects of energy-resolved reflexive sputtering.

When a simulated ion impinges on the target surface, a recoil cascade occurs, which dissipates a portion of the ion's energy into the target through nuclear collisions and electronic stopping. These nuclear collisions create energetic recoils which go on to incite further nuclear collisions leading to the so-called recoil cascade. Sputtering in the simulation is defined as the phenomenon whereby energetic particles leave the bulk of the target and escape into vacuum after first surmounting the surface binding energy. Each of these recoils leading to sputtering, of course, has its own velocity and direction, which can be further characterized as a kinetic energy. Unsurprisingly, due to the statistical nature of the collision cascade, ejected particles leave the surface with a range of energies and directions. In chapter 2 the angular probability distribution (relating to the range of directions of ejected particles) was shown by figure 2.3.3; however, it was implicitly assumed that the energies of these sputtered atoms were low and indistinguishable. When studying the effects of rough surfaces on the angular distribution, as shown in section §4.5, it became clear that the higher energy first-knock-on peak was dependent on surface effects, which in turn prompted the study of energy-

*As the first-knock-on peak is not comprised solely of first generation impacts, there is a degree of peak broadening that occurs, as is shown later in figure 5.4.1.

resolved angular distributions. A typical sputtering angular distribution for an incidence angle of 80° is shown in figure 5.1.1; however, this angular distribution (equal to the gradient density model distribution shown in figure 4.5.3 when summed over all energies) shows normalized angular distributions for different ranges or bands of ejection energies. The simulation results shown in figure 5.1.1 are quite striking as they indicate a strong directed focusing effect in the distribution of ejection angles, which increases with increasing ejection energy. Through BCA simulations of silicon ions impinging on a silicon target, it is known that the non-negligible sputtering starts to occur for energies as low as 200 eV, and by 2000 eV, net sputtering can clearly be demonstrated for a range of incidence angles. These energy-resolved sputtering angular distributions indicate that there could be an additional source of sputtering caused by high energy sputtered particles in the real experiments; however, the question of the relative rarity of these high energy particles bears addressing.

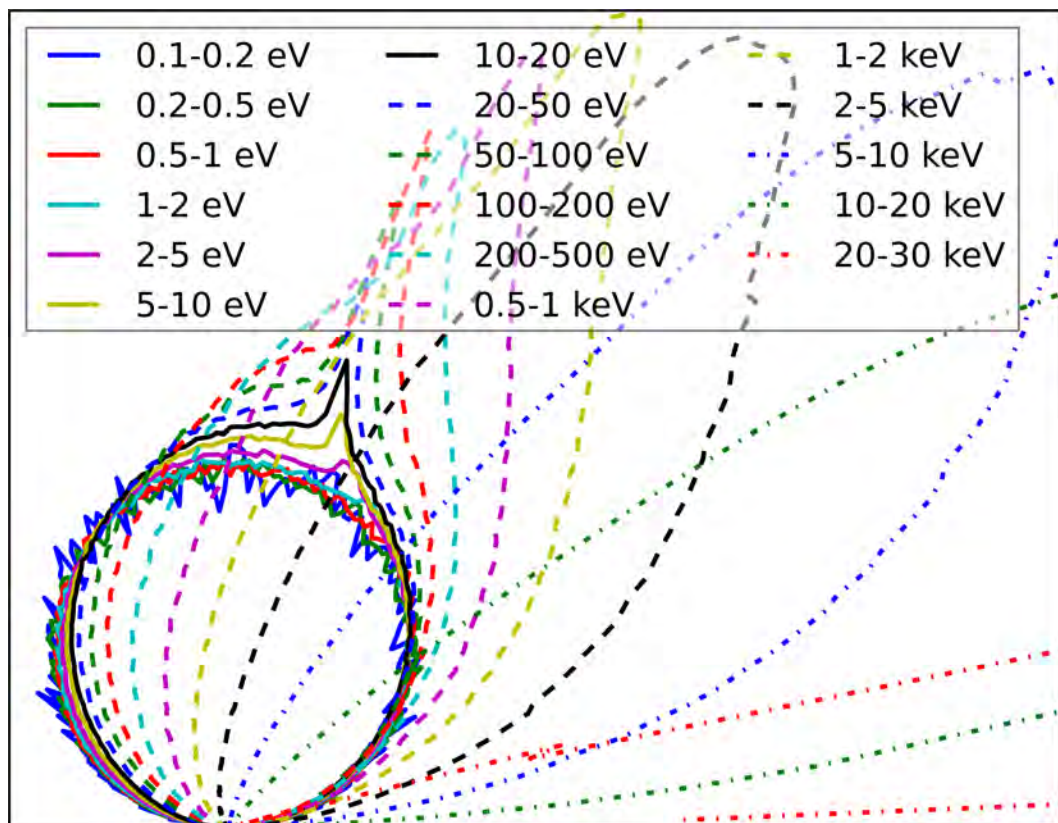


Figure 5.1.1 – A polar plot of the angular distribution of sputtered target atoms shown for different ejection energy bands at an incidence angle of 80° . Energy bands are shown normalized for clarity. Low energy (0.1-2.0 eV) sputtered atoms exhibit a nearly cosine angular probability distribution. As the ejection energy increases the angular distribution becomes more focused and trends towards more glancing ejection angles with respect to the surface normal. These sputtering simulations are conducted using the gradient density model for surface roughness.

A shortcoming of figure 5.1.1 is that the angular distributions for each energy band are shown normalized, leaving considerable uncertainty about the relative rarity of each band of ejection energies.

The fractional energy distributions for sputtered particles are shown in figure 5.1.2 (indicated by the blue curve), also for an incidence angle of 80° , in an attempt to address this shortcoming. The energy distribution of sputtered particles, as indicated by the blue line shown in figure 5.1.2, lends a degree of validity to the assumption made in chapter 2 that sputtered particles by and large contribute mostly to redeposition. This assumption is supported by the large number of sputtered particles emerging with between 1 and 20 eV of energy; furthermore, the green curve, showing the cumulative fraction of particles sputtered at energies greater than a given energy (simply a re-representation of the data shown in the blue curve), clearly indicates that greater than 50% of sputtered particles are sputtered with ≤ 20 eV of energy post-ejection. The red curve, plotting the maximum sputtering yield for silicon-silicon interactions[†], tells a different story. The total population of sputtered atoms with energy greater than 1000 eV is only on the order of 5%; however, the sputter yield is nearly four atoms per energetically sputtered target atom. This is further enhanced by the fact that when sputtering near the sputtering yield maximum, there are 18 target atoms (of varying energies) sputtered for each incident ion, of which 5% or ≈ 1 atom will have sufficient energy to lead to more sputtering. By these back-of-the-envelope calculations, it is clear that sputtering due to energetically sputtered target atoms (reflexive sputtering) could, in some circumstances, represent additional sputtering of similar magnitude to sputtering by backscattered ions. The existence of an unaccounted effect similar in magnitude to the backscattering flux, which was already shown in figure 2.4.1 to tangibly affect simulation results, provides the impetus for further investigation through the devise of a new model that includes the previously unaccounted for effect of reflexive sputtering. A model that can resolve such self-sputtering effects must carefully consider the energy distribution of the ejecta. Implementation of such an energy-resolved model also allows for an implementation of sputtering by backscattered ions that does not make use of the mono-energetic approximation discussed in section 2.1.3. In order to characterize the effect of reflexive sputtering, and furthermore of more accurate backscatter sputtering on topography simulations, it was necessary to extend the model shown in chapter 2 to adequately resolve energetic effects, as will be shown in section §5.3. Furthermore, simulations using an implementation of the extended model (described in section §5.4) were also completed and characterized, as will be shown in section §5.5, demonstrating that not only is this extended model plausible, but it is possible to use it in simulation.

[†]Maximum sputtering yield here refers to the maximum of the incidence angle dependent sputtering yield for a silicon atom energy. This represents the upper-bound for the amount of possible sputtering; however, as a back of the envelope proxy for more precise estimates, this upper-bound is sufficient.

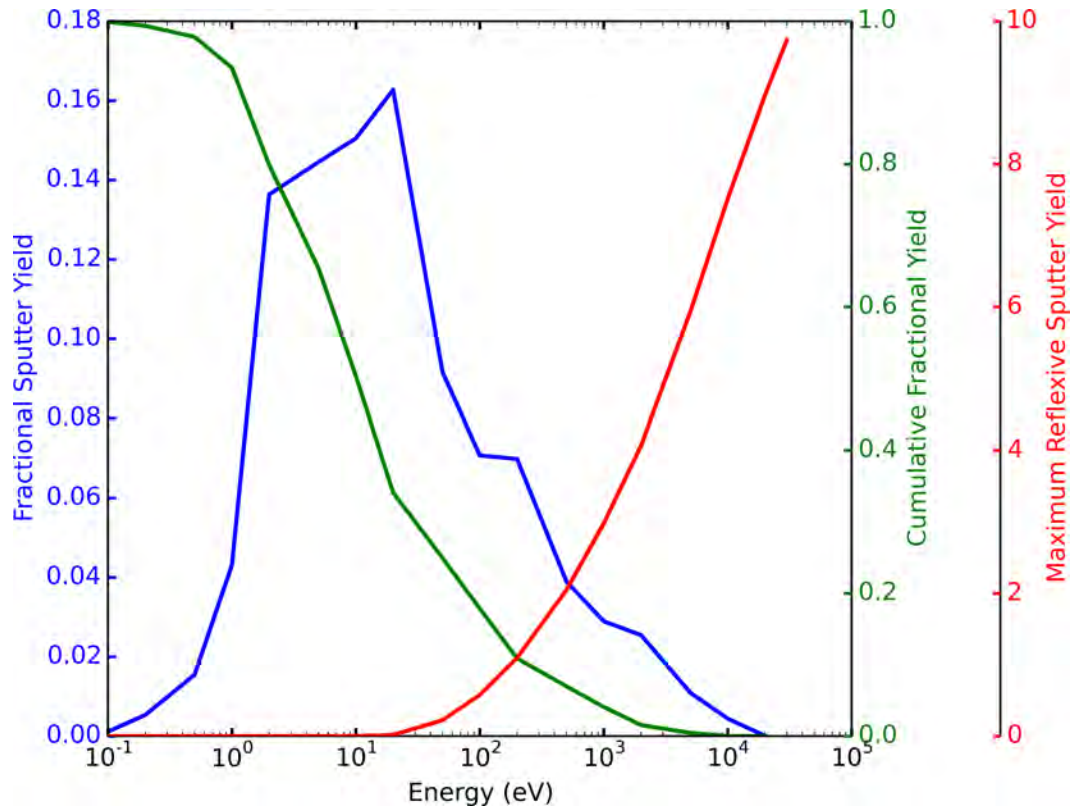


Figure 5.1.2 – The fractional sputter yield of ejected target atoms across different energy bands for an incidence angle of 80° is shown in blue; the majority of sputtered target atoms have an energy between 1 eV and 50 eV. The cumulative fractional yield is also shown indicating the fraction of sputtered atoms possessing an energy greater than the energy indicated by the X-coordinate of the plot shown in green indicating that approximately 5% of sputtered target atoms possess energies greater than 1 keV. The red curve indicates the maximum sputtering yield attainable if a target atom with the given energy were to re-intersect with the target. It can be seen that redeposition is canceled out (sputter yield > 1) for ejected particles with an energy greater than 200 eV.

5.2 Old Equations of Motion in New Nomenclature

The energy-resolved reflexive sputtering model presented in this chapter is significantly more complex than the simple model for sputtering and redeposition presented in chapter 2. In the model presented earlier it was convenient to use long form English names to refer to and define the various simulated fluxes; however, now that reflexive sputtering requires the simulation of two sputtering species, the nomenclature used in the previous chapters is too cumbersome to use to clearly express the new model presented in this chapter. Furthermore, the assumptions employed in between the model presented in chapter 2 and the model presented in this chapter change. The assumptions of the simple model were addressed in the text in chapter 2; however, to facilitate clarity, the assumptions for both models presented in this chapter (the reformulation of the model presented in chapter 2, and the new energy-resolved model) are stated both in tabulated and textual form. In this section the

reformulation of the simple model presented in chapter 2 is presented in the new nomenclature.

5.2.1 Sputtering Model Presented in the New Nomenclature

The simple model presented in chapter 2 makes the assumptions listed in table 5.2.1. The first assumption is that the system can be modeled using only 3 levels of flux evaluation making it a third order simulation (with orders being referred to as zeroth, first, and second order as the primary beam interaction is considered to be a trivial zeroth-order effect)*. While it is possible to formulate the model for arbitrarily high orders of simulation, the source term for the second order redeposition of target atoms by backscattered ions is based on the assumption that the energy loss to backscattered ions is negligible. As there are indubitably unconsidered energy losses experienced by the backscattered ions, coupled with the trench geometries usually studied (backscatter yields are only non-negligible for glancing incidence angles which occur at sidewalls in trenches, of which there are normally only two) drive the choice to limit simulation complexity to three orders. Furthermore, each additional order of complexity adds the cube of the number of nodes worth of computational effort $O(n^3)$, as each node acts as both an emitter and a sink for flux and emissions at the emitter depend upon the incidence angles of the fluxes entering the emitter, thereby requiring a triple loop[†] over all nodes. The beam used in these simulations is assumed to be monochromatic and to have a Gaussian spatial dose distribution. Additionally, in the simple simulation, dynamic implantation effects are neglected. The sputtering yields used in the simulation (garnered from BCA simulations) are matched to the steady-state sputtering rates obtained from experiments [179, 181] at normal incidence which physically contain a small amount of implanted gallium. Neglecting this gallium was shown in section 4.3.1 to be of arguably small importance. As the composition of the target is static, the zeroth-order sputtering effects of sputtering yield and backscattered ion yield are assumed to strictly depend on the incidence angle between the beam and the receiving node.

First-order redeposition (caused by zeroth-order sputtering[‡]), being those target atoms that were sputtered by the primary beam ions and subsequently redeposited, is assumed in the simple model to lead strictly to sticking. Practically, this assumption means that the fraction of sputtered atoms with ejection energies greater than 2 eV are negligible. These assumed low-energy target atoms

*Arguably the simulation could be said to be only 2.5 orders, as the final level of simulation the redeposition flux resulting from secondary sputtering by backscattered ions is modeled using a simple cosine rule.

[†]A loop over all destinations, sources, and sources of the sources. This $O(n^3)$ behavior is better than the naive recursive formulation which is $O(n^k)$ complex where k is the number of simulated orders of complexity.

[‡]In table 5.2.1 redeposition is listed as a first order term shared with zeroth-order sputtering, this is due to the two different viewpoints available. Zeroth-order sputtering leads to depletion of material at the zeroth-order node, making it a clear zeroth order effect; however if the flux of zeroth-order sputtered target atoms re-impinges with the target, it will result in additional material being added at a first-order node. Furthermore, in chapter 2 redeposition was treated as a first-class concept thus both terms are used.

are sputtered by the incident ion beam and travel along the paths dictated by the angular sputtering distribution of sputtered ions until they either encounter another surface in the simulation or are lost to the vacuum chamber. If this low-energy assumption is made, then the additional assumption that these freed target atoms simply stick with 100% efficiency to whatever they encounter is plausible. However, the assumption of wholly low-energy emission of sputtered particles is brought into question by the energy distributions shown in figure 5.1.2, which is, of course, the eventual topic of this chapter. These redeposited target atoms are strictly of the target species (in this example silicon) in these simulations, as there is no effort made to keep track of the gallium in the target. Furthermore, this simplification prevents the proper simulation of multi-component targets (for instance layered structures) because volumetric material domains may exist in the simulation, but no model exists to simulate the effects of intermixing driven by redeposition. On the same order as redeposition, one also finds the antagonistic process of sputtering due to backscattered ions. In the simple model, energy loss of backscattered ions is assumed to be negligible and therefore zero. As with redeposition of target atoms, there is no facility in the simple model to accommodate the subsequent implantation of backscattered ions when they re-impinge with the target. The sticking factor of these backscattered ions is therefore zero, after they have lead to sputtering, indicating that they are removed from the simulation.

Finally, in the second order of the simulation, the target atoms that have been sputtered by the backscattered ions go on to be redeposited in the simulation. This redeposition of the backscattered ion sputter flux occurs using the scaled cosine approximation that was discussed in section 2.1.4. The cosine approximation is used for efficiency, as it avoids a complete triple loop in the last order. Furthermore, the approximation is plausible as the geometries of trenches indicate that most sputtering by backscattered ions occurs with incidence angles that are nearly normal to the target. For near-normal incidence angles, it was demonstrated in figure 2.3.3 that a cosine approximation is in good agreement with the simulated angular distribution from BCA.

The goal of the new nomenclature presented in this chapter is to compactly show both the order of a simulated effect as well as the species involved. To that end, general forms of the fluxes and node velocities (for the simple model[§]) which are valid for any order of complexity are shown in equation (5.2.1), equation (5.2.2), and equation (5.2.3). The three orders of complexity presented in this work are shown in figure 5.2.1 as a schematic diagram demonstrating the coordinate system for zeroth, first, and second-order effects. Through the manipulation of these equations, starting with the zeroth order of complexity, it is possible to derive the complete set of equations that were presented

[§]Simplified general equations are presented containing only terms that will eventually be useful. As will be seen in the models presented later, the addition of either different species or different energies causes the equations to quickly balloon in size and complexity.

Property:	Assumption:
Order of Simulation	3
(0 th order) Beam Energy	30 keV (monochromatic)
(0 th order) Target Composition	Si (static composition)
(0 th order) Beam Shape	Gaussian, Error Function, or Superposition of Gaussians (Overlapped beam)
(0 th order) Sputtering Yield	Dependent on Local Incidence Angle θ
(0 th order) Backscattering Yield	Dependent on Local Incidence Angle θ
(0 th order) Sputtered Atom Energy (1 st order) Redeposition Energy	0-2 eV (sticking only)
(0 th order) Sputtered Atom Composition (1 st order) Redeposition Composition	Si
(0 th order) Sputtered Atom Shape (1 st order) Redeposition Shape	Angular Distribution from BCA
(1 st order) Sticking Coefficient	1
(1 st order) Backscattering Energy	30 keV (monochromatic)
(1 st order) Backscattering Composition	Ga
(1 st order) Backscattering Shape	Angular Distribution from BCA
(1 st order) Backscattering Sticking Coefficient	0
(1 st order) Backscatter Sputtering Yield	Dependent on Local Incidence Angle θ and Backscatter Flux
(1 st order) Sputtered Atom Energy (2 nd order) Redeposition Energy	0-2eV (sticking only)
(1 st order) Sputtered Atom Composition (2 nd order) Redeposition Composition	Si
(1 st order) Sputtered Atom Shape (2 nd order) Redeposition Shape	Scaled Cosine
(2 nd order) Sticking Coefficient	1

Table 5.2.1 – Assumptions made in the simple model presented first in chapter 2.

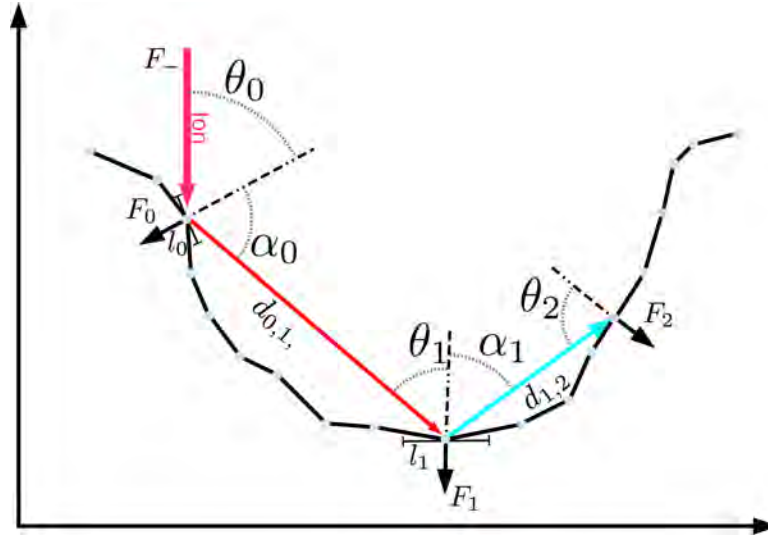


Figure 5.2.1 – A sketch demonstrating the coordinate system used in the new nomenclature. The angle of incidence between incoming fluxes is indicated by θ_i , while the ejection angles of outgoing fluxes from a node are indicated by α_i . By convention, the initial beam flux is defined to be zeroth order, $i = 0$.

in chapter 2. This derivation will be shown after a moment is taken to explain the conventions of the nomenclature. Fluxes in this nomenclature are indicated by a capital F and are differentiated at any order of complexity by the species of atom that they track; in the case of equation (5.2.1), $F_{Ga, i \leftarrow i-1}$ is the flux of gallium (as indicated by the subscript Ga) arriving at the node from an $i-1^{\text{th}}$ order node for an i^{th} order interaction, transformed to be normal to the surface at the node. $F_{Ga, i \leftarrow i-1}$ is dependent on the incidence angle θ_i between the evaluated node and the source node and the ejection angle to the i^{th} order node from the $i-1^{\text{th}}$ source node as indicated by α_{i-1} . These angles are defined by the geometric locations of the i^{th} and $i-1^{\text{th}}$ nodes used in the simulation[¶]. On the right hand side of equation (5.2.1) it can be seen that the flux arriving at the i^{th} node is proportional to the flux coming from the $i-1^{\text{th}}$ node, as indicated by the inclusion of the previous ordered flux of gallium $F_{Ga, i-1 \leftarrow i-2}$, this ($i-1^{\text{th}}$) incoming flux is itself dependent upon the flux coming from the $i-2^{\text{nd}}$ order node (as indicated by the summation over all $i-2^{\text{nd}}$ source nodes), which is multiplied by the backscatter yield of the previous ($i-1^{\text{th}}$) order node $Y_{back, Ga|Ga}(\theta_{i-1})$ and the backscatter angular distribution at that node $f_{back, Ga|Ga}(\alpha_{i-1}, \theta_{i-1})$. Where capital Y indicates a sputtering or backscattering yield (the type of yield is indicated by subscript), and a lowercase f indicates an angular distribution of either a sputtered or backscattered species. The subscript separated by a vertical bar shown in both the yield and angular distribution quantities indicates the relevant interaction pair with the shown example $Ga|Ga$ indicating that the quantity concerns the amount of gallium excited by gallium, consequently the quantity $Y_{sput, Si|Ga}(\theta_{i-1})$ shown in equation (5.2.2) indicates the amount of silicon sputtered

[¶]Furthermore, relative incidence angles θ_i between any two nodes are geometrically defined and do not change between orders except in the special case of the incidence beam flux $F_{Ga, -}$ where the incidence angle is defined as the angle between the surface-normal at the node and the beam angle θ_0 .

by gallium. This example equation is ended by the geometric projection factor $\frac{l_{i-1}}{d_{i-1,i}} \cos \theta_i$ which compensates for the projection and the spreading of the flux over the solid angle between the $i - 1^{\text{th}}$ source and the current i^{th} order destination node. The geometric projection factor is comprised of the length segment of the source l_{i-1} , the distance between the source and the evaluated destination node $d_{i-1,i}$. The node velocity^{||} due to i^{th} order effects is presented in equation (5.2.3) where it can be seen that the i^{th} order velocity only depends on i^{th} order fluxes (which depend on the previous order flux terms). As with the equations presented in chapter 2 it is necessary to sum over all visible source nodes in order to know the velocity of a given destination node. This is handled in equation (5.2.3) by the summation of fluxes over the visible $i - 1^{\text{th}}$ order source nodes as indicated by the term $\sum_{\text{visible}_{i-1}}$. The remaining term is atomic volume of silicon v_{Si} (the reciprocal of the atomic density of silicon), which is used to convert the flux into a volumetric change at the node, which leads to the node velocity. The silicon term of the node velocity is equal to the sum of the incoming silicon fluxes times unity, as this model assumes that redeposition occurs with a sticking coefficient of 1, as this term is positive it indicates redeposition; while the gallium driven term above it is negative to indicate sputtering.

Note that the flux impinging on any i^{th} order destination node depends on the total flux impinging on $i - 1^{\text{th}}$ order source nodes from all of its visible source nodes.

$$F_{Ga, i \leftarrow i-1} = \left\{ \sum_{\text{visible}_{i-2}} F_{Ga, i-1 \leftarrow i-2} \cdot \begin{bmatrix} Y_{\text{back}, Ga|Ga}(\theta_{i-1}) \cdot \\ f_{\text{back}, Ga|Ga}(\alpha_{i-1}, \theta_{i-1}) \end{bmatrix} \right\} \cdot \frac{l_{i-1}}{d_{i-1,i}} \cos \theta_i \quad (5.2.1)$$

$$F_{Si, i \leftarrow i-1} = \left\{ \sum_{\text{visible}_{i-2}} F_{Ga, i-1 \leftarrow i-2} \cdot \begin{bmatrix} Y_{\text{sput}, Si|Ga}(\theta_{i-1}) \cdot \\ f_{\text{sput}, Si|Ga}(\alpha_{i-1}, \theta_{i-1}) \end{bmatrix} \right\} \cdot \frac{l_{i-1}}{d_{i-1,i}} \cos \theta_i \quad (5.2.2)$$

$$V_i(\theta_i, F_{Ga, i \leftarrow i-1}, F_{Si, i \leftarrow i-1}) = v_{Si} \cdot \begin{bmatrix} \sum_{\text{visible}_{i-1}} F_{Ga, i \leftarrow i-1} \cdot [-Y_{\text{sput}, Si|Ga}(\theta_i)] + \\ \sum_{\text{visible}_{i-1}} F_{Si, i \leftarrow i-1} \cdot [(1)] \end{bmatrix} \quad (5.2.3)$$

In order to transform these equations into the set of equations presented in chapter 2, one starts with the assumptions. The initial assumption was that a pure gallium beam is the sole excitation in the

^{||}The node velocity is really the only equation of motion, as it is the only term that dictates motion; however, without evaluation of the fluxes the node velocity would be useless, therefore the set is presented as the equations of motion.

system; therefore, the zeroth-order flux for silicon is zero, leading to $F_{Si,0} = \{0\}$, and the zeroth-order flux of gallium is strictly determined by the beam yielding $F_{Ga,0} = \{F_{Ga,-}\} \cdot \cos \theta_0$, the summation is neglected as the beam flux is independent of the geometry outside of the precisely defined incidence angle θ_0 . Substitution into equation (5.2.3) yields equation (5.2.4), where the summation over visible source nodes is neglected due to the only flux source being the beam. Moving on to the first-order, the gallium flux $F_{Ga,1\leftarrow 0}$ becomes as shown in equation (5.2.5), this quantity was known in chapter 2 as the flux of backscattered ions (equation (2.1.3)), the lack of a meaningful set of $i - 2^{\text{nd}}$ order source nodes the summation to be dropped**. What was known as the redeposition flux (equation (2.1.2)) in chapter 2 is now indicated by the first-order flux of silicon atoms $F_{Si,1\leftarrow 0}$ which are wholly generated in this simple model from interactions between the beam ions and the target as shown in equation (5.2.6). The first-order velocity shown in equation (5.2.7) is comprised of the flux of backscattered atoms and the redeposition flux. As the sticking coefficient for redeposition is unity, the bottom silicon term is precisely the redeposition flux from chapter 2. Multiplication of the first order gallium flux $F_{Ga,1\leftarrow 0}$ times the sputtering yield of silicon by gallium $Y_{sput,Si|Ga}(\theta_1)$ yields the term referred to in chapter 2 as the silicon sputtering flux due to backscattered ions (shown here in the top half of equation (5.2.7)), as shown in equation (2.1.4). As there are now source nodes in the first-order node velocity $V_1(\theta_1, F_{Ga,1\leftarrow 0}, F_{Si,1\leftarrow 0})$, the summation over the visible sources cannot be neglected as it could be in the zeroth-order node velocity equation.

$$V_0(\theta_0, F_{Ga,0}, F_{Si,0}) = -v_{Si} \cdot [F_{Ga,-} \cdot Y_{sput,Si|Ga}(\theta_i) \cdot \cos \theta_0] \quad (5.2.4)$$

$$F_{Ga,1\leftarrow 0} = \left\{ F_{Ga,0} \cdot \left[Y_{back,Ga|Ga}(\theta_0) \cdot f_{back,Ga|Ga}(\alpha_0, \theta_0) \right] \right\} \cdot \frac{l_0}{d_{0,1}} \cos \theta_1 \quad (5.2.5)$$

$$F_{Si,1\leftarrow 0} = \left\{ F_{Ga,0} \cdot [Y_{sput,Si|Ga}(\theta_0) \cdot f_{sput,Si|Ga}(\alpha_0, \theta_0)] \right\} \cdot \frac{l_0}{d_{0,1}} \cos \theta_1 \quad (5.2.6)$$

$$V_1(\theta_1, F_{Ga,1\leftarrow 0}, F_{Si,1\leftarrow 0}) = v_{Si} \cdot \left[\begin{array}{c} \sum_{visible_0} F_{Ga,1\leftarrow 0} \cdot [-Y_{sput,Si|Ga}(\theta_1)] + \\ \sum_{visible_0} F_{Si,1\leftarrow 0} \cdot [(1)] \end{array} \right] \quad (5.2.7)$$

The second-order equations are once again a special case and make use of the initial assump-

**The independence of the beam flux on source incidence angles means that the summation of all considered gallium fluxes are degenerate. The summations shown in equation (5.2.1) and equation (5.2.2) are only meaningful for order greater than 1. As gallium fluxes are removed from the simulation after order 1, the summation may be neglected for all gallium cases.

tions stated at the beginning of this section. The second-order gallium flux $F_{Ga, 2\leftarrow 1}$ is taken to be zero due to the assumption that backscattered ions make only one hop and do not experience multiple backscatter events yielding equation (5.2.8). In the second-order silicon flux equation $F_{Si, 2\leftarrow 1}$, the angular distribution of sputtered atoms $f_{sput, Si|Ga}(\alpha_{i-1}, \theta_{i-1})$ has been replaced by the cosine approximation $c_1 \cdot \cos^n(\alpha_1)$ as the simple model estimates the second-order redeposition distribution using a cosine approximation, as indicated in table 5.2.1. The second-order flux of silicon atoms at a given second-order node (equation (5.2.9)) is the sum of all gallium backscatter ions that arrived at the first-order source node times their sputtering yields and distributed by the cosine approximation. The cosine approximation saves computation as it allows the reuse of the quantity $\sum_{visible_0} F_{Ga, 1\leftarrow 0} \cdot [Y_{sput, Si|Ga}(\theta_1)]$, which was calculated earlier in the top part of 5.2.7. As the second-order gallium flux is zero, the node velocity is simple to calculate and is simply the sum over all the source destinations for the second order silicon flux multiplied by the reciprocal of the density, as shown in equation (5.2.10). Summing up every order's contribution to the node velocities yields precisely the same equation presented in section 2.1.5 of chapter 2.

$$F_{Ga, 2\leftarrow 1} = \{0\} \quad (5.2.8)$$

$$F_{Si, 2\leftarrow 1} = \left\{ \sum_{visible_0} F_{Ga, 1\leftarrow 0} \cdot [Y_{sput, Si|Ga}(\theta_1)] \right\} \cdot c_1 \cdot \cos^n(\alpha_1) \cdot \frac{l_0}{d_{0,1}} \cos \theta_2 \quad (5.2.9)$$

$$V_2(\theta_2, F_{Si, 2\leftarrow 1}) = v_{Si} \cdot \left[\begin{array}{c} \{0\} + \\ \sum_{visible_1} F_{Si, 2\leftarrow 1} \cdot [(1)] \end{array} \right] \quad (5.2.10)$$

††

A summary of the new notation for the equations of the simple model is shown in table 5.2.2, which is re-expressed to facilitate comparison with the energy-resolved model presented later.

††In the second-order node velocity equation (5.2.10) term the summation over visible nodes $\sum_{visible_1}$ is written with separate limits of summation than was presented in the first-order node velocity equation (5.2.7), where $\sum_{visible_0}$ was used. This distinction is made purely for notational clarity, as the nodes do not move between evaluations of the different order fluxes; the limits therefore are the same and $visible_0 = visible_1$ as far as the limits are concerned. Clearly the argument of the summations are different, leading to different evaluations of the velocity due to the respective fluxes.

Equation of Motion		
$F_{Si,0} = \{0\}$		
$F_{Ga,0} = \{F_{Ga,-}\} \cdot \cos \theta_0$		
$V_0(\theta_0, F_{Ga,0}) = F_{Ga,0} \cdot [-v_{Si} \cdot Y_{sput, Si Ga}(\theta_0)]$		
$F_{Ga,1\leftarrow 0} = \{F_{Ga,0} \cdot [Y_{back, Ga Ga}(\theta_0) \cdot f_{back, Ga Ga}(\alpha_0, \theta_0)]\} \cdot \frac{l_0}{d_{0,1}} \cos \theta_1$	5.2.5	
$F_{Si,1\leftarrow 0} = \{F_{Ga,0} \cdot [Y_{sput, Si Ga}(\theta_0) \cdot f_{sput, Si Ga}(\alpha_0, \theta_0)]\} \cdot \frac{l_0}{d_{0,1}} \cos \theta_1$	5.2.6	
$V_1(\theta_1, F_{Ga,1\leftarrow 0}, F_{Si,1\leftarrow 0}) = v_{Si} \cdot \left[\sum_{visible_0} F_{Ga,1\leftarrow 0} \cdot [-Y_{sput, Si Ga}(\theta_1)] + \sum_{visible_0} F_{Si,1\leftarrow 0} \cdot [(1)] \right]$	5.2.7	
$F_{Ga,2\leftarrow 1} = \{0\}$		5.2.8
$F_{Si,2\leftarrow 1} = \sum_{visible_0} \{F_{Ga,1\leftarrow 0} \cdot [Y_{sput, Si Ga}(\theta_1) \cdot c_1 \cdot \cos^n(\alpha_1)]\} \cdot \frac{l_0}{d_{0,1}} \cos \theta_2$	5.2.9	
$V_2(\theta_2, F_{Si,2\leftarrow 1}) = v_{Si} \cdot \left[\sum_{visible_1} F_{Si,2\leftarrow 1} \cdot [(1)] \right]$	5.2.10	

Table 5.2.2 – The complete equations of motion for the simple model, re-presented for clarity.

5.3 Equations of Motion for Sputtering Simulations Including Reflexive Sputtering

Consideration of reflexive sputtering by previously sputtered silicon atoms requires knowledge of the energies of the particles that will incite sputtering (discussed and shown in section 5.4.4, previewed in figure 5.1.2), in order to determine the number of particles that are sputtered. Furthermore, as was shown in figure 5.1.1, the angular distribution varies with respect to the ejection energy of ejected particles—for both backscattered primary ions and sputtered target atoms, as will be discussed in section 5.4.2 and section 5.4.1. Additionally, and quite intuitively, the sputter rates of these particles of different species and energy vary strongly with the energy of the sputtering particle, as discussed and shown in section 5.4.3. It is therefore essential that the energies of ejected particles of either species be explicitly defined within the equations of motion; this requirement will be demonstrated in section §5.6, where approximations of the energy dependence are studied and presented.

In dynamic-BCA simulations, the energy effects of sputtering caused due to ejecta are implicitly handled—there are no restrictions on the number of intermediate energies within the simulation; however, in this presented hybrid approach, utilizing a continuum model and sputtering statistics, energy effects must be dealt with explicitly. Statistically speaking the energy distribution of the sputtering ejecta is a continuous function when taken as a limit of an infinite number of sputtering events; realistically however, the quality of the statistical approximation is bounded by the number of simulated sputtering events which prevents knowing a full continuous probability distribution. When using BCA to generate input files for a hybrid simulation one must balance simulation time and preprocess-

ing challenges^{‡‡} and therefore, the continuous energy distribution must be discretized. The energy dependence is thus handled in this model by creating statistical ejecta distributions along discrete energy ranges or slices chosen along logarithmic intervals. Discretization of the energy distributions avoids the difficult problem of integrating the statistical ejection distributions over energy, which would be both computationally expensive in the evaluation and the derivation of said distributions. These extracted statistical sputtering inputs are described in section §5.4.

In the remainder of this section the full set of equations of motions and the related assumptions for the energy-resolved sputtering model will be presented. For convenience the equations of motions are summarized at the end of this section in table 5.3.2; representative data of the statistical input parameters will be presented in section §5.4.

5.3.1 Assumptions Employed by the Energy-Resolved Sputtering Model

As with the previous model, the energy-resolved model is first presented as a set of simulation assumptions from which governing equations are developed in section 5.3.2. As with the simple model previously presented in this chapter, only three orders of complexity are assumed to be sufficient to represent the phenomena modeled. In the previous model this meant that gallium was only allowed to backscatter once; sputtering thus occurred at the zeroth and first order nodes which in turn lead to redeposition at the first and second order nodes. In this energy-resolved model these gallium assumptions are unchanged; however, sputtering may now be incited by both beam and target atoms which adds additional terms to the equations. It also creates the opportunity for backscattering to occur by either species, though the most important feature of the energy resolved model is that silicon is allowed to sputter silicon through the process of reflexive sputtering. The one-hop limit for backscattering is still used, but it is applied to both species at different orders of simulation complexity (gallium stops backscattering in the first order, and silicon in the second); furthermore, sputtering by backscattered silicon is not considered in this model as that would require a fourth order of complexity. Due to the fact that the incoming flux of silicon atoms leading to silicon backscattering is polychromatic, a BCA derived angular distribution is not used, and the angular distribution of backscattered silicon atoms is approximated with a cosine, this backscattered silicon is taken as only contributing towards second-order redeposition. This choice of a cosine approximation for a backscatter angular distri-

^{‡‡}While the capabilities to resolve the statistical distributions as a function of energy could be added to the BCA simulator IMSIL, this exploratory work makes use of post-processed trajectory files. The size of these trajectory files presented an additional challenge to generating the input data used in the simulation as a large number of simulated particles were needed in order to have statistically robust distributions along the discrete energy bands, especially in the case of backscattered particles. Future work on this topic would strongly benefit from making the statistical output of IMSIL compatible with energy resolved statistical distributions, as this feature would improve the quality of the input data which is currently limited by the maximum trajectory file size that may be conveniently post-processed.

bution is suspect and is investigated further in appendix C; however, the effect is minor due to the relatively small population of backscattered silicon. A monochromatic gallium beam with a Gaussian shape and a beam energy of 30 keV is used in this model, as with the previously described models. Implantation effects are neglected in this model and the implantation of gallium does not lead directly* to mass gain at any simulation nodes. Thereby, the zeroth-order sputtering yield of target silicon sputtered by the gallium beam and the backscatter yield of those gallium ions, is dependent solely upon the local incidence angle as there are no concentration dependent sputtering yields used in this model.

In the first order of the model, the precursor to reflexive-sputtering makes its first appearance in the form of the redeposition energy, which in the earlier models was assumed to be strictly of low-energy. In the energy-resolved model, the redeposition energy (the energies of the sputtered target atoms) are now allowed to have energies between 0 eV and the beam energy of 30 keV. This spectrum of energies allows for both redeposition and further sputtering. As with the simple model (section 5.2.1), only target atoms are redeposited; however, the angular distribution of these ejected atoms that may lead to redeposition (or further sputtering) now depends on the energy with which they were ejected. The sticking coefficient for redeposited atoms is still 1; however, as the atoms that would have lead to redeposition in the simple model now have the opportunity to sputter or be backscattered, the total magnitude of redeposition at a given node may be reduced in the energy-resolved model as compared to the simple mode. In this model, the energy loss for backscattered gallium beam ions is now modeled (however, for only one hop), which also entails the modeling of the energy-resolved backscatter angular distribution for gallium ions. As with the simple model, these backscattered ions may prompt sputtering, but may not, themselves, be implanted. If the backscattered gallium atoms do go on to prompt sputtering, then the energy of those backscattered ions must once again be taken into account in the form of an incident ion-energy and angle dependent sputtering yield. At the second-order of the model, redeposition of silicon atoms sputtered by backscattered gallium ions, reflexively sputtered silicon atoms, and silicon atoms backscattered from the first-order node is considered using a cosine distribution. The second-order redeposited atoms are assumed to be strictly silicon, and low-energy, no attempt is made to resolve the energies of the silicon atoms ejected from the first-order node, leading to redeposition at the second-order nodes; furthermore these redeposition atoms are once again assumed to stick to the surface at the second-order node with 100% efficiency.

*However positive mass transfer may occur at nodes due to redeposited silicon that has been excited by an incident or backscattered gallium ion.

Property:	Assumption:
Order of Simulation	3
(0 th order) Beam Energy	30 keV (monochromatic)
(0 th order) Target Composition	Si (static composition)
(0 th order) Beam Shape	Gaussian, Error Function, or Superposition of Gaussians (Overlapped beam)
(0 th order) Sputtering Yield	Dependent on Local Incidence Angle θ
(0 th order) Backscattering Yield	Dependent on Local Incidence Angle θ
(0 th order) Sputtered Atom Energy (1 st order) Redeposition Energy	0-30 keV (Leading to Redeposition and Further Sputtering)
(0 th order) Sputtered Atom Composition (1 st order) Redeposition Composition	Si
(0 th order) Sputtered Atom Shape (1 st order) Redeposition Shape	Angular Distribution from BCA Dependent on Ejection Energy
(1 st order) Sticking Coefficient	1
(1 st order) Backscattering Energy	0-30 keV
(1 st order) Backscattering Composition	Ga
(1 st order) Backscattering Shape	Angular Distribution from BCA Dependent on Ejection Energy
(1 st order) Backscattering Sticking Coefficient	0
(1 st order) Backscatter Sputtering Yield	Dependent on Local Incidence Angle θ and Energy of Impinging Ions
(1 st order) Sputtered Atom Energy (2 nd order) Redeposition Energy	0-2eV (sticking only)
(1 st order) Sputtered Atom Composition (2 nd order) Redeposition Composition	Si
(1 st order) Sputtered Atom Shape (2 nd order) Redeposition Shape	Scaled Cosine
(2 nd order) Sticking Coefficient	1

Table 5.3.1 – Assumptions made in the energy-resolved sputtering model.

5.3.2 Equations of Motion: Energy-Resolved Sputtering

5.3.2.1 General i^{th} Order Form

As with the old model presented in section §5.2, the equations of motion are first presented in a general i^{th} order form before assumptions are made to simplify the equations to the zeroth, first, and second-order governing equations of motion. The general form equations make use of all the nomenclature presented in section §5.2. Additionally in the equation for the i^{th} order gallium flux, the energy-resolved statistical functions* for the backscatter yield of gallium $Y_{back, Ga|Ga}(\theta_{i-1}; E_l)$, the energy distribution of backscattered gallium $g_{back, Ga|Ga}(\theta_{i-1}; E_l; E_k)$, and the angular distribution of backscattered gallium ions $f_{back, Ga|Ga}(\alpha_{i-1}, \theta_{i-1}; E_l; E_k)$ are now added in order to add energy resolution to the model. The notation for the energy-dependence uses E_l and E_k in order to indicate that the quantity is defined for a certain energy level (in the implementation of this model, each energy level corresponds to segment of the energy spectrum defined by logarithmic spacing with three bands per decade starting from a minimum energy of 0.1 eV and going to the beam energy of 30 keV), where the semi-colon indicates that the quantity is coarsely discretized over energy. Two terms for energy dependence are used in the statistical functions used in the flux equations, E_l indicates the energy exciting the emission, while E_k indicates the energy of the emitted particles. A summation over k is performed in the general model to yield the total number of excited particles arriving at any given energy level where $l_{max} = k_{max}$ as both maxima are determined by the beam energy. However, as this model is limited to three orders with sputtering only occurring at the zeroth and first orders, summation over both k and l is never needed at any of the three orders. As can be seen from the general form for the flux of gallium equation (5.3.1), gallium only enters the model from the beam and through backscattering of the beam, whereas the silicon flux at an arbitrary order node, equation (5.3.2), receives contributions from silicon sputtered by gallium, silicon sputtered by silicon, and backscattered silicon. As with the formulation of the simple model presented in section §5.2, the incoming flux at any i^{th} order node from the $i - 1^{\text{th}}$ order node is a summation over all possible $i - 2^{\text{nd}}$ order source nodes; however, as with the previous model, many of these summations are degenerate when only three orders of complexity are considered. Furthermore, as implanted gallium is neglected in this model, the i^{th} order node velocity depends solely on the amount of silicon added or removed at the node, thereby leading to the mixed term in the i^{th} order sputtering flux $F_{Si, i \leftarrow i-1}$ that is absent in the gallium flux. Without gallium in the target there can be no gallium sputtered due to energetic silicon bombardment. The velocity term $V_i(\theta_i, F_{Ga, i \leftarrow i-1}, F_{Si, i \leftarrow i-1})$ indicates that the total amount

*A greater number of energy-resolved statistical functions show up in the general form of the equations than are seen in section §5.4, as the assumption of only a 3 order model allows for a number of simplifying assumptions.

of arriving $i - 1^{\text{th}}$ order fluxes remaining at an i^{th} order node is equal to the incoming silicon flux minus silicon sputtered by gallium, silicon sputtered by silicon, and whatever incoming silicon flux is backscattered at the node, where the total node-flux may be negative indicating a greater degree of sputtering than redeposition.

$$F_{Ga, i \leftarrow i-1} = \sum_{k=0}^{k_{max}} \left\{ \sum_{visible_{i-2}} F_{Ga, i-1 \leftarrow i-2} \cdot \begin{bmatrix} Y_{back, Ga|Ga}(\theta_{i-1}; E_l) \cdot \\ g_{back, Ga|Ga}(\theta_{i-1}; E_l; E_k) \cdot \\ f_{back, Ga|Ga}(\alpha_{i-1}, \theta_{i-1}; E_l; E_k) \end{bmatrix} \right\} \cdot \frac{l_{i-1}}{d_{i-1, i}} \cos \theta_i \quad (5.3.1)$$

$$F_{Si, i \leftarrow i-1} = \sum_{k=0}^{k_{max}} \left\{ \sum_{visible_{i-2}} F_{Ga, i-1 \leftarrow i-2} \cdot \begin{bmatrix} Y_{sput, Si|Ga}(\theta_{i-1}; E_l) \cdot \\ g_{sput, Si|Ga}(\theta_{i-1}; E_l; E_k) \cdot \\ f_{sput, Si|Ga}(\alpha_{i-1}, \theta_{i-1}; E_l; E_k) \end{bmatrix} + \sum_{visible_{i-2}} F_{Si, i-1 \leftarrow i-2} \cdot \begin{bmatrix} Y_{sput, Si|Si}(\theta_{i-1}; E_l) \cdot \\ g_{sput, Si|Si}(\theta_{i-1}; E_l; E_k) \cdot \\ f_{sput, Si|Si}(\alpha_{i-1}, \theta_{i-1}; E_l; E_k) \end{bmatrix} + \begin{bmatrix} Y_{back, Si|Si}(\theta_{i-1}; E_l) \cdot \\ g_{back, Si|Si}(\theta_{i-1}; E_l; E_k) \cdot \\ f_{back, Si|Si}(\alpha_{i-1}, \theta_{i-1}; E_l; E_k) \end{bmatrix} \right\} \cdot \frac{l_{i-1}}{d_{i-1, i}} \cos \theta_i \quad (5.3.2)$$

$$V_i(\theta_i, F_{Ga, i \leftarrow i-1}, F_{Si, i \leftarrow i-1}) = v_{Si} \cdot \sum_{l=0}^{l_{max}} \left\{ \sum_{visible_{i-1}} \begin{bmatrix} 1 - \\ Y_{sput, Si|Si}(\theta_i; E_l) - \\ Y_{back, Si|Si}(\theta_i; E_l) \end{bmatrix} \cdot F_{Si, i \leftarrow i-1} - \sum_{visible_{i-1}} Y_{sput, Si|Ga}(\theta_i; E_l) \cdot F_{Ga, i \leftarrow i-1} \right\} \quad (5.3.3)$$

5.3.2.2 Zeroth, First, and Second-Order Equations of Motion

As this simulation model is constructed to model FIB milling, the initial flux of silicon atoms impinging at the zeroth order node is zero, because it is assumed that the only initial flux is gallium, as shown in equation (5.3.4); this is identical to the situation assumed in the model presented in section 5.2.1. Furthermore, the initial gallium flux at the zeroth order node is defined strictly by the beam ($F_{Ga,-}$), as shown in equation (5.3.5), once again with a geometric cosine term ($\cos \theta_0$) compensating for any beam tilt introduced by the local topography at the node. As the beam flux is degenerate and represents a parallel non-dispersive flux of particles the summation seen in equation (5.3.1) is a summation over a single term and thus dropped.

$$F_{Si,0} = \{0\} \quad (5.3.4)$$

$$F_{Ga,0} = \{F_{Ga,-}\} \cdot \cos \theta_0 \quad (5.3.5)$$

Zeroth-order node velocity is therefore simply the product of the zeroth order gallium flux ($F_{Ga,0}$) and the atomic volume (v_{Si}) multiplied by the incidence-angle dependent sputtering yield of silicon by gallium at the excitation energy ($Y_{sput, Si|Ga}(\theta_0)$) as shown in equation (5.3.6). As per table 5.3.1, it is assumed that the beam is monochromatic and that the sputtering yield therefore can be expressed as $Y_{sput, Si|Ga}(\theta_0)^\dagger$, a sputtering yield for a pure 30keV beam of gallium. This assumption fits well with commercial FIB beams utilizing a gallium LMIS (section 1.1.1.1), as gallium predominately ionizes to a single species. The equations of motion at the zeroth order are still identical to the equations of motion presented in chapter 2.

$$V_0(\theta_0, F_{Ga,0}) = F_{Ga,0} \cdot [-v_{Si} \cdot Y_{sput, Si|Ga}(\theta_0)] \quad (5.3.6)$$

Model complexity increases, however, when the first-order fluxes are considered, as shown in equation (5.3.7) and equation (5.3.8). The first notable change in the expressed fluxes is the addition of an energy dependence in each flux, e.g. $F_{Si,1 \leftarrow 0}$ where the flux of silicon atoms arriving at a given first-order node now has a discrete energy dependence as indicated by E_l prefaced by a semicolon. E_l refers to the l th energy band, where bands are chosen along logarithmic intervals, and influences two statistical properties[‡] on the left side of the first-order flux equations. These

[†]Use of this monochromatic assumption for the zeroth and first order nodes allows one to neglect the equivalent sputtering yield \bar{Y} , that is necessary for non-monochromatic incident fluxes.

[‡]Statistical property refers to an unspecified statistical rate or distribution as obtained from experiments or BCA simulations such as the sputtering yield or sputtering angular distribution.

two statistical properties are the energy distribution, e.g. $g_{sput, Si|Ga}(\theta_0; E_k)$ for silicon target atoms sputtered by impinging gallium, which is defined as the fraction of silicon sputtering events with energies in the energy band E_k incited by a gallium ion impinging with an incidence angle θ and an energy distribution E_l , although E_l is not shown because the beam is monochromatic; the second property is the energetically resolved angular distribution of sputtered particles. The energetically resolved angular distribution, e.g. $f_{sput, Si|Ga}(\alpha_0, \theta_0; E_k)$ for silicon atoms sputtered by gallium, is defined as the normalized angular distribution in 2D of sputtered atoms in the energy band E_k , where the normalization is such that the integral of the probability density of sputtering across all exit angles α_0 is equal to unity. In equations (5.3.7) and (5.3.8) the energy-resolved angular probability distribution (referred to in equation (2.1.2) as $f_{sput}(\gamma, \theta)$ neglecting particle energies) is separable into components $g_{sput, Si|Ga}(\theta_0; E_k)$ and $f_{sput, Si|Ga}(\alpha_0, \theta_0; E_k)$. Equations (5.3.7) and (5.3.8) express the quantity and the energy range of both sputtered silicon and backscattered gallium atoms arriving at the first-order simulation node; however, they are insufficient to express any sputtering resulting from their arrival. Once again at the first order of complexity, the only source terms for either equation are the zeroth-order gallium flux which leads to a degeneracy, and therefore a further dropping of the summation over source terms as the zeroth-order sources are all uniquely described by the beam. Furthermore the summation over k may also be dropped as there is a single excitation energy.

$$F_{Si, 1 \leftarrow 0} = \left\{ F_{Ga, 0} \cdot \begin{bmatrix} Y_{sput, Si|Ga}(\theta_0) \cdot \\ g_{sput, Si|Ga}(\theta_0; E_k) \cdot \\ f_{sput, Si|Ga}(\alpha_0, \theta_0; E_k) \end{bmatrix} \right\} \cdot \frac{l_0}{d_{0,1}} \cos \theta_1 \quad (5.3.7)$$

$$F_{Ga, 1 \leftarrow 0} = \left\{ F_{Ga, 0} \cdot \begin{bmatrix} Y_{back, Ga|Ga}(\theta_0) \cdot \\ g_{back, Ga|Ga}(\theta_0; E_l) \cdot \\ f_{back, Ga|Ga}(\alpha_0, \theta_0; E_l) \end{bmatrix} \right\} \cdot \frac{l_0}{d_{0,1}} \cos \theta_1 \quad (5.3.8)$$

The total node velocity due to a first-order interaction is shown in equation (5.3.9). The influence of impinging silicon atoms is threefold, all of the silicon atoms arriving at the first-order node might lead to redeposition; however, a fraction of those impinging silicon atoms will be backscattered and lead to redeposition at a second-order node or escape into the vacuum; additionally, some of these impacting sputtered atoms will lead to further sputtering, causing yet another source of negative mass transfer at the node. The influence of impinging backscattered gallium atoms at the first-order node level is limited to additional sputtering of silicon target atoms. Notably, the mass transfer effects due to implanted gallium atoms are neglected entirely in this model; however, opportunities exist to use either dynamic-BCA simulations or a further enhanced hybrid model to study gallium intermixing

effects (however consideration of implantation would considerably increase the complexity of any resulting simulator [199]). Gallium intermixing is, however, outside of the scope of this current work, and the results of dynamic-BCA simulations [122] imply that the effect is subtle.

$$V_1(\theta_0, \theta_1, F_{Ga, 1\leftarrow 0}, F_{Si, 1\leftarrow 0}) = v_{Si} \cdot \sum_{l=0}^{l_{max}} \left\{ \begin{array}{l} \sum_{visible_0} \left[F_{Si, 1\leftarrow 0} \cdot \left(\begin{array}{c} 1 - \\ \bar{Y}_{back, Si|Si}(\theta_0, \theta_1, E_l) - \\ \bar{Y}_{sput, Si|Si}(\theta_0, \theta_1, E_l) \end{array} \right) \right] - \\ \sum_{visible_0} [F_{Ga, 1\leftarrow 0} \cdot \bar{Y}_{sput, Si|Ga}(\theta_0, \theta_1; E_l)] \end{array} \right\} \quad (5.3.9)$$

Equation (5.3.9), the velocity of a node due to first-order effects, notes the inclusion of a new term $\bar{Y}(\theta_0, \theta_1, E_l)$; this term represents the equivalent[§] sputtering yield over the energy band E_l . As $F_{Si, 1\leftarrow 0}$ is an incoming flux E_1 is used due to the re-impinging particles now being considered to excite rather than to have been excited. Equivalence being defined such that $\bar{Y}(\theta_0, \theta_1, E_l)$ is equal to the generalized term $Y(\theta_i; E_l)$ used in section 5.3.2.1, where the new $i - 1$ dependence shown in \bar{Y} indicates that the energy distribution of the inciting atoms depends on the incidence angle at the source node. The equivalent sputtering yield is a linear interpolation between the known simulated yields at the endpoints ($Y(\theta_1, E_1)$ and $Y(\theta_1, E_2)$, where E_1 and E_2 represent the endpoints energies) of an energy band evaluated at a weighted mean energy $\bar{E}(g(\theta_0, E_l))$ for the energy band (described in more depth in appendix D). Specifically the linear approximation of the sputtering yields are expressed by equation (5.3.10), equation (5.3.11), and equation (5.3.12). While the mean energy is calculated through the use of equation (5.3.13) and equation (5.3.14) where the \bar{E} is calculated through a closed-form integration of an assumed power-law energy distribution evaluated on the intervals $E_1 \cdots E_{mid}$, and $E_{mid} \cdots E_2$ where $E_{mid} = \sqrt{E_1 \cdot E_2}$.

The exact quantity expressed by $F_{Si, 1\leftarrow 0}$ is the flux of silicon atoms arriving at the given node within the energy band E_l ; however, as this energy-band has a finite energy-width, uncertainty as to the intra-band energy distribution arises. Furthermore, the statistical sputtering yields extracted from the BCA simulation are defined only for monochromatic excitation particles. It is therefore necessary to make use of an equivalent yield that emulates the yield of the population using known sputtering yields located at the endpoints of the energy band and an estimate of the shape of the energy distribution within the band. As the equivalent yield is dependent upon the shape of the

[§]Equivalent denotes that the sputtering yield calculated by these functions represents the weighting and sum of the sputtering yield across the simulated energy band, other terms such as mean or effective sputtering yield could also be used; however, equivalence was the goal in the derivation of these equations and is thus the term chosen to describe them.

energy distribution within the band, it is therefore also dependent upon the incidence angle at the zeroth-order node θ_0 , as the energy distribution is incidence angle dependent.

$$\bar{Y}(\theta_0, \theta_1; E_l) = m(\theta_1; E_l) \cdot \bar{E}(\theta_0; E_l) + b(\theta_1; E_l) \quad (5.3.10)$$

$$m(\theta_1; E_l) = \frac{Y_{sput}(\theta_1; E_2) - Y_{sput}(\theta_1; E_1)}{E_2 - E_1} \quad (5.3.11)$$

$$b(\theta_1; E_l) = Y_{sput}(\theta_1; E_2) - \frac{Y_{sput}(\theta_1; E_2) - Y_{sput}(\theta_1; E_1)}{E_2 - E_1} \cdot E_2 \quad (5.3.12)$$

$$\bar{E}(\theta_0; E_l) = \frac{1 - k_2}{2 - k_2} \cdot \frac{g(\theta_0; E_{mid, 2})^2 \cdot E_2 - g(\theta_0; E_1, mid)^2 \cdot E_1}{g(\theta_0; E_{mid, 2})^2 - g(\theta_0; E_1, mid)^2} \quad (5.3.13)$$

$$1 - k_2 = \frac{\ln \frac{g(\theta_0; E_1, mid)}{g(\theta_0; E_{mid, 2})}}{\ln \frac{E_{mid}}{E_2}} \quad (5.3.14)$$

To determine the velocity of a node due to first-order effects, it is necessary to sum the effects due to each simulated energy band as shown in equation (5.3.9) by the inclusion of the term $\sum_{l=0}^{l_{max}}$. This summation over the energy levels is required in addition to the loops over all visible source and destination nodes. The performance of the simulation is thus inversely dependent upon the number of chosen energy levels used in the simulation. A notable exclusion in equation (5.3.9) is a term considering the flux of backscattered gallium atoms emerging from a first-order node; while the quantity is available from the statistical data, it is neglected because the presented model only considers a single backscatter hop as stated in the assumptions. Both gallium and silicon are removed from the simulation after a single backscattering, although backscattered silicon is allowed to contribute to redeposition, backscattered gallium ions do not directly lead to redeposition as the present model does not have the facilities to simulate intermixing and are therefore neglectable at this order of complexity. Physically, this approximation is plausible, as significant energy loss occurs whenever an ion enters the target and the energy remaining after a first hop should be negligible; furthermore, with trench topographies, it is extremely likely that the incidence angles at first-order nodes will be more perpendicular than those leading to large backscattering yields at zeroth-order nodes. This is due to the trend for high backscattering yields to be associated (for the silicon-gallium system) with glancing angle incidence —implying that high backscatter yields occur on sidewalls; the bottom of the trench is therefore the next likely point of impact, which will be nearly perpendicular with respect to the backscattered ion. In topographies not resembling trenches, where multiple low angle reflections are

expected, this simplification is more suspect.

$$F_{Si, 2\leftarrow 1} = \sum_{k=0}^{k_{max}} \left\{ \begin{array}{l} \sum_{visible_0} F_{Si, 1\leftarrow 0} \cdot \left[\begin{array}{l} \bar{Y}_{back, Si|Si}(\theta_0, \theta_1; E_k) \cdot c_1 \cdot \cos^n(\alpha_1) + \\ \bar{Y}_{sput, Si|Si}(\theta_0, \theta_1; E_k) \cdot c_1 \cdot \cos^n(\alpha_1) \end{array} \right] + \\ \sum_{visible_0} F_{Ga, 1\leftarrow 0} \cdot [\bar{Y}_{sput, Si|Ga}(\theta_0, \theta_1; E_k) \cdot c_1 \cdot \cos^n(\alpha_1)] \end{array} \right\} \cdot \frac{l_1}{d_{1,2}} \cos \theta_2 \quad (5.3.15)$$

$$F_{Ga, 2} = \{0\} \quad (5.3.16)$$

$$V_2(\theta_2, F_{Si, 2\leftarrow 1}) = \sum_{visible_1} F_{Si, 2\leftarrow 1} \cdot [v_{Si} \cdot (1)] \quad (5.3.17)$$

The second-order nodes are limited to redeposition effects with a simplified angular distribution as indicated by a lack of negative terms in the velocity the second-order node shown in equation (5.3.17). The cosine distribution is used for the angular distribution of second-order redeposition similarly to how it was presented in equation (2.1.5). There are three source terms for the second-order flux of silicon atoms (equation (5.3.15)); the redeposition due to sputtering caused by backscattered gallium ions: $F_{Ga, 1\leftarrow 0} \cdot [\bar{Y}_{sput, Si|Ga}(\theta_0, \theta_1; E_l) \cdot c_1 \cdot \cos^n(\alpha_1)]$, the redeposition due to sputtering caused by reflexive sputtering by sputtered target atoms: $F_{Si, 1\leftarrow 0} \cdot [\bar{Y}_{sput, Si|Si}(\theta_0, \theta_1, E_l) \cdot c_1 \cdot \cos^n(\alpha_1)]$, and redeposition due to backscattered[¶] energetic sputtered silicon atoms: $F_{Si, 1\leftarrow 0} \cdot [\bar{Y}_{back, Si|Si}(\theta_0, \theta_1, E_l) \cdot c_1 \cdot \cos^n(\alpha_1)]$. All three of these terms need summation over the $i - 2^{\text{nd}}$ order source nodes in order to calculate the total flux emitted from the $i - 1^{\text{st}}$ order source node similarly to how the second order redeposition flux was calculated in section §5.2. The redeposition flux due to implanted gallium atoms is taken to be zero (equation (5.3.16)) due to the fact that this model neglects the effects of gallium implantation and intermixing. Therefore, the velocity of the second-order nodes is strictly positive, indicating redeposition, and is characterized by equation (5.3.17). Use of the cosine approximation also removed the need for the statistical quantities of $g_{sput, Si|Si}(\theta_{i-1}; E_l)$, $f_{sput, Si|Si}(\alpha_{i-1}, \theta_{i-1}; E_l)$, $g_{back, Si|Si}(\theta_{i-1}; E_l)$, and $f_{back, Si|Si}(\alpha_{i-1}, \theta_{i-1}; E_l)$. As appendix C shows, in typical simulations the

[¶]As discussed in 2.3.2.2 the angular distributions of backscattered ions are quite often very poorly approximated by the aforementioned cosine distribution. It is, however, impractical to reevaluate the system at a third order using the correct angular distributions. A choice between neglecting the flux of backscattered energetically sputtered target atoms or considering them with a poorly chosen redeposition model must be made. In this work the target atom backscatter flux is retained and redistributed using the flawed model due to a hesitation to *wantonly discard* calculated matter streams in the simulation. As is demonstrated in 2nd Order Redeposition from Reflexive Sputtering (appendix C), this particular flux has very negligible effects on the simulated topographies.

contribution to redeposition from a cosine approximation of second-order backscattered silicon atoms is small, and excusable as proper modeling would require another energy-resolved order of complexity. The total amount of silicon to be redeposited at the second-order node naturally contains contributions from sputtering by all energy levels, thereby necessitating the summation over k seen in $F_{Si, 2\leftarrow 1}$. As the flux terms contribute only to redeposition (inciting no further sputtering), the second-order node velocity is simply the atomic volume of silicon times the sum of all $F_{Si, 2\leftarrow 1}$ fluxes from visible nodes.

In the following section (section §5.4), the representative processed and fitted data will be shown for the statistical quantities involved in the model. To enhance readability, the complete set of energy-resolved equations of motion is summarized in table 5.3.2.

Equation of Motion		
$F_{Si, 0} = \{0\}$		5.3.4
$F_{Ga, 0} = \{F_{Ga, -}\} \cdot \cos \theta_0$		5.3.5
$V_0(\theta_0, F_{Ga, 0}) = F_{Ga, 0} \cdot [-v_{Si} \cdot Y_{sput, Si Ga}(\theta_0)]$		5.3.6
$F_{Si, 1\leftarrow 0} = \left\{ F_{Ga, 0} \cdot \begin{bmatrix} Y_{sput, Si Ga}(\theta_0) \cdot \\ g_{sput, Si Ga}(\theta_0; E_l) \cdot \\ f_{sput, Si Ga}(\alpha_0, \theta_0; E_l) \end{bmatrix} \right\} \cdot \frac{l_0}{d_{0,1}} \cos \theta_1$		5.3.7
$F_{Ga, 1\leftarrow 0} = \left\{ F_{Ga, 0} \cdot \begin{bmatrix} Y_{back, Ga Ga}(\theta_0) \cdot \\ g_{back, Ga Ga}(\theta_0; E_l) \cdot \\ f_{back, Ga Ga}(\alpha_0, \theta_0; E_l) \end{bmatrix} \right\} \cdot \frac{l_0}{d_{0,1}} \cos \theta_1$		5.3.8
$v_{Si} \cdot \sum_{l=0}^{l_{max}} \left\{ \begin{array}{l} \sum_{visible_0} \left[F_{Si, 1\leftarrow 0} \cdot \begin{pmatrix} 1 - \\ \bar{Y}_{back, Si Si}(\theta_0, \theta_1, E_l) - \\ \bar{Y}_{sput, Si Si}(\theta_0, \theta_1, E_l) \end{pmatrix} \right] - \\ \sum_{visible_0} [F_{Ga, 1\leftarrow 0} \cdot \bar{Y}_{sput, Si Ga}(\theta_0, \theta_1; E_l)] \end{array} \right\}$		5.3.9
$F_{Si, 2\leftarrow 1} = \sum_{k=0}^{k_{max}} \left\{ \begin{array}{l} \sum_{visible_0} F_{Si, 1\leftarrow 0} \cdot \left[\bar{Y}_{back, Si Si}(\theta_0, \theta_1, E_k) \cdot c_1 \cdot \cos^n(\alpha_1) + \right. \\ \left. \bar{Y}_{sput, Si Si}(\theta_0, \theta_1, E_k) \cdot c_1 \cdot \cos^n(\alpha_1) \right] + \\ \sum_{visible_0} F_{Ga, 1\leftarrow 0} \cdot [\bar{Y}_{sput, Si Ga}(\theta_0, \theta_1; E_k) \cdot c_1 \cdot \cos^n(\alpha_1)] \end{array} \right\} \cdot \frac{l_1}{d_{1,2}} \cos \theta_2$		5.3.15
$F_{Ga, 2}(\theta_2) = \{0\}$		5.3.16
$V_2(\theta_2, F_{Si, 2\leftarrow 1}) = \sum_{visible_1} F_{Si, 2\leftarrow 1} \cdot [v_{Si} \cdot (1)]$		5.3.17

Table 5.3.2 – The complete equations of motion for the energy-resolved model, represented for clarity.

5.3.3 2D Simulation of the Energy-Resolved Model

2D simulations are deemed to be sufficient for the phenomenological study of the energy-resolved model presented in this chapter. Completing the simulation in 2D greatly simplifies the equations of motion by removing yet another angle and reducing the dimensionality of the required tables. The model works in 2D as long as the definition of the term θ_1 does not depend upon the depth into

the page. Geometrically, θ_1 does depend on the depth direction of a simulation, as the effective incidence angle changes depending on the Y-depth of the simulation, increasing with the inter-plane distance. A 3D correction factor (described in appendix A) is required to correct for these 3D-effects, in particular 3D-effects due to sputtering by energetically sputtered silicon, and the energy-resolved simulations presented in section §5.5 implement this correction factor. The 2D simulations presented in chapter 2 and chapter 3 do not need a 3D correction factor because the backscatter angular distribution of backscattered ions is tightly distributed along the plane defined by the incidence angle and the surface.

5.4 Physical Inputs and their Parameterizations

As with section §2.3 in chapter 2 this section explains implementation details and shows representative data for the physical inputs derived from BCA simulations used in the energy-resolved model.

5.4.1 Energy Resolved Angular Distributions

Equation (5.3.7) makes use of the normalized energy-resolved angular probability distribution for sputtered target atoms $f_{sput, Si|Ga}(\alpha_0, \theta_0; E_l)$ shown in figure 5.4.1. These probability distributions are extracted from trajectory files obtained through 1-D static BCA simulations using IMSIL implementing the gradient density model of surface roughness discussed in section 4.4.2.1. Trajectory files used as inputs for the hybrid model contain the recoils that lead to sputtering of either primary ions or target atoms, each recoil is characterized by the 3-space position at which it exceeds the surface binding energy and is counted as sputtering, along with the kinetic energy and direction vector of the sputtered particle. The presented distributions are obtained by counting the number of target atoms sputtered with a given polar angle $\alpha \pm \Delta\alpha$ where $\Delta\alpha$ is the width of each histogram bin, determined by the lateral and depth components of the direction vector, and an ejection energy in a given range. These counts produce an individual one-dimensional histogram at each energy interval (or band) for a single simulated incidence angle θ ; each histogram is then normalized such that the total sputtering probability for a given incidence angle θ at a given energy band E_l is unity. The relative probabilities across energy bands expressed as $g_{sput, Si|Ga}(\theta_0; E_l)$ (or $g_{back, Ga|Ga}(\theta_0; E_l)$ for gallium backscatter events*) is determined by taking the total number of counts at a given energy interval and determining the fraction with regards to the total number of sputter events, also normalized per incidence angle.

*The energy distribution of backscattered energetic silicon atoms $g_{back, Si|Si}(\theta_1; E_l)$ is not calculated or extracted due to the cosine approximation employed at the second-order of complexity. This simplification allows the use of energy distributions with a monochromatic excitation energy as opposed to excitation energies across an entire energy band E_l .

The data for $g_{sput, Si|Ga}(\theta_0; E_l)$ used in the simulation is shown and discussed in section 5.4.4. The weighted superposition of all energy bands is equal to the non-energy-resolved angular probability distribution shown in figure 2.3.4. Functionally these normalized histograms as implemented in the simulation as a set of two-dimensional spline interpolations across the independent variables of θ and α . These spline interpolations are used without the linear component discussed in section 2.3.2.1, as the behavior of the directed sputtering ridge is not as easily characterized in the energy-resolved regime as it was in the superposition.

A number of notable features to the energy-resolved angular probability distribution of sputtered atoms can be seen in figure 5.4.1, chiefly that at low ejection-energies (< 10 eV) the probability distribution at incidence angles lower than 75° is in good agreement to the cosine approximation. At low energies and glancing incidence angles (characterized by larger θ s) the lateral component of the impinging ions direction vector is apparent in a preferential sputtering peak around a given ejection angle. The location of this peak ejection angle is initially approximately a 90° rightward rotation from the incidence angle, however as ejection energies increase it trends toward ejection angles less perpendicular (angles $> 90^\circ$ with respect to the incident direction) to the surface normal. This preferential sputtering shows up in the angular distribution as a faint diagonal peak along the right side of the distribution plots shown in figure 5.4.1. At low ejection energies the peak is necessarily diffuse due to the better obfuscation of the initial ion vector through multiple collisions; higher energy ejection events are correlated with early energetic collisions leading to sputtering. At ejection energies greater than 100 eV, the entire distribution has clearly shifted to greater (more glancing) ejection angles, with relatively few high energy ejections returning in the direction of the impinging ion (corresponding to a negative ejection angle). With increasing ejection energy the sputtering peak becomes more sharply defined and more of the sputtering occurs in the vicinity of the peak. This shift in the shape and the center of the angular distribution at higher ejection energies necessitates the use of an energy-resolved model to study reflexive sputtering.

5.4.2 Energy-Resolved Backscatter Distributions

The energy-resolved backscattering angular distribution $f_{back, Ga|Ga}(\alpha_0, \theta_0; E_l)^*$ shown in figure 5.4.2 is obtained in the same manner as described in section 5.4.1, with the notable exception of counting the emergent gallium ions rather than sputtered silicon atoms. The general trend absent of a cosine distribution holds (shown as a polar plot for $\theta = 80^\circ$ in figure 5.4.3), with the centroid of the angular distribution of backscattered ions moving upward to higher ejection angles with increasing ejection

*The subscripts shown in the backscatter angular distribution indicate that this quantity is only useful when defined for a zeroth-order node, as this angular distribution assumes a monochromatic excitation energy of 30 keV.

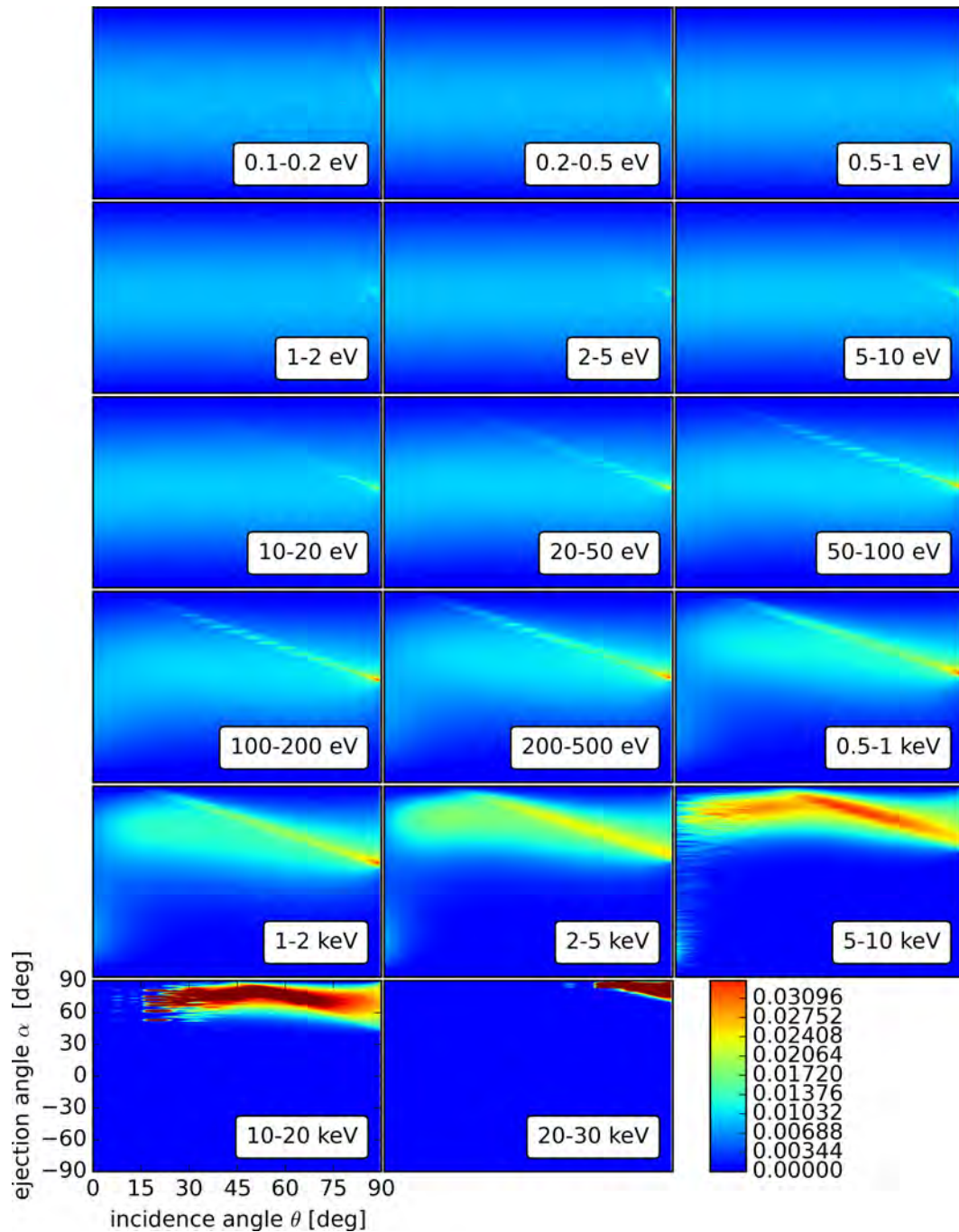


Figure 5.4.1 – Normalized angular sputtering probability distributions $f_{sput, Si|Ga}(\alpha_0, \theta_0; E_l)$ for silicon atoms sputtered by 30 keV gallium ions separated by energy of ejected target atoms. Notice that the directed peak of sputtered atoms opposite the specular reflection angle becomes more dominant with increasing ejection energy, indicating a pseudo-focusing effect among high energy sputtering events. The cosine approximation for the sputtering angular distribution is clearly invalid for particles sputtered with energy in excess of 100 eV.

energy. A very notable difference in the distributions (between figure 5.4.1 and figure 5.4.2) is the slope of the peak in the distribution as seen in the surface plot as a slight positive slope with respect to the horizontal axis, which is reversed and increasing as opposed to the decreasing behavior shown in the sputtering distributions (which also show a linear peak). In the backscattering distribution the peak ejection angle α_{max} increases with increasing incidence angle θ , following the expected specular behavior. The energy distribution discussed in section 5.4.4 indicates that the majority of backscattered ions suffer minor energy loss, and the effect of considering energy-resolved backscatter sputtering versus non-energy-resolved backscatter sputtering on topography simulations will be investigated in section §5.5.

A polar plot of the energy trend of the backscattered ions is shown in figure 5.4.3 for an incidence angle of 80° . The low energy distributions are noisy due to the limited frequency of low energy emission. This noise should not negatively affect the simulations as it is doubly compensated by the energy distribution $g_{back, Ga|Ga}(\theta_0; E_l)$ and the energy-resolved sputtering yield, both of which act to minimize the magnitude of the product at low energies. Furthermore, as gallium redeposition is neglected in this model, the effects of the noise due to statistically rare events are further minimized. Simulation of a greater number of collisions is feasible in that the visible noise could be reduced through BCA simulations that could be completed in only a number of weeks; however, the noise characteristics are sufficient in these simulations for use as source data for preliminary investigations. With increasing ejection energy the angular data becomes markedly more smooth.

5.4.3 Sputtering Rates as a Function of Species and Energy

Two new cases with regards to energy-resolved sputtering are encountered in the revised model. In the case of sputtering occurring due to backscattered primary ions, the addition of energy resolution necessitates the use of sputtering yields with implantation energies less than the primary FIB energy. As backscatter sputtering was already present in the previous model, the only change in this enhanced model is that energy-resolved sputtering by backscattered ions $Y_{sput, Si|Ga}(\theta_i; E_l)^*$ shall be reduced as compared to the simple model, which assumed that all backscattered ions impinged the target with the simulated FIB energy. As the energies under investigation are in the low to intermediate range, where sputtering is still dominated by nuclear interactions [200], the general trend with respect to decreasing bombardment energy is a reduction in sputtering yield as shown in figure 5.4.4. However, the scaling is not simply linear and the incidence angle θ dependence also changes with decreasing energy, notably seen in a leftward shift of the sputtering yield maximum; therefore, full

*This is a notation used for convenience, only equivalent yields are defined over an energy band as simulated yields are ascertained for discrete monochromatic energies and not bands (see appendix D).

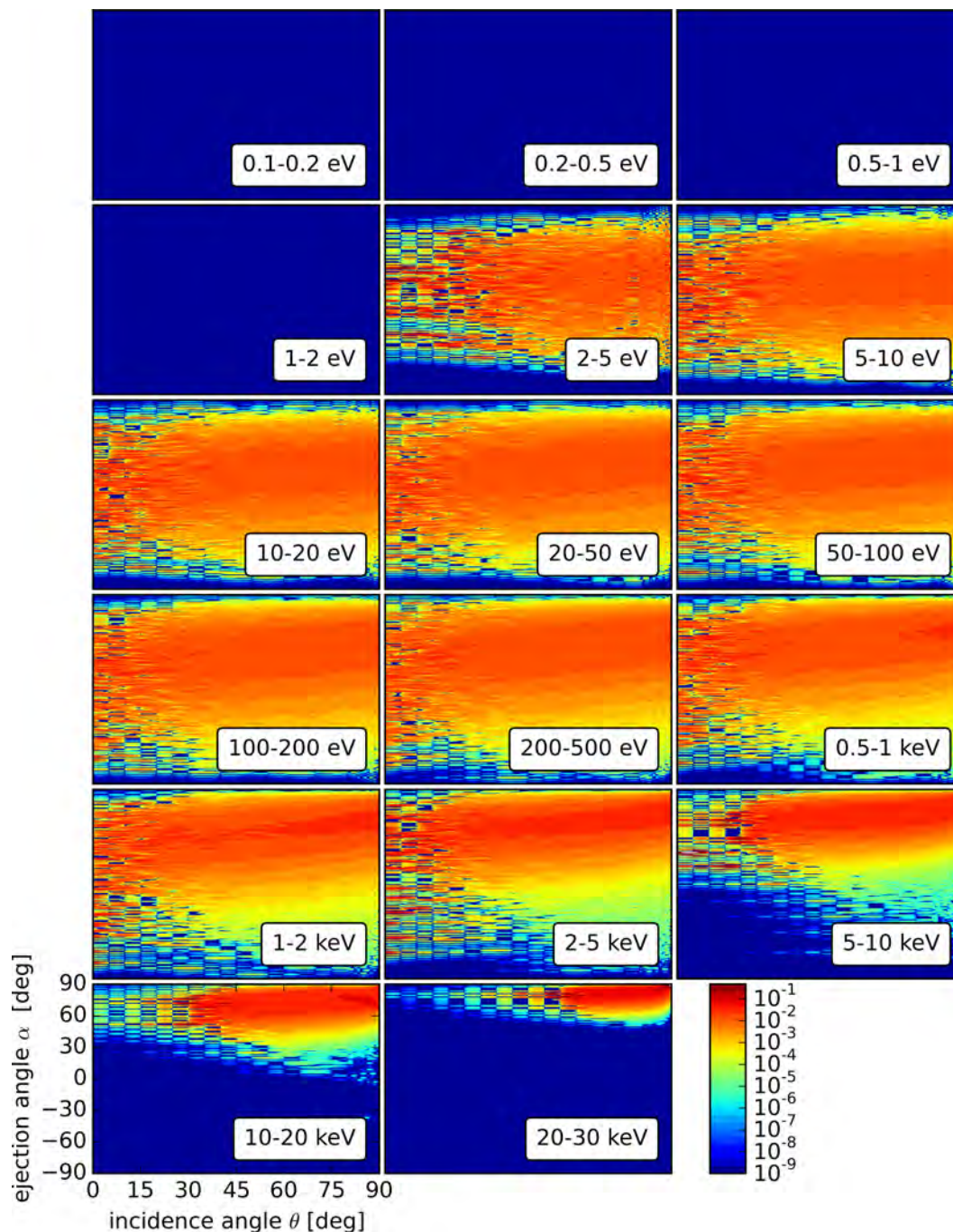


Figure 5.4.2 – Normalized angular backscattering probability distributions $f_{back, Ga|Ga}(\alpha_0, \theta_0; E_i)$ for 30 keV gallium ions striking an amorphous silicon target separated by energy of ejected target atoms. Due to the sharp peaks in the backscatter angular distribution, a log color scale is used. No ion-backscattering events occur with ejection energies less than 2 eV, this is due to the requirement that an ion deposit energy and reverse direction in order to produce a low energy backscattering event. As with the sputtering angular distribution shown in figure 5.4.1, backscattering angular distributions become increasingly distributed around a peak that moves toward higher ejection angles with increasing ejection energy.

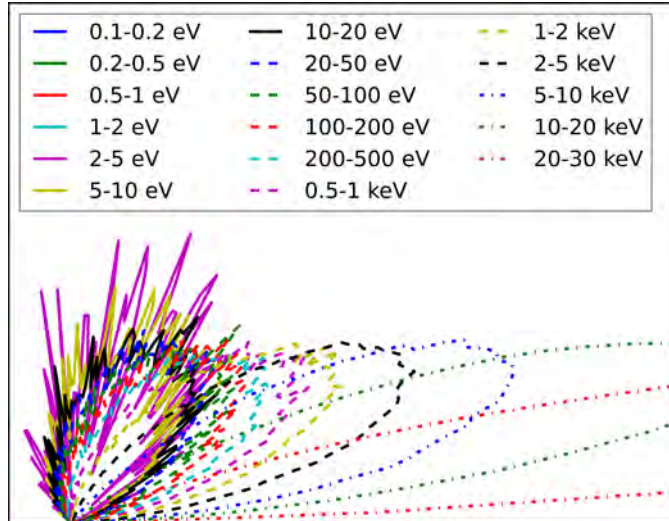


Figure 5.4.3 – A polar plot of the normalized probability that a single backscattered ion in a given energy band will have a desired ejection angle α , shown for a beam-target incidence angle θ of 80° from perpendicular.

simulated yields from BCA are used and no attempt is made to make an analytical approximation. In order to be fully consistent with the results of chapter 4 these yield simulations are carried out using the density gradient model of surface roughness.

Secondly, the yields for silicon atoms sputtering by energetic silicon atoms must also be considered. In the case of silicon both the silicon sputtering yield, the yield of silicon atoms displaced by an energetic silicon atom re-impinging on the silicon target $Y_{sput, Si|Si}(\theta_i; E_i)$, and the backscatter silicon yield $Y_{back, Si|Si}(\theta_i; E_i)$, the fraction of the re-impinging silicon atoms that leave the target must be considered. As shown in equations (5.3.10)–(5.3.12), the energy-resolved yields are used with the construction for equivalent yield to determine the amount of material sputtered or backscattered at the first-order node[†]. In the calculation of the velocity of the first-order node equation (5.3.9) the backscattering yield of silicon indicates the flux of backscattered silicon atoms that are reflected from the target at the first order node. Similar to the gallium backscattering yield at beam energy (shown in section 2.3.1.2) the backscattering yield is incidence-angle dependent, which for gallium at glancing angles can result in complete reflection in the case when the backscatter yield is equal to 1; however, complete reflection is shown to not occur for any incidence angle or energy with silicon backscattering from silicon as seen in figure 5.4.6. Reflexive sputtering is calculated using the sputtering yield for silicon-silicon interactions represented in the equations by the term $\bar{Y}_{sput, Si|Si}(\theta_0, \theta_1, E_l)$, which is also a zeroth-order node dependent equivalent yield. A similar term $\bar{Y}_{back, Si|Si}(\theta_0, \theta_1, E_l)$ for silicon-silicon backscattering is also used.

Sputtering and backscattering yields for silicon impinging on a silicon target are shown in fig-

[†] Additionally these yields are used for the source term of the silicon flux that will be redeposited at the second-order node.

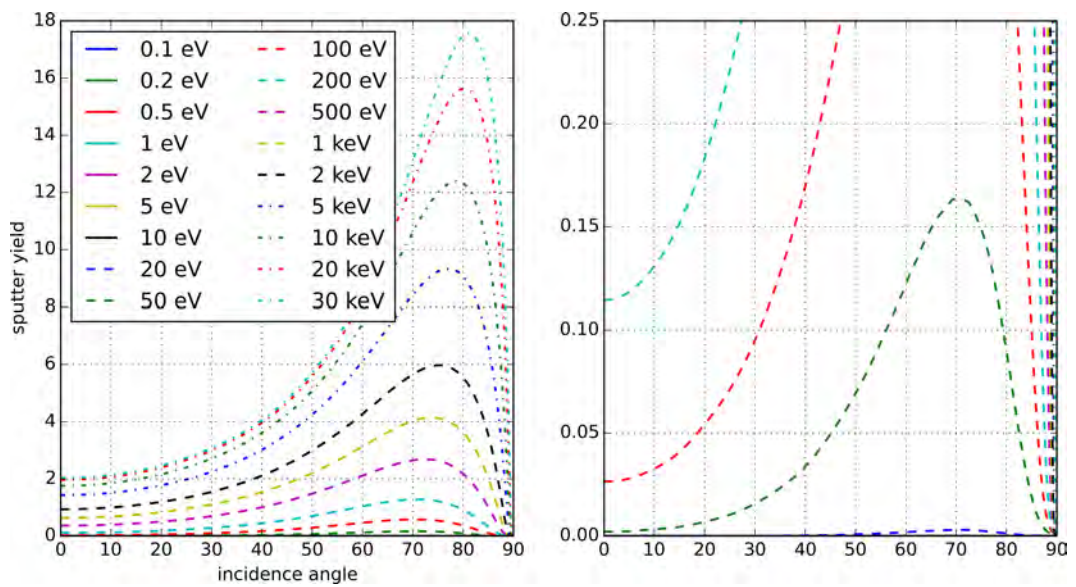


Figure 5.4.4 – The sputtering yield as a function of energy for gallium impinging on pure silicon $Y_{sput, Si|Ga}(\theta_i; E)$. The right side shows a vertical magnification of the data presented on the left side.

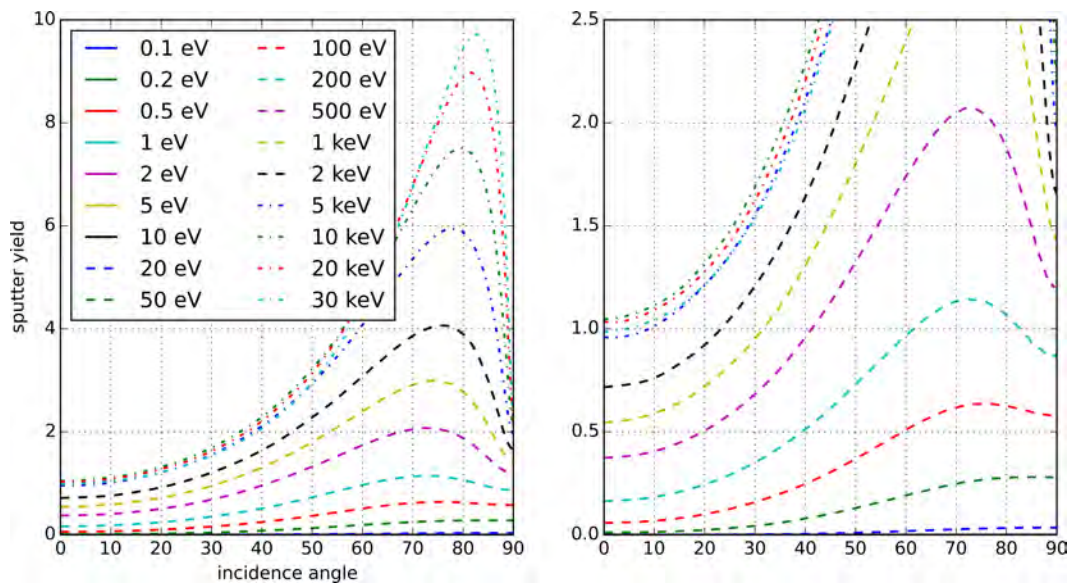


Figure 5.4.5 – The sputtering yield as a function of energy for silicon impinging on silicon $Y_{sput, Si|Si}(\theta_i; E)$. The right side shows a vertical magnification of the data presented on the left side.

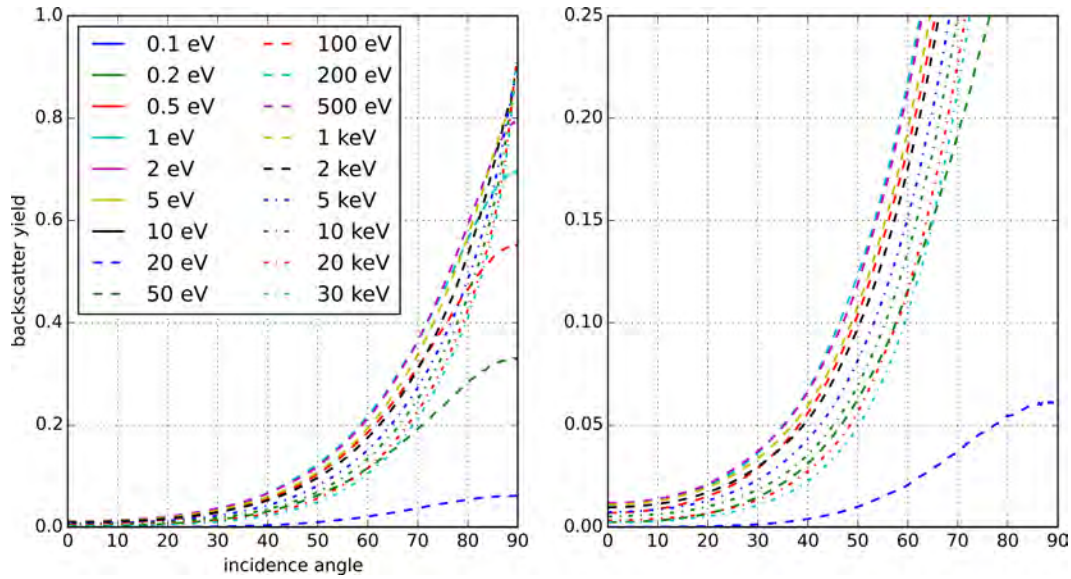


Figure 5.4.6 – The backscattering yield as a function of energy for silicon impinging on silicon $Y_{back, Si|Si}(\theta_i; E)$. The right side shows a vertical magnification of the data presented on the left side.

ure 5.4.5 and figure 5.4.6 respectively. The sputtering yields show similar patterns to the energetic sputtering yield trends shown in gallium when studying the location and movement of the sputtering yield maximum. At extreme glancing angles in silicon the sputtering yields $Y_{sput, Si|Si}(\theta_i; E_l)$ do not return to zero. The attractive force provided by the surface binding energy of the target acts to refract the path of the ion into the target both increasing sputtering and preventing total reflection. The backscattering yield of silicon impacting silicon $Y_{back, Si|Si}(\theta_i; E_l)$ shows some interesting trends. An important feature to note in the backscattering yield is that the yield only truly goes to zero at a perpendicular incidence angles for very low energies. Contradicting the simple sticking coefficient of unity used in chapter 2 for redeposited atoms as nearly half sputtered silicon atoms should have energies greater than 20 eV as was shown in figure 5.1.2. Furthermore, there is an energy dependence among the normal-incidence backscattering rates, with a maximum occurring somewhere between 500 and 1000 eV; however, at the minimum and maximum energy levels shown, 20 eV and 30 keV, both exhibit nearly zero backscattering yield for normal-incidence. Furthermore, due to ion capture, the backscatter rate never goes all the way to unity, indicating that total reflection never occurs when using the rough surface model specified in section 4.4.2.1. In all three sets of energy-dependent yield data a hard minimum energy of 20 eV is used with lower energies being zero-filled. This is due to the BCA simulator IMSIL not being optimized for low energy implantation. While optimizations can be made, they would slow down all of the calculations even at higher energies and it is presumed that assuming a sticking coefficient of unity with zero sputtering for energies less than 20 eV is reasonable. This approximation is further justified by considering that trench geometries dictate that

glancing-angle impact events at a first-order node are likely caused by glancing-angle ejections at the zeroth-order node due to there being two sidewalls for every trench bottom. As was shown in figure 5.4.1, the angular probability for glancing angle ejections is relatively low, especially at the low energies affected by the 20 eV sputtering yield simulation cutoff. The validity of this assumption is, of course, a valid avenue for future research projects.

5.4.4 Energy Distribution of Sputtered and Backscattered Atoms

Energy distributions showing the relative likelihood of finding an ejected particle in a given energy band $g(\theta_0; E_l)$ for sputtered target atoms and backscattered ions are shown in figure 5.4.7 and figure 5.4.8 respectively. The energy distribution of sputtered target atoms can be seen to depend very slightly on incidence angle across the majority of the angular range. As a general trend the portion of the energy spectrum occupied by high energy ejecta increases slightly with increasing incidence angle, as can be seen by the increasing portions at the top of the plot. This increase in the number of high energy events is due to the reduction in cascade depth that occurs at larger incidence angles. As the collision cascade nears the surface, there is a greater likelihood that an energetic collision can lead to sputtering near the surface without requiring further collisions that will reduce the energy of the ejected particle. At less glancing angles (corresponding to smaller incidence angles) the majority of the incoming ions energy is directed into the target, with more energy being deposited at a greater depth. The likelihood of this energy reaching the surface without being attenuated by further collisions is low, and therefore high energy events are more likely to be found at glancing angles among the sputtered target atoms. In the case of backscattered ions this trend is even more apparent as seen in figure 5.4.8. The highest energy, indicated by red, experiences negligible energy loss at extremely glancing angles near $\theta_0 = 90^\circ$. This low energy loss regime is indicative of the gallium ions reflecting off of the silicon substrate and closely corresponds to the increase in the backscatter yield at glancing angles as shown in figure 4.4.7.

The energy distribution of ejecta is used for two purposes in the simulation; primarily as the pre-factor $g(\theta_0; E_l)$ when calculating the yield at an energy level, but also secondarily in the calculation of the weighted mean energy \bar{E} for the equivalent yield as expressed in equation (5.3.13) and equation (5.3.14). Notably the calculation of \bar{E} requires that the energy levels E_l be further partitioned using the geometric mean E_{mid} . Furthermore, the evaluation of \bar{E} is computationally expensive due to the natural logs that must be calculated. Since the midpoint partitions are only used in the calculation of the equivalent yield and can be easily separated from energy-resolved yield evaluations, the entire right hand side of equation (5.3.14) is therefore pre-calculated as a function of incidence angle

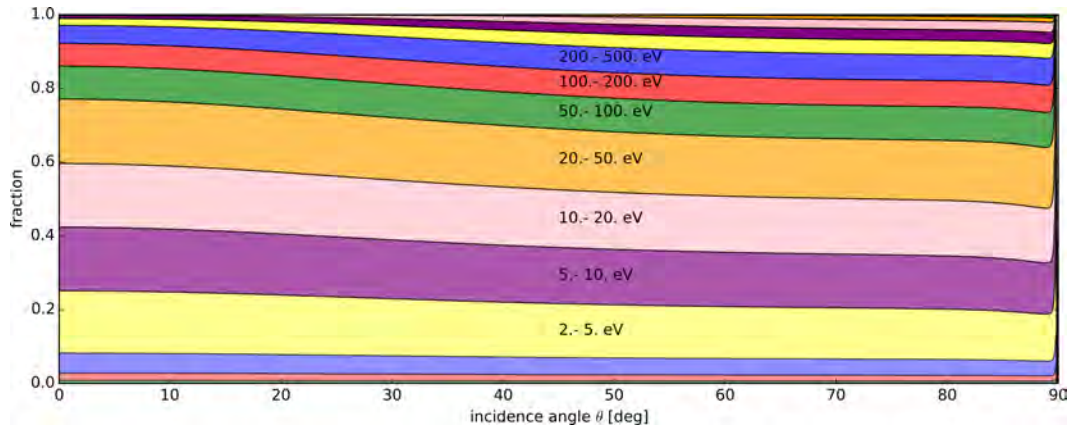


Figure 5.4.7 – The energy-resolved fractional sputtering yield for silicon sputtered by 30 keV gallium as a function of incidence angle. Vertical cut-lines across the color bands show the fraction of silicon atoms ejected in a given energy band. The central pink color band represents the 10-20 eV energy band, the color bands are sorted with higher energy bands at the top of the figure in a 1,2,5 logarithmic scale between 0.1 eV and 30 keV.

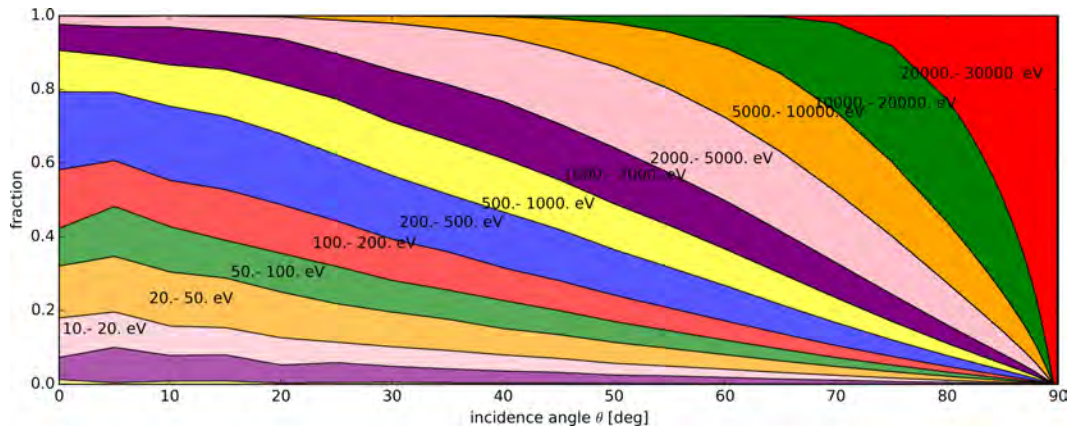


Figure 5.4.8 – The energy-resolved fractional sputtering yield for backscattered 30 keV gallium as a function of incidence angle. Vertical cut-lines across the color bands show the fraction of silicon atoms ejected in a given energy band. The central red color band represents the 100-200 eV energy band, the color bands are sorted with higher energy bands at the top of the figure in a 1,2,5 logarithmic scale between 0.1 eV and 30 keV.

θ as is described in greater detail in appendix D.

5.5 Comparison of Simulation Results to the Simple Model

The preceding sections took time to describe the motivation for extending the sputtering model into the energy domain in order to simulate reflexive sputtering (section §5.1), describe the equations used for flux transfer in the energy-resolved model (section §5.3), and describe and demonstrate representative processed input data derived from BCA simulations that is used to drive the extended model (section §5.4); leaving the lingering question as to the effects of this extended model upon topography simulations. In this section simulated topographies from identical simulated beam pa-

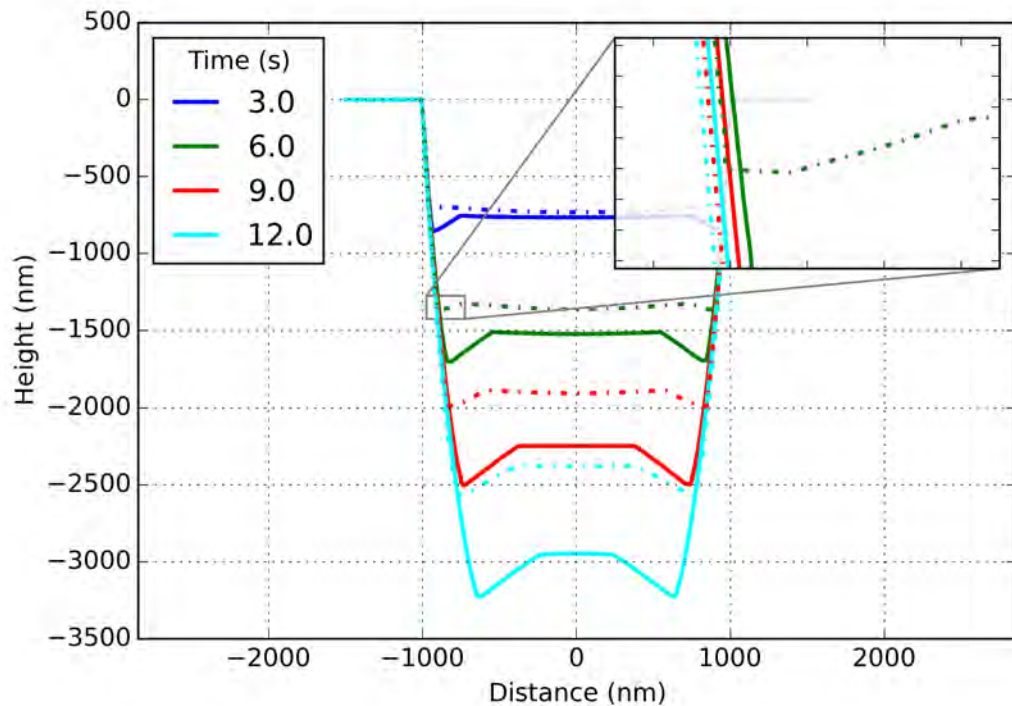


Figure 5.5.1 – Topography simulation making use of the energy-resolved reflexive model [with 3D-effects] (solid line) as compared to the model from chapter 2 (dash-dotted line). Simulation parameters were the same as in figure 2.4.1, except these simulations neglect shadowing (explained in *Shadowing Effects*).

rameters are compared to demonstrate the effect of considering reflexive sputtering upon the resultant simulated topography. Additionally the validity of the earlier assumption of energy independence for the backscattering yield is closely studied by simulating an energy-resolved analog to the simple model presented in chapter 2 that neglects the newly considered effects of reflexive sputtering (a model implementing just energy-resolved backscattering of ions). The presented simulations remain models, and have not been compared to well designed experiments searching for the phenomenon of reflexive sputtering; therefore, these models can only suggest a previously understudied mechanism for sputtering enhancement. However, topographical effects of considering self-sputtering are by no means subtle and the basic physical mechanisms presented in section 5.3.2 are self-consistent with present models of the physical phenomenon of sputtering; therefore, while the presented model is strictly a model, it is a plausible scenario that would lead to enhanced sputtering in the gallium-silicon system. These simulations are not without some comparison to reality and experiment; section §5.7 compares the revised model to an experimental result of an inverse modeling experiment. The revised model incorporating the simulation of reflexive sputtering better, yet still imperfectly, reproduces the effects seen in the experiment lending credence to the plausibility of the presented model.

An energy-resolved simulation implementing reflexive sputtering is shown compared to a non-

energy-resolved model neglecting reflexive sputtering in figure 5.5.1. The simulation implements a $2\ \mu\text{m}$ wide scan width with a simulated gallium beam having a $FWHM$ of $15\ \text{nm}$ and a current density of $5\ \text{mA}\cdot\text{cm}^{-2}$; the simulated beam is implemented using the overlapped beam as described in section §3.4. Use of the overlapped beam corresponds to an experiment completed in a large number of passes (over the $2\ \mu\text{m}$ scan width), where the duration of a single pass is negligible as compared to the experiment duration, thus the simulation operates in the limit at which scan speed effects may be neglected. Furthermore, these simulations only implement simple visibility and not the more complete shadowing algorithm. It is shown in *Shadowing Effects* (section §B.1) that while the effects of neglecting shadowing can be seen in the simulation results, they do not affect the findings of the current simulations. All presented simulations use input parameters derived from the same set of BCA simulations, meaning that they share statistical data for the condition of $30\ \text{keV}$ gallium impinging on an assumed amorphous silicon target that includes surface roughness with a thickness of $8.27\ \text{\AA}$ as implemented by the density gradient model described in section 4.4.2.1. Energy-resolved models are presented including the correction factor for 3D-effects as implemented using the parallel virtual wall model described in *Validity of 3D Simulations* (appendix A).

As figure 5.5.1 shows, the initial response at low doses (3.0s cumulative exposure shown in blue) for both the new energy-resolved reflexive sputtering model (solid lines) and the simple non energy-resolved model described in chapter 2 (dot-dashed lines) is very similar as far as total milling volume; however, the reflexive sputtering simulation shows more pronounced micro-trenching even at low aspect ratios of approximately 1:2. As dose increases (6.0s cumulative exposure shown in green), both sets of simulations begin to exhibit micro-trenching as emphasized by the magnified inset for the non-energy-resolved model. Characteristic in the micro-trenching that occurs in all subsequently shown doses, the width and sharpness of the milled micro-trenches in the energy-resolved model are wider and less pronounced albeit exhibiting greater magnitude than those produced by the non-energy-resolved model. This reduced sharpness is due to the broader width of the angular distribution peaks for energetically sputtered atoms as compared to backscattered ions, as shown in figure 5.4.1 and figure 5.4.2. Another perceptible difference between the simulated topographies produced by either model is the steeper sidewall angle for a given depth; though this trend is difficult to see in the simplified test case, it is very apparent in the comparison to the inverse modeling experiment shown in figure 5.7.1. Finally, the total milling efficiency with respect to both depth obtained and volume milled increases by as much as approximately 28% as compared to the non-energy-resolved model. This validates the hypothesis made in section §5.1 that sputtering due to secondary impacts of sputtered target atoms can have a perceptible effect, thereby justifying the construction of this new model. Notably, even with this enhanced sputtering due to reflexive sputtering, the total simulated

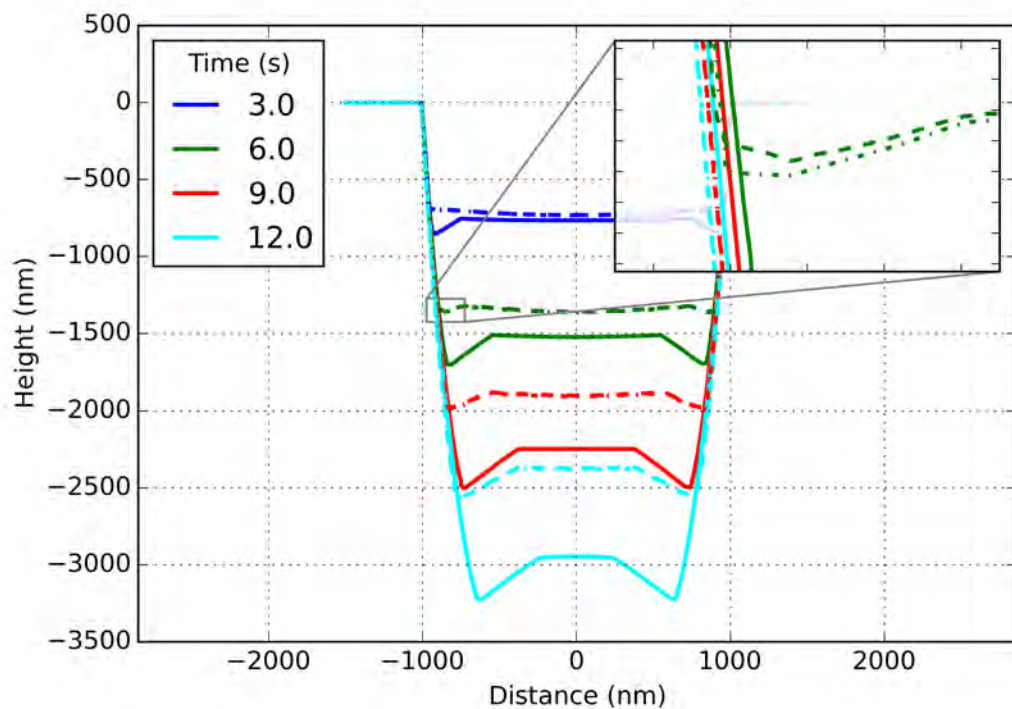


Figure 5.5.2 – Topography simulation making use of the energy-resolved reflexive model (solid line) as compared to the model from chapter 2 (dash-dotted line), as further compared to an energy-resolved model with no reflexive sputtering [energy-resolved backscattering only] (dashed-line). Shared simulation parameters were the same as in figure 2.4.1, except these simulations neglect shadowing (explained in *Shadowing Effects*). Energy resolved simulations implement the correction for 3D-effects.

milling volume is still less than that expected by simulations neglecting redeposition, as shown in figure 2.4.1; therefore, this model remains within the bounds of reason.

A secondary effect of the energy-resolved model is the change made with respect to the consideration of sputtering due to backscattered ions, which is in the new model now simulated taking into account the energy-distribution of the backscattered ions as compared to the assumption made in chapter 2 that the backscattered ions suffer no energy loss as they are re-emitted by the target. In figure 5.5.2 this assumption is evaluated by comparing three models; the full reflexive sputtering model, the simplified model from chapter 2, and an energy-resolved model showing only the fluxes considered in chapter 2. Specifically the newly compared model, referred to as the energy-resolved model without reflexive sputtering (only energy-resolved backscatter sputtering by ions), calculates first-order sputtering and redeposition in the same manner as the chapter 2 model with the addition of energy-resolved sputtering from backscattered ions and the resultant second-order redeposition. This energy-resolved analog for the simple chapter 2 model (shown as dashed lines in figure 5.5.2) is expected to closely mirror the chapter 2 model* (dash-dotted lines), as it can be seen to do in

*Since it was argued that the energy distribution of backscattered ions was negligible, the expected magnitude of any differences are also expected to be small. Furthermore, using the correct energy distribution reduces the number of high-

figure 5.5.2; in fact the difference between the simple model and its analog are not visible when plotted at full scale and a magnified inset is required to see any differences. The magnified inset shows that the energy-resolved model without reflexive sputtering shows a slight reduction in milling depth, consistent with there being a measurable amount of energy loss as the backscattered ions change direction in the target. However, the assumption made in chapter 2 that the energy loss of backscattered ions is mostly negligible appears to be valid in most cases as the total effect towards the simulation results is quite small; the effect is diminishingly small when compared to the effect of not considering reflexive sputtering.

5.6 Comparison to Simpler Approximations of Reflexive Sputtering

As discussed in section §5.5 the extended model considering energy-resolved reflexive sputtering exhibits a tangible effect on simulated topographies, and while experimental evidence is still wanting, the plausibility of the model has been confirmed. There is, however, a significant drawback to the canonical form of the model presented in section 5.3.2, namely the performance of the simulations. While the presented model has been parallelized using accumulators for each energy level of the computation, there still exists a sizable performance delta between the non energy-resolved model and the presented energy-resolved model. This performance delta in terms of computational effort scales as a function of the number of evaluated energy levels with the presented model taking approximately 5x the CPU time as the single thread simple model even on an 8-core (16-threaded) workstation. This significant performance delta justifies the effort of determining whether the model must truly be as complex as it is presented. Two approaches are undertaken to investigate simpler formulations of a model involving reflexive sputtering; the first questions whether energy-resolved angular distributions might be neglected (presented in section 5.6.1) as these angular distributions must be evaluated between every source and destination ($\approx N^2$ where N is the number of simulation nodes) for each energy band, the second approach decreases the number of required energy bands by combining bands with similar angular distributions (presented in section 5.6.2). The result of this simplification study is to show that an approach neglecting the change in angular distribution with energy is *completely erroneous* and does not replicate the higher order model; however, compression of the number of energy bands used in the simulation represents a tenable optimization avenue.

energy backscattered ions available to prompt sputtering, therefore the total amount of backscatter ion induced sputtering is reduced.

5.6.1 Simulations Neglecting Energy-Resolved Angular Distributions

The model approximation in this section is an example of a proof by contradiction. The development of the canonical model presented in section 5.3.2 *assumes*, based on the appearance of the statistical data from BCA simulations, that precise treatment of the angular distribution is necessary to accurately describe reflexive sputtering. In this section a plausible counter model presuming that the angular distribution may be neglected is developed and shown to be ineffective; this demonstration does not, of course, indicate the validity of the energy-resolved model; however, it does highlight the importance of the dependence of the angular distributions upon ejection energy.

In the formulation of a counter-model that does not depend on an energy-resolved angular distribution the equations of motion for the canonical models are modified, where specifically the angular distribution of backscattered $f_{back, Ga|Ga}(\alpha_0, \theta_0)$ and sputtered $f_{sput, Si|Ga}(\alpha_0, \theta_0)$ atoms are taken to be independent of energy. The energy-resolved flux of silicon atoms at a first-order destination node $F_{Si, 1}(\alpha_0, \theta_0, \theta_1; E_l)$ in the model presented in section 5.3.2.2 is dependent on energy by two quantities; the primary incidence angle dependent energy distribution $g_{sput, Si|Ga}(\theta_0; E_l)$ and the energy-resolved angular distribution $f_{sput, Si|Ga}(\alpha_0, \theta_0; E_l)$. In this counter model it is assumed that the angular distribution of sputtered atoms does not change across energy bands and therefore $f_{sput, Si|Ga}(\alpha_0, \theta_0; E_l)$ can be simplified to $f_{sput, Si|Ga}(\alpha_0, \theta_0)$. Gallium backscatter terms also experience a similar simplification with $f_{back, Ga|Ga}(\alpha_0, \theta_0)$ replacing the energy-resolved term $f_{back, Ga|Ga}(\alpha_0, \theta_0; E_l)$. The remaining energy-resolved term $g_{sput, Si|Ga}(\theta_0; E_l)$ is left unchanged (the corresponding backscattered gallium term is also left unmodified as $g_{back, Ga|Ga}(\theta_0; E_l)$), furthermore the equivalent yields \bar{Y} (for both silicon and backscattered gallium) are also still taken to be functions of energy. While it is possible to derive an even lower-order model and further remove energy dependence through numerous approximations (such as a bi-level approximation of energy distributions), said approach does not answer the question as to the necessity of an ejection-energy dependent angular distribution in the manner that this model does.

As the second-order silicon flux (equation (5.3.15)) is already independent of the angular distribution, except where it uses the first-order fluxes as inputs, no further changes are needed to reformulate the model.

Simulation results of the reformulated model including 3D-effects (see *Validity of 3D Simulations*, appendix A) are shown in figure 5.6.1, as compared to the canonical model including 3D-effects, as further compared to the simple model presented in chapter 2 (neglecting 3D-effects). 3D-effects are not included in the simple model as the simple model acts as a benchmark; furthermore, the 3D effects are not implementable without energy distributions. As can clearly be seen from the figure,

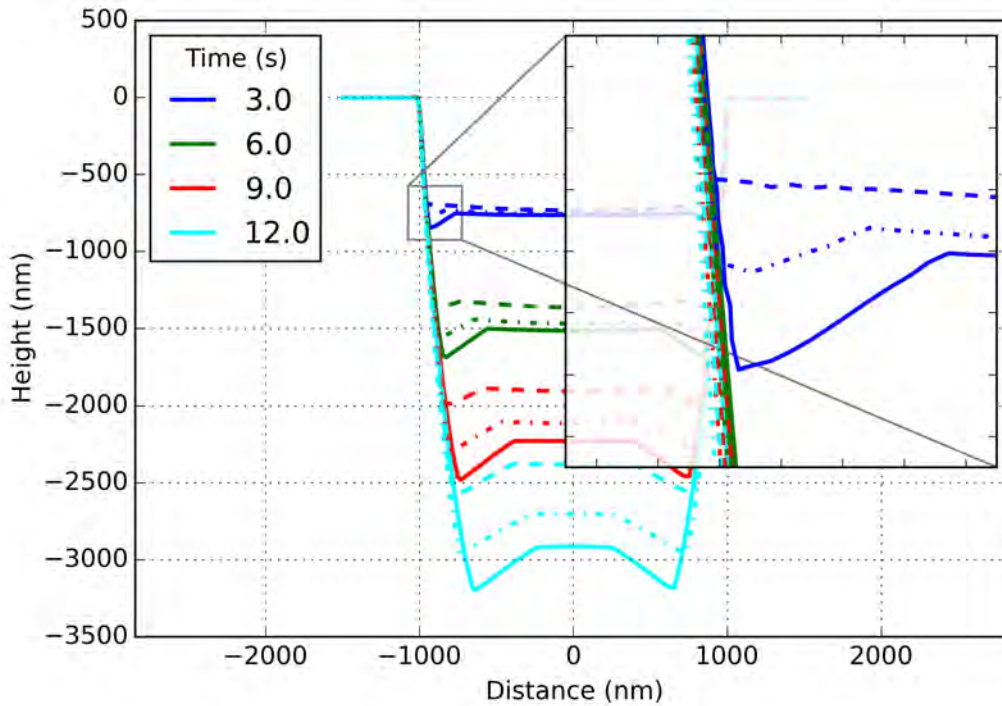


Figure 5.6.1 – Topography simulations comparing the canonical model (solid line) [with 3D-effects], the model for reflexive sputtering neglecting energy-resolution in the angular distribution (dot-dashed line) [with 3D-effects], and a non-energy-resolved model from chapter 2 (dashed line) [neglecting 3D-effects].

the model neglecting to implement energy-resolved angular distributions shows a large discrepancy to the canonical model presented in this chapter; however when compared to the simple model, the non-energy-resolved angular distribution model exhibits an intermediate response between the canonical and simple model from chapter 2.

This simplified model compares very poorly with the canonical model and the large mismatch between simulation results can be explained through consideration of the sputtering angular distributions. In the counter-model, the summed total average angular distribution across all ejection angles was used. This average distribution exhibits roughly a cosine distribution with respect to ejection angle α ; in fact a cosine distribution is used as an approximation for second-order redeposition fluxes in both the simple model (equation (2.1.5)) and the canonical energy-resolved model (equation (5.3.15)); however, the energy-resolved angular distributions at high ejection energies are notably non-cosine with a heavy weighting towards glancing ejection angles. Furthermore, the energy distributions as a function of incidence angle θ_0 indicate that the population of high energy ejections only increases at glancing primary incidence angles. In the trenches used in the test case the counter-model fails in both conceivable scenarios for second-order sputtering. In the first case, where a beam impinges on the flat portion of the trench bottom, the likelihood of reflexive sputtering

is very low due to the fact that where the angular distribution is relatively high (small ejection angles, near normal), there is only vacuum and energetically ejected target atoms will encounter nothing with which to sputter; furthermore, at the near normal incidence angles as presented at the bottom of the trench the population of high energy ejections is small as indicated by $g_{sput, Si|Ga}(\theta_0; E_l)$ in figure 5.4.7. In the other conceivable case of irradiation along the trench wall it is clear that there is a high likelihood of energetic target atoms being sputtered due to the glancing incidence angle and the energy distribution $g_{sput, Si|Ga}(\theta_0; E_l)$; however, most of these energetic particles still emerge nearly normal to the surface (again due to the cosine-like nature of the non-energy-resolved angular distribution $f_{sput, Si|Ga}(\alpha_0, \theta_0)$), thereby causing sputtering mostly on the opposite trench wall, which is almost totally counteracted by cosine redeposition from that wall. An increase of trench width is also visible in the simplified model presented in this section, this increase in trench width is likely due to the cosine-similar angular distribution of sputtered silicon atoms for the reasons already expressed. It should therefore be clear that energy resolution of the angular distribution is essential to the correct modeling of reflexive sputtering; this counter-model indicates that the terms in the model are near their simplest forms. However, the terms of the equations of motion are not the only area of model optimization. The choice of energy levels in the canonical model fit a first approximation of the data as the energy distribution is roughly linear in logarithmic intervals; however, there is no compelling argument for equal-sized populations per energy band or the use of 3 bands per decade, and it could therefore be possible to further optimize the choice of energy bands—as is discussed in the following section.

5.6.2 Simulations Compressing Similar Energy-Resolved Angular Distributions

In the previous section (section 5.6.1) it was demonstrated that the changing shape of the angular distribution of ejected particles as a function of ejection energy is important to accurate simulations considering reflexive sputtering. It was also mentioned that the canonical form presented in section 5.3.2 used logical but essentially unoptimized criteria for the selection of the energy levels over which to partition the BCA data; this fact is clearly seen in figure 5.4.1, where the first few energy bands are basically indistinguishable from each other. As the computational complexity of the simulation increases linearly with the number of evaluated energy bands, it is worthwhile to explore whether the number of energy bands may be reduced. The canonical formulation of the energy-resolved model simulating reflexive sputtering makes use of energy bands described by their endpoints starting at 0.1 eV and following a 1, 2, 5, 10... progression approximating logarithmic spacing to the beam

energy of 30 keV; in the preliminary attempt at optimization of the selected energy bands the following series is used 0.1 eV, 5.0 eV, 50.0 eV, 200.0 eV, 500.0 eV, 1.0 keV, 2.0 keV, 5.0 keV, 10.0 keV, 20.0 keV, to 30.0 keV. This new series of energy partitions reduces the total number of energy bands to evaluate from 17 in the canonical model to 11 in the reduced set, which should lead to a near halving of computational effort. The energy intervals were chosen by eye after inspecting figure 5.1.1, where the angular distributions between 0.1 eV and 5.0 eV were determined not to strongly vary, the second interval (5.0-50.0 eV) was chosen to correspond with the strong onset of the rotation of the first-knock-on peak, while the last conjoined interval (50.0-200.0 eV) represents the final range that exhibits distribution shapes resembling a skewed and rotated cosine added to a sharp peak, after 200.0 eV the canonical logarithmic partitioning is used.

New physical input data was extracted from the BCA simulation trajectories including a new set of 3D corrections factors (*Validity of 3D Simulations*) using the reduced set of energy intervals. These physical inputs were used to conduct benchmark simulations of the type described in section §5.5; the comparison between the compressed dataset and the canonical dataset is shown in figure 5.6.2 using 3D correction factors but neglecting shadowing effects. The difference between the simulations is nearly imperceptible without magnification and the compressed set of energy intervals reproduces the canonical data with less than 0.5% error. The error is expected to be a slight under-estimation* of reflexive sputtering or secondary sputtering due to energetically ejected target atoms, as the interesting portions of the backscattered ion energy distributions are undisturbed by the compression of the energy bands (as the backscatter ion-distribution is mostly high energy). Furthermore, this technique is a valid optimization vector as the run-time reduced by nearly a factor of two for the compressed simulations when compared to the canonical simulations. Further optimizations in this regime, as the optimization criteria could very likely be further refined, are an interesting avenue for future research.

5.7 Comparison to Experimental Deep Trench

The final test for the extended model presented in this chapter is a comparison to the anomalous experimental data mentioned in section §3.6 (3.6.1 on page 70), whereby an inverse modeling experiment failed to match simulation by a large factor that could not be explained simply through experimental error or imprecise physical inputs. The experimental data shown in figure 5.7.1 shows how a number of factors of the experimental trench failed to match the expected profile (shown in

*Underestimation is expected because the optimization of energy bands is accomplished by reducing the sampling at low energies where only marginal sputtering is expected to occur. As the weighting of the equivalent yields (appendix D) occurs through fitting a decaying exponential function, an increase in the sampling ΔE would push a greater portion of the yield to the low energy side of the energy band thus reducing the calculated equivalent yield.

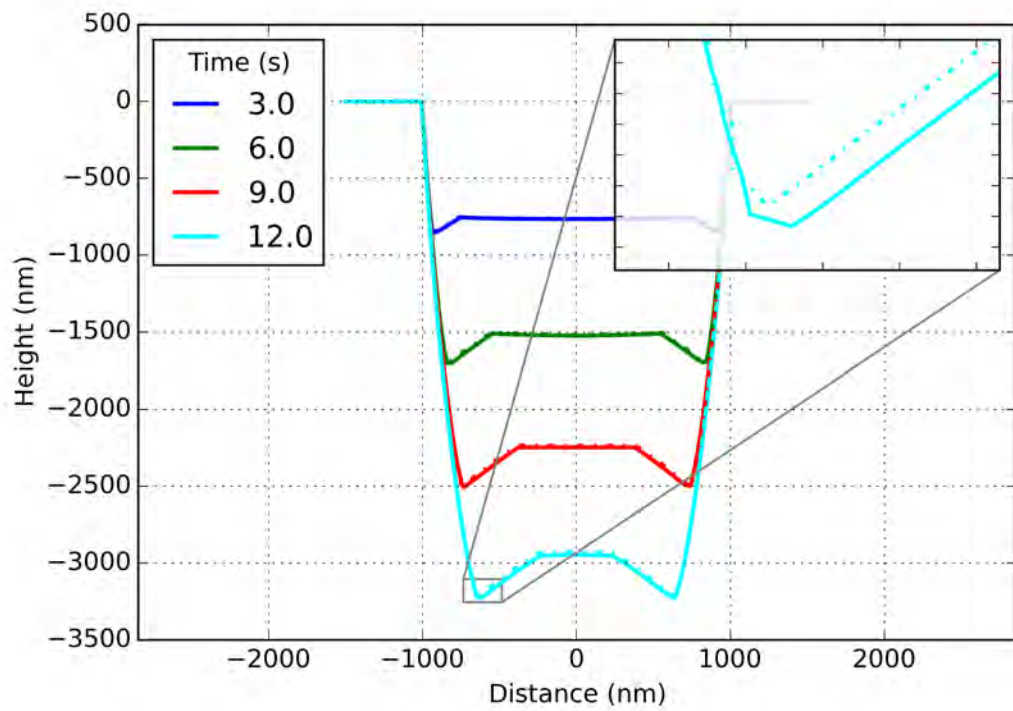


Figure 5.6.2 – A comparison between simulations conducted with the canonical formulation for energy levels (logarithmic indicated by a solid line) and the hand optimized energy levels (described in text, data indicated by a dashed-dotted line). Total error between simulations is $< 0.5\%$ with the hand optimized dataset leading to a near 50% reduction in computational effort. Both simulations compensate for 3D-effects.

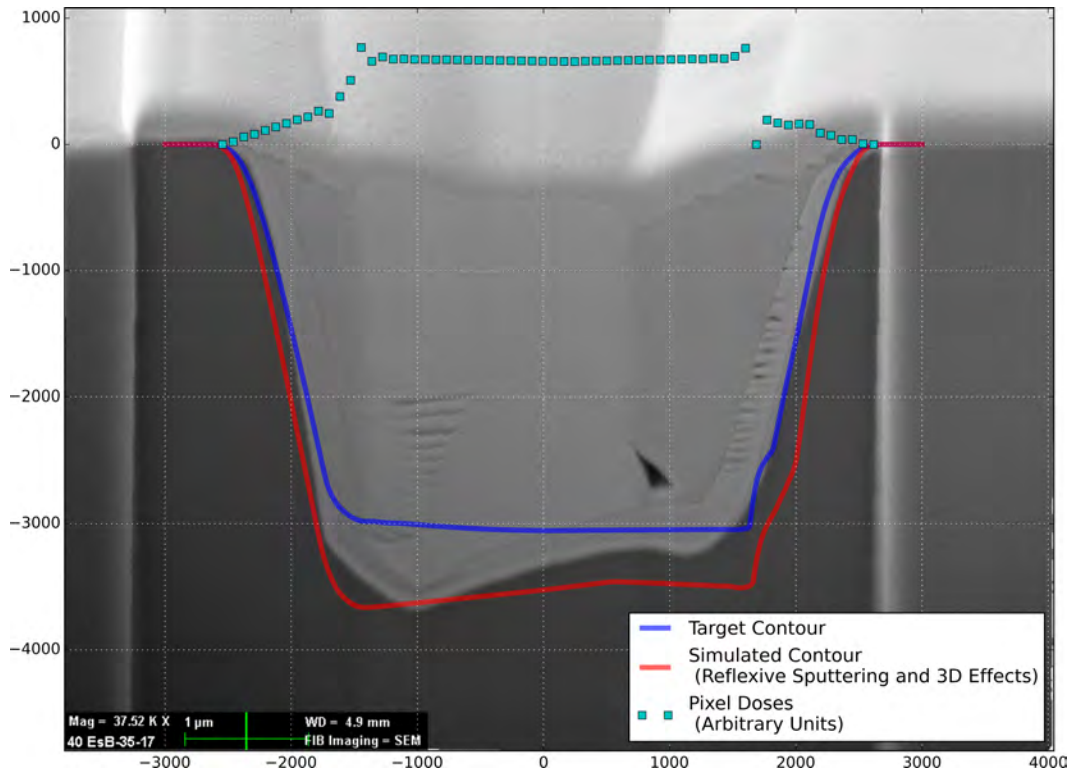


Figure 5.7.1 – The input parameters specified for the experiment presented in section §3.6 are shown here, in a simulation including the reflexive sputtering model and 3D effects. The depth prediction shows good quantitative agreement. Qualitatively the asymmetry and the location of the inflection point of the asymmetry on the trench bottom is reproduced.

blue). The simulation results of the energy-resolved model including 3D effects and reflexive sputtering are shown by the red contour. This contour does not completely agree with the experimental data; however, compared to the model discussed in chapter 2, the new model shows much better qualitative agreement with the experiment. The new model reproduces the unexpected asymmetry and micro-trenching seen in the experiment. The milled volume and sidewall angles also show slightly better agreement to the experiment. While a better experimental fit would be desired, the quality of this unoptimized fit to the model should not be discounted as this experiment is conducted under wide aperture and high current conditions. There are many experimental uncertainties from charging, depth of focus, beam-shape, and beam symmetry under such experimental conditions. Furthermore, the compensation model for 3D-effects presently used in these simulations (see *3D Effects with Reflexive Sputtering Model*) is known to be a primitive first-approximation. Therefore, while this single experimental comparison is promising, there is still a need for deliberate experimental data studying the effects of reflexive sputtering in the gallium on silicon system. The energy-resolved model presented in this text will remain only plausible until more experimental or alternative simulation techniques either support or disprove the modeled phenomenon.

Chapter 6

Conclusion and Outlook

A number of topics have been covered in the preceding chapters, from a justification for studying FIB sputtering through simulation (chapter 1), to an explanation on how to use hybrid-continuum-BCA simulations to track topography evolution (chapter 2), to practical applications of a topography simulator in the form of inverse modeling (chapter 3), to focused BCA studies indicating the importance of surface roughness considerations in sputtering simulations (chapter 4), and finally culminating in the presentation of a new model for topography simulation studying the hitherto unquantified phenomenon of reflexive sputtering (chapter 5). In this short conclusion the important discoveries of each chapter are highlighted with regards to their technical or scientific importance, the viability of the hybrid simulation approach upon which this work is based is shortly analyzed, the hybrid approach is questioned when compared to alternative methods of sputtering simulation, the *post-facto* utility of these simulations is investigated, and the remaining directions for both scientific and technical inquiry are explored.

6.1 Discoveries

In this dissertation a functional hybrid topography simulation combining a continuum model and sputtering statistics derived from BCA simulations was presented in two forms. A simple scale-invariant (figure 2.5.1) hybrid model exhibiting the accepted phenomena of primary sputtering, redeposition, secondary sputtering due to backscattered ions, and secondary redeposition was described and demonstrated to be functional in modeling said phenomena and represents the state of the art local model at the point in time when this research was conducted (chapter 2). An extended model (chapter 5) that additionally considered the less studied phenomena of secondary sputtering due to energetically ejected target atoms (reflexive sputtering) and the coinciding redeposition was also

described and evaluated with respect to the state of the art. The extended model was found to exhibit increased sputtering ($\approx 28\%$ increase in depth) as compared to the simple model (figure 5.5.1), especially at greater aspect ratios when primary sputtering loses dominancy over redeposition. Experimental evidence implies that the simple model is deficient (figure 3.6.1), and while the extended model is also imperfect compared to the limitedly available experimental data, the extended model provides a better qualitative representation of the experimental data (figure 5.7.1).

A robust method of inverse modeling utilizing the demonstrated hybrid model was demonstrated (figure 3.5.1) and provides a practical application for the described forward simulation. This inverse modeling method was shown, experimentally, to be able to produce user-defined low aspect ratio structures having the shape of a cylindrical micro-lens. Higher aspect ratio structures were less successful (figure 3.6.1) and became part of the impetus to explore the extension of the forward simulation to a model that considered reflexive sputtering. As the experimental collaboration ended before the completion of the extended model, no inverse modeling has been attempted with the extended reflexive sputtering model. Preliminary optimization studies indicate that the canonical definition for the selection energy levels in the reflexive sputtering model is non-optimal and extensive optimization while retaining functionality may be possible (figure 5.6.2); therefore, use of the presented inverse modeling algorithm with the extended model remains feasible for future research.

Finally the parameters for BCA simulations were optimized to best represent experimental sputtering yield data (figure 4.4.7) conducted across many incidence angles including extremely glancing angles, where it was found that a degree of simulated surface roughness was essential in order to reproduce experimental sputtering yields at glancing angles. This discovery was shown to be roughly independent of the choice of simulated roughness model (section 4.4.2.2), in that it was possible to fit multiple roughness models to the experimental data. However, the compared roughness models disagree as to the predicted thickness of the layer emulating surface roughness; therefore, the fitting factors cannot be used to predict what experimental values of surface roughness one would expect to find after ion-beam irradiation. Analysis shows that the disagreement between roughness models is likely due to minimum wavelength restrictions present in one of the compared roughness models; that is not found in the 1D roughness model. Both models were shown to have a perceptible effect on the angular probability distribution of sputtered atoms (section §4.5) indicating that surface roughness also affects higher order terms than the simple sputtering yield.

Angular probability distributions for sputtered and backscattered atoms were also shown to exhibit a strong dependence upon the ejection energy of the sputtered or backscattered atoms (figure 5.4.1). Higher ejection energies exhibited a less cosine distribution and a more sharply directed probability distribution that was projected to more glancing ejection angles with increasing energy. This variance

in the angular probability distribution as a function of ejection angle provided the groundwork for the extended model implementing reflexive sputtering, as the change in angular distribution leads to pseudo-focusing of energetic sputtered atoms or backscattered ions which have sufficient energy to incite sputtering. Though the result of this work is to show that 30 keV gallium impinging on silicon may produce non-negligible amounts of reflexive sputtering, it should be remembered that these results are only applicable to the gallium-silicon system at this beam energy (30 keV). Furthermore, it was shown that low aspect ratio features such as those resulting from low total doses exhibit minimal reflexive sputtering effects.

6.2 Viability of Hybrid Simulation Approach

A question that has not been seriously addressed in this text is whether the hybrid simulation approach itself is viable. To answer this question the goals of the simulation should be carefully defined. Scientifically a goal for the hybrid simulation is to have an approach that enables the systematic study of the phenomena under investigation. In this respect the presented models, both the simple model and the reflexive sputtering model, are quite viable. The separate simulation of each flux used in the model allows for quantification of each individual simulated flux, as was shown in numerous comparisons throughout this text. In many ways this explicit separability due to the continuum definitions is more advantageous than attempting the same with dynamic BCA or MD simulations, as these atomistic simulations would require the use of completely non-physical heuristic approximations in order to separate out the influence of higher order fluxes*. For example in order to run a simulation without reflexive sputtering in a dynamic BCA simulation, one would be forced to detect high-energy sputtered particles and procedurally lower their energy below the sputtering threshold. *Maintaining the ability to make such changes would have an impact on the design of simulation code written to perform dynamic BCA simulations.* The hybrid model approach therefore enables systematic analysis of the model used in the simulation from a scientific standpoint. If the hybrid continuum model needs to be extended, however, the complexity of the hybrid model will only increase, which increases the likelihood of both implementation errors and model derivation errors. As an example, the presented model neglects the volume change due to implantation of the primary ion. While it is certainly possible to extend the model to include implantation, this change represents a considerable increase in complexity for a phenomenon that is automatically handled by the dynamic-BCA software IMSIL [122]. Therefore, while the hybrid approach to simulation is presently valid for studying the

*Obviously this could be done in BCA or MD, but the architecture of continuum models makes these non-physical separations more intuitively simple.

covered phenomena scientifically, it seems indubitable that at some point in the future the models will become so complex as to be un-extensible.

The other metric by which the hybrid simulation point must be evaluated is its industrial viability, whereby the question of whether for known phenomena, where prediction of final topographies are desired, does simulation offer an advantage to physically performing an experiment? In the case of performance the answer becomes complex. Simulations currently take orders of magnitude more time to compute than the corresponding scan parameters take to be milled using a physical FIB. However, when one includes the analysis time needed to cross-section an experimental sample to determine what was milled, the total time investments are similar, and multiple simulations can be run inexpensively across multiple workstations, thus providing a net win for simulation. By this same token, when a target topography is desired, the time investment in using inverse modeling is significantly smaller than the human effort required to hand-optimize a dose profile experimentally and repeatedly perform cross-sectional analysis. The current inverse modeling method and hybrid simulation approach is therefore industrially viable in the case of high-value projects. The hybrid approach, when coupled with inverse modeling, does not yet represent the ideal of an enabling technology by which a minimally trained operator might define and optimize a target geometry in the time that it takes the instrument to reach an operational level of vacuum. However, this lack of speed is mostly due to a lack of optimization and design for performance, and it is plausible to increase the speed of the simulations for both inverse modeling (section 6.5.2) and the forward modeling (section 6.5.5) portions.

6.3 Complexity “Is This Method Optimal?”

As mentioned in section §6.2, the complexity of the extended model is significant and additional extension of the model, as will be suggested in sections 6.5.3 to 6.5.5, will only act to increase this complexity, begging the question of when complexity outweighs the value gained through complexity. The implementation of the reflexive sputtering model saw an increase in the number of defined data files from 4 files used in the simple model presented in chapter 2 to 175 files used in the canonical model for reflexive sputtering. Mild optimization of the number of energy levels (as described in section 5.6.2) reduced that number to 135 files. Extrapolating to an implementation of a hybrid model including implantation effects would suggest another order of magnitude of complexity as statistical properties for different compositions of target-ion mixtures must also now be considered. The complexity of implementing a hybrid continuum model quickly becomes the limiting factor, especially when compared to atomistic simulations such as dynamic-BCA simulations, as characterized by the

dynamic mode of IMSIL [122]. These dynamic-BCA simulations by virtue of their atomistic nature automatically consider the effects of implantation and correctly track the energy and trajectory of all sputtered particles, thereby removing the requirement for complex models for each matter flux. The 1D surface roughness model described in section 4.4.2 could even conceivably be applied to 2D and 3D dynamic-BCA simulations, thereby relaxing the resolution required to track topography evolution. One major limitation of pure dynamic-BCA simulations is, however, their speed. Even though dynamic-BCA simulations for sputtering could be amenable to parallelization, they remain at least an order of magnitude slower than models based on the hybrid approach; therefore, hybrid approaches will remain optimal when simulation speed is important. Due to the complexity of these hybrid simulations, however, it is unlikely that much advancement or optimization will be done in the future without a clear and defined industrial purpose requiring the offered speed benefits.

The other conceivable atomistic solutions would be to attempt to simulate sputtering with MD or Density Functional Theory (DFT). Both of these simulation methods are sub-optimal when compared to either dynamic-BCA or the hybrid-continuum-BCA approach, as they are *even slower*[†] than dynamic-BCA. In terms of accuracy, MD offers the promise of better characterization of low-energy scattering events but it requires significant complexity to model electronic stopping. DFT should in theory handle electronic stopping in a rigorous manner; however, currently it is impractical to simulate more than a few hundred atoms, which corresponds to a target volume of $\approx 2 \text{ nm}^2$. The only reasonable comparison is therefore between the hybrid model and a pure dynamic-BCA simulation.

6.4 Utility

The final question to be addressed is the utility of this work, what benefit can be said to have come from this body of work to the scientific community. First and foremost this work highlights the hitherto less than explicitly studied effect of reflexive sputtering by previously sputtered target atoms. Previous hybrid approaches and non-atomistic formulations for sputtering theories assume that sputtered target atoms contribute wholly to redeposition and that high energy ejections are rare enough to be neglected. This work and the results of simulations presented herein showing the effects of considering reflexive sputtering on simple trench geometries very much brings that assumption into question. The primary utility presented by this work is to bring awareness that an additional source of sputtering should be considered in sputtering theories. Additionally an attempt has been made to present benchmark simulations representing beam parameters that could possibly be experimentally

[†]Fast MD simulations are still many orders of magnitude slower than dynamic-BCA, which means the statistical nature of sputtering is lost as one can't afford to spend the time to simulate a statistically significant fraction of ions.

reproduced, thereby affording experimentalists the opportunity to compare and thus support or disprove the findings of the presented model simulating reflexive sputtering effects. The final scientific utility represented by this work comes in the form of the sputtering yield BCA simulations presented, which incorporate surface roughness effects, the results of which will hopefully spur greater numbers of glancing angle sputtering yield measurements as well as provide a plausible error term when comparing experimental yields with simulated yields available to the greater scientific community. The technical utility of this work is that it provides a framework from which additional hybrid simulations might be constructed, where the simulation might be tuned for specific performance goals, whereas the code demonstrated herein is mostly optimized for clarity and extensibility. The novel inverse modeling technique presented has less clear scientific benefits; however, it must not be forgotten that the drive to develop the energy-resolved model came in part from attempts to experimentally verify the inverse modeler. From an applications standpoint the inverse modeler is extremely valuable because it is the easiest discovery to monetize.

6.5 Outlook and Future Works

While many useful scientific and technical discoveries and successes were accomplished over the course of this research (as summarized in section §6.1), there were naturally time and funding constraints that prevented all avenues of inquiry from being completely explored. In the following subsections future research directions on the topics of surface roughness (section 6.5.1), inverse modeling (section 6.5.2), extension of the model to handle ion implantation (section 6.5.3), possible alternative implementations of the model such as in 3D (section 6.5.4) and on a GPU or cluster (section 6.5.5), and finally possible experimental work that could be performed to confirm or disprove the reflexive sputtering model (section 6.5.6). As was mentioned in the preceding sections, the presented reflexive sputtering model is rather complex; therefore, in its current embodiment (as a simulation code), it is likely a dead-end, as further extension might be better performed on code that is purposefully designed to implement the desired model efficiently and elegantly. The amount of work required to develop a new code-base is not insignificant and would probably require a clear use case that requires the speed offered by the hybrid simulation method. This work, however, demonstrates that these models can be implemented, and pending experimental or independent verification also demonstrates that the reflexive model tangibly changes the results of topography simulations as compared to the previous state of the art. As discussed in section 6.5.4, in light of the 3D effects shown in *3D Effects with Reflexive Sputtering Model*, it is desirable to conduct reflexive sputtering simulations in 3D. The short-term outlook for this work is therefore the extension to 3D, either by modification of

the current code base or as a clean sheet design, and the experimental verification of the simulated effects.

6.5.1 Further Study on Surface Roughness

Surface roughness effects on the glancing angle sputtering yield were shown in chapter 4 to be significant and non-negligible, where they were also shown to affect the angular probability distribution of sputtered atoms. It was shown that a degree of simulated surface roughness is essential in the reproduction of experimental sputtering yields at glancing angles; however, the scientific conclusions with regard to this simulated surface roughness were far from satisfying. A major shortcoming was that, as mentioned in section 4.4.1.1, it was not possible to obtain plausible experimental values for surface roughness due to surface oxidation developing between the FIB experiment and AFM characterization. In order to better understand and characterize the surface roughness that evolves under glancing angle FIB irradiation, it would be desirable to either simulate the growth of surface roughness (as described in section 6.5.1.1) or design experiments to compare experimentally measured surface roughness with simulated surface roughness, with the sputtering yield being used as a correspondence check (as described in section 6.5.1.2). Finally as was discussed in section §4.6, it would be desirable to have a semi-empirical model to predict the amount of simulated surface roughness needed for a particular ion-target pairing as a function of beam energy. Obtaining the necessary data to derive this model would require additional glancing angle sputtering yield experiments (as outlined in section 6.5.1.3).

6.5.1.1 Simulation of the Evolution of Surface Roughness

There are two conceivable ways in which to study the surface roughness that evolves under glancing angle FIB irradiation, namely to perform experiments and to perform atomistic simulations of the surface evolution as a function of time and dose. Both methods present drawbacks and a good scientific study would approach the problem from both sides. With regard to the simulated evolution of surface roughness, the two plausible approaches are MD or simulations combining Kinetic Monte Carlo (KMC)* and MD, both are desirable as they are able to precisely model surface effects at the target-vacuum interface. Due to the relative rarity of MD-KMC for sputtering simulation, it is likely that any MD-KMC results would have to be confirmed with MD and experiments, as the strength of KMC is its ability to simulate long time-scale interactions and MD alone would likely be insufficient to confirm

*Multi-scale KMC has been demonstrated [201–203], even in fluids (also amorphous) and KMC has been used to simulate radiation effects in materials [204], roughness modeling under irradiation has only so far been completed through the coupling with MD [205].

viability. The advantages to simulating surface roughness are two-fold; firstly the simulation results do not suffer any experimental uncertainty in the characterization of the evolved surface, secondly, as the surface roughness evolution can be tracked during simulated irradiation the steady-state criteria for surface roughness can be precisely defined. Drawbacks to simulation of surface roughness evolution are of course the simulation-cell size, or the number of distinct atoms included in the simulation, and the slowness of simulations that are sufficiently large to contain the collision cascade. The simulation-cell should be large enough when considering the periodic boundary conditions so that simulated ion impacts do not interact with themselves due to any periodic boundary conditions. At glancing incidence angles, internal studies suggest that in order to simulate an incidence angle of 88.5° an optimized simulation cell of 500 \AA by 300 \AA by 100 \AA would be required, leading to months of required simulation time, even on dedicated clusters. Large scale MD simulations are therefore best performed by those with experience, due to the high cost with regard to simulation time. If the evolution of surface roughness were successfully completed, that data would enable the surface roughness models presented in this work to be revised to become more physically representative of actual surface roughness.

6.5.1.2 Measurement of Surface Roughness

The accompaniment or alternative to simulations of evolved surface roughness are actual measurements of surface roughness evolving from experimental FIB exposure. These measurements are difficult, especially in silicon as the growth of a native oxide almost requires that surface roughness experiments be conducted *in-situ* (at atomic resolution), without breaking the system vacuum (or allowing oxide growth). Experimental apparatuses capable of performing AFM without breaking vacuum on FIBed samples exist, but they are relatively rare and there is no guarantee that the lateral resolution is sufficient to characterize all frequencies; however, the data would be useful in attempting to characterize the experimental surface roughness. Changing the target material away from silicon to a more inert material could remove the effect of native oxide growth and would enable a greater understanding of evolved surface roughness, though as surface diffusion is expected to play a role in the evolution of a rough surface under irradiation, it is still not clear that results in an inert material would be transferable to the gallium-silicon system. Finally, as comparison to the presented 1D model, it may be possible to use density mapping techniques such as small angle neutron scattering [206] to characterize the interface as a function of density.

6.5.1.3 Glancing Angle Yield Studies at Different Energies

The simplest avenue for future work with regard to surface roughness induced under glancing angle irradiation would be the completion of further sputtering yield experiments like those performed by FEI as presented in figure 4.2.1 at different energies. Hopefully this data would provide hints towards the production of a semi-empirical model with which the expected degree of simulated surface roughness could be predicted as a function of energy. If such a semi-empirical law were to be derived, it would enable the arbitrary simulation of a range of beam energies, which would greatly enhance the industrial usefulness of the presented simulations. A drawback of this method is that it would only tell the equivalent surface roughness needed for a simulation as each yield experiment would be subject to obtaining equilibrium roughness under the effect of redeposition and second order sputtering.

6.5.2 Possible Inverse Modeling Improvements

The inverse modeling algorithm presented in chapter 3 is robust and a good first implementation of inverse modeling making use of the simple sputtering model presented in chapter 2; however, the presented algorithm implements an unneeded restriction of finding a time-invariant solution (referred to in the text as quasi-stationary solution). A refinement to the inverse modeling algorithm would be to vary the spatial dose profile as a function of time. Such a change to a time-variant solution is expected to increase simulation stability as each intermediate solution would require a smaller milled volume to be simulated. Moreover time-variant solutions offer additional opportunities for parallelization, as each intermediate solution could be optimized assuming that the previous intermediate solution had been completely optimized. This proposed algorithm is similar to the multiple surface driving method proposed by Kim [163], with the remaining hurdle of choosing intermediate solutions. The proposed algorithm would combine the efficiency of the cage-function algorithm and Kim's concept of intermediate target profiles providing the enhanced efficiency of the cage-function with the advantages of time variant solutions such as parallelizability and simulation stability. A proposed method of choosing an intermediate surface would be through fitting a cubic spline* through the final target nodes and back interpolating to a flat starting surface, insuring that nodes never cross. Each intermediate subsurface could be chosen such that volume of material removed between subsurfaces is constant. Furthermore, intermediate time variant solutions provide extra opportunities to confirm experimentally the fidelity of the forward modeling approach to experimental reality. Extension of the inverse

*A cubic spline is advantageous as it can be set to match the slope of the surface normal at the starting and target node locations. Interpolation of the sub volumes could be accomplished by linear segmentation along the length of the spline.

modeling algorithm to 3D would also be desirable, but that would require a complete and efficient 3D forward simulation be available. In order to enable real-time inverse modeling, the forward simulation portion must be significantly optimized for performance.

6.5.3 Consideration of Implanted Species

Conceptually, the challenge of extending the model for the hybrid approach to consider implanted species is plausible (in fact generalized equations are in existence addressing the mathematics of such a model [199]); however, practical implementation is subtly more difficult. Primary ions are implanted into the target and are no longer a phenomenon that can be adequately modeled using only surface properties. Therefore, in order to model implantation effects using a hybrid model, some method of modeling the depth and penetration of the ion is needed. It is supposed that a subsurface simulation surface (however a simple layer data-structure may be sufficient) might be used to keep track of both the concentration and volume of the implanted species. This subsurface would increase in depth as ions are implanted at nearly normal incidence angle and the primary simulation surface could approach, but never cross the subsurface if the yield is sufficiently high to sputter away the implanted region. The other quantity stored in the subsurface would be the average concentration over the simulated volume, which is needed to make use of pre-calculated sputtering yields as a function of impurity concentration. It seems also possible that a concentration and a depth stored at every surface node (the simple layer approach) might be sufficient to model implantation; although details must be explored, e.g. through BCA simulations. With this method it would also be possible to model intermixing through redeposition. This proposed model, even as simply described, represents a massive increase in simulation complexity, as the total number of datasets would increase as a factor of the number of intermediate concentrations considered in the simulation. While this model is very likely implementable using a hybrid approach, in the case of TopSim it would require touching and rewriting nearly every component of the simulation —as even the surface and gridding models would require modification. Implementation would require compelling evidence that the expected effects are significant over a broad range of topography simulations. For isolated scientific studies it seems like dynamic-BCA simulations are a better fit to the problem.

6.5.4 Full 3D Simulations

Extension of the presented reflexive sputtering yield to 3D is quite desirable as *3D Effects with Reflexive Sputtering Model* indicates that the 2D approximation used in this work needs significant compensation for 3D effects due to the dispersed nature of the angular distributions of energetically

ejected target atoms. The primary limitation preventing the current code-base from being extended to 3D is the hesitance to use 3D tables for angular distributions. This hesitance is justified, as 3D tables are very difficult to spot-check and visualize; however, they are essential for 3D simulations and are a logical extension of this work. Another challenge is the current over-simplicity of the 3D grid as implemented currently in TopSim (discussed in section 2.2.4.1), though efficient 3D meshing strategies are a well studied topic and numerous plausible solutions exist e.g. [207–209], however there is presently no specifically suggested meshing method.

6.5.5 GPU and/or Massively Parallel Implementation

The rule-of-thumb performance penalty for running interpreted python code using optimized numerical libraries as opposed to optimized compiled code in a language such as C is often stated as being between *as fast* and 3-6x slower, meaning that a compiled rewrite should be worth a 3x to 6x performance increase. Any additional performance must come from parallelization, be it in the form of a GPU implementation or an MPI implementation on a computational cluster. As future work, it appears to make the most sense to start with a GPU approach, though a cluster of GPU enabled machines might be useful for accelerating inverse modeling simulations as those are expected to be less latency-sensitive.

Parallelization can only take place within a single time-step, which generates a large degree of latency dependence, as a large number of time-steps are needed to track the evolution of the surface. Alternative surface advancement models (such as Budil's [133]) and more aggressive adaptive time-step algorithms may improve this matter in future implementations. However, within a single time-step, the hybrid model approach is very amenable being ported to GPU hardware. The two largest time constraints in the simulation are the calculation of the distance matrix, used to determine the distance from every node to every other visible node and the evaluation of yields and angular distributions. Exploratory studies indicate that the calculation of the distance function, while easily decomposable and trivial to solve on a GPU, is severely limited by IO delays in transferring the matrix in and out of the GPU. This problem may be addressable by keeping and evolving the surface on the GPU using a vertex shader, thereby avoiding IO penalties. The second bottleneck of the yield and angular distribution evaluations maps nearly perfectly to a GPU, as these table look-ups are analogous to interpolated texture look-ups which are handled directly in hardware for 1D, 2D, 3D, and even 4D tables. It therefore seems very promising to re-implement TopSim on a GPU; however, the scientific utility of such a project is low. Industrial interest would have to be found to make the trouble of re-implementation worthwhile. Such a re-implementation would almost certainly be in 3D, as the

utility of a highly optimized 2D-only simulation is extremely low and the increased difficulty between 2D and 3D is small compared to the work required to port the model to a GPU.

6.5.6 Experimental Confirmation of Reflexive Sputtering

A scientifically most rewarding but difficult future work, would be an experimental series that proves or disproves in a clear way the findings with the reflexive sputtering model. While the model seems logical and is a best-practices effort, it remains only a plausible explanation for the anomalous experimental data presented in section §5.7 until deliberate experimental studies have been made, searching for enhanced sputtering due to reflexive sputtering. This set of experiments would require careful simulation of milling parameters (perhaps with a form of inverse modeling) to find a dose profile where reflexive sputtering clearly dominates sputtering by backscattered ions.

6.6 Closing Words

In closing, it is important to reiterate that while, as with any path of scientific inquiry, more questions and objectives remain at the end of the project than at the beginning, this dissertation demonstrates a robust inverse modeling algorithm, which may in the future pace the way for new industrial applications in FIB. The state of the art of BCA sputtering simulations has also been advanced with the creation of a computationally efficient 1D model for surface roughness, which has been shown to be essential in replicating experimental sputtering yields for glancing incidence angles. A functional simulation method for a model considering reflexive sputtering was demonstrated. Furthermore, the results of these simulations indicate that reflexive sputtering might play a non-negligible role in topography evolution for deep trenches. The knowledge gained over the course of this doctoral study has enhanced the state of the art and brings to light a phenomenon that was long assumed to be negligible.

Thank you to the reader for the compliment and time investment made to study this dissertation.

Appendix A

3D Effects with Reflexive Sputtering Model

A.1 3D Effects: Validity of 2D Simulations and a Method to Compensate for a Missing Depth Dimension

As mentioned in section §5.5, the presented simulations make use of a correction factor for 3D effects. This is contrary to the model presented in chapter 2, where the only concession to 3D effects was in the scaling of the beam dose. The model, as described in section 2.3.2.1 and section 5.4.1, makes use of only the 2D angular distributions of sputtered and backscattered atoms. This 2D distribution is generated by histogramming the ejection angles of the simulated ions or target atoms where the ejection angle is defined as the arctangent of the horizontal component divided by the vertical component, $\alpha = \tan^{-1}(dx/dz)$, whereby the horizontal component is in the direction of the incoming ion (coordinates described in figure A.1.1). The in-plane component is neglected in the calculation of the ejection angle and each bin for a given ejection angle, α , corresponds to a 2D fan emerging from the incidence point with an inclination of α degrees. This 2D approximation is used as a simplification to avoid having to use 3D tables (as the angular distributions depend not only on the ejection angle α , but also the ion incidence angle θ , adding a polar angle ϕ would increase dimensionality to three), and due to the fact that the primary interest is in 2D simulations. These 2D simulations lack a real depth component, and therefore in practice three-dimensional tables would be integrated down to two dimensions. This integral is thus done as a part of the normalization process when the two-dimensional angular distribution tables are generated.

Use of 2D angular distribution tables is well justified in the simple model presented in chapter 2,

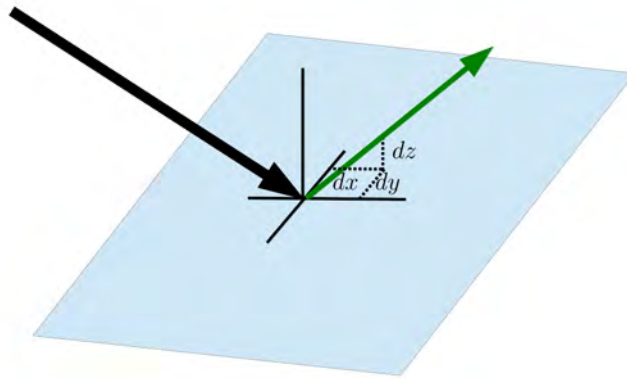


Figure A.1.1 – A schematic sketch of the coordinate system used in trajectory files for simulated sputtering with IMSIL. The thick black arrow represents an incident ion while the green arrow represents an ejected species, the ejection vector has components dx , dy , and dz where the x axis is parallel to the projection of the direction of the incident ion into the (x, y) plane. When considering the 2D angular distributions used in this text, dy is neglected.

where the tables are used to calculate the angular response of redeposited target atoms along infinitely long two-dimensional trenches. As the sticking coefficient for redeposited atoms in the model is independent of redeposition-impact-angle, the super-position of redeposited target atoms along the infinite length of the simulated trench is precisely represented by the two-dimensional approximation employed. When considering sputtering due to backscattered primary ions, the situation becomes a bit more complicated. The sputtering yield, contrary to the redeposition rate, *is dependent upon incidence angle*, thus in a perfectly precise simulation the polar angle should be considered. Considering this polar angle effect would necessitate integrating down the entire length of the trench, as the 2D incidence angle (described as θ_1 in figure A.1.2) is the smallest possible incidence angle along an infinite trench wall. Any displacement into or out of the 2D simulation plane results in a more glancing incidence angle with respect to the surface normal; however, these effects were assumed to be minor in the case of the model presented in chapter 2 due to the assumption, supported by angular data (shown in figure A.1.6), that energetic backscattered ions are predominantly found nearly following the path of the primary ion, thus leading to a tight distribution near $\phi = 0^\circ$. This pointy angular distribution of the backscattered ions in both α and ϕ justified use of a simpler 2D approximation when using the model that did not consider reflexive sputtering due to sputtered target atoms.

As was shown in figure 5.1.1 the angular distributions of sputtered target atoms are far less pointy than the angular distributions of backscattered ions; as the reflexive sputtering model presented in this chapter also depends on the incidence angle of the sputtered target atoms that go on to sputter, a correction must be made to compensate for 3D effects. In keeping with the goal of the simulation to only consider infinite 2D trenches, it is desirable to avoid the explicit integration along the trench length in simulation space. Explicit integration is avoided through the use of a virtual infinite trench

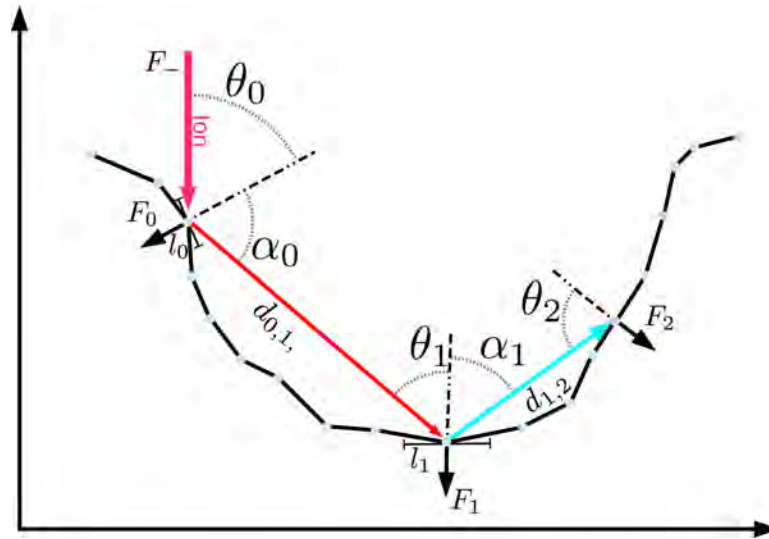


Figure A.1.2 – A sketch demonstrating the coordinate system used in the new nomenclature. The angle of incidence between incoming fluxes is indicated by θ_i , while the ejection angles of outgoing fluxes from a node are indicated by α_i . By convention, the initial beam flux is defined to be zeroth order, $i = 0$.

wall that allows for the pre-calculation of the possible 3D incidence angles along the virtual trench wall. In this construction the 2D incidence angle becomes β' (equal to θ_1 in the sketch) and the actual 3D incidence angle is expressed as β , where β is dependent upon the inclination of the virtual trench wall with respect to the incidence angle of the primary ion θ . A more precise construction would consider the β to be independent of θ ; however, that construction would necessitate the use of 3D tables, whereby an angular distribution analog that was dependent on θ_0 , α_1 , and θ_1 where θ_1 would relate to an integral over all β s. The addition and validation of 3D tables in TopSim would be outside of the scope of this exploratory work. Using a primary-incidence angle dependent construction, it is possible to create a sputtering yield correction factor dependent upon θ_0 which is defined by the choice of the virtual trench wall. In order to estimate the effect of the arbitrary choice of the virtual trench wall, three constructions are demonstrated and compared. The primary construction assumes that the virtual trench wall is parallel to the incidence angle of the primary ion; as shown in figure A.1.3, this construction is assumed to best represent a milled trench, as atoms sputtered by normal incident ions will most likely encounter sidewalls which will have an inclination similar to that of the incident ion. The second construction is the opposite construction (see figure A.1.4), whereby the virtual trench wall is inclined to be anti-parallel to the incident ion. This construction is chosen to define an envelope of possible 3D effects. Finally, a construction with a vertical virtual trench wall is considered (see figure A.1.5). This construction straddles the envelope of the possible virtual walls, it is also the only plausible incidence angle independent construction for deep trench simulations. Finally it must be emphasized that the correction factor for the 3D effects is *doubly dependent on* θ_0 in all but the perpendicular construction. The dependence upon the choice of the virtual wall

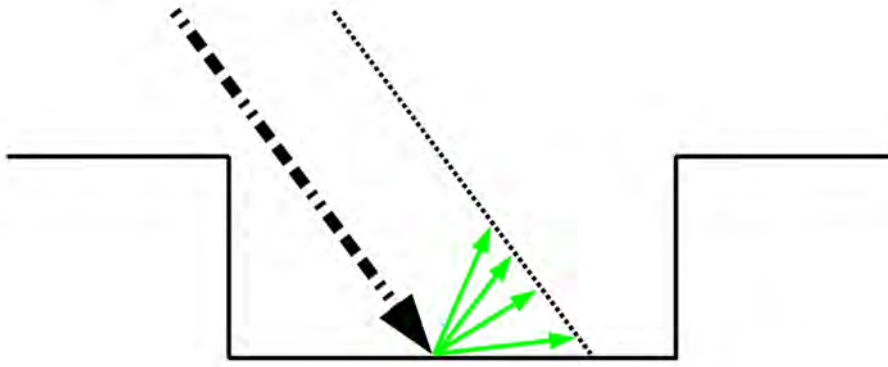


Figure A.1.3 – A schematic sketch of the 3D effect construction employing a parallel virtual trench wall (indicated by the dotted line). This virtual trench wall is defined as parallel to the incident ion path. Ejected ions are shown in green. Only forward ejections are shown; however, backward ejections are also considered in the model. This is the construction used in the body of this dissertation whenever compensation for 3D effects is mentioned.

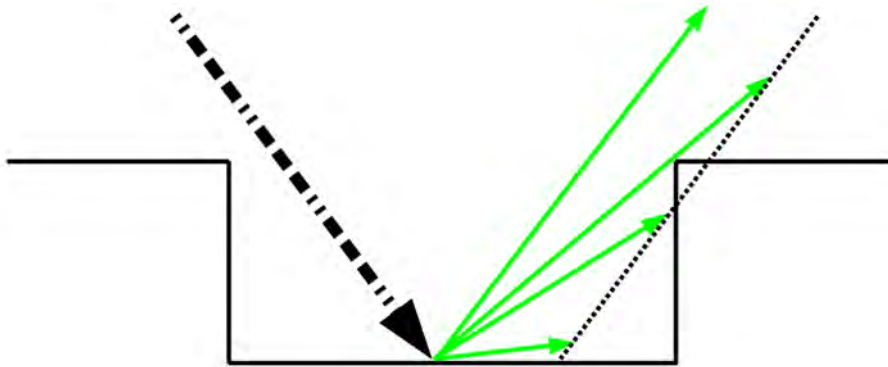


Figure A.1.4 – A schematic sketch of the 3D effect construction employing an anti-parallel virtual trench wall (indicated by the dotted line). This virtual trench wall is defined as anti-parallel to the incident ion path. Ejected ions are shown in green. Only forward ejections are shown; however, backward ejections are also considered in the model.

inclination is clear, as wall inclination is defined with respect to θ_0 . However, the fact that the shape of the angular distribution is heavily influenced by the ion-incidence-angle θ_0 (which also has an effect on the energy distribution of ejecta) must not be neglected.

The β dependence of the angular distribution for an incidence angle of 80° and an ejection energy range of 1-2 keV is shown in figure A.1.6 under the primary test condition of a parallel virtual wall. The strict 2D angular distribution would have all of the ion probabilities falling on the zig-zag delineating the smallest possible 2D angles across the plots. As the actual dy components of the simulated ejection events are not all zero valued; there exists a width to the zig-zag line in the positive beta direction. This positive only behavior is due to the geometric definition of β which must always have an incidence angle $\geq \beta'$, as movement into or out of the simulation plane lengthens the vector dy . The distribution of β s for backscattered gallium atoms shows the expected tight distribution around the 2D nominal incidence angle β' , while the distribution of the sputtered atoms covers a wider

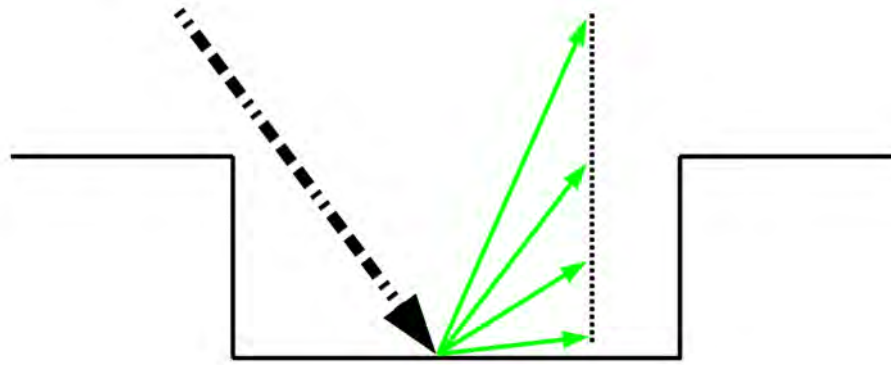


Figure A.1.5 – A schematic sketch of the 3D effect construction employing a perpendicular virtual trench wall (indicated by the dotted line). This virtual trench wall is defined as perpendicular to the simulation plane and does not change orientation to track the local topography. Ejected ions are shown in green. Only forward ejections are shown; however, backward ejections are also considered in the model.

range of possible incidence angles. In order to calculate the integrated correction factor for the second-order sputtering yields it is necessary to convolve these relative probabilities with the correct energy-resolved sputtering yields at the incidence angles β .

The β angle dependence indicates that the energetically sputtered target atoms shown in figure A.1.6 are not tightly distributed along the direction of the incidence angle θ_0 , and that 3D effects are not likely to be negligible in the case of reflexive sputtering. It is difficult from the β distribution shown to estimate the quantitative effect of neglecting 3D effects. This is due to the non-linearities in the sputtering yield as shown in figure 5.4.5. The β distribution in the test case is not sufficient on its own to estimate the magnitude of the 3D effects; the β distribution must be combined with the sputtering yields as shown in figure A.1.7. The relative sputtering rates between the 3D test case implementing a parallel virtual wall and a strict 2D test case are shown for various energies in figure A.1.7 for a representative incidence angle $\theta = 80^\circ$. The baseline 2D case (dashed line) is calculated by taking the 2D secondary incidence angle α on the virtual parallel wall and multiplying the probability of a single sputtered target atom emerging at that angle and energy with the sputtering yield at the secondary incidence angle α . 3D effects are estimated using the proper fraction of β s yielding in most cases to an increase in the effective sputtering yield. This increase is due to the fact that the sputtering yield is increasing for most of its angular range. In the case of backscattered ions, the differences between considering 3D effects and a 2D approximation are much less apparent, due to the relatively tight distribution of corrected incidence angles β . As expected from the energy-resolved angular distributions, the divergence between the 2D and 3D approximations decreases towards the end of the energy spectrum when the angular distributions themselves become less dispersed.

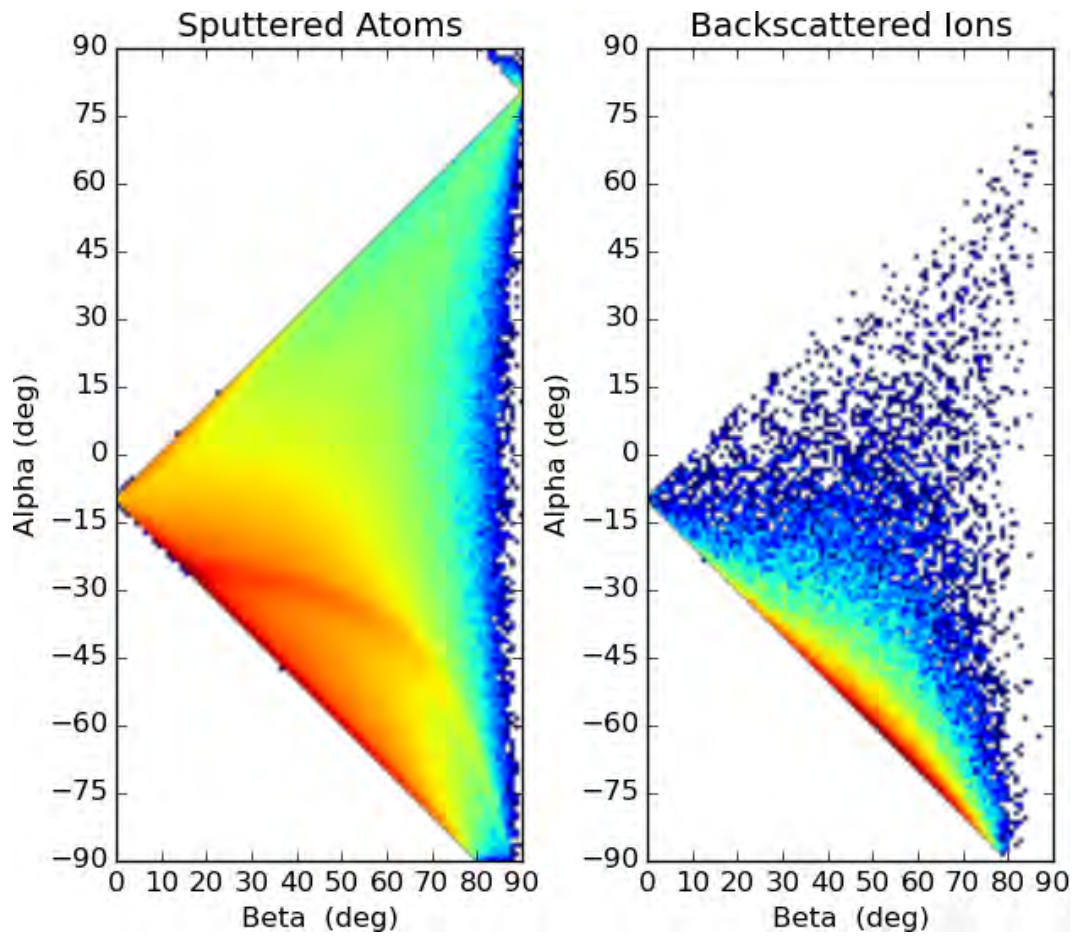


Figure A.1.6 – A plot of the β probabilities for an energy range of 1-2 keV under parallel virtual wall conditions is shown for both energetic sputtered atoms and backscattered ions. The vertical axis expresses the 2D ejection angle α and the heat map shows a logarithmically scaled probability of a given projectile with ejection angle α hitting the virtual wall with an incidence angle β . Notice that the backscattered ions are more tightly distributed around β' than the sputtered target atoms.

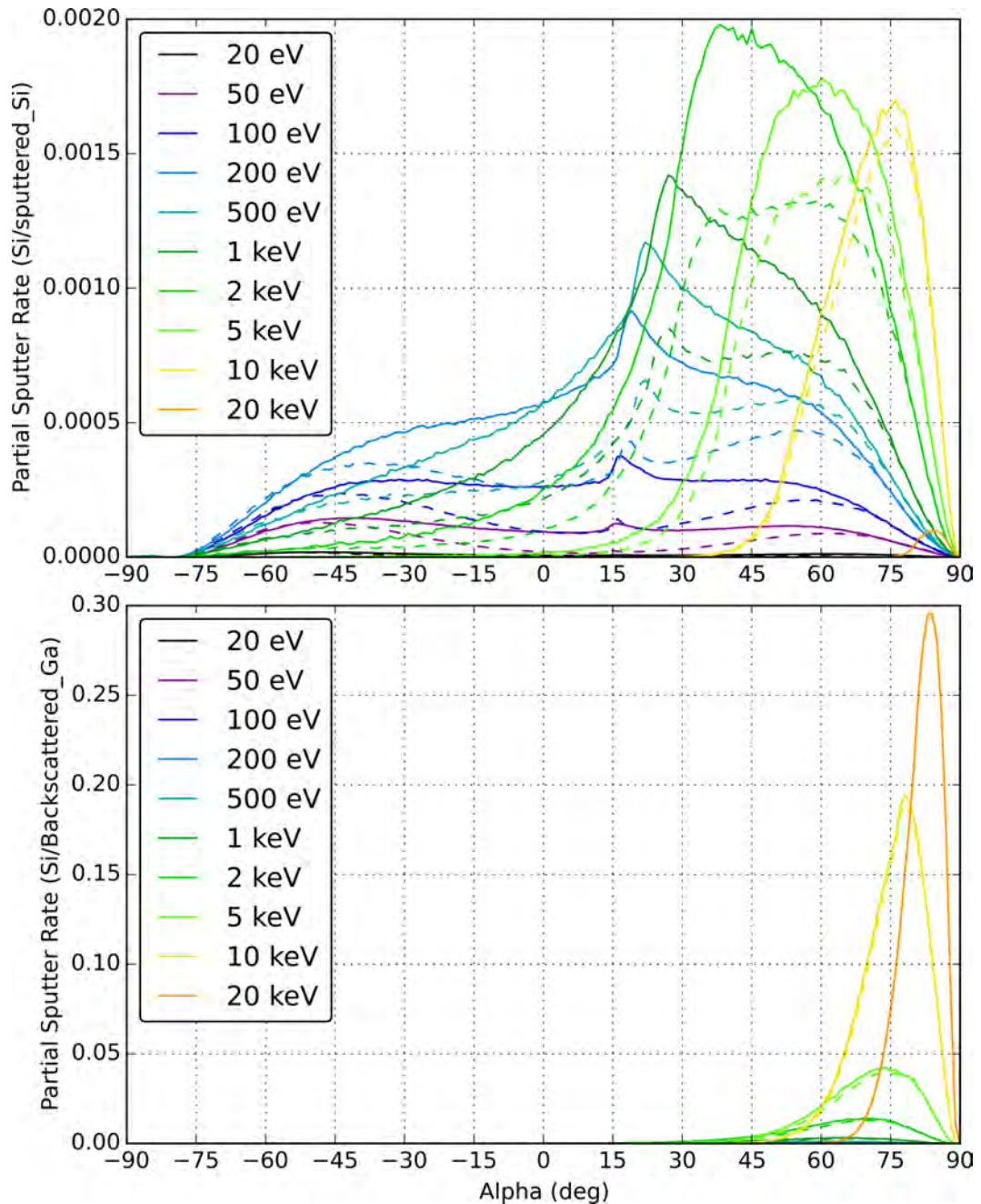


Figure A.1.7 – The amount of extra sputtering due to the local incidence angle in $3D\beta$, for all energies at an incidence angle θ of 80° . The dashed lines indicate the 2D approximation where the local incidence angle on the parallel virtual wall is simply the 2D incidence angle α , as compared to yields incorporating the 3D effects as shown by solid lines. Yields (sputter rates) are calculated by multiplying the fraction of events having a given incidence angle on the virtual wall β times the energy-resolved sputtering yield for said incidence angle. The lower energy of the energy band is used in this estimate, not the equivalent yields discussed in section 5.4.3. The upper chart demonstrates sputtering due to reflexive sputtering, while the lower chart shows sputtering due to backscattered primary ions.

3D effects are best dealt with through the use of a full three-dimensional simulation; however, this work is limited to 2D simulations. It is therefore desirable to devise a method by which the 3D effects may be approximated in a two-dimensional topography simulation. The method employed in this

work makes use of a correction factor for the sputtering yield, where 3D effects are considered as an enhancement to the sputtering yield. This correction factor is applied after the number of sputtered target atoms due to secondary sputtering resulting from either backscattered ions or energetically sputtered target atoms has been calculated at the simulation node. This correction factor $B(\theta_0)$ is taken to depend only on the primary incidence angle. This dependence is chosen as a compromise between simulation complexity and accuracy, as the primary incidence angle θ_0 heavily impacts the number of particles sputtered. Two energy-independent correction factors are defined $B(\theta_0)$ and $B_{back}(\theta_0)$, which are derived from the β distributions of the sputtered target atoms and backscattered ions respectively. The total yield difference per secondary incidence angle α is shown in figure A.1.8, which shows the summation across all calculated energies. In order to remove the dependence upon α , the data shown in figure A.1.8 for the summed yields between 3D and 2D models are integrated over all α where $B(\theta_0) = \frac{\int Y_{3D}(\theta_0, \alpha) d\alpha}{\int Y_{2D}(\theta_0, \alpha) d\alpha}$, defined as the ratio between the area of the 3D model and the area of the 2D model. A cubic spline is then fit to the integrated correction factors as a function of the primary incidence angle θ_0 ; this correction factor is applied to the scaled sputtering yields used in the simulation for each time-step.

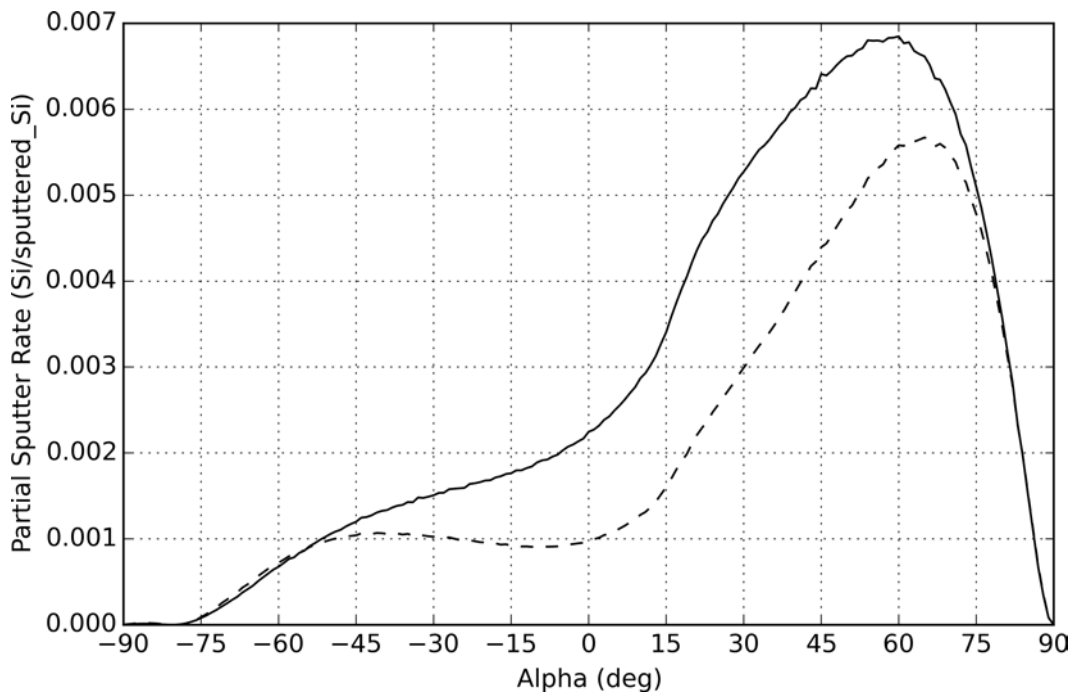


Figure A.1.8 – The total 3D effects summed over all energies for reflexively sputtered target atoms under the parallel virtual wall condition with an incidence angle θ of 80° . This plot shows the summation of the data shown in the upper plot of figure A.1.7. The 3D correction factor $B(\theta_0)$ used to correct the sputtering yield for 3D effects in the simulation is defined as the ratio between the area under each curve as a function of primary ion incidence angle θ_0 , where once again the dashed line represents the strict 2D yield and the solid line represents the 3D model.

The effect of the compensation-factors for the 3D-effect upon topography simulations using the

extended energy-resolved model discussed in chapter 5 is shown in figure A.1.9, where simulations involving each virtual wall arrangement depicted in figures A.1.3-A.1.5 are compared to a simulation lacking 3D-effect compensation. Simulations compensating for 3D-effects show a similar shape to the simulation neglecting 3D-effect compensation; the primary effect of the limited 3D compensation is to modify the volumetric sputtering efficiency. Though a full 3D simulation would be expected to exhibit other higher-order effects upon simulated topographies, the simple energy-independent compensation model that depends solely on the primary incidence angle θ_0 as used here can only be expected to show the volumetric changes seen in figure A.1.9. There is a slight variance in the micro-trenching between the three different virtual-wall approximations shown, which is due to differences in sputtering yield from backscattered ions, as there are separate correction factors derived for reflexive sputtering and backscattered ion-sputtering. Consideration of 3D effects leads to approximately a 3-6% difference in maximum sputtering depth when compared to a model neglecting to consider 3D effects with regard to second-order sputtering. This difference is clearly visible even at aspect ratios near 1:1, justifying the careful consideration of 2D effects when broad angular distributions or secondary sputtering are considered. These 3D effects, while measurable, are still small compared to neglecting reflexive sputtering, as was demonstrated in figure 5.5.1; however, these results are not universal, as they depend on the 3D angular distribution of sputtered or backscattered target atoms or ions, which is highly dependent upon the energy and species of the target and ions.

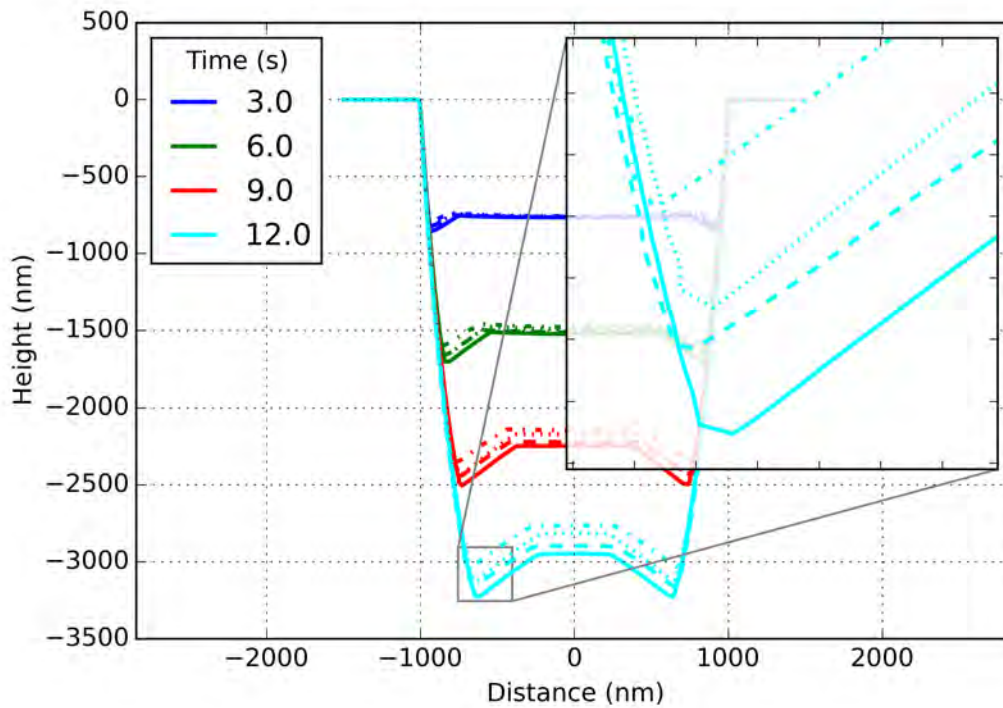


Figure A.1.9 – Topography Simulations implementing the energy-resolved model including reflexive sputtering for different 3D-effect compensation models. The solid line is a simulation implementing a *parallel* virtual wall for compensation of 3D effects (as presented in figure 5.5.1), the dot-dashed line is the reflexive model neglecting 3D effects, while the dashed line implements an *anti-parallel* virtual wall, finally the dotted line implements a *perpendicular* virtual wall. All models for 3D effects increase volumetric sputtering efficiency when compared to simulations not compensating for 3D effects.

Appendix B

Shadowing Effects

B.1 Limited Effects of Shadowing On Deep Trenches

The presented Topography simulator TopSim has two available options for determining the visibility of a second-order node (a node that receives backscatter flux or redeposition/reflexive-sputtering flux). The primary approach is referred to as simple visibility and excludes all second-order nodes where the ejection or incidence angle is greater than $\pm 90^\circ$ from the simulated surface normal. The secondary approach is to further exclude *shadowed* nodes that would be occluded by the topography of the surface; this approach is referred to as simulations involving shadowing. Shadowing is expected to play a larger role in simulations of topographies involving multiple local minima.

The shadowing algorithm was developed by another researcher ([210]) for this project and avoids the computational overhead of strict ray-casting in two dimensions by searching the nodes visible by simple visibility for direction changes as a function of the ejection angle α . Direction changes can be taken to indicate local maxima or minima which then delineates the beginning of a shadowed region. The probable ejection angle α_{start} between a given source point and the start of the shadowed region is stored for later comparison. A contiguous region is thus defined, ending when the α of a succeeding node exceeds the α_{start} of the beginning of the shadowed region. This brief description neglects the handling of edge cases; however, as implemented the algorithm is geometrically robust.

A limitation of the shadowing algorithm is that only hard shadows can be implemented (consistent with a strictly local model where matter can only enter or exit at a simulation node); therefore, if a single or short string of nodes becomes an outlier this node will shadow other nodes. This outlier node(s) will also act as a redeposition sink and receive redeposition flux while shadowing neighboring nodes, which can in many cases lead to runaway cases and numerical instability. Practically this numerical instability is rarely seen when simulating scanning beams as the majority of the beam flux

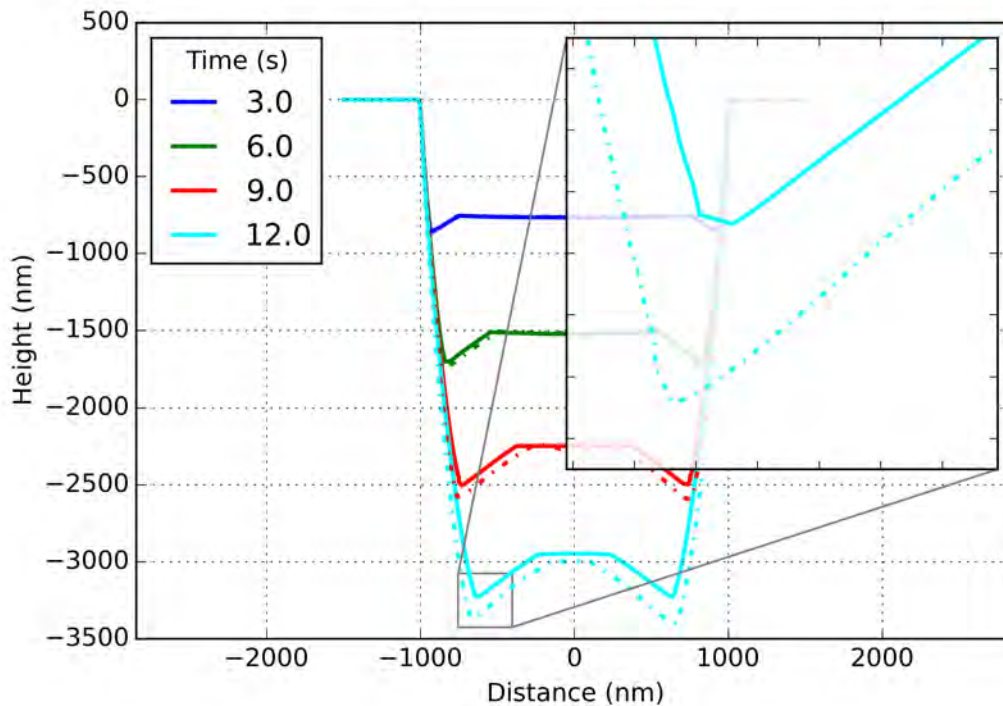


Figure B.1.1 – A comparison between benchmark simulations for an energy-resolved model with reflexive sputtering (chapter 5) without (solid) and with (dot-dashed) the full shadowing model enabled. When shadowing is enabled, the notable first-order effect is to increase the magnitude of the simulated microtrenches. Without proper consideration of shadowing (simple visibility) redeposition flux from the left micro-trench could be transferred to the right micro-trench. Use of the shadowing model plays the largest role in redeposition.

is used to drive a small divot back and forth across the bottom of the simulated trench. Movement of this crater as a function of time acts to smooth out the numerical instabilities and would-be runaway-nodes are squashed as the beam moves over them. However, in the case of the overlapped beam simulations, these runaway cases can be quite detrimental to the fidelity of the simulation. These runaway effects are caused by numerical instabilities of the simulation grid, and thus are very dependent on the selection of the grid parameters such as the grid spacing and adaptive grid parameters. When runaway effects do not occur over the course of an overlapped beam simulation, the shadowing effect is repeatable even under varying grid parameters (of the set of non-runaway conditions); therefore, the shadowing model is valid —albeit suffering from occasional numerical instability.

The simulations presented in this work use the simple visibility model, unless otherwise stated, in order to use a fixed grid criteria for all presented simulations. The effect of neglecting to use the more complete shadowing model is minor, as shown in figure B.1.1, where use of the shadowing model increases micro-trench depth by a maximum of 4% in the presented benchmark trench. The topography effects of using the complete shadowing model are limited to areas where the shadowing model would differ from the simple visibility construction. Notably with respect to trench geometries these

areas are characterized by local minima/maxima in the topography that are not also global maxima/minima; in the test case these are the microtrenches themselves. All higher-order matter fluxes in the simulation have the propensity to be influenced by the consideration of shadowing, but the flux with the most visible effect is the redeposition flux. The other fluxes, such as the backscattered ion flux and the energetically sputtered target atom flux also depend upon the incidence angle at which they re-interact with the target. The redeposition flux has no such restrictions and always deposits with 100% yield. Use of the shadowing model prevents inter-micro-trench redeposition and therefore the microtrenches can grow at a greater rate when shadowing is considered. The magnitude of the shadowing effects in trench geometries, even those with pronounced micro-trenching, remains rather small compared to the other compared features of the models used in this dissertation; therefore, the choice not to apply the shadowing model universal due to numerical stability concerns is justified.

Appendix C

2nd Order Redeposition from Reflexive Sputtering

C.1 A Supposedly Minor Approximation

Throughout this text, special effort has been made to impart the stark differences between the angular probability distributions between sputtered atoms and backscattered ions. In fact the differences between the cosine distribution and the angular distribution for sputtered atoms in a non-energy-resolved model are small enough that the 3D mode of TopSim still uses a cosine model for redeposition*. The backscatter angular distributions of beam ions (as first shown in figure 2.3.5) are characteristically not like a cosine distribution at the energies shown. Therefore the assumption made in equation (5.3.15), repeated here as equation (C.1.1), that the redistribution flux of energetic target atoms that were backscattered from first order nodes (characterized by: $F_{Si,1}(\alpha_0, \theta_0, \theta_1, E_l) \cdot \bar{Y}_{back, Si|Si}(\theta_0, \theta_1, E_l) \cdot c_1 \cdot \cos(\alpha_1) \cdot \frac{l_1}{d_{1,2}} \cos \theta_2$) might be modeled using a cosine model for angular distribution is extremely suspect.

$$F_{Si,2}(\alpha_1, \theta_2, F_{Ga,1}, F_{Si,1}; E_l) = \left\{ \begin{array}{l} \sum_{visible_0} F_{Si,1}(\alpha_0, \theta_1; E_l) \cdot \left[\bar{Y}_{back, Si|Si}(\theta_0, \theta_1; E_l) \cdot c_1 \cdot \cos^n(\alpha_1) + \right. \\ \left. \bar{Y}_{sput, Si|Si}(\theta_0, \theta_1; E_l) \cdot c_1 \cdot \cos^n(\alpha_1) \right] + \\ \sum_{visible_0} F_{Ga,1}(\alpha_0, \theta_1; E_l) \cdot \left[\bar{Y}_{sput, Si|Ga}(\theta_0, \theta_1; E_l) \cdot c_1 \cdot \cos^n(\alpha_1) \right] \end{array} \right\} \cdot \frac{l_1}{d_{1,2}} \cos \theta_2 \quad (C.1.1)$$

*The 3D mode lacks the ability to simulate backscattered ions or higher order terms.

However, as mentioned in section 1.2.2, every model exists as a compromise; thereby begging the question: What alternatives exist to simulating the second order redeposition flux from backscatter events prompted by energetically sputtered target atoms other than using the cosine approximation for angular distribution. The trivial solution is push the approximation to a higher degree of complexity by correctly modeling the angular distribution of the backscattered target atoms and moving the residues to a third-order calculation of the silicon fluxes. This trivial solution is undesirable for two reasons, primarily that increasing the complexity of the simulation will nearly double the computational work-load of the simulation per time-step[†], furthermore, this trivial solution is not a solution. Moving the offending error to a higher degree leads to redeposition source terms of the third-order, where once again the choice to truncate, approximate, or extend to a $N + 1$ order must be made. Outside of the trivial choice to increase complexity there are two remaining choices, namely truncation and false approximation (using the cosine approximation). Truncation in this sense is defined as simply neglecting the consideration of the flux of backscattered target atoms as a source of redeposition flux in the second-order flux calculation. False approximation is the approach taken in equation (C.1.1), whereby the angular distribution of the backscattered target flux is considered to be approximated by a cosine distribution. There are compelling arguments for both approaches. The truncation approach avoids simulating any effect that cannot be properly quantized, in other words: do nothing that is known to be incorrect. However, in truncating the source terms for the second-order redeposition flux one is choosing to remove matter from the simulation, as the equation for the first-order node velocity (equation (5.3.9), repeated as equation (C.1.2)) already considers the effect of backscattering of energetic target atoms. This truncation in order to correct a second-order inconsistency therefore requires first-order changes. Furthermore the false approximation technique leaves the equations in an extensible state by minimizing the number of assumptions made that require reformulation of the equations. This systematic and aesthetic argument, namely that implementing the truncation hinders the understandability of the system of equations through the injection of a further asystematic approximation at an intermediate order of complexity (as opposed to an assumption on either either an initial or final formulations) is not a compelling argument in its own right. However, if the magnitude of the error under typical conditions can be shown to be small in either approximation (truncation or false-approximation) as is shown in section §C.3, then the luxury of an aesthetically pleasing construction may be afforded. The false-approximation approach is used in the simulations presented in chapter 5, precisely because the approximation is negligible and neither truncation or the cosine

[†]One would be tempted to say that the that the incremental increase in work is closer to a 25% increase in workload, however that discounts that a third-order flux would need to be energy resolved and resolution of the energy effect dominates the computation in the presented second-order flux model. Therefore extending to correctly consider non-energy resolved angular distributions on the third-order resolved over the energy of the impinging projectiles is approximately a $2N$ increase in work. If one were to resolve the energies of the angular distributions in the third order the workload would scale as N^2 .

approximation is totally correct, however the cosine approximation preserves the symmetry of the presented equations which might aid future understanding of the model; especially if the model is extended to higher orders.

$$V_1(\theta_0, \theta_1, F_{Ga, 1\leftarrow 0}, F_{Si, 1\leftarrow 0}) = v_{Si} \cdot \sum_{l=0}^{l_{max}} \left\{ \left[\begin{array}{c} F_{Si, 1\leftarrow 0} \cdot \left(\begin{array}{c} 1 - \\ \bar{Y}_{back, Si|Si}(\theta_0, \theta_1, E_l) - \\ \bar{Y}_{sput, Si|Si}(\theta_0, \theta_1, E_l) \end{array} \right) \\ [F_{Ga, 1\leftarrow 0} \cdot \bar{Y}_{sput, Si|Ga}(\theta_0, \theta_1; E_l)] \end{array} \right] - \right\} \quad (C.1.2)$$

C.2 What do the Angular Distributions of Backscattered Reflexively Sputtered Atoms Look Like?

The backscatter angular distributions presented in chapter 2 (section 2.3.2.2) and later in chapter 5 (section 5.4.2) concerned high energy impacts of gallium ions on silicon. This is different from the effects of silicon striking silicon for two reasons, the mass of gallium in the earlier presented data is greater than silicon, and all of the impacts occur with high energy as the backscattering angular distribution is only considered under beam impacts. Therefore to highlight the problem addressed in this appendix, a small number of backscatter angular distributions due to silicon-silicon impacts are shown for different incidence angles θ and different implantation energies. As shown in figure C.2.1, the backscatter angular distributions of silicon-silicon interactions do not correspond with a cosine distribution, as explained and predicted in the previous section. The degree of skewedness of the silicon-silicon backscatter angular distributions is reduced as compared to the gallium-silicon case, even at the full beam energy of 30 keV; however, a cosine approximation remains a poor fit.

The presented backscattering angular distribution data also shows another interesting effect, namely, that low energy backscattered silicon atoms emerge with a more glancing angle when the incidence angle is near normal. As the incidence angle increases, as in the case of $\theta = 80^\circ$, the ejection angles become more glancing for high-energy impacts than the low-energy impacts. These presented backscatter angular distributions are not energy resolved and thus represent the behavior over the entire ensemble.

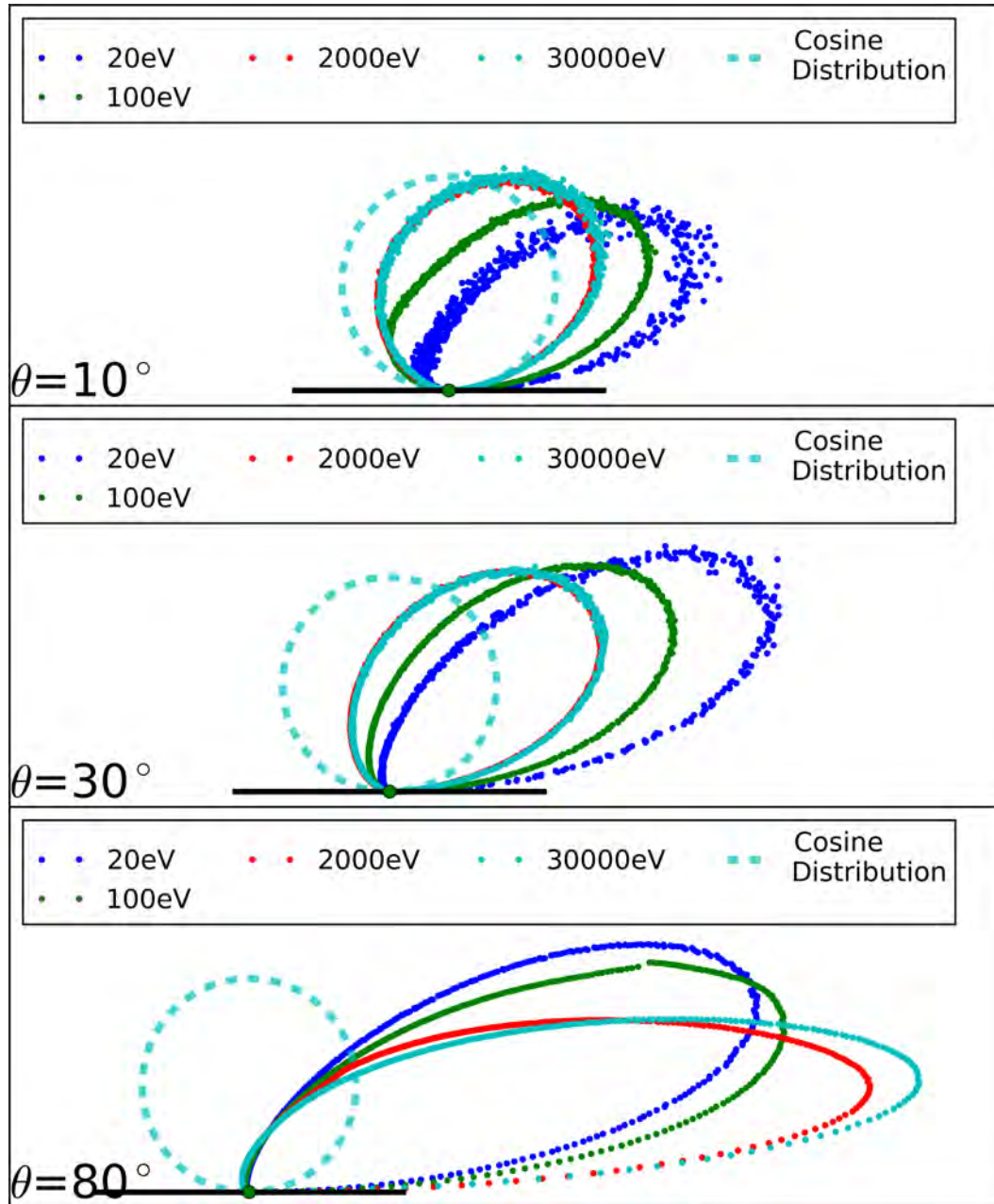


Figure C.2.1 – Normalized backscatter angular distributions for silicon impinging on silicon at different energies and incidence angles are shown. Please note how high energy impacts near normal incidence (10°) can roughly be approximated by a cosine distribution. At higher incidence angles all angular distributions become strongly non-cosine.

C.3 How Important is Redeposition due to Backscattered Reflexively Sputtered Target Atoms In Simulations?

In order to quantify the effect of this approximation of considering the redeposition flux of backscattered silicon atoms due to sputtering by energetic silicon atoms two simulations are compared. The first simulation (indicated by solid lines in figure C.3.1) uses the cosine approximation as discussed in section §5.3, while the second simulation (indicated by dot-dashed lines) removes backscattered silicon from the simulation before it can be redeposited. The equation for the impinging flux due to interactions at the first-order node that will lead to redeposition at the second-order node is shown for each model in equation (C.3.1) (cosine approximation for backscattering), and equation (C.3.2) (a model neglecting redeposition from backscattered silicon). The simulation results indicate that, as expected, removing backscattered silicon as a source for redeposition in the simulation leads to slightly increased trench depths due to the overall reduction in second-order redeposition. As can be seen in figure C.3.1; however, the total magnitude of the effect is rather small and therefore the presented solution of including silicon backscattering using a cosine distribution is justified in the case of the test geometries.

$$F_{Si,2}(\alpha_1, \theta_2, F_{Ga,1\leftarrow 0}, F_{Si,1\leftarrow 0}; E_l) = \left\{ \begin{array}{l} \sum_{visible_0} F_{Si,1\leftarrow 0} \cdot \left[\bar{Y}_{back,Si|Si}(\theta_0, \theta_1, E_l) \cdot c_1 \cdot \cos(\alpha_1) + \right. \\ \left. \bar{Y}_{sput,Si|Si}(\theta_0, \theta_1, E_l) \cdot c_1 \cdot \cos(\alpha_1) \right] + \\ \sum_{visible_0} F_{Ga,1\leftarrow 0} \cdot [\bar{Y}_{sput,Si|Ga}(\theta_0, \theta_1; E_l) \cdot c_1 \cdot \cos(\alpha_1)] \end{array} \right\} \cdot \frac{l_1}{d_{1,2}} \cos \theta_2 \quad (C.3.1)$$

$$F_{Si,2}(\alpha_1, \theta_2, F_{Ga,1\leftarrow 0}, F_{Si,1\leftarrow 0}; E_l) = \left\{ \begin{array}{l} \sum_{visible_0} F_{Si,1\leftarrow 0} \cdot [\bar{Y}_{sput,Si|Si}(\theta_0, \theta_1, E_l) \cdot c_1 \cdot \cos(\alpha_1)] + \\ \sum_{visible_0} F_{Ga,1\leftarrow 0} \cdot [\bar{Y}_{sput,Si|Ga}(\theta_0, \theta_1; E_l) \cdot c_1 \cdot \cos(\alpha_1)] \end{array} \right\} \cdot \frac{l_1}{d_{1,2}} \cos \theta_2 \quad (C.3.2)$$

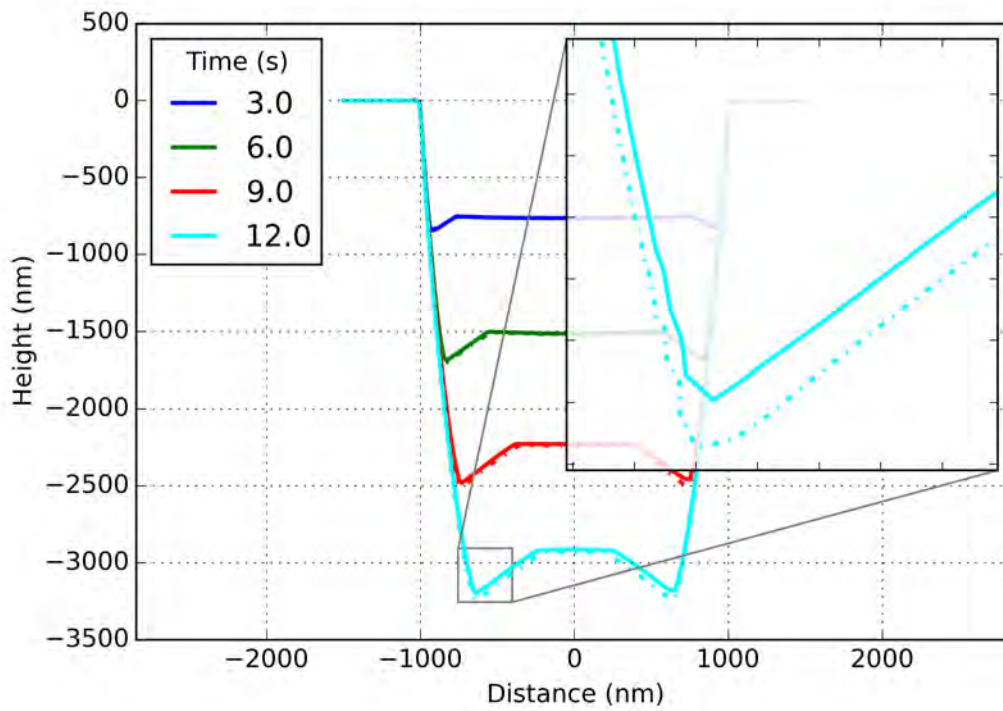


Figure C.3.1 – Simulations using a model using a cosine approximation for redeposition of backscattered silicon (solid) and a model neglecting the effect of backscattered silicon (dot-dashed). Neglecting the consideration of backscattered silicon as a source for redeposition leads to a slight reduction in the overall degree of redeposition. This effect is minor compared to other portions of the simulation.

Appendix D

Calculation of Equivalent Yields

Calculation of the sputtering yield due to reflexively impinging atoms, backscattered ions, or backscattered target atoms is complicated by the consideration of non-monochromatic excitations. This complication arises due to the inherent energy dependence of the incidence angle dependent sputtering yield ($Y_{sput}(\theta)$ or $Y_{back}(\theta)$ discussed for monochromatic excitation energy in section 2.3.1.1) coupled with the limitation that simulated yields as obtained from BCA are calculated for discrete incidence angles*. The total sputtering yield for a non-monochromatic excitation depends on both the incidence angle and the energy distribution of the impinging particles ($g_{sput, Si|Si}(\theta_{i-1}; E_l)$ as shown in the nomenclature from chapter 5) where that energy distribution is dependent upon the incidence angle at the source location. The sputtering yield of a first order impact as seen in the velocity equation for first order nodes (equation (5.3.9)) is therefore dependent on the initial beam incidence angle θ_0 , the incidence angle at the receiving node θ_1 , and the energy segment of interest E_l . In this appendix a function to describe an equivalent sputtering yield for first order events, $\bar{Y}(\theta_0, \theta_1; E_l)$, as a function of both incidence angles for a given energy segment is presented.

There exist two challenges in determining the number of particles sputtered by a group of incidence particles having an energy distributions described over a band E_l . The first challenge as mentioned earlier, is that the sputtering yield is only known at discrete energies and not bands. The second challenge is to approximate the shape of the energy distribution over a given energy band. The first challenge is addressed by making use of the fact that the sputtering yield is locally linear[†] as a function of energy. Local linearity makes it possible to derive a linear equation of the format

*Though there is no conceptual limitation to simulating the sputtering yield from a finite energy-width of exciting particles using BCA, there are an infinite number of possible energy distributions that could be simulated leading to the parameterization discussed herein.

[†]The number of sampled energy levels used to calculate the equivalent yield is not explicitly coupled to the number of energy levels used to determine the angular distributions of emitted particles in the simulation; therefore, a sufficient sampling of sputtering yield energies may always be chosen such that the linear assumption is valid.

$y = m \cdot E + b$ for the yield as a function of excitation energy, where m and b are determined through evaluations of the sputtering yield for excitation energies at either endpoint of a given energy band E_l . The total yield across an energy distribution $f(E)$ for a single band would therefore be equal to $\int_{E_1}^{E_2} (m \cdot E + b) \cdot f(E) \cdot dE$. However, as m and b are constants and do not depend on $f(E)$ it is possible to rewrite the total yield across the energy band as $\bar{Y} = m \cdot \bar{E} + b$, where $\bar{E} = \int_{E_1}^{E_2} E \cdot f(E) \cdot dE$. Therefor the problem remaining is to determine a way to calculate \bar{E} . As the coefficients for m (equation (D.0.1)) and b (equation (D.0.2)) are trivial to calculate and are listed below, as is an explicit formulation for \bar{Y} (equation (D.0.3)).

$$m(\theta_1; E_l) = \frac{Y_{sput}(\theta_1; E_2) - Y_{sput}(\theta_1; E_1)}{E_2 - E_1} \quad (\text{D.0.1})$$

$$b(\theta_1; E_l) = Y_{sput}(\theta_1; E_2) - \frac{Y_{sput}(\theta_1; E_2) - Y_{sput}(\theta_1; E_1)}{E_2 - E_1} \cdot E_2 \quad (\text{D.0.2})$$

$$\bar{Y}(\theta_0, \theta_1; E_l) = m(\theta_1; E_l) \cdot \bar{E}(\theta_0; E_l) + b(\theta_1; E_l) \quad (\text{D.0.3})$$

Calculation of \bar{E} requires the use of a second assumption; namely, that the energy distribution between any two endpoints of the energy band may be represented as a power function of the form equation (D.0.4).

$$f(E) = k_1 \cdot E^{-k_2} \quad (\text{D.0.4})$$

A power law is assumed due to the linearity of the energy distribution function $g_{sput, Si|Si}(\theta_{i-1}; E_l)$ when plotted on a log-log scale as shown in figure D.0.1. As figure D.0.1 shows, the power-law assumption holds for low to moderately high energies, at extremely high energies and small incidence angles θ , the power-law assumption breaks down. The power law assumption is still better than a linear assumption over most of the energy range.

The average energy \bar{E} is calculated by integration, where the average energy of the energy distribution is defined as such $\bar{E} = \int_{E_1}^{E_2} E \cdot f(E) \cdot dE$. Two equations are necessary to determine the two unknowns k_1 and k_2 in equation (D.0.4) which necessitates knowing the evaluation of the energy distribution across two subintervals across the interval $E_1 \dots E_2$. Selection of the intermediate energy defining the partition between the subintervals at the point of the geometric mean $E_{mid} = \sqrt{(E_1 \cdot E_2)}$ allows for further simplification of variables. By definition a system of equations is generated allowing for the symbolic solution of k_1 and k_2 , where the integral of the energy distribution between E_1 and E_{mid} is equal to the total fraction of particles emerging with energy in that band, written as

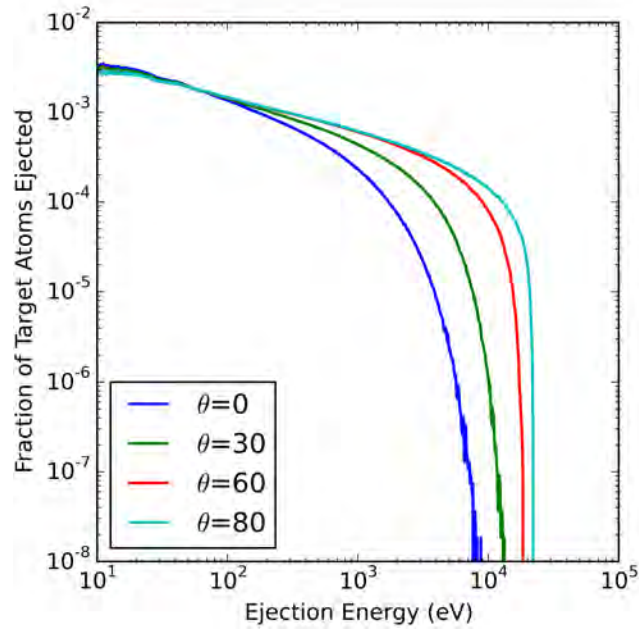


Figure D.0.1 – A log-log plot of the energy distribution of sputtered particles for different incidence angles (silicon sputtered by 30 keV gallium). The linear regions are where the power-law assumption is accurate.

$g(\theta_0; E_{1, mid})$; conversely the same is true for the interval between E_{mid} and E_2 as exemplified by equation (D.0.5) and equation (D.0.6). Solving this system of equations results in functions for k_1 and $1 - k_2^\ddagger$ shown in equation (D.0.7) and equation (D.0.8).

$$g(\theta_0; E_{1, mid}) = \int_{E_1}^{E_{mid}} k_1 \cdot E^{-k_2} \cdot dE \quad (D.0.5)$$

$$g(\theta_0; E_{mid, 2}) = \int_{E_{mid}}^{E_2} k_1 \cdot E^{-k_2} \cdot dE \quad (D.0.6)$$

$$k_1 = \frac{1 - k_2}{E_1^{1-k_2}} \cdot \frac{g(\theta_0; E_{1, mid})^2}{g(\theta_0; E_{mid, 2}) - g(\theta_0; E_{1, mid})} \quad (D.0.7)$$

$$1 - k_2 = \frac{\ln \frac{g(\theta_0; E_{1, mid})}{g(\theta_0; E_{mid, 2})}}{\ln \frac{E_{mid}}{E_2}} \quad (D.0.8)$$

With knowledge of k_1 and $1 - k_2$ for equation (D.0.4) the analytical solution for \bar{E} may be found through definite integration and that result is expressed in equation (D.0.9). \bar{E} is dependent upon evaluations of the energy distribution function at discrete energy bands $E_{1, mid}$ and $E_{mid, 2}$. As these sub-interval energy distributions ($g(\theta_0; E_{1, mid})$ and $g(\theta_0; E_{mid, 2})$) are only required in the calculation

[‡] $1 - k_2$ is not reduced because this form is more convenient for the expression of k_1 .

of the equivalent yield and calculation of \bar{E} requires the evaluation of natural logs, a piecewise-linear cubic-spline interpolation of the pre-calculated $\bar{E}(\theta_0; E_l)$ is used in the presented simulation.

$$\bar{E}(\theta_0; E_l) = \frac{1 - k_2}{2 - k_2} \cdot \frac{g(\theta_0; E_{mid,2})^2 \cdot E_2 - g(\theta_0; E_{1,mid})^2 \cdot E_1}{g(\theta_0; E_{mid,2})^2 - g(\theta_0; E_{1,mid})^2} \quad (\text{D.0.9})$$

Acknowledgements

This work could never have been completed without the aid and guidance provided by Ao. Univ.-Prof. Dipl.-Ing. Dr. Techn. Gerhard Hobler. His knowledge of sputtering phenomena and simulation techniques was invaluable in the timely completion of this research. Furthermore, his patience and support over the entire process was an unquantifiable asset. The experimental work presented in this dissertation owes a great debt of gratitude to Dr. techn. Simon Waid in his time at the FKE, and the research team of Mostafa Maazouz at FEI for the completion of FIB experiments as well as numerous constructive conversations about the physics of FIB.

Funding for this work was provided by FEI under the project “Focused Ion Beam Simulation” as well as funding from the Austrian Promotion Agency, Austrian Nano Initiative Program, NILaustria project under the project “NILaustria”.

The text of this dissertation owes MA. BA. Julia Schallauer gratitude for the patient review and correction of grammar and wording. Additionally Dr. Hobler must once again be thanked for his tireless assistance in refining the nomenclature presented in chapter 5. At this point, thanks are also generally extended to all of the students and faculty of the FKE for their support, inspiration, and friendship over the course of these studies.

Bibliography

- [1] Melngailis, J. "Focused ion beam technology and applications." *Journal of Vacuum Science & Technology B*, vol. 5, no. 2, pp. 469–495 (Mar. 1987). ISSN 2166-2746, 2166-2754. URL <http://dx.doi.org/10.1116/1.583937> [Accessed: 2014-03-26].
- [2] Krohn, V. E. and Ringo, G. R. "Ion source of high brightness using liquid metal." *Applied Physics Letters*, vol. 27, no. 9, pp. 479–481 (Sep. 2008). ISSN 0003-6951, 1077-3118. URL <http://dx.doi.org/10.1063/1.88540> [Accessed: 2014-01-13].
- [3] Orloff, J. *Handbook of Charged Particle Optics, Second Edition* (CRC Press, 2008). ISBN 9781420045550.
- [4] Ward, B. W., Notte, J. A., and Economou, N. "Helium ion microscope: A new tool for nanoscale microscopy and metrology." *Journal of Vacuum Science Technology B: Microelectronics and Nanometer Structures*, vol. 24, no. 6, pp. 2871–2874 (2006). ISSN 1071-1023. URL <http://dx.doi.org/10.1116/1.2357967>.
- [5] Langford, R. M., Nellen, P. M., Gierak, J., and Fu, Y. "Focused Ion Beam Micro- and Nano-engineering." *MRS Bulletin*, vol. 32, no. 05, pp. 417–423 (2007). URL <http://dx.doi.org/10.1557/mrs2007.65>.
- [6] Matsui, S. and Ochiai, Y. "Focused ion beam applications to solid state devices." *Nanotechnology*, vol. 7, no. 3, p. 247 (Sep. 1996). ISSN 0957-4484. URL <http://dx.doi.org/10.1088/0957-4484/7/3/013> [Accessed: 2014-01-10].
- [7] Bischoff, L. "Alloy liquid metal ion sources and their application in mass separated focused ion beams." *Ultramicroscopy*, vol. 103, no. 1, pp. 59–66 (Apr. 2005). ISSN 0304-3991. URL <http://dx.doi.org/10.1016/j.ultramicro.2004.11.020> [Accessed: 2014-01-20].
- [8] Müller, E. W. "Das Feldionenmikroskop." *Zeitschrift für Physik*, vol. 131, no. 1, pp. 136–142 (Mar. 1951). ISSN 0044-3328. URL <http://dx.doi.org/10.1007/BF01329651> [Accessed: 2014-11-06].

- [9] Müller, E. W. "Resolution of the Atomic Structure of a Metal Surface by the Field Ion Microscope." *Journal of Applied Physics*, vol. 27, no. 5, pp. 474–476 (May 1956). ISSN 0021-8979, 1089-7550. URL <http://dx.doi.org/10.1063/1.1722406> [Accessed: 2014-11-06].
- [10] Pitters, J. L., Urban, R., and Wolkow, R. A. "Creation and recovery of a W(111) single atom gas field ion source." *The Journal of Chemical Physics*, vol. 136, no. 15, p. 154704 (Apr. 2012). ISSN 0021-9606, 1089-7690. URL <http://dx.doi.org/10.1063/1.3702209> [Accessed: 2014-11-06].
- [11] Urban, R., Pitters, J. L., and Wolkow, R. A. "Gas field ion source current stability for trimer and single atom terminated W(111) tips." *Applied Physics Letters*, vol. 100, no. 26, p. 263105 (Jun. 2012). ISSN 0003-6951, 1077-3118. URL <http://dx.doi.org/10.1063/1.4726112> [Accessed: 2014-11-06].
- [12] Livengood, R. H., Tan, S., Hallstein, R., Notte, J., McVey, S., and Faridur Rahman, F. H. M. "The neon gas field ion source—a first characterization of neon nanomachining properties." *Nuclear Instruments and Methods in Physics Research Section A: Accelerators, Spectrometers, Detectors and Associated Equipment*, vol. 645, no. 1, pp. 136–140 (Jul. 2011). ISSN 0168-9002. URL <http://dx.doi.org/10.1016/j.nima.2010.12.220> [Accessed: 2014-11-06].
- [13] Chen, P., Veldhoven, E. v., Sanford, C. A., Salemink, H. W. M., Maas, D. J., Smith, D. A., Rack, P. D., and Alkemade, P. F. A. "Nanopillar growth by focused helium ion-beam-induced deposition." *Nanotechnology*, vol. 21, no. 45, p. 455302 (Nov. 2010). ISSN 0957-4484. URL <http://dx.doi.org/10.1088/0957-4484/21/45/455302> [Accessed: 2014-11-05].
- [14] Ward, J. W., Kubena, R., and Utlaut, M. "Transverse thermal velocity broadening of focused beams from liquid metal ion sources." *Journal of Vacuum Science Technology B: Microelectronics and Nanometer Structures*, vol. 6, no. 6, pp. 2090–2094 (1988). ISSN 1071-1023. URL <http://dx.doi.org/10.1116/1.584117>.
- [15] Utke, I., Hoffmann, P., and Melngailis, J. "Gas-assisted focused electron beam and ion beam processing and fabrication." *Journal of Vacuum Science & Technology B*, vol. 26, no. 4, pp. 1197–1276 (Aug. 2008). ISSN 2166-2746, 2166-2754. URL <http://dx.doi.org/10.1116/1.2955728> [Accessed: 2014-01-20].
- [16] Callegari, V. and Nellen, P. M. "Spontaneous growth of uniformly distributed In nanodots and In₃ nanowires on InP induced by a focused ion beam." *physica status solidi (a)*, vol. 204, no. 6, pp. 1665–1671 (2007). ISSN 1862-6319. URL <http://dx.doi.org/10.1002/pssa.200675337> [Accessed: 2014-01-20].

- [17] Philips and Electronics, N. "Materials Analysis FIB." Commercial Tech. Note 19 (Apr. 2008). URL <http://www.innovationservices.philips.com/sites/default/files/materials-analysis-fib.pdf> [Accessed: 2014-01-21].
- [18] Giannuzzi, L. A. and Stevie, F. A. "A review of focused ion beam milling techniques for TEM specimen preparation." *Micron*, vol. 30, no. 3, pp. 197–204 (Jun. 1999). ISSN 0968-4328. URL [http://dx.doi.org/10.1016/S0968-4328\(99\)00005-0](http://dx.doi.org/10.1016/S0968-4328(99)00005-0) [Accessed: 2014-01-13].
- [19] Stokes, D. J., Morrissey, F., and Lich, B. H. "A New Approach to Studying Biological and Soft Materials Using Focused Ion Beam Scanning Electron Microscopy (FIB SEM)." *Journal of Physics: Conference Series*, vol. 26, no. 1, p. 50 (Feb. 2006). ISSN 1742-6596. URL <http://dx.doi.org/10.1088/1742-6596/26/1/012> [Accessed: 2014-01-21].
- [20] Nikawa, K., Nasu, K., Murase, M., Kaito, T., Adachi, T., and Inoue, S. "New applications of focused ion beam technique to failure analysis and process monitoring of VLSI." In "Reliability Physics Symposium, 1989. 27th Annual Proceedings., International," (pp. 43–52) (1989). URL <http://dx.doi.org/10.1109/RELPHY.1989.36316>.
- [21] Schenkel, T., Radmilovic, V., Stach, E. A., Park, S.-J., and Persaud, A. "Formation of a few nanometer wide holes in membranes with a dual beam focused ion beam system." *Journal of Vacuum Science & Technology B*, vol. 21, no. 6, pp. 2720–2723 (Dec. 2003). ISSN 2166-2746, 2166-2754. URL <http://dx.doi.org/10.1116/1.1622935> [Accessed: 2014-01-21].
- [22] Van Vaeck, L., Adriaens, A., and Gijbels, R. "Static secondary ion mass spectrometry (S-SIMS) Part 1: methodology and structural interpretation." *Mass Spectrometry Reviews*, vol. 18, no. 1, pp. 1–47 (1999). ISSN 1098-2787. URL [http://dx.doi.org/10.1002/\(SICI\)1098-2787\(1999\)18:1<1::AID-MAS1>3.0.CO;2-W](http://dx.doi.org/10.1002/(SICI)1098-2787(1999)18:1<1::AID-MAS1>3.0.CO;2-W) [Accessed: 2014-01-21].
- [23] Seiler, H. "Secondary electron emission in the scanning electron microscope." *Journal of Applied Physics*, vol. 54, no. 11, pp. R1–R18 (Nov. 1983). ISSN 0021-8979, 1089-7550. URL <http://dx.doi.org/10.1063/1.332840> [Accessed: 2014-01-21].
- [24] Uchic, M. D., Groeber, M. A., Dimiduk, D. M., and Simmons, J. P. "3D microstructural characterization of nickel superalloys via serial-sectioning using a dual beam FIB-SEM." *Scripta Materialia*, vol. 55, no. 1, pp. 23–28 (Jul. 2006). ISSN 1359-6462. URL <http://dx.doi.org/10.1016/j.scriptamat.2006.02.039> [Accessed: 2014-01-21].
- [25] Stokes, D. J., Vystavel, T., and Morrissey, F. "Focused ion beam (FIB) milling of electrically insulating specimens using simultaneous primary electron and ion beam irradiation." *Journal*

of Physics D: Applied Physics, vol. 40, no. 3, p. 874 (Feb. 2007). ISSN 0022-3727. URL <http://dx.doi.org/10.1088/0022-3727/40/3/028> [Accessed: 2014-10-03].

- [26] Friedli, V. and Utke, I. "Optimized molecule supply from nozzle-based gas injection systems for focused electron- and ion-beam induced deposition and etching: simulation and experiment." *Journal of Physics D: Applied Physics*, vol. 42, no. 12, p. 125305 (Jun. 2009). ISSN 0022-3727. URL <http://dx.doi.org/10.1088/0022-3727/42/12/125305> [Accessed: 2014-01-21].
- [27] Cecere, M. A. "Thermoelectric cooling in gas-assisted FIB system." (May 1998). U.S. Classification: 250/492.21; 118/723.0FI; 118/726; 250/251 International Classification: H01J 37317, URL <http://www.google.com/patents?id=0XsdAAAAEBAJ> [Accessed: 2014-01-21].
- [28] Cleaver, J. R. A., Kirk, E. C. G., Young, R. J., and Ahmed, H. "Scanning ion beam techniques for the examination of microelectronic devices." *Journal of Vacuum Science & Technology B*, vol. 6, no. 3, pp. 1026–1029 (May 1988). ISSN 2166-2746, 2166-2754. URL <http://dx.doi.org/10.1116/1.584341> [Accessed: 2014-01-22].
- [29] Drummond, I. W. and Long, J. V. P. "Scanning Ion Microscopy and Ion Beam Micro-machining." *Nature*, vol. 215, no. 5104, pp. 950–952 (Aug. 1967). URL <http://dx.doi.org/10.1038/215950a0> [Accessed: 2014-01-22].
- [30] Phaneuf, M. W. "Applications of focused ion beam microscopy to materials science specimens." *Micron*, vol. 30, no. 3, pp. 277–288 (Jun. 1999). ISSN 0968-4328. URL [http://dx.doi.org/10.1016/S0968-4328\(99\)00012-8](http://dx.doi.org/10.1016/S0968-4328(99)00012-8) [Accessed: 2014-01-22].
- [31] Levi-Setti, R., Fox, T. R., and Lam, K. "Ion channeling effects in scanning ion microscopy with a 60 keV Ga⁺ probe." *Nuclear Instruments and Methods in Physics Research*, vol. 205, no. 1–2, pp. 299–309 (Jan. 1983). ISSN 0167-5087. URL [http://dx.doi.org/10.1016/0167-5087\(83\)90201-6](http://dx.doi.org/10.1016/0167-5087(83)90201-6) [Accessed: 2014-01-22].
- [32] Franklin, R. E., Kirk, E. C. G., Cleaver, J. R. A., and Ahmed, H. "Channelling ion image contrast and sputtering in gold specimens observed in a high-resolution scanning ion microscope." *Journal of Materials Science Letters*, vol. 7, no. 1, pp. 39–41 (Jan. 1988). ISSN 0261-8028, 1573-4811. URL <http://dx.doi.org/10.1007/BF01729909> [Accessed: 2014-01-22].
- [33] Castaing, R. and Slodzian, G. "Analytical microscopy by secondary ion imaging techniques." *Journal of Physics E: Scientific Instruments*, vol. 14, no. 10, p. 1119 (Oct. 1981). ISSN 0022-3735. URL <http://dx.doi.org/10.1088/0022-3735/14/10/002> [Accessed: 2014-01-22].

- [34] Pint, B. A., Martin, J. R., and Hobbs, L. W. "18O/SIMS characterization of the growth mechanism of doped and undoped α -Al₂O₃." *Oxidation of Metals*, vol. 39, no. 3-4, pp. 167–195 (Apr. 1993). ISSN 0030-770X, 1573-4889. URL <http://dx.doi.org/10.1007/BF00665610> [Accessed: 2014-01-22].
- [35] De Souza, R. A., Kilner, J. A., and Walker, J. F. "A SIMS study of oxygen tracer diffusion and surface exchange in La_{0.8}Sr_{0.2}MnO_{3+ δ} ." *Materials Letters*, vol. 43, no. 1–2, pp. 43–52 (Mar. 2000). ISSN 0167-577X. URL [http://dx.doi.org/10.1016/S0167-577X\(99\)00228-1](http://dx.doi.org/10.1016/S0167-577X(99)00228-1) [Accessed: 2014-01-22].
- [36] Chabala, J. M., Soni, K. K., Li, J., Gavrilov, K. L., and Levi-Setti, R. "High-resolution chemical imaging with scanning ion probe SIMS." *International Journal of Mass Spectrometry and Ion Processes*, vol. 143, pp. 191–212 (May 1995). ISSN 0168-1176. URL [http://dx.doi.org/10.1016/0168-1176\(94\)04119-R](http://dx.doi.org/10.1016/0168-1176(94)04119-R) [Accessed: 2014-01-22].
- [37] Zeindl, H. P., Wegehaupt, T., Eisele, I., Oppolzer, H., Reisinger, H., Tempel, G., and Koch, F. "Growth and characterization of a delta-function doping layer in Si." *Applied Physics Letters*, vol. 50, no. 17, pp. 1164–1166 (Apr. 1987). ISSN 0003-6951, 1077-3118. URL <http://dx.doi.org/10.1063/1.97950> [Accessed: 2014-01-22].
- [38] Gibbons, J. F., Gronet, C. M., and Williams, K. E. "Limited reaction processing: Silicon epitaxy." *Applied Physics Letters*, vol. 47, no. 7, pp. 721–723 (Oct. 1985). ISSN 0003-6951, 1077-3118. URL <http://dx.doi.org/10.1063/1.96015> [Accessed: 2014-01-22].
- [39] Efimov, A. E., Tonevitsky, A. G., Dittrich, M., and Matsko, N. B. "Atomic force microscope (AFM) combined with the ultramicrotome: a novel device for the serial section tomography and AFM/TEM complementary structural analysis of biological and polymer samples." *Journal of Microscopy*, vol. 226, no. 3, pp. 207–216 (2007). ISSN 1365-2818. URL <http://dx.doi.org/10.1111/j.1365-2818.2007.01773.x> [Accessed: 2014-01-22].
- [40] Newcomb, S. B., Boothroyd, C. B., and Stobbs, W. M. "Specimen preparation methods for the examination of surfaces and interfaces in the transmission electron microscope." *Journal of Microscopy*, vol. 140, no. 2, pp. 195–207 (1985). ISSN 1365-2818. URL <http://dx.doi.org/10.1111/j.1365-2818.1985.tb02675.x> [Accessed: 2014-01-22].
- [41] Benedict, J., Anderson, R., and Klepeis, S. J. "Recent Developments in the use of the Tripod Polisher for TEM Specimen Preparation." *MRS Online Proceedings Library*, vol. 254 (1991). URL <http://dx.doi.org/10.1557/PROC-254-121>.

- [42] Li, J., Malis, T., and Dionne, S. "Recent advances in FIB-TEM specimen preparation techniques." *Materials Characterization*, vol. 57, no. 1, pp. 64-70 (Jul. 2006). ISSN 1044-5803. URL <http://dx.doi.org/10.1016/j.matchar.2005.12.007> [Accessed: 2014-01-22].
- [43] McCaffrey, J. P., Phaneuf, M. W., and Madsen, L. D. "Surface damage formation during ion-beam thinning of samples for transmission electron microscopy." *Ultramicroscopy*, vol. 87, no. 3, pp. 97-104 (Apr. 2001). ISSN 0304-3991. URL [http://dx.doi.org/10.1016/S0304-3991\(00\)00096-6](http://dx.doi.org/10.1016/S0304-3991(00)00096-6) [Accessed: 2014-01-22].
- [44] Langford, R. M. and Rogers, M. "In situ lift-out: Steps to improve yield and a comparison with other FIB TEM sample preparation techniques." *Micron*, vol. 39, no. 8, pp. 1325-1330 (Dec. 2008). ISSN 0968-4328. URL <http://dx.doi.org/10.1016/j.micron.2008.02.006> [Accessed: 2014-01-22].
- [45] Weste, N. H. and Money, D. *CMOS Vlsi Design* (Pearson/Addison Wesley, 2005). URL <http://web.ewu.edu/groups/technology/Claudio/ee430/Lectures/L1-print.pdf> [Accessed: 2014-01-24].
- [46] Boyd, S. B. "Semiconductor Manufacturing Trends in Product Type and Geography." In "Life-Cycle Assessment of Semiconductors," (pp. 27-35) (Springer New York, 2012). ISBN 978-1-4419-9987-0, 978-1-4419-9988-7. URL http://link.springer.com/chapter/10.1007/978-1-4419-9988-7_3 [Accessed: 2014-01-24].
- [47] Kim, D.-W., Choi, S., Yoon, J. S., and Chung, C. "Future logic device technologies beyond the 28nm node." In "2012 IEEE 11th International Conference on Solid-State and Integrated Circuit Technology (ICSICT)," (pp. 1-4) (2012). URL <http://dx.doi.org/10.1109/ICSICT.2012.6467592>.
- [48] Mashiko, Y., Morimoto, H., Koyama, H., Kawazu, S., Kaito, T., and Adachi, T. "A New VLSI Diagnosis Technique: Focused Ion Beam Assisted Multi-level Circuit Probing." In "Reliability Physics Symposium, 1987. 25th Annual," (pp. 111-117) (1987). URL <http://dx.doi.org/10.1109/IRPS.1987.362165>.
- [49] Banerjee, I., Tracy, B., Davies, P., and McDonald, B. "Use of advanced analytical techniques for VLSI failure analysis." In "Reliability Physics Symposium, 1990. 28th Annual Proceedings., International," (pp. 61-68) (1990). URL <http://dx.doi.org/10.1109/RELPHY.1990.66063>.

- [50] Xiao-ling, L. and Xiao-wen, Z. "FIB fast positioning technology and its application." In "Physical and Failure Analysis of Integrated Circuits (IPFA), 2013 20th IEEE International Symposium on the," (pp. 537–541) (2013). URL <http://dx.doi.org/10.1109/IPFA.2013.6599218>.
- [51] Chen, K.-A., Chang, T.-W., Wu, M.-C., Chao, M.-T., Jou, J.-Y., and Chen, S. "Design-for-debug layout adjustment for FIB probing and circuit editing." In "Test Conference (ITC), 2011 IEEE International," (pp. 1–9) (2011). URL <http://dx.doi.org/10.1109/TEST.2011.6139155>.
- [52] Malek, C. K., Hartley, F. T., and Neogi, J. "Fast prototyping of high-aspect ratio, high-resolution X-ray masks by gas-assisted focused ion beam." *Microsystem Technologies*, vol. 9, no. 6-7, pp. 409–412 (Sep. 2003). ISSN 0946-7076, 1432-1858. URL <http://dx.doi.org/10.1007/s00542-002-0215-5> [Accessed: 2014-01-24].
- [53] Abramo, M. T. and Hahn, L. L. "The application of advanced techniques for complex focused-ion-beam device modification." *Microelectronics Reliability*, vol. 36, no. 11–12, pp. 1775–1778 (Nov. 1996). ISSN 0026-2714. URL [http://dx.doi.org/10.1016/0026-2714\(96\)00195-3](http://dx.doi.org/10.1016/0026-2714(96)00195-3) [Accessed: 2014-01-24].
- [54] Khan, A. M. "Circuit Edit Technology for Submicron Structures in Semiconductor Devices." *International Journal of Engineering and Advanced Technology*, vol. 2, no. 5, pp. 255–257 (2013). URL <http://www.doaj.org/doaj?func=fulltext&aId=1507105> [Accessed: 2014-01-23].
- [55] Song, Z., Loh, S. K., Neo, S. P., Zheng, X. H., and Teo, H. T. "Application of FIB Circuit Edit and Electrical Characterization in Failure Analysis for Invisible Defect Issues." In "Physical and Failure Analysis of Integrated Circuits, 2006. 13th International Symposium on the," (pp. 187–191) (2006). URL <http://dx.doi.org/10.1109/IPFA.2006.251027>.
- [56] Schlangen, R., Kerst, U., Kabakow, A., and Boit, C. "Electrical Performance Evaluation of FIB Edited Circuits through Chip Backside Exposing Shallow Trench Isolations." *Microelectronics Reliability*, vol. 45, no. 9–11, pp. 1544–1549 (Sep. 2005). ISSN 0026-2714. URL <http://dx.doi.org/10.1016/j.microrel.2005.07.033> [Accessed: 2014-01-23].
- [57] Miura, K., Kobatake, T., Nakamae, K., and Fujioka, H. "A low energy FIB processing, repair, and test system." *Microelectronics Reliability*, vol. 43, no. 9–11, pp. 1627–1631 (Sep. 2003). ISSN 0026-2714. URL [http://dx.doi.org/10.1016/S0026-2714\(03\)00286-5](http://dx.doi.org/10.1016/S0026-2714(03)00286-5) [Accessed: 2014-01-23].

- [58] Ray, V. "High Aspect Ratio Via Milling Endpoint Phenomena in Focused Ion Beam Modification of Integrated Circuits." In "ISTFA 2004: 30 th International Symposium for Testing and Failure Analysis," (pp. 658–659) (2004). URL http://partbeamsystech.com/papers/HAR_Endpoint.pdf [Accessed: 2014-01-23].
- [59] Edwards, C. "Save big, don't go small - [electronics chip design]." *Engineering Technology*, vol. 4, no. 13, pp. 36–37 (2009). ISSN 1750-9637.
- [60] Gu, G., Bassom, N., Casey, J., J.D., Scipioni, L., Saxonis, A., and Huynh, C. "FIB-induced deposition of conducting material with intermediate resistivity for design debugging." In "Reliability Physics Symposium Proceedings, 2003. 41st Annual. 2003 IEEE International," (pp. 590–591) (2003). URL <http://dx.doi.org/10.1109/RELPHY.2003.1197820>.
- [61] Cho, J. and Thompson, C. V. "Grain size dependence of electromigration-induced failures in narrow interconnects." *Applied Physics Letters*, vol. 54, no. 25, pp. 2577–2579 (Jun. 1989). ISSN 0003-6951, 1077-3118. URL <http://dx.doi.org/10.1063/1.101054> [Accessed: 2014-01-24].
- [62] Nikawa, K. "Applications of focused ion beam technique to failure analysis of very large scale integrations: A review." *Journal of Vacuum Science & Technology B*, vol. 9, no. 5, pp. 2566–2577 (Sep. 1991). ISSN 2166-2746, 2166-2754. URL <http://dx.doi.org/10.1116/1.585694> [Accessed: 2014-01-23].
- [63] Eom, G. Y. and Oh, H.-S. "Improvement of sub 0.1 μm VLSI Device Quality Using a Novel Titanium Silicide Formation Process." *Journal of the Korean Physical Society*, vol. 40, no. 2, pp. 335–338 (2002). URL <http://www.kps.or.kr/home/kor/journal/library/downloadPdf.asp?articleid=%7B20D602DD-25F6-42B7-813F-C32925E2CF9D%7D> [Accessed: 2014-01-23].
- [64] Yeoh, T. S., Ives, N. A., Presser, N., Stupian, G. W., Leung, M. S., McCollum, J. L., and Hawley, F. W. "Focused ion beam tomography of a microelectronic device with sub-2-nm resolution." *Journal of Vacuum Science & Technology B*, vol. 25, no. 3, pp. 922–925 (May 2007). ISSN 2166-2746, 2166-2754. URL <http://dx.doi.org/10.1116/1.2740288> [Accessed: 2014-01-24].
- [65] Reyntjens, S. and Puers, R. "Focused ion beam induced deposition: fabrication of three-dimensional microstructures and Young's modulus of the deposited material." *Journal of Micromechanics and Microengineering*, vol. 10, no. 2, p. 181 (Jun. 2000). ISSN 0960-1317. URL <http://dx.doi.org/10.1088/0960-1317/10/2/314> [Accessed: 2014-02-24].

- [66] Prewett, P., Eastwood, A., Turner, G., and Watson, J. "Gallium staining in FIB repair of photomasks." *Microelectronic Engineering*, vol. 21, no. 1–4, pp. 191–196 (Apr. 1993). ISSN 0167-9317. URL [http://dx.doi.org/10.1016/0167-9317\(93\)90053-8](http://dx.doi.org/10.1016/0167-9317(93)90053-8) [Accessed: 2014-02-24].
- [67] Cui, Z., Prewett, P. D., and Watson, J. G. "Focused ion beam biased repair of conventional and phase shift masks." *Journal of Vacuum Science & Technology B*, vol. 14, no. 6, pp. 3942–3946 (Nov. 1996). ISSN 2166-2746, 2166-2754. URL <http://dx.doi.org/10.1116/1.588700> [Accessed: 2014-02-04].
- [68] Liang, T., Frenberg, E., Lieberman, B., and Stivers, A. "Advanced photolithographic mask repair using electron beams." *Journal of Vacuum Science & Technology B*, vol. 23, no. 6, pp. 3101–3105 (Dec. 2005). ISSN 2166-2746, 2166-2754. URL <http://dx.doi.org/10.1116/1.2062428> [Accessed: 2014-02-24].
- [69] Chen, B. K., Zhang, Y., Perovic, D. D., and Sun, Y. "MEMS microgrippers with thin gripping tips." *Journal of Micromechanics and Microengineering*, vol. 21, no. 10, p. 105004 (Oct. 2011). ISSN 0960-1317. URL <http://dx.doi.org/10.1088/0960-1317/21/10/105004> [Accessed: 2014-02-28].
- [70] Meister, A., Liley, M., Brugger, J., Pugin, R., and Heinzelmann, H. "Nanodispenser for attoliter volume deposition using atomic force microscopy probes modified by focused-ion-beam milling." *Applied Physics Letters*, vol. 85, no. 25, pp. 6260–6262 (Dec. 2004). ISSN 0003-6951, 1077-3118. URL <http://dx.doi.org/10.1063/1.1842352> [Accessed: 2014-03-04].
- [71] Meijer, J., Vogel, T., Burchard, B., Rangelow, I. W., Bischoff, L., Wrachtrup, J., Domhan, M., Jelezko, F., Schnitzler, W., Schulz, S. A., Singer, K., and Schmidt-Kaler, F. "Concept of deterministic single ion doping with sub-nm spatial resolution." *Applied Physics A*, vol. 83, no. 2, pp. 321–327 (May 2006). ISSN 0947-8396, 1432-0630. URL <http://dx.doi.org/10.1007/s00339-006-3497-0> [Accessed: 2014-03-04].
- [72] Nam, C. Y., Kim, J. Y., and Fischer, J. E. "Focused-ion-beam platinum nanopatterning for GaN nanowires: Ohmic contacts and patterned growth." *Applied Physics Letters*, vol. 86, no. 19, p. 193112 (May 2005). ISSN 0003-6951, 1077-3118. URL <http://dx.doi.org/10.1063/1.1925775> [Accessed: 2014-02-28].
- [73] Ross, I. M., Luxmoore, I. J., Cullis, A. G., Orr, J., Buckle, P. D., and Jefferson, J. H. "Characterisation of tungsten nano-wires prepared by electron and ion beam induced chemical vapour deposition." *Journal of Physics: Conference Series*, vol. 26, no. 1, p. 363 (Feb. 2006). ISSN

1742-6596. URL <http://dx.doi.org/10.1088/1742-6596/26/1/088> [Accessed: 2014-02-28].

- [74] Song, M., Mitsuishi, K., Tanaka, M., Takeguchi, M., Shimojo, M., and Furuya, K. "Fabrication of self-standing nanowires, nanodendrites, and nanofractal-like trees on insulator substrates with an electron-beam-induced deposition." *Applied Physics A: Materials Science & Processing*, vol. 80, pp. 1431–1436 (Apr. 2005). ISSN 0947-8396. URL <http://dx.doi.org/10.1007/s00339-004-2997-z> [Accessed: 2014-11-11].
- [75] Klein, K. L., Randolph, S. J., Fowlkes, J. D., Allard, L. F., Lii, H. M. M., Simpson, M. L., and Rack, P. D. "Single-crystal nanowires grown via electron-beam-induced deposition." *Nanotechnology*, vol. 19, no. 34, p. 345705 (Aug. 2008). ISSN 0957-4484. URL <http://dx.doi.org/10.1088/0957-4484/19/34/345705> [Accessed: 2014-11-11].
- [76] Liu, Z.-Q., Mitsuishi, K., and Furuya, K. "Effects of focus change on the fabrication of tungsten nanowire by electron-beam-induced deposition." *Nanotechnology*, vol. 15, no. 6, p. S414 (Jun. 2004). ISSN 0957-4484. URL <http://dx.doi.org/10.1088/0957-4484/15/6/019> [Accessed: 2014-11-11].
- [77] Wu, H. M., Stern, L. A., Chen, J. H., Huth, M., Schwalb, C. H., Winhold, M., Porrati, F., Gonzalez, C. M., Timilsina, R., and Rack, P. D. "Synthesis of nanowires via helium and neon focused ion beam induced deposition with the gas field ion microscope." *Nanotechnology*, vol. 24, no. 17, p. 175302 (May 2013). ISSN 0957-4484. URL <http://dx.doi.org/10.1088/0957-4484/24/17/175302> [Accessed: 2014-11-05].
- [78] Alkemade, P. F. A., Miro, H., Veldhoven, E. v., Maas, D. J., Smith, D. A., and Rack, P. D. "Pulsed helium ion beam induced deposition: A means to high growth rates." *Journal of Vacuum Science & Technology B*, vol. 29, no. 6, p. 06FG05 (Nov. 2011). ISSN 2166-2746, 2166-2754. URL <http://dx.doi.org/10.1116/1.3656347> [Accessed: 2014-11-05].
- [79] Teng, J. and Prewett, P. D. "Focused ion beam fabrication of thermally actuated bimorph cantilevers." *Sensors and Actuators A: Physical*, vol. 123–124, pp. 608–613 (Sep. 2005). ISSN 0924-4247. URL <http://dx.doi.org/10.1016/j.sna.2005.04.030> [Accessed: 2014-02-28].
- [80] Urbánek, M., Uhlíř, V., Bátor, P., Kolíbalová, E., Hrnčíř, T., Spousta, J., and Šikola, T. "Focused ion beam fabrication of spintronic nanostructures: an optimization of the milling process." *Nanotechnology*, vol. 21, no. 14, p. 145304 (Apr. 2010). ISSN 0957-4484. URL <http://dx.doi.org/10.1088/0957-4484/21/14/145304> [Accessed: 2014-02-28].

- [81] Daniel, J. H., Moore, D. F., and F Walker, J. "Focused ion beams and silicon-on-insulator - a novel approach to MEMS." *Smart Materials and Structures*, vol. 9, no. 3, p. 284 (Jun. 2000). ISSN 0964-1726. URL <http://dx.doi.org/10.1088/0964-1726/9/3/306> [Accessed: 2014-02-28].
- [82] Hao, L., Macfarlane, J., Gallop, J. C., Romans, E., Cox, D., Hutson, D., and Chen, J. "Spatial Resolution Assessment of Nano-SQUIDs Made by Focused Ion Beam." *IEEE Transactions on Applied Superconductivity*, vol. 17, no. 2, pp. 742–745 (Jun. 2007). ISSN 1051-8223. URL <http://dx.doi.org/10.1109/TASC.2007.898068>.
- [83] Hao, L., Macfarlane, J. C., Gallop, J. C., Cox, D., Beyer, J., Drung, D., and Schurig, T. "Measurement and noise performance of nano-superconducting-quantum-interference devices fabricated by focused ion beam." *Applied Physics Letters*, vol. 92, no. 19, p. 192507 (May 2008). ISSN 0003-6951, 1077-3118. URL <http://dx.doi.org/10.1063/1.2917580> [Accessed: 2014-03-03].
- [84] Guo, L. J. "Nanoimprint Lithography: Methods and Material Requirements." *Advanced Materials*, vol. 19, no. 4, pp. 495–513 (2007). ISSN 1521-4095. URL <http://dx.doi.org/10.1002/adma.200600882> [Accessed: 2014-03-03].
- [85] Ong, N. S., Koh, Y. H., and Fu, Y. Q. "Microlens array produced using hot embossing process." *Microelectronic Engineering*, vol. 60, no. 3–4, pp. 365–379 (Apr. 2002). ISSN 0167-9317. URL [http://dx.doi.org/10.1016/S0167-9317\(01\)00695-5](http://dx.doi.org/10.1016/S0167-9317(01)00695-5) [Accessed: 2014-02-28].
- [86] Watanabe, K., Morita, T., Kometani, R., Hoshino, T., Kondo, K., Kanda, K., Haruyama, Y., Kaito, T., Fujita, J., Ishida, M., Ochiai, Y., Tajima, T., and Matsui, S. "Nanoimprint using three-dimensional microlens mold made by focused-ion-beam chemical vapor deposition." *Journal of Vacuum Science & Technology B*, vol. 22, no. 1, pp. 22–26 (Dec. 2003). ISSN 2166-2746, 2166-2754. URL <http://dx.doi.org/10.1116/1.1633281> [Accessed: 2014-02-28].
- [87] Taniguchi, J., Koga, K., Kogo, Y., and Miyamoto, I. "Rapid and three-dimensional nanoimprint template fabrication technology using focused ion beam lithography." *Microelectronic Engineering*, vol. 83, no. 4–9, pp. 940–943 (Apr. 2006). ISSN 0167-9317. URL <http://dx.doi.org/10.1016/j.mee.2006.01.101> [Accessed: 2014-03-05].
- [88] Arshak, K., Mihov, M., Nakahara, S., Arshak, A., and McDonagh, D. "A novel focused-ion-beam lithography process for sub-100 nanometer technology nodes." *Superlattices and Microstructures*, vol. 36, no. 1–3, pp. 335–343 (Jul. 2004). ISSN 0749-6036. URL <http://dx.doi.org/10.1016/j.spmi.2004.08.030> [Accessed: 2014-03-05].

- [89] Chekurov, N., Grigoras, K., Peltonen, A., Franssila, S., and Tittonen, I. "The fabrication of silicon nanostructures by local gallium implantation and cryogenic deep reactive ion etching." *Nanotechnology*, vol. 20, no. 6, p. 065307 (Feb. 2009). ISSN 0957-4484. URL <http://dx.doi.org/10.1088/0957-4484/20/6/065307> [Accessed: 2014-03-04].
- [90] Sievilä, P., Chekurov, N., and Tittonen, I. "The fabrication of silicon nanostructures by focused-ion-beam implantation and TMAH wet etching." *Nanotechnology*, vol. 21, no. 14, p. 145301 (Apr. 2010). ISSN 0957-4484. URL <http://dx.doi.org/10.1088/0957-4484/21/14/145301> [Accessed: 2014-03-05].
- [91] Bischoff, L., Schmidt, B., Akhmadaliev, C., and Mücklich, A. "Investigation of FIB assisted CoSi₂ nanowire growth." *Microelectronic Engineering*, vol. 83, no. 4–9, pp. 800–803 (Apr. 2006). ISSN 0167-9317. URL <http://dx.doi.org/10.1016/j.mee.2006.01.129> [Accessed: 2014-02-28].
- [92] Hetzel, M., Lugstein, A., Zeiner, C., Wójcik, T., Pongratz, P., and Bertagnolli, E. "Ultra-fast vapour–liquid–solid synthesis of Si nanowires using ion-beam implanted gallium as catalyst." *Nanotechnology*, vol. 22, no. 39, p. 395601 (Sep. 2011). ISSN 0957-4484. URL <http://dx.doi.org/10.1088/0957-4484/22/39/395601> [Accessed: 2014-03-05].
- [93] De Marco, A. J. and Melngailis, J. "Maskless fabrication of JFETs via focused ion beams." *Solid-State Electronics*, vol. 48, no. 10–11, pp. 1833–1836 (Oct. 2004). ISSN 0038-1101. URL <http://dx.doi.org/10.1016/j.sse.2004.05.022> [Accessed: 2014-03-05].
- [94] Sazio, P. J. A., Vijendran, S., Yu, W., Beere, H. E., Jones, G. A. C., Linfield, E. H., and Ritchie, D. A. "Focused ion molecular-beam epitaxy – a novel approach to 3D device fabrication using simultaneous p- and n-type doping." *Journal of Crystal Growth*, vol. 201–202, pp. 12–16 (May 1999). ISSN 0022-0248. URL [http://dx.doi.org/10.1016/S0022-0248\(98\)01267-6](http://dx.doi.org/10.1016/S0022-0248(98)01267-6) [Accessed: 2014-03-05].
- [95] Meier, C., Reuter, D., Riedesel, C., and Wieck, A. D. "Fabrication of two-dimensional electron systems by focused ion beam doping of III/V semiconductor heterostructures." *Journal of Applied Physics*, vol. 93, no. 10, pp. 6100–6106 (May 2003). ISSN 0021-8979, 1089-7550. URL <http://dx.doi.org/10.1063/1.1563032> [Accessed: 2014-03-05].
- [96] Reuter, D., Meier, C., Riedesel, C., and Wieck, A. D. "Local two-dimensional electron gas formation in p-doped GaAs/InyGa1-yAs/AlxGa1-xAs heterostructures by focused Si-implantation doping." *Semiconductor Science and Technology*, vol. 17, no. 6, p. 585 (Jun. 2002). ISSN

- 0268-1242. URL <http://dx.doi.org/10.1088/0268-1242/17/6/315> [Accessed: 2014-03-05].
- [97] Sigmund, P. "Theory of Sputtering. I. Sputtering Yield of Amorphous and Polycrystalline Targets." *Physical Review*, vol. 184, no. 2, pp. 383–416 (Aug. 1969). URL <http://dx.doi.org/10.1103/PhysRev.184.383> [Accessed: 2014-03-13].
- [98] Sigmund, P. "Recollections of fifty years with sputtering." *Thin Solid Films*, vol. 520, no. 19, pp. 6031–6049 (Jul. 2012). ISSN 0040-6090. URL <http://dx.doi.org/10.1016/j.tsf.2012.06.003> [Accessed: 2014-03-13].
- [99] Fetz, H. "Über die Kathodenzerstäubung bei schieferm Aufparall der Ionen." *Zeitschrift für Physik*, vol. 119, no. 9-10, pp. 590–601 (Sep. 1942). ISSN 0044-3328. URL <http://dx.doi.org/10.1007/BF01337787> [Accessed: 2014-03-11].
- [100] Campillo, I., Pitarke, J. M., and Eguiluz, A. G. "Electronic stopping power of aluminum crystal." *Physical Review B*, vol. 58, no. 16, pp. 10307–10314 (Oct. 1998). URL <http://dx.doi.org/10.1103/PhysRevB.58.10307> [Accessed: 2014-03-11].
- [101] van Gunsteren, W. F. and Berendsen, H. J. C. "Computer Simulation of Molecular Dynamics: Methodology, Applications, and Perspectives in Chemistry." *Angewandte Chemie International Edition in English*, vol. 29, no. 9, pp. 992–1023 (1990). ISSN 1521-3773. URL <http://dx.doi.org/10.1002/anie.199009921> [Accessed: 2014-03-11].
- [102] Urbassek, H. M. "Molecular-dynamics simulation of sputtering." *Nuclear Instruments and Methods in Physics Research Section B: Beam Interactions with Materials and Atoms*, vol. 122, no. 3, pp. 427–441 (Feb. 1997). ISSN 0168-583X. URL [http://dx.doi.org/10.1016/S0168-583X\(96\)00681-7](http://dx.doi.org/10.1016/S0168-583X(96)00681-7) [Accessed: 2014-03-11].
- [103] Thijsse, B. J., Klaver, T. P. C., and Haddeman, E. F. C. "Molecular dynamics simulation of silicon sputtering: sensitivity to the choice of potential." *Applied Surface Science*, vol. 231–232, pp. 29–38 (Jun. 2004). ISSN 0169-4332. URL <http://dx.doi.org/10.1016/j.apsusc.2004.03.207> [Accessed: 2014-03-11].
- [104] Bringa, E. M. and Johnson, R. E. "Coulomb Explosion and Thermal Spikes." *Physical Review Letters*, vol. 88, no. 16, p. 165501 (Apr. 2002). URL <http://dx.doi.org/10.1103/PhysRevLett.88.165501> [Accessed: 2014-03-11].
- [105] Bringa, E. M., Johnson, R. E., and Dutkiewicz, L. "Molecular dynamics study of non-equilibrium energy transport from a cylindrical track: Part II: Spike models for sputtering yield." *Nuclear*

Instruments and Methods in Physics Research Section B: Beam Interactions with Materials and Atoms, vol. 152, no. 2–3, pp. 267–290 (May 1999). ISSN 0168-583X. URL [http://dx.doi.org/10.1016/S0168-583X\(99\)00066-X](http://dx.doi.org/10.1016/S0168-583X(99)00066-X) [Accessed: 2014-03-11].

- [106] Bringa, E. M. and Johnson, R. E. “Molecular dynamics study of non-equilibrium energy transport from a cylindrical track: I. Test of “spike” models.” *Nuclear Instruments and Methods in Physics Research Section B: Beam Interactions with Materials and Atoms*, vol. 143, no. 4, pp. 513–535 (Oct. 1998). ISSN 0168-583X. URL [http://dx.doi.org/10.1016/S0168-583X\(98\)00405-4](http://dx.doi.org/10.1016/S0168-583X(98)00405-4) [Accessed: 2014-03-12].
- [107] Ghaly, M. and Averback, R. S. “Effect of viscous flow on ion damage near solid surfaces.” *Physical Review Letters*, vol. 72, no. 3, pp. 364–367 (Jan. 1994). URL <http://dx.doi.org/10.1103/PhysRevLett.72.364> [Accessed: 2014-11-12].
- [108] Baumer, R. E. and Demkowicz, M. J. “Prediction of Spontaneous Plastic Deformation of Irradiated Metallic Glasses due to Thermal Spike-Induced Plasticity.” *Materials Research Letters*, vol. 2, no. 4, pp. 221–226 (May 2014). ISSN null. URL <http://dx.doi.org/10.1080/21663831.2014.916760> [Accessed: 2014-11-12].
- [109] Greaves, G., Hinks, J. A., Busby, P., Mellors, N. J., Ilinov, A., Kuronen, A., Nordlund, K., and Donnelly, S. E. “Enhanced Sputtering Yields from Single-Ion Impacts on Gold Nanorods.” *Physical Review Letters*, vol. 111, no. 6, p. 065504 (Aug. 2013). URL <http://dx.doi.org/10.1103/PhysRevLett.111.065504> [Accessed: 2014-11-12].
- [110] Winograd, N. “The magic of cluster SIMS.” *Analytical Chemistry*, vol. 77, no. 7, pp. 142–A (2005). URL <http://pubs.acs.org/doi/pdf/10.1021/ac053355f> [Accessed: 2014-03-12].
- [111] Fenyő, D., Sundqvist, B. U. R., Karlsson, B. R., and Johnson, R. E. “Molecular-dynamics study of electronic sputtering of large organic molecules.” *Physical Review B*, vol. 42, no. 4, pp. 1895–1902 (Aug. 1990). URL <http://dx.doi.org/10.1103/PhysRevB.42.1895> [Accessed: 2014-03-11].
- [112] Russo, M. F., Postawa, Z., and Garrison, B. J. “A Computational Investigation of C60 Depth Profiling of Ag: Molecular Dynamics of Multiple Impact Events.” *The Journal of Physical Chemistry C*, vol. 113, no. 8, pp. 3270–3276 (Feb. 2009). ISSN 1932-7447. URL <http://dx.doi.org/10.1021/jp808706y> [Accessed: 2014-03-12].

- [113] Robinson, M. T. and Torrens, I. M. "Computer simulation of atomic-displacement cascades in solids in the binary-collision approximation." *Physical Review B*, vol. 9, no. 12, pp. 5008–5024 (Jun. 1974). URL <http://dx.doi.org/10.1103/PhysRevB.9.5008> [Accessed: 2014-03-25].
- [114] Biersack, J. P. and Eckstein, W. "Sputtering studies with the Monte Carlo Program TRIM.SP." *Applied Physics A*, vol. 34, no. 2, pp. 73–94 (Jun. 1984). ISSN 0947-8396, 1432-0630. URL <http://dx.doi.org/10.1007/BF00614759> [Accessed: 2014-03-25].
- [115] Ebm, C. and Hobler, G. "Assessment of approximations for efficient topography simulation of ion beam processes: 10 keV Ar on Si." *Nuclear Instruments and Methods in Physics Research Section B: Beam Interactions with Materials and Atoms*, vol. 267, no. 18, pp. 2987–2990 (Sep. 2009). ISSN 0168-583X. URL <http://dx.doi.org/10.1016/j.nimb.2009.06.014> [Accessed: 2014-03-13].
- [116] Robinson, M. T. "Computer simulation of collision cascades in monazite." *Physical Review B*, vol. 27, no. 9, pp. 5347–5359 (May 1983). URL <http://dx.doi.org/10.1103/PhysRevB.27.5347> [Accessed: 2014-03-13].
- [117] Hobler, G. "Assessment of surface potential models by molecular dynamics simulations of atom ejection from (1 0 0)-Si surfaces." *Nuclear Instruments and Methods in Physics Research Section B: Beam Interactions with Materials and Atoms*, vol. 303, pp. 165–169 (May 2013). ISSN 0168-583X. URL <http://dx.doi.org/10.1016/j.nimb.2012.11.022> [Accessed: 2014-03-25].
- [118] Ramachandra, R., Griffin, B., and Joy, D. "A model of secondary electron imaging in the helium ion scanning microscope." *Ultramicroscopy*, vol. 109, no. 6, pp. 748–757 (May 2009). ISSN 0304-3991. URL <http://dx.doi.org/10.1016/j.ultramic.2009.01.013> [Accessed: 2014-11-05].
- [119] Smith, D. A., Joy, D. C., and Rack, P. D. "Monte Carlo simulation of focused helium ion beam induced deposition." *Nanotechnology*, vol. 21, no. 17, p. 175302 (Apr. 2010). ISSN 0957-4484. URL <http://dx.doi.org/10.1088/0957-4484/21/17/175302> [Accessed: 2014-11-05].
- [120] Timilsina, R., Smith, D. A., and Rack, P. D. "A comparison of neon versus helium ion beam induced deposition via Monte Carlo simulations." *Nanotechnology*, vol. 24, no. 11, p. 115302 (Mar. 2013). ISSN 0957-4484. URL <http://dx.doi.org/10.1088/0957-4484/24/11/115302> [Accessed: 2014-11-05].

- [121] Kang, H. J., Shimizu, R., Saito, T., and Yamakawa, H. "Computer simulation of damage processes during ion implantation." *Journal of Applied Physics*, vol. 62, no. 7, pp. 2733–2737 (Oct. 1987). ISSN 0021-8979, 1089-7550. URL <http://dx.doi.org/10.1063/1.339400> [Accessed: 2014-03-25].
- [122] Hobler, G. and Kovač, D. "Dynamic binary collision simulation of focused ion beam milling of deep trenches." *Nuclear Instruments and Methods in Physics Research Section B: Beam Interactions with Materials and Atoms*, vol. 269, no. 14, pp. 1609–1613 (Jul. 2011). ISSN 0168-583X. URL <http://dx.doi.org/10.1016/j.nimb.2010.12.076> [Accessed: 2014-03-25].
- [123] Boxleitner, W. and Hobler, G. "FIBSIM – dynamic Monte Carlo simulation of compositional and topography changes caused by focused ion beam milling." *Nuclear Instruments and Methods in Physics Research Section B: Beam Interactions with Materials and Atoms*, vol. 180, no. 1–4, pp. 125–129 (Jun. 2001). ISSN 0168-583X. URL [http://dx.doi.org/10.1016/S0168-583X\(01\)00406-2](http://dx.doi.org/10.1016/S0168-583X(01)00406-2) [Accessed: 2014-04-15].
- [124] Möller, W. and Eckstein, W. "Tridyn — A TRIM simulation code including dynamic composition changes." *Nuclear Instruments and Methods in Physics Research Section B: Beam Interactions with Materials and Atoms*, vol. 2, no. 1–3, pp. 814–818 (Mar. 1984). ISSN 0168-583X. URL [http://dx.doi.org/10.1016/0168-583X\(84\)90321-5](http://dx.doi.org/10.1016/0168-583X(84)90321-5) [Accessed: 2014-03-25].
- [125] Hobler, G. "Combined binary collision and continuum mechanics model applied to focused ion beam milling of a silicon membrane." *Nuclear Instruments and Methods in Physics Research Section B: Beam Interactions with Materials and Atoms*. ISSN 0168-583X. URL <http://dx.doi.org/10.1016/j.nimb.2014.11.109> [Accessed: 2015-01-14].
- [126] Eckstein, W. and Preuss, R. "New fit formulae for the sputtering yield." *Journal of Nuclear Materials*, vol. 320, no. 3, pp. 209–213 (Aug. 2003). ISSN 00223115. URL [http://dx.doi.org/10.1016/S0022-3115\(03\)00192-2](http://dx.doi.org/10.1016/S0022-3115(03)00192-2) [Accessed: 2014-04-15].
- [127] YAMAMURA, Y. and TAWARA, H. "Energy dependence of ion-induced sputtering yields from monatomic solids at normal incidence." *Atomic Data and Nuclear Data Tables*, vol. 62, no. 2, pp. 149–253 (Mar. 1996). ISSN 0092-640X. URL <http://dx.doi.org/10.1006/adnd.1996.0005> [Accessed: 2014-04-15].
- [128] Bohdansky, J. "A universal relation for the sputtering yield of monoatomic solids at normal ion incidence." (1983). URL http://inis.iaea.org/Search/search.aspx?orig_q=RN:15000193 [Accessed: 2014-04-15].

- [129] Vasile, M. J., Xie, J., and Nassar, R. "Depth control of focused ion-beam milling from a numerical model of the sputter process." *Journal of Vacuum Science & Technology B*, vol. 17, no. 6, pp. 3085–3090 (Nov. 1999). ISSN 2166-2746, 2166-2754. URL <http://dx.doi.org/10.1116/1.590959> [Accessed: 2014-04-15].
- [130] Zhang, Z. L. and Zhang, L. "Anisotropic angular distribution of sputtered atoms." *Radiation Effects and Defects in Solids*, vol. 159, no. 5, pp. 301–307 (May 2004). ISSN 1042-0150, 1029-4953. URL <http://dx.doi.org/10.1080/10420150410001724495> [Accessed: 2014-04-15].
- [131] Boxleitner, W., Hobler, G., Klüppel, V., and Cerva, H. "Simulation of topography evolution and damage formation during TEM sample preparation using focused ion beams." *Nuclear Instruments and Methods in Physics Research Section B: Beam Interactions with Materials and Atoms*, vol. 175–177, pp. 102–107 (Apr. 2001). ISSN 0168-583X. URL [http://dx.doi.org/10.1016/S0168-583X\(01\)00334-2](http://dx.doi.org/10.1016/S0168-583X(01)00334-2) [Accessed: 2014-04-15].
- [132] Kim, H.-B., Hobler, G., Steiger, A., Lugstein, A., and Bertagnolli, E. "Level set approach for the simulation of focused ion beam processing on the micro/nano scale." *Nanotechnology*, vol. 18, no. 26, p. 265307 (Jul. 2007). ISSN 0957-4484. URL <http://dx.doi.org/10.1088/0957-4484/18/26/265307> [Accessed: 2014-04-15].
- [133] Budil, M. and Hobler, G. "Topography simulation of sputtering using an algorithm with second order approximation in space." *Nuclear Instruments and Methods in Physics Research Section B: Beam Interactions with Materials and Atoms*, vol. 269, no. 14, pp. 1614–1618 (Jul. 2011). ISSN 0168-583X. URL <http://dx.doi.org/10.1016/j.nimb.2010.11.010> [Accessed: 2014-04-15].
- [134] Kunder, D. *3D Simulation of Sputter Etching with the Monte-Carlo Approach: 3D Simulation Des Zerstäubungsätzens Mittels Der Monte-Carlo Methode* (2011).
- [135] Youngner, D. W. and Haynes, C. M. "Modeling ion beam milling." *Journal of Vacuum Science & Technology*, vol. 21, no. 2, pp. 677–680 (Jul. 1982). ISSN 0022-5355. URL <http://dx.doi.org/10.1116/1.571812> [Accessed: 2014-04-15].
- [136] Lindsey, S. and Hobler, G. "The significance of redeposition and backscattering in nanostructure formation by focused ion beams." *Nuclear Instruments and Methods in Physics Research Section B: Beam Interactions with Materials and Atoms*, vol. 282, pp. 12–16 (Jul. 2012). ISSN 0168-583X. URL <http://dx.doi.org/10.1016/j.nimb.2011.08.051> [Accessed: 2014-04-15].

- [137] Moreno-Marin, J. C., Valles-Abarca, J. A., and Gras-Marti, A. "Secondary effects in ion milling." *Journal of Vacuum Science & Technology B*, vol. 4, no. 1, pp. 322–325 (Jan. 1986). ISSN 2166-2746, 2166-2754. URL <http://dx.doi.org/10.1116/1.583323> [Accessed: 2014-04-15].
- [138] van Delft, F. C., Ebm, C., Naburgh, E. P., Platzgummer, E., Loeschner, H., and Gross, G. "Three-dimensional projection mask-less patterning (PMLP) of micro-lenses and cones: Monitoring and modelling of ion multi-beam kinetic sputtering in GaAs." *Microelectronic Engineering*, vol. 85, no. 5-6, pp. 937–941 (May 2008). ISSN 01679317. URL <http://dx.doi.org/10.1016/j.mee.2007.12.021> [Accessed: 2013-06-07].
- [139] Ebm, C., Hobler, G., Waid, S., and Wanzenboeck, H. D. "Quantitative simulation of ion-beam induced deposition of nanostructures." *Journal of Vacuum Science & Technology B*, vol. 29, no. 1, p. 011031 (2011). URL <http://scitation.aip.org/content/avs/journal/jvstb/29/1/10.1116/1.3533951> [Accessed: 2014-04-15].
- [140] Ebm, C., Platzgummer, E., Loeschner, H., Eder-Kapl, S., Joechl, P., Kuemmel, M., Reitingner, R., Hobler, G., Koeck, A., Hainberger, R., Wellenzohn, M., Letzkus, F., and Irmischer, M. "Ion multibeam nanopatterning for photonic applications: Experiments and simulations, including study of precursor gas induced etching and deposition." *Journal of Vacuum Science & Technology B: Microelectronics and Nanometer Structures*, vol. 27, no. 6, p. 2668 (2009). ISSN 10711023. URL <http://dx.doi.org/10.1116/1.3242693> [Accessed: 2014-04-15].
- [141] Kim, H.-B., Hobler, G., Lugstein, A., and Bertagnolli, E. "Simulation of ion beam induced micro/nano fabrication." *Journal of Micromechanics and Microengineering*, vol. 17, no. 6, pp. 1178–1183 (Jun. 2007). ISSN 0960-1317, 1361-6439. URL <http://dx.doi.org/10.1088/0960-1317/17/6/011> [Accessed: 2014-04-15].
- [142] Kim, H.-B., Hobler, G., Steiger, A., Lugstein, A., and Bertagnolli, E. "Full three-dimensional simulation of focused ion beam micro/nanofabrication." *Nanotechnology*, vol. 18, no. 24, p. 245303 (Jun. 2007). ISSN 0957-4484, 1361-6528. URL <http://dx.doi.org/10.1088/0957-4484/18/24/245303> [Accessed: 2014-04-15].
- [143] Kim, H.-B., Hobler, G., Steiger, A., Lugstein, A., and Bertagnolli, E. "Simulation-based approach for the accurate fabrication of blazed grating structures by FIB." *Optics Express*, vol. 15, no. 15, pp. 9444–9449 (Jul. 2007). URL <http://dx.doi.org/10.1364/OE.15.009444> [Accessed: 2014-04-15].
- [144] Kunder, D., Baer, E., Sekowski, M., Pichler, P., and Rommel, M. "Simulation of focused ion beam etching by coupling a topography simulator and a Monte-Carlo sputtering yield simulator."

- Microelectronic Engineering*, vol. 87, no. 5–8, pp. 1597–1599 (May 2010). ISSN 0167-9317. URL <http://dx.doi.org/10.1016/j.mee.2009.11.007> [Accessed: 2014-04-17].
- [145] “Welcome to Python.org.” URL <https://www.python.org/> [Accessed: 2014-12-02].
- [146] Perez, F., Granger, B., and Hunter, J. “Python: An Ecosystem for Scientific Computing.” *Computing in Science Engineering*, vol. 13, no. 2, pp. 13–21 (Mar. 2011). ISSN 1521-9615. URL <http://dx.doi.org/10.1109/MCSE.2010.119>.
- [147] Developers, N. *Scientific computing tools for python-numpy* (Numpy, 2010).
- [148] Jones, E., Oliphant, T., Peterson, P., et al. “SciPy: Open source scientific tools for Python.” *Web* <http://www.scipy.org> (2001).
- [149] Samet, H. “The Quadtree and Related Hierarchical Data Structures.” *ACM Comput. Surv.*, vol. 16, no. 2, pp. 187–260 (Jun. 1984). ISSN 0360-0300. URL <http://dx.doi.org/10.1145/356924.356930> [Accessed: 2014-06-03].
- [150] “scipy.interpolate.splrep — SciPy v0.14.0 Reference Guide.” URL <http://docs.scipy.org/doc/scipy-0.14.0/reference/generated/scipy.interpolate.splrep.html#scipy.interpolate.splrep> [Accessed: 2014-11-22].
- [151] Dierckx, P. “Curve and surface fitting with splines, 1993.” *Monographs on Numerical Analysis*, Oxford University Press.
- [152] Dierckx, P. “An improved algorithm for curve fitting with spline functions.” *TW Reports* (1981).
- [153] Dierckx, P. “A fast algorithm for smoothing data on a rectangular grid while using spline functions.” *SIAM Journal on Numerical Analysis*, vol. 19, no. 6, pp. 1286–1304 (1982).
- [154] Dierckx, P. “An algorithm for smoothing, differentiation and integration of experimental data using spline functions.” *Journal of Computational and Applied Mathematics*, vol. 1, no. 3, pp. 165–184 (Sep. 1975). ISSN 0377-0427. URL [http://dx.doi.org/10.1016/0771-050X\(75\)90034-0](http://dx.doi.org/10.1016/0771-050X(75)90034-0) [Accessed: 2014-11-22].
- [155] “scipy.interpolate.SmoothBivariateSpline — SciPy v0.14.0 Reference Guide.” URL <http://docs.scipy.org/doc/scipy-0.14.0/reference/generated/scipy.interpolate.SmoothBivariateSpline.html> [Accessed: 2014-11-22].
- [156] “scipy.interpolate.bisplrep — SciPy v0.14.0 Reference Guide.” URL <http://docs.scipy.org/doc/scipy-0.14.0/reference/generated/scipy.interpolate.bisplrep.html> [Accessed: 2014-11-24].

- [157] Yamamura, Y., Mössner, C., and Oechsner, H. "Angular distributions of sputtered atoms from ion-bombarded surfaces." *Radiation Effects*, vol. 105, no. 1-2, pp. 31–41 (1987). ISSN 0033-7579. URL <http://dx.doi.org/10.1080/00337578708210060> [Accessed: 2014-06-05].
- [158] Lindsey, S., Waid, S., Hobler, G., Wanzenböck, H. D., and Bertagnolli, E. "Inverse modeling of FIB milling by dose profile optimization." *Nuclear Instruments and Methods in Physics Research Section B: Beam Interactions with Materials and Atoms*, vol. 341, no. 15, pp. 77–83 (Dec. 2014). ISSN 0168-583X. URL <http://dx.doi.org/10.1016/j.nimb.2014.09.006> [Accessed: 2014-10-10].
- [159] Vasile, M. J., Niu, Z., Nassar, R., Zhang, W., and Liu, S. "Focused ion beam milling: depth control for three-dimensional microfabrication." *Journal of Vacuum Science & Technology B*, vol. 15, no. 6, pp. 2350–2354 (1997). URL <http://scitation.aip.org/content/avs/journal/jvstb/15/6/10.1116/1.589644> [Accessed: 2014-04-15].
- [160] Fu, Y. and Bryan, N. K. A. "Fabrication of three-dimensional microstructures by two-dimensional slice by slice approaching via focused ion beam milling." *Journal of Vacuum Science & Technology B: Microelectronics and Nanometer Structures*, vol. 22, no. 4, p. 1672 (2004). ISSN 0734211X. URL <http://dx.doi.org/10.1116/1.1761460> [Accessed: 2014-04-15].
- [161] Vasile, M. J., Xie, J., and Nassar, R. "Depth control of focused ion-beam milling from a numerical model of the sputter process." *Journal of Vacuum Science & Technology B*, vol. 17, no. 6, pp. 3085–3090 (1999). URL <http://scitation.aip.org/content/avs/journal/jvstb/17/6/10.1116/1.590959> [Accessed: 2014-04-15].
- [162] Vasile, M. J. "Focused ion beam technology applied to microstructure fabrication." *Journal of Vacuum Science & Technology B: Microelectronics and Nanometer Structures*, vol. 16, no. 4, p. 2499 (Jul. 1998). ISSN 0734211X. URL <http://dx.doi.org/10.1116/1.590198> [Accessed: 2014-04-15].
- [163] Kim, H.-B. "Multiple surface driving method for the accurate sculpting of predefined arbitrary surfaces in the micro/nano regime." *Microelectronic Engineering*, vol. 91, pp. 14–18 (Mar. 2012). ISSN 01679317. URL <http://dx.doi.org/10.1016/j.mee.2011.11.015> [Accessed: 2014-04-15].
- [164] Svintsov, A., Zaitsev, S., Lalev, G., Dimov, S., Velkova, V., and Hirshy, H. "FIB sputtering optimization using Ion Reverse Software." *Microelectronic Engineering*, vol. 86, no. 4-6, pp.

- 544–547 (Apr. 2009). ISSN 01679317. URL <http://dx.doi.org/10.1016/j.mee.2009.01.073> [Accessed: 2014-04-15].
- [165] Jones, E., Oliphant, T., and Peterson, P. “SciPy: Open source scientific tools for Python.” (2001). URL http://www.scipy.org/Citing_SciPy [Accessed: 2014-06-07].
- [166] Garbow, B. S., Hillstom, K. E., and Moré, J. J. “Implementation guide for MINPACK-1.” (1980). URL <http://cds.cern.ch/record/125926> [Accessed: 2014-06-07].
- [167] Moré, J. J., Garbow, B. S., and Hillstom, K. E. “User guide for MINPACK-1.” (Aug. 1980). URL <http://cds.cern.ch/record/126569> [Accessed: 2014-06-07].
- [168] Moré, J. J. “The Levenberg-Marquardt algorithm: Implementation and theory.” In Watson, G. A. (Editor), “Numerical Analysis,” No. 630 in Lecture Notes in Mathematics, (pp. 105–116) (Springer Berlin Heidelberg, 1978). ISBN 978-3-540-08538-6, 978-3-540-35972-2. URL <http://link.springer.com/chapter/10.1007/BFb0067700> [Accessed: 2014-06-07].
- [169] “scipy.optimize.leastsq — SciPy v0.14.0 Reference Guide.” URL <http://docs.scipy.org/doc/scipy/reference/generated/scipy.optimize.leastsq.html> [Accessed: 2014-06-09].
- [170] Chidrawar, S., Bhaskarwar, S., and Patre, B. “Implementation of Neural Network for Generalized Predictive Control: A Comparison between a Newton Raphson and Levenberg Marquardt Implementation.” In “2009 WRI World Congress on Computer Science and Information Engineering,” vol. 1, (pp. 669–673) (2009). URL <http://dx.doi.org/10.1109/CSIE.2009.849>.
- [171] Battiti, R. “First- and Second-Order Methods for Learning: Between Steepest Descent and Newton’s Method.” *Neural Computation*, vol. 4, no. 2, pp. 141–166 (Mar. 1992). ISSN 0899-7667. URL <http://dx.doi.org/10.1162/neco.1992.4.2.141> [Accessed: 2014-06-09].
- [172] “scipy.optimize.nnls — SciPy v0.13.0 Reference Guide.” URL <http://docs.scipy.org/doc/scipy-0.13.0/reference/generated/scipy.optimize.nnls.html> [Accessed: 2014-06-09].
- [173] Lawson, C. and Hanson, R. *Solving Least Squares Problems*. Classics in Applied Mathematics (Society for Industrial and Applied Mathematics, 1995). ISBN 978-0-89871-356-5. URL <http://epubs.siam.org/doi/book/10.1137/1.9781611971217> [Accessed: 2014-06-09].
- [174] Santamore, D., Edinger, K., Orloff, J., and Melngailis, J. “Focused ion beam sputter yield change as a function of scan speed.” *Journal of Vacuum Science & Technology B*, vol. 15, no. 6, pp. 2346–2349 (Nov. 1997). ISSN 2166-2746, 2166-2754. URL <http://dx.doi.org/10.1116/1.589643> [Accessed: 2014-06-12].

- [175] Waid, S. "Private Communication." (Nov. 2011).
- [176] Waid, S. "Fabrication of 3D Axon Isolation Channels by Inverse Modelling Assisted Focused Ion Beam Patterning." (Sep. 2012). URL http://www.mne12.org/en/?page_id=964 [Accessed: 2014-12-25].
- [177] Waid, S. "Private Communication." (Jun. 2012).
- [178] Garrison, B. J., Reimann, C. T., Winograd, N., and Harrison, D. E. "Energy and angular distributions of Rh atoms ejected due to ion bombardment from Rh{111}: A theoretical study." *Physical Review B*, vol. 36, no. 7, pp. 3516–3521 (Sep. 1987). URL <http://dx.doi.org/10.1103/PhysRevB.36.3516> [Accessed: 2014-11-26].
- [179] Frey, L., Lehrer, C., and Ryssel, H. "Nanoscale effects in focused ion beam processing." *Applied Physics A: Materials Science & Processing*, vol. 76, no. 7, pp. 1017–1023 (May 2003). ISSN 0947-8396, 1432-0630. URL <http://dx.doi.org/10.1007/s00339-002-1943-1> [Accessed: 2014-04-15].
- [180] Hobler, G. "IMSIL Manual." *TU Vienna, Austria* (2003).
- [181] M. Maazouz, FEI Company. "Private Communication." (2012).
- [182] Ziegler, J. F. and Biersack, J. P. "SRIM-2008, Stopping Power and Range of Ions in Matter." (2008).
- [183] Lindhard, J. and Scharff, M. "Energy Dissipation by Ions in the keV Region." *Physical Review*, vol. 124, no. 1, pp. 128–130 (Oct. 1961). URL <http://dx.doi.org/10.1103/PhysRev.124.128> [Accessed: 2014-06-25].
- [184] S Oen, O. and T Robinson, M. "Computer studies of the reflection of light ions from solids." *Nuclear Instruments and Methods*, vol. 132, pp. 647–653 (1976).
- [185] Lindsey, S. and Hobler, G. "Sputtering of silicon at glancing incidence." *Nuclear Instruments and Methods in Physics Research Section B: Beam Interactions with Materials and Atoms*, vol. 303, pp. 142–147 (May 2013). ISSN 0168-583X. URL <http://dx.doi.org/10.1016/j.nimb.2012.12.087> [Accessed: 2014-04-15].
- [186] Eckstein, W. *Computer simulation of ion-solid interactions*, vol. 10 (Springer-Verlag Berlin, 1991). URL <http://tocs.ulb.tu-darmstadt.de/16483154.pdf> [Accessed: 2014-06-24].

- [187] Olesinski, R. W., Kanani, N., and Abbaschian, G. J. "The Ga-Si (Gallium-Silicon) system." *Bulletin of Alloy Phase Diagrams*, vol. 6, no. 4, pp. 362–364 (Aug. 1985). ISSN 0197-0216. URL <http://dx.doi.org/10.1007/BF02880523> [Accessed: 2014-06-25].
- [188] Frost, F., Ziberi, B., Höche, T., and Rauschenbach, B. "The shape and ordering of self-organized nanostructures by ion sputtering." *Nuclear Instruments and Methods in Physics Research Section B: Beam Interactions with Materials and Atoms*, vol. 216, pp. 9–19 (Feb. 2004). ISSN 0168-583X. URL <http://dx.doi.org/10.1016/j.nimb.2003.11.014> [Accessed: 2014-06-26].
- [189] Erlebacher, J., Aziz, M. J., Chason, E., Sinclair, M. B., and Floro, J. A. "Nonlinear amplitude evolution during spontaneous patterning of ion-bombarded Si(001)." *Journal of Vacuum Science & Technology A*, vol. 18, no. 1, pp. 115–120 (Jan. 2000). ISSN 0734-2101, 1520-8559. URL <http://dx.doi.org/10.1116/1.582127> [Accessed: 2014-06-26].
- [190] Erlebacher, J., Aziz, M. J., Chason, E., Sinclair, M. B., and Floro, J. A. "Spontaneous Pattern Formation on Ion Bombarded Si(001)." *Physical Review Letters*, vol. 82, no. 11, pp. 2330–2333 (Mar. 1999). URL <http://dx.doi.org/10.1103/PhysRevLett.82.2330> [Accessed: 2014-06-26].
- [191] Chason, E. and Aziz, M. J. "Spontaneous formation of patterns on sputtered surfaces." *Scripta Materialia*, vol. 49, no. 10, pp. 953–959 (Nov. 2003). ISSN 1359-6462. URL [http://dx.doi.org/10.1016/S1359-6462\(03\)00474-3](http://dx.doi.org/10.1016/S1359-6462(03)00474-3) [Accessed: 2014-06-26].
- [192] Norris, S. A., Samela, J., Bukonte, L., Backman, M., Djurabekova, F., Nordlund, K., Madi, C. S., Brenner, M. P., and Aziz, M. J. "Molecular dynamics of single-particle impacts predicts phase diagrams for large scale pattern formation." *Nature Communications*, vol. 2, p. 276 (Apr. 2011). URL <http://dx.doi.org/10.1038/ncomms1280> [Accessed: 2014-06-26].
- [193] Chason, E., Chan, W. L., and Bharathi, M. S. "Kinetic Monte Carlo simulations of ion-induced ripple formation: Dependence on flux, temperature, and defect concentration in the linear regime." *Physical Review B*, vol. 74, no. 22, p. 224103 (Dec. 2006). URL <http://dx.doi.org/10.1103/PhysRevB.74.224103> [Accessed: 2014-06-26].
- [194] Yamamura, Y., Mössner, C., and Oechsner, H. "The bombarding-angle dependence of sputtering yields under various surface conditions." *Radiation Effects*, vol. 103, no. 1-4, pp. 25–43 (1987). ISSN 0033-7579. URL <http://dx.doi.org/10.1080/00337578708221239> [Accessed: 2014-06-26].

- [195] Yamamura, Y., Mössner, C., and Oechsner, H. "Angular distributions of sputtered atoms from ion-bombarded surfaces." *Radiation Effects*, vol. 105, no. 1-2, pp. 31–41 (1987). ISSN 0033-7579. URL <http://dx.doi.org/10.1080/00337578708210060> [Accessed: 2014-06-26].
- [196] Fahrion, J. "Private Communication." (May 2012).
- [197] Woyak, K. "Private Communication." (Nov. 2011).
- [198] Okutani, T., Shikata, M., Ichimura, S., and Shimizu, R. "Angular distribution of Si atoms sputtered by keV Ar⁺ ions." *Journal of Applied Physics*, vol. 51, no. 5, pp. 2884–2887 (May 1980). ISSN 0021-8979, 1089-7550. URL <http://dx.doi.org/10.1063/1.327957> [Accessed: 2014-09-04].
- [199] Hobler, G. "Private Communication." (Jan. 2015).
- [200] Ziegler, J. F. *Ion Implantation Science and Technology 2e* (Elsevier, 2012). ISBN 9780323161657.
- [201] Chatterjee, A. and Vlachos, D. G. "Multiscale spatial Monte Carlo simulations: Multigriding, computational singular perturbation, and hierarchical stochastic closures." *The Journal of Chemical Physics*, vol. 124, no. 6, p. 064110 (Feb. 2006). ISSN 0021-9606, 1089-7690. URL <http://dx.doi.org/10.1063/1.2166380> [Accessed: 2014-12-03].
- [202] Katsoulakis, M. A. and Vlachos, D. G. "Coarse-grained stochastic processes and kinetic Monte Carlo simulators for the diffusion of interacting particles." *The Journal of Chemical Physics*, vol. 119, no. 18, pp. 9412–9427 (Nov. 2003). ISSN 0021-9606, 1089-7690. URL <http://dx.doi.org/10.1063/1.1616513> [Accessed: 2014-12-03].
- [203] Chatterjee, A. and Vlachos, D. G. "An overview of spatial microscopic and accelerated kinetic Monte Carlo methods." *Journal of Computer-Aided Materials Design*, vol. 14, no. 2, pp. 253–308 (Jul. 2007). ISSN 0928-1045, 1573-4900. URL <http://dx.doi.org/10.1007/s10820-006-9042-9> [Accessed: 2014-12-03].
- [204] Xu, H., Osetsky, Y., and Stoller, R. "Simulating complex atomistic processes: On-the-fly kinetic Monte Carlo scheme with selective active volumes." *Physical Review B*, vol. 84, no. 13, p. 132103 (Oct. 2011). URL <http://dx.doi.org/10.1103/PhysRevB.84.132103> [Accessed: 2014-12-03].
- [205] Scott, C. and Smith, R. "Sputtering of Au surfaces at realistic dose rates using molecular dynamics and on-the-fly kinetic Monte Carlo." *Nuclear Instruments and Methods in Physics*

- Research Section B: Beam Interactions with Materials and Atoms*, vol. 303, pp. 192–195 (May 2013). ISSN 0168-583X. URL <http://dx.doi.org/10.1016/j.nimb.2012.10.017> [Accessed: 2014-12-03].
- [206] Schmatz, W., Springer, T., Schelten, J., and Ibel, K. “Neutron small-angle scattering: experimental techniques and applications.” *Journal of Applied Crystallography*, vol. 7, no. 2, pp. 96–116 (Apr. 1974). ISSN 0021-8898. URL <http://dx.doi.org/10.1107/S0021889874008880> [Accessed: 2014-10-10].
- [207] Scheckler, E. and Neureuther, A. R. “Models and algorithms for three-dimensional topography simulation with SAMPLE-3D.” *IEEE Transactions on Computer-Aided Design of Integrated Circuits and Systems*, vol. 13, no. 2, pp. 219–230 (Feb. 1994). ISSN 0278-0070. URL <http://dx.doi.org/10.1109/43.259945>.
- [208] Cristini, V., Bławdziewicz, J., and Loewenberg, M. “An Adaptive Mesh Algorithm for Evolving Surfaces: Simulations of Drop Breakup and Coalescence.” *Journal of Computational Physics*, vol. 168, no. 2, pp. 445–463 (Apr. 2001). ISSN 0021-9991. URL <http://dx.doi.org/10.1006/jcph.2001.6713> [Accessed: 2014-12-03].
- [209] Rivara, M. C. “Algorithms for refining triangular grids suitable for adaptive and multigrid techniques.” *International Journal for Numerical Methods in Engineering*, vol. 20, no. 4, pp. 745–756 (Apr. 1984). ISSN 1097-0207. URL <http://dx.doi.org/10.1002/nme.1620200412> [Accessed: 2014-12-03].
- [210] Giovannini, D. “Private Communication.” (Sep. 2012).

Acronyms

AFM Atomic Force Microscopy

A surface characterization technique whereby a fine mechanical probe is used to measure different surface properties such as height by repetitively sampling the surface, e.g. using a tapping motion, thereby producing a heightmap with sub nanometer resolution. Variations of the technique can be used to measure other surface properties as a function of position such as resistance or mechanical properties.

BCA Binary Colisions Approximation is a subset of atomistic Monte-Carlo techniques often used to simulate energetic ion interactions in solids. The technique is notable because the multi-part of the multi-bodied problem of classical atomic interactions is neglected and only pair-wise potentials are used.

CVD Chemical Vapor Deposition is a materials synthesis technique whereby thermal deposition occurs from a low to moderate pressure gas phase over a temperature gradient. Often a working fluid such as iodine vapor is used to increase efficiency of the reaction. This method is used for the production of novel nano-structures and deposition of films. Nanowires are often grown with the aid of a noble metal catalyst which localizes and stabilizes the growth of nanowires.

DFT Density Functional Theory is an ab-initio quantum dynamical modeling method that takes into account the many-bodied electron behavior in atomic systems. DFT may be combined with classical MD in order to generate quantum dynamically consistent interatomic potentials leading to atomic displacements.

DRIE Deep Reactive Ion Etching is a highly anisotropic etch process that utilizes chemically active ions in a low pressure plasma to remove the substrate. Anisotropy is enhanced through the use of either cryogenic temperatures or the Bosch process which consists the time-multiplexed deposition of an etch stop.

EBS Electron BackScatter Diffraction

A technique used in scanning electron microscopy (SEM) to measure the diffraction patterns of backscattered electrons, this technique gives information about the crystal orientation of a specimen.

EDX Energy Dispersive X-ray Spectroscopy

An analysis technique that measures the energies of X-rays emitted as electrons are ionized in the shells of specimen atoms, this provides information as to the elemental content of the specimen.

FEV Field Evaporation

A process by which a strong field gradient draws an ion out of a liquid.

FIB Focused Ion Beam

A focused beam of charged atoms or molecules, that can be scanned across a specimen roughly analogously to an scanning electron beam in a SEM. As ions have a greater mass and size than electrons they interact more strongly with matter and can induce sputtering.

FIM Field Ion Microscopy is a technique where noble gases interact with a highly charged cryogenic metallic tip (acting as the sample) where they are ionized through interactions with individual atoms. These ionized ions are collected and imaged on a scintillator where angstrom resolutions can be achieved allowing for the imaging of individual atoms.

FWHM Full Width at Half Maximum

A metric used to describe the width of a function with an arbitrary peak, though usually applied to near Gaussian distributions, based on the width of the function as measured at the half value of the functions maximum.

GFIS Gas phase Field Ionization Sources are ion sources where the accelerated species originally comes from a gas phase and is field ionized by a highly sharpened metal tip. The tips can be trimers (coming to a point made up of three atoms) or single atom.

HIM Helium ion microscopy is a form of focused ion beam technology whereby a focused helium beam from a GFIS is used to image or nano-machine a sample with high lateral resolution.

KMC Kinetic Monte Carlo refers to a subset of Monte Carlo simulations where atom displacements are driven by stochastic migration phenomena. Atomistic simulations involving KMC usually involve the mobilities of a simulated species and are used to study diffusive phenomena. As atomic displacements occur by hopping, KMC simulations can be significantly faster than MD.

LMIS Liquid Metal Ion Source

A source of ions for FIB where a liquidized metal is ionized through field evaporation at the end of a sharpened emitter tip subjected to high electric fields.

MBE Molecular Beam Epitaxy is a synthesis technique for high-purity, low-disorder, crystal layers whereby sublimed source elements are deposited under ultra-high-vacuum conditions onto a target substrate. MBE usually involves numerous source elements and a system of computer controlled shutters to precisely control the growth rate and composition of epitaxially grown crystals.

MC Monte Carlo simulations attempt to reduce a system to event probabilities. The probabilities are usually deterministically used in a model system to predict average behavior, enabling simpler physical models to be accurate with respect to the average behavior.

MD Molecular Dynamics is the simulation of classical Newtonian dynamics using inter-atomic potentials in order to simulate the time evolution of atomic systems. The multi-bodied system is solved by calculating the resultant force imparted on each simulation particle by every other particle within an interaction volume. This force is converted into a velocity over a time period defined by the simulation timestep which results in a finite displacement, after which the force fields are re-evaluated and movements occur over the next time step.

MEMS MicroElectroMechanical Systems

Small scale electrical and/or mechanical systems that make use of the interesting physics at small scales.

NIL Nano Imprint Lithography is a pattern formation technique whereby small scale templates are used to physically modify materials through intimate contact. Usually the modification takes place through the mechanisms of embossing or casting in place.

RIE Reactive Ion Etching is an anisotropic etching process whereby chemically reactive ions are electrically accelerated at a substrate through a vacuum atmosphere where the substrate is chemically etched by the ions and any sputtering is outweighed by chemical effects. The anisotropic effect comes from the directed nature of the exposure and the degree of anisotropy can be adjusted through modification of the degree of vacuum used.

SAT Single atom terminated tips are a demonstrated GFIS tip geometry whereby the emitter tip ends in a single atom instead of the trimer normally used in GFIS.

- SEM** Scanning Electron Microscopy or REM Raster Electron Microscopy is a surface, or near-surface, sensitive imaging technique by which imaging is accomplished by scanning a focused electron beam over the sample. Topographical and compositional contrast can be observed within the beam interaction volume with the target. Typical signal acquisition is accomplished by spatial correlation of ejected secondary electrons (excited by the electron beam), similar to the mechanism used in SIM. As electrons scatter more easily than ions, SEM is usually more surface sensitive than SIM.
- SIM** Scanning Ion Microscopy
A technique using an ion beam as a probe to produce a magnified image of a microscopic feature; the detected particles can be either ions or electrons.
- SIMS** Secondary Ion Mass Spectroscopy
An analysis technique that measures the mass of ions ejected from a specimen undergoing ion irradiation; that information is used to determine the chemical species found in the specimen.
- STM** Scanning Tunneling Microscopy is an imaging technique where the electron tunneling current between a highly sharpened probe tip and a sample surface is used to physically map and probe atomic locations. Additionally, due to the single atom resolution of this technique it is sometimes used to push individual atoms across a surface.
- TEM** Transmission Electron Microscopy
An electron microscopy technique where electrons are passed through a thin electron-transparent specimen and the attenuation and deflection of these electrons is used to analyze the specimen.
- TMAH** Tetramethylammonium hydroxide is a quaternary ammonium salt with the molecular formula $N(CH_3)_4^+ OH^-$ commonly used to anisotropically etch silicon.
- VLSI** Very Large Scale Integration
An integrated circuit containing greater than 10,000 gates (as compared to LSI, MSI, and SSI for large, medium, and small scale integration).

Index

A

amorphization threshold, 7
amorphous, 72, 75, 95
amorphous silicon, 97, 131, 138
anisotropic etching, 13
auger electron microprobe, 94

B

beam blanker, 4

C

collision cascade, 15, 19, 96, 104, 135, 154
coulomb repulsion, 4

D

dimpling, 2

E

electron beam assisted etching, 2
electron gun, 5, 6
electrostatic lens, 1, 4
eucentric point, 5

F

Faraday cup, 4
first-knock-on, 29, 96, 103, 144
free-flight-path, 73
FWHM, 47, 58

G

gas assisted deposition, 1, 6, 8, 12, 14, 16
gas assisted etching, 1, 6, 9, 10, 15, 17, 52

Gaussian distribution, 4

GFIS, 2

H

Holtzmark distribution, 4

I

imaging, 2, 5–7, 10–12, 16

implantation window, 82

IMSIL, 23, 28, 38, 71–74, 76, 81, 103, 127, 134,
151

inter-atomic potentials, 18

K

knock-on, 43

L

level-set, 21

lift-out, 8

Line implant, 82

LMIS, 2, 11, 14, 15

M

MARLOWE, 19, 20

microtome, 2, 8

microtrench, 48

micro-trenching, 138

miscibility gap, 79

N

nanoimprint template, 13

O

overlapped beam, 46, 66, 67, 138

P

photo-lithography, 2, 9, 12, 13

precision doping, 1, 11, 14

projected range, 82

S

saturation, 46

simple visibility, 138

snow-plow effect, 48, 53, 66

SRIM, 73, 74

String method, 22

string method, 22, 23, 34

T

topographical modification, 1, 2, 12

TopSim, 23, 26, 33, 35–37, 51, 53–55, 64, 66,
156, 157, 161

TRIM, 19, 20

Curriculum vitae

Sloan Jobe Lindsey
 Rudolf-Nurejew-Promenade 9/20/13
 1220 Vienna, Austria
 +43 680 3247482
 sloan.lindsey@gmail.com

**Education**

-
- Jan. 2011 to (Feb. 2015) **Dr. techn.**
 Electrical Engineering: Simulation of Focused Ion Beams
 Institute for Solid State Electronics: Vienna University of
 Technology,
 Floragasse 7
 A-1040 Vienna
 GPA 4.0
- Aug. 2006 to Aug. 2010 **Master of Science**
 Materials Science and Engineering
 Clemson University,
 SC 29634, USA
 GPA 3.50
- Aug. 2002 to May 2006 **Bachelor of Science**
 Major: Physics and Astronomy
 Minor: Mathematics
 Clemson University
 GPA 3.03

Research Experience

-
- Sept. 2010 to Sept. 2014 Project Assistant
 Institute for Solid State Electronics (fke), TUWien
 Advisor: Professor Gerhard Hobler
 Project: Simulation of Focused Ion Beam Milling
- Aug. 2006 to Aug. 2010 Graduate Research Assistant
 Dept. Materials Science and Engineering, Clemson University
 Advisor: Professor Terry Tritt
 Projects include research on: half-Heusler composites, Zintl phase
 materials, low carrier alloys.
- Oct. 2008 to July 2009 Student Researcher Exchange
 Dept. Materials Science, State Key Lab of Silicon Materials
 Zhejiang University, Hangzhou, China
 Advisor: Professor Xinbing Zhao
 Project: Single crystal growth and characterization of Zintl phase
 materials with rare earth doping.
- Oct. 2004 to Aug. 2006 Undergraduate Researcher
 Dept. Physics and Astronomy, Clemson University
 Advisor: Professor Terry Tritt
 Project: Design, construction and testing of a high temperature

probe to measure Seebeck and resistivity as a function of temperature.

- Nov. 2003 to Aug. 2004 Undergraduate Researcher
Dept. Physics and Astronomy, Clemson University
Advisor: Professor Miguel Larsen
Project: SPIRIT II and EQUIS II
- May 2001 to July 2001 Research Intern
Dept. Chemical Engineering, University of South Carolina
Advisor: Professor White
Project: Design and testing of an apparatus to measure oxygen diffusion and permeability coefficients for PEM fuel cell membranes

Publications

- S. Lindsey, S. Waid, G. Hobler, H.D. Wanzenböck, E. Bertagnolli. "Inverse modeling of FIB milling by dose profile optimization." *N.I.M.B.*, 341, (2014), Pages 77-83, <http://dx.doi.org/10.1016/j.nimb.2014.09.006>.
- S. Lindsey, and G. Hobler. "Sputtering of silicon at glancing incidence." *N.I.M.B.*, 303 (2013): 142-147, <http://dx.doi.org/10.1016/j.nimb.2012.12.087>.
- S. Lindsey, and G. Hobler. "The significance of redeposition and backscattering in nanostructure formation by focused ion beams." *N.I.M.B.*, 282 (2012): 12-16, <http://dx.doi.org/10.1016/j.nimb.2011.08.051>.
- Ponnambalam, V., S. Lindsey, W. Xie, D. Thompson, F. Drymiotis, and Terry M. Tritt. "High Seebeck coefficient AMXP2 (A= Ca and Yb; M, X= Zn, Cu and Mn) Zintl phosphides as high-temperature thermoelectric materials." *Journal of Physics D: Applied Physics* 44, no. 15 (2011): 155406.
- Capps, J., B. Ma, T. Drye, C. Nucklos, S. Lindsey, D. Rhodes, Q. Zhang, K. Modic, S. Cawthorne, and F. Drymiotis. "The effect of Ag concentration on the structural, electrical and thermal transport behavior of Pb: Te: Ag: Se mixtures and improvement of thermoelectric performance via Cu doping." *Journal of Alloys and Compounds* 509, no. 5 (2011): 1544-1549.
- Drymiotis, F. R., S. Lindsey, J. Capps, J. C. Lashley, D. Rhodes, Q. R. Zhang, C. Nucklos, and T. B. Drye. "Excess vibrational modes and high thermoelectric performance of the quenched and slow-cooled two-phase alloy $\text{Cu}_0.2\text{Ag}_2.8\text{SbSeTe}_2$." *Journal of Physics: Condensed Matter* 23, no. 13 (2011): 135305.
- Capps, J., F. Drymiotis, S. Lindsey, and T. M. Tritt. "Significant enhancement of the dimensionless thermoelectric figure of merit of the binary Ag_2Te ." *Philosophical Magazine Letters* 90, no. 9 (2010): 677-681.
- Drymiotis, F., T. Drye, D. Rhodes, Q. Zhang, J. C. Lashey, Y. Wang, S. Cawthorne, B. Ma, S. Lindsey, and T. Tritt. "Glassy thermal conductivity in the two-phase $\text{Cu}_x\text{Ag}_{3-x}\text{SbSeTe}_2$ alloy and high temperature thermoelectric behavior." *Journal of Physics: Condensed Matter* 22, no. 3 (2010): 035801.

Ponnambalam, V., X. Gao, S. Lindsey, P. Alboni, Zhe Su, B. Zhang, F. Drymiotis, M. S. Daw, and Terry M. Tritt. "Thermoelectric properties and electronic structure calculations of low thermal conductivity Zintl phase series $M_{16}X_{11}$ ($M = \text{Ca}$ and Yb ; $X = \text{Sb}$ and Bi)." *Journal of Alloys and Compounds* 484, no. 1 (2009): 80-85.

Ponnambalam, V., S. Lindsey, N. S. Hickman, and Terry M. Tritt. "Sample probe to measure resistivity and thermopower in the temperature range of 300-1000K." *Review of scientific instruments* 77, no. 7 (2006): 073904.

Presentations

- | | |
|-----------|--|
| May 2013 | Submitted (but did not attend):
Inverse Modeling of FIB Milling by Dose Profile Optimization
E-MRS 2013 (European Materials Research Society) |
| June 2012 | Oral: Sputtering of silicon at glancing incidence.
COSIRES 2012 (Computer Simulation of Radiation Effects in Solids)
Santa Fe, NM, USA |
| May 2011 | Poster: The significance of redeposition and backscattering in nanostructure formation by focused ion beams.
E-MRS 2011 (European Materials Research Society)
Nice, France |
| July 2009 | Poster: Synthesis and thermoelectric properties of non-La rare earth doped $\text{Yb}_{14}\text{MnSb}_{11}$ Zintl phase materials
ICT 2009 (28 th International Conference on Thermoelectrics),
Freiburg, Germany |

Teaching Experience

- | | |
|-------------------------|--|
| Sept. 2010 to July 2014 | Scientific English Instructor,
Scientific English, FH Tulln
Responsibilities: Lecturing and grading in classes on practical scientific English for non-native speakers |
| Jan. 2007 to May 2008 | Laboratory Teaching Assistant,
PHYS 325-326 Experimental Methods in Physics, Clemson University
Responsibilities: Grading lab reports and directing students in the use of equipment |

Technical Skills

Programming languages: Python (Numpy, Scipy), C/C++, Fortran 77/95, Labview, Java
 Software: Maple, AutoCAD, Solidworks
 SEM Microscopy, EDX, WDX, Backscatter
 Sample Preparation, Lab work including Soldering
 Flux Growth for Semi-metals, Induction Melting, Arc Melting
 Transport Measurement (Thermal and Electrical)
 Instrument Design and Automation
 Linux/Unix/BSD
 Cryogenic System and High Vacuum